Synchronized Sensing for Wide-Area Situational Awareness of Electrical Grids in Non-Stationary Operating Conditions

Thèse N° 7359

Présentée le 15 novembre 2019

à la Faculté des sciences et techniques de l'ingénieur
Laboratoire des systèmes électriques distribués
Programme doctoral en génie électrique

pour l'obtention du grade de Docteur ès Sciences

par

Asja DERVIŠKADIĆ

Acceptée sur proposition du jury

Dr S.-R. Cherkaoui, président du jury
Prof. M. Paolone, directeur de thèse
Dr C. Y. Evrenosoglu, rapporteur
Prof. D. Macii, rapporteur
Prof. M. Kezunovic, rapporteur
Prof. J.-Y. Le Boudec, rapporteur

2019

ÉCOLE POLYTECHNIQUE
FÉDÉRALE DE LAUSANNE

> An experiment is a question which science poses to Nature,
> and a measurement is the recording of Nature's answer.
>
> — Max Planck

To my brother and to my parents

Acknowledgements

I would like to thank my Thesis Director Prof. Mario Paolone for the careful guidance and for the unconditional support throughout the past 4 years of my Ph.D. studies. You taught me how to solve with a positive attitude all sort of problems, scientific and personal, and I truthfully believe that you helped me grow both as a researcher and as a person. Thank you!

A special thank goes to Dr. Rachid Cherkaoui, for all the scientific advice that you gave me, but also for your endless positiveness. I would further like to thank the members of my Ph.D. committee, Dr. Yaman Evrenosoglu, Prof. Mladen Kezunović, Prof. Jean-Yves Le Boudec, and Prof. David Macii, for their time in reviewing the Thesis and for the technical discussions.

Many thanks to all the friends and colleagues of DESL, PWRS and EMC laboratories. I was privileged to work in a unique environment, based on mutual respect and solidarity. In particular, I am grateful to my friends Paolo and Guglielmo, who patiently taught me most of the things that I have learned, and to my friends Yihui, Reza, Daniele, Marco and Lorenzo, who I had the opportunity to collaborate with. Also, I would like to thank all the students that I have supervised: your curiosity inspired my research.

My sincere gratitude goes to all my friends in Lausanne, in Rome, and all over the world. “Can miles truly separate you from friends... If you want to be with someone you love, aren’t you already there?” Enrica, you are the best friend that I could have possibly imagined for joining me in this journey, Fabrizio and Emil, you are like two big brothers. Together we went through the good and the tough times, that made our friendship everlasting. But also Chiara, Mireille, Vivian, Giacomo, Giulia, Margherita, Riccardo, Silvia, Giulia, Chiara, Stefano, Paola, Francesca, Cristina. I thank you all for being there for me, no matter what.

Finally, I warmly thank all the members of my family, the beloved ones in Rome, in Sarajevo and in Padova. I sincerely thank my brother Arman, my mum and my dad for making my education always your first priority and for having always high expectations for me. You are my motivation for improving myself and I love you!

Last but not least, Antonio, thank you for brightening (and troubling) my days!

Abstract

Situational-awareness methods and technologies are crucial elements to ensure power systems reliability and security as they are used by automated decision-making processes of mission-critical applications. Inadequate system monitoring results in incorrect or delayed actions that may potentially lead to unsafe and unstable evolution of the grid state. The distributed and time-synchronized sensing of the so-called synchrophasors is becoming increasingly adopted by systems operators especially when they plan the refurbishment of their electrical grids with Phasor Measurement Units (PMU) that provide highly accurate, low latency, and high refresh-rate estimates of voltage and current phasors. However, the concept of synchrophasor is based on a static signal model and, therefore, it provides a reliable estimation of the monitored power system signal only for quasi-steady-state conditions. Given the massive integration of inverter-connected renewable energy resources that, as such, do not provide any inertia to the system, modern electrical grids are expected to experience larger dynamics, high shares of harmonic and inter-harmonic pollution, and unprecedented electromechanical transients. Processing tools able to correctly and timely track these conditions, are certainly needed as they may enhance the overall power system situational awareness and its associated security.

Within this context, this Thesis first proposes advanced synchrophasor networks for the monitoring and control of power grids operating in close-to-stationary conditions. More specifically, enhanced processing tools able to accurately and timely estimate the synchrophasors using extremely short observation intervals are proposed. The first method is based on the interpolated discrete Fourier transform that iteratively estimates and compensates the effects of the spectral leakage produced by interfering tones, harmonic or inter-harmonic, and the negative image of the fundamental tone. As an evolution of this algorithm, the second one adopts the same routine to minimize the effect of interfering tones and is based on the Hilbert transform. The latter eliminates the spectral interference generated by the negative image of all the tones under analysis, therefore enabling a further reduction of the observation window. The compliance of the proposed methods with respect to international standards for measurement and protection applications is verified (i.e., the IEEE Std. C37.118). The integration of the proposed algorithms into embedded hardware platforms demonstrates their prospective deployability into a new PMU prototype. Further, the developed PMU is synchronized with respect to time using cutting-edge time dissemination technologies like the one provided by the White Rabbit protocol. The superior accuracy in estimating the synchrophasors provided by the algorithms and the PMU devices developed in this Thesis, calls for a calibration process of exceptional performance. In this view, the hardware and software architecture of an advanced validation platform for PMU type-testing is presented and metrologically characterized. Finally, the seamless streaming of synchrophasor data over the underlying communication infrastructure is investigated by considering wired and wireless physical layers and by proposing a time-deterministic phasor data concentrator.

For power systems operating in non-stationary operating conditions, the Thesis has finally proposed an innovative approach for the modeling of reduced-inertia electrical grids that goes beyond the concept of static phasor. The study is inspired by the theory on analytic signals and is based on the Hilbert transform that enables the modeling of dynamic signals. A theoretical formulation is outlined and validated over real-world data-sets, demonstrating the effectiveness of Hilbert transform-based methods. These results may contribute to the development of novel sensing technologies and may yield to a disruptive innovation in the field of power systems modeling.

Keywords: Power System Situational Awareness, Synchrophasor Networks, Synchrophasor Estimation, Phasor Measurement Unit, Discrete Fourier Transform, Hilbert Transform, Calibration, IEEE Std. C37.118, Time-synchronization, White Rabbit Protocol

Résumé

Le système de surveillance d'un réseau électrique est un élément fondamental pour assurer la fiabilité et la sécurité de son fonctionnement. Elle permet d'automatiser les procédures liées aux applications critiques. Une surveillance inadéquate du système peut conduire à des actions incorrectes ou différées, qui pourraient potentiellement mettre le réseau électrique en danger et en instabilité. Les réseaux de synchrophaseurs, deviennent de plus en plus rependus en tant que système de surveillance des réseaux électriques. Les « phasor measurement units » (PMU) fournissent des estimations des phaseurs de tension et de courant très précises, synchronisées, à faible latence et à fréquence d'échantillonnage élevée. Cependant, étant basé sur un modèle de signal stationnaire, les synchrophasors ne fournissent une estimation fiable de l'état du réseau surveillé que lorsque celui-ci est en d'équilibre stationnaire. En raison de l'intégration massive des ressources d'énergie renouvelable et distribuées, dont les convertisseurs ne fournissent aucune inertie au système, les réseaux électriques modernes font l'objet de régimes transitoires qui se caractérisent par des dynamiques rapides, de fortes proportions en termes de pollution harmonique et inter-harmonique et des transitoires électromécaniques sans précédent. Un outil de traitement des données capable de détecter correctement et en temps opportun ces transitoires, améliorerait certainement le système de surveillance du réseau électrique et la sécurité associée.

Dans ce contexte, cette thèse analyse l'utilisation des réseaux de synchrophaseurs pour la surveillance et le contrôle des réseaux électriques fonctionnant dans un état quasi-stationnaire. Initialement, des outils de traitement du signal avancés sont proposés. Ils sont capables d'estimer avec précision et en temps opportun les phaseurs en utilisant des intervalles d'observation extrêmement courts. La première méthode proposée est basée sur l'interpolation de la transformation de Fourier discrète qui estime et compense de manière itérative les effets des interférences spectrales produites par les fréquences interférentes, harmoniques ou inter-harmoniques, et par l'image négative de la fréquence fondamental. Comme évolution de cette méthode, la deuxième adopte la même routine pour minimiser l'effet des fréquences interférentes et est basé sur la transformation de Hilbert. Cette dernière élimine les interférences spectrales générées par l'image négative de toutes les fréquences analysées, permettant ainsi une réduction supplémentaire de l'intervalle d'observation. La conformité des deux méthodes proposées aux normes internationales pour les applications de mesure et de protection est vérifiée (IEEE Std. C37.118). L'intégration des algorithmes proposés dans des plates-formes intégrées démontre la possibilité de les déployer dans des réseaux électriques réelles. De plus, le PMU développé est synchronisé par rapport au temps au moyen de technologies de synchronisation temporelle de pointe, comme le protocole White Rabbit. En raison de la haute qualité de l'estimation des synchrophaseurs par les méthodes et les PMUs développés dans cette Thèse, il est nécessaire de recourir à un système d'étalonnage de haute précision. À cet égard, une plate-forme d'étalonnage de PMUs est décrite en termes d'architecture hardware et software, et sa calibration métrologique est vérifiée et présentée. Enfin, la transmission de manière rapide et fiable des données horodatées des PMU est validée dans différentes infrastructures de télécommunication (avec fil et sans fil) et un concentrateur de données des PMU est proposé.

Pour les systèmes électriques fonctionnant dans un état non stationnaire, la thèse propose une approche innovante pour la modélisation des réseaux électriques à inertie réduite qui dépasse le concept de phaseur statique. L'étude s'inspire de la théorie des représentations analytiques des signaux et est basée sur la transformation de Hilbert qui permet la modélisation des signaux dynamiques. Une formulation théorique est proposée et validée en s'appuyant sur des ensembles de données réelles, démontrant ainsi l'efficacité des méthodes basées sur la transformation de Hilbert. Celles-ci pourraient dans le futur inspirer des technologies de détection innovantes et également de nouvelles approches dans le domaine de la modélisation des systèmes électriques.

Mots clés : Systèmes de surveillance des réseaux électriques, Réseaux de synchrophaseurs, Estimation de synchrophaseurs, Phasor Measurement Unit, Transformation de Fourier discrète, Transformation de Hilbert, Étalonnage, IEEE Std. C37.118, Synchronisation temporelle, protocole White Rabbit

Contents

1 Introduction

Context and Motivations

Power systems are rapidly evolving towards low-inertia networks, and system operators are facing new challenges to operating their grids safely. Renewable energy sources and inverter-connected devices, on the one hand, do not usually provide any inertia to counteract power system disturbances, on the other hand, introduce harmonics and inter-harmonics into the system. As a consequence, phenomena that used to be uncommon in traditional power grids, such as frequency modulations, rapid frequency variations or sudden amplitude steps, are nowadays more likely to be experienced. Network operators are therefore expected to adopt advanced wide-area situational awareness tools to monitor their systems reliably. In this field, one of the most promising technologies is represented by the distributed monitoring of the so-called synchrophasors via Phasor Measurement Units (PMUs). PMUs are measurement devices that phase align phasors over different locations of an electrical grid thanks to tight time synchronization, and report these measurements with high reporting rates.

A synchrophasor is, by definition, a mathematical representation of the fundamental tone of the power system signal under analysis. Nevertheless, during electromechanical transients triggered by significant contingencies, the transmission of electrical power may take place in a broad spectrum well beyond the single fundamental component. That is particularly true of low-inertia grids, where the dynamics are faster than those experienced in bulk power systems. Traditional modeling approaches rely on the phasor representation derived from the application of the Discrete Fourier Transform (DFT) to the signal under analysis. During large transients, though, DFT-based analysis may fail to identify the fundamental component parameters accurately as the power transfer through the grid is conveyed over a broad spectrum and cannot be appropriately approximated by a finite series of DFT-coefficients. Therefore, there is a need for using mathematical transformations that go beyond the concept of phasor.

Within this context, for power grids operating in close-to-nominal frequency conditions, the Thesis analyses the use of synchronized, high refresh-rate, low latency PMU measurements to serve advanced situational awareness and control applications. All the involved technological aspects are described and experimentally validated: the measurement device hardware and software implementation, the time synchronization via innovative dissemination techniques, the measurement streaming across different telecom layers, the time-deterministic measurement collection, the PMU metrological calibration.

The Thesis further formulates advanced signal processing tools for synchrophasor estimation, to be deployed in PMUs able to estimate in real-time, and with reduced response time, power system signals parameters in highly polluted operating conditions. From a theoretical perspective, the challenges in analyzing real-world signals adopting extremely short observation windows are thoroughly described and efficiently solved. The developed algorithms are compliant with respect to the official international standards and are integrated into embedded PMU devices.

Finally, with respect to the challenging topic of sensing in low-inertia grids, the Thesis proposes a novel approach for the modeling of reduced-inertia power systems that goes beyond the traditional one based on the DFT. In this respect, an advanced technique based on the Hilbert transform is proposed. The study is mostly theoretical, covering the basics of power system modeling in the Hilbert domain and is validated over real-world data-sets.

Thesis Outline

The Thesis is organized as follows.

Chapter 2 frames the context of synchrophasor networks serving modern power system applications. The chapter discusses the appropriateness and the metrological significance of the synchrophasor model in the estimation of frequency and rate-of-change-of-frequency (ROCOF). The Chapter also provides the technical and metrological dictionary.

Chapter 3 proposes a synchrophasor estimation algorithm capable of simultaneously matching the accuracy and response requirements of both P and M performance classes as defined by the IEEE Std. C37.118. The method is based on the interpolated discrete Fourier transform (IpDFT), and iteratively estimates and compensates the effects of the spectral leakage produced by both a generic interfering tone, harmonic or inter-harmonic, and the negative image of the fundamental tone. Compliance with respect to the IEEE Std. C37.118 is fully characterized.

Chapter 4 proposes a synchrophasor estimation algorithm that enables the reduction of the observation window up to two cycles of a signal at the rated power system frequency, while still matching most of the accuracy requirements dictated by the IEEE Std. C37.118. The estimator is based on a joint application of the IpDFT and of the Hilbert transform. Specifically, the Hilbert transform enables the suppression of the spectral interference generated by the negative image of the tones under analysis, whereas the IpDFT limits the effects of spectrum granularity. The performance is assessed with respect to all the test conditions defined in the IEEE Std. C37.118, in order to detect the main uncertainty sources as well as possible room for enhancement.

Chapter 5 presents the hardware and software architecture of a highly accurate PMU calibrator for the definition of reference synchrophasors for static and dynamic characterization of PMUs. The reference values are estimated using a non-linear least-squares approach. The Chapter evaluates the quality of the generated test waveforms, and provides a thorough metrological characterization of the uncertainty contributions inherent in the calibration process.

Chapter 6 focuses on innovative time synchronization techniques for the measurement time alignment and on the reduction of the latency associated to the propagation of the synchrophasor information towards applications. Specifically, the White Rabbit time dissemination technology is studied and its implementation into a dedicated PMU device is described. With respect to state-of-the-art time synchronization techniques, the protocol provides enhanced features in terms of security, accuracy and accessibility. In addition, the architecture and experimental validation of a low latency and time deterministic phasor data concentrator is described. The function is aimed at minimizing the delay introduced by the concentration point without decreasing the data completeness.

Chapter 7 challenges the concept of synchrophasor in describing inertia-reduced power systems and, inspired by the literature on analytic signals, proposes a new approach for the modeling of transient operating conditions based on the Hilbert transform. Indeed, given the possibility to identify the whole spectrum, the Hilbert transform enables the tracking of signal dynamics. Its applicability to power system analysis is presented, opening new scenarios for the modeling of electrical grids and for modern situational awareness systems that rely on a broad spectrum.

Chapter 8 summarizes the main outcomes of the present study and future perspectives.

In view of the large amount of subjects treated by the Thesis, the literature survey is integrated at the beginning of each Chapter.

Contributions

The original contributions of this Thesis are listed in the following.

- Definition of two synchrophasor estimation algorithms capable of matching the accuracy and response requirements of advanced synchrophasor networks. The first one, is based on the interpolated DFT (IpDFT), and iteratively estimates and compensates the effects of the spectral leakage produced by both a generic interfering tone, harmonic or inter-harmonic, and the negative image of the fundamental tone. The second one aims at mitigating the uncertainty contributions of traditional DFT approaches, and is based on a joint application of the IpDFT and of the Hilbert transform. Specifically, the Hilbert transform enables the suppression of the spectral interference generated by the negative image of the tones under analysis, whereas the IpDFT limits the effects of spectrum granularity. Compliance with respect to the reference standard for PMUs is thoroughly characterized, demonstrating that the proposed algorithms fulfill the requirements of both PMU performance classes without changing the algorithm's parameters. The iterative IpDFT is also integrated into an FPGA-based PMU device, demonstrating its potential applicability to real-world synchrophasor networks.

- Design and metrological characterization of a highly accurate PMU calibrator, that is capable of reproducing all the test conditions dictated by the reference standard for PMUs as well as user defined scenarios. Hardware and software details are described in detail, in order to quantify the uncertainty contributions in estimating the reference synchrophasor, computed by means of a non-linear least-squares approach. The metrological characterization shows that the errors in estimating the reference synchrophasors are at least one order of magnitude lower than those of modern PMUs, demonstrating the suitability of the proposed calibrator for PMU type testing.

- Integration of the White Rabbit (WR) time protocol within an embedded PMU device. The WR is a low-latency, time-deterministic, Ethernet-based time dissemination technique, whose accuracy is meant to achieve the sub-nanosecond. The performance of the developed WR-synchronized PMU is thoroughly characterized, and compared to state-of-the-art time dissemination technologies for PMUs, i.e., the Global Positioning System (GPS) and the Precision Time Protocol (PTP). It is shown that the WR protocol minimizes the time uncertainty contribution to synchrophasor estimation, thus optimizing the overall PMU accuracy.

- Design of a low-latency and time-deterministic Phasor Data Concentrator (PDC) intended to minimize the latency introduced by the PDC without worsening the data delivery to subsequent applications. The developed PDC implements three different data pushing logic, that differ in the management of the PDC wait time. The performance of the three logic is assessed and compared in terms of reliability, determinism and reduction of the overall latency in two real PMU installations relying on wired (optic fiber) and wireless (4G LTE) telecom infrastructures. The experimental validation demonstrates that the developed PDC is capable of mitigating the synchrophasor data latency variations, independently from the physical layer utilized to stream PMU data, while preserving the data completeness.

- Definition of a novel approach for power system analysis based on the Hilbert transform. The inadequacy of traditional DFT-based approaches in defining the frequency during transients is studied and quantified. Elementary circuit theory laws are formulated using the Hilbert transform, proving the applicability of the proposed approach for studying power system dynamics. The performance of the proposed method is assessed in a simulated environment using synthetic datasets, real-world acquisitions as well as the results of a contingency analysis.

2 Synchrophasor Networks and Phasor Measurement Units

Modern power grids are largely reducing the inertia of generation assets making these systems prone to experience extreme dynamics. The consequence is that, during transient conditions triggered by large contingencies, the transmission of electrical power may take place over a broad spectrum around the rated grid frequency. In such conditions, the synchrophasor model loses its appropriateness as the signal energy cannot be approximated as a sequence of narrow-band sinusoidal components. Within this context, the Chapter investigates the applicability of PMU measurements in modern power system applications, discussing the appropriateness and the metrological significance of the synchrophasor model.

The chapter includes results of publications [1, 2, 3, 4, 5, 6, 7].

2.1 Introduction

The IEEE Standard for Synchrophasor Measurements for Power Systems C37.118.1 [19, 20] and the IEEE Standard for Synchrophasor Data Transfer for Power Systems C37.118.2 [21] are the international reference for synchrophasor networks [22][1]. The former deals with the measurement of synchrophasors and related performance requirements. The latter addresses the real-time transfer of synchrophasor data over communication systems. According to these Standards, the architecture of any synchrophasor network consists of at least four building blocks, that are thoroughly analyzed and experimentally validated in this Thesis (see Fig. 2.1):

1. The *sensing layer*, comprising voltage and current transducers coupled with Phasor Measurement Units (PMU), that estimate and phase align phasors located in different positions of an electrical grid;

---

[1] The Thesis interchangeably refers to the IEEE Std. C37.118 or the IEC/IEEE Std. 60255-118-1 [23].

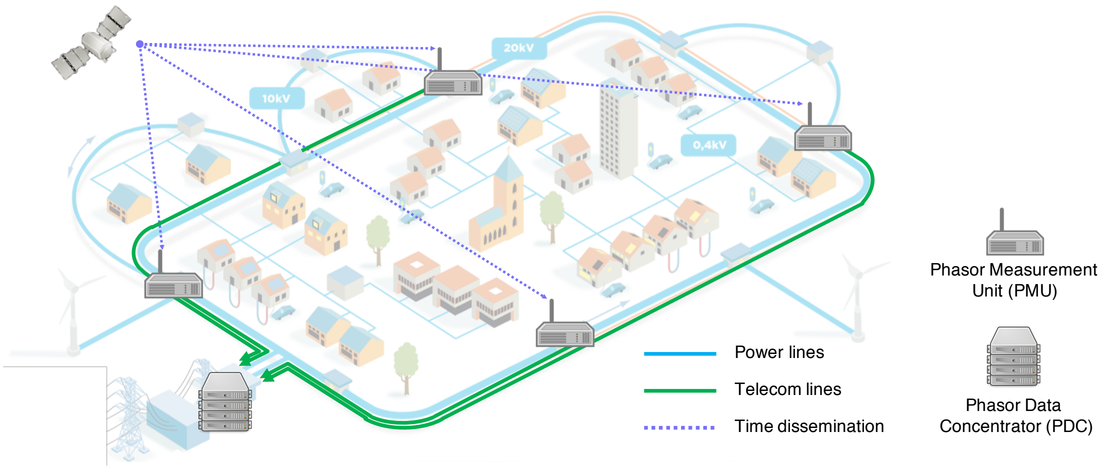

Figure 2.1 – Example of a generic synchrophasor network, including the sensing layer, the time dissemination layer, the data communication layer and the data processing layer.

2. The *time dissemination layer*, providing an accurate and reliable time reference to synchronize the phase of all PMU measurements to the UTC;
3. The *data communication layer*, that enables the streaming of PMU data and is characterized by sufficiently high bandwidth, low end-to-end latency and limited packet loss;
4. The *data processing layer*, comprising the Phasor Data Concentrator (PDC), that collects and time-aligns synchrophasors from the various PMUs in the network and eventually streams that flow of data to dedicated applications.

Among the main involved aspects, this Chapter opens the Thesis by providing a critical analysis of the most elementary and fundamental element, i.e., the concept of *synchrophasor*. According to the IEEE Std. C37.118, a synchrophasor is defined as a phasor calculated from data samples associated with a current or voltage waveform, using a standard time signal as the reference for the measurement. By definition, the synchrophasor representation relies on a static and single-tone signal model.

However, voltage and current signals are rarely in steady-state, therefore, the synchrophasor model may lose its appropriateness in real-world scenarios [24, 25, 11, 18]. This observation is particularly relevant for modern grids that, in view of integrating converter-interfaced renewable energy resources, are rapidly evolving towards low-inertia networks [26, 27, 28, 29, 30]. Inverter-connected devices, as such, do not provide any inertia to filter and attenuate the dynamics originated by power system disturbances [31, 32, 33, 34]. Also, they inject a significant level of harmonic and inter-harmonic distortion into the grid [35, 36, 37, 38]. As a consequence, phenomena that used to be exceptional in traditional networks, such as rapid frequency variations, sudden amplitude steps, frequency modulations or heavy harmonic distortion are nowadays more likely to be experienced.

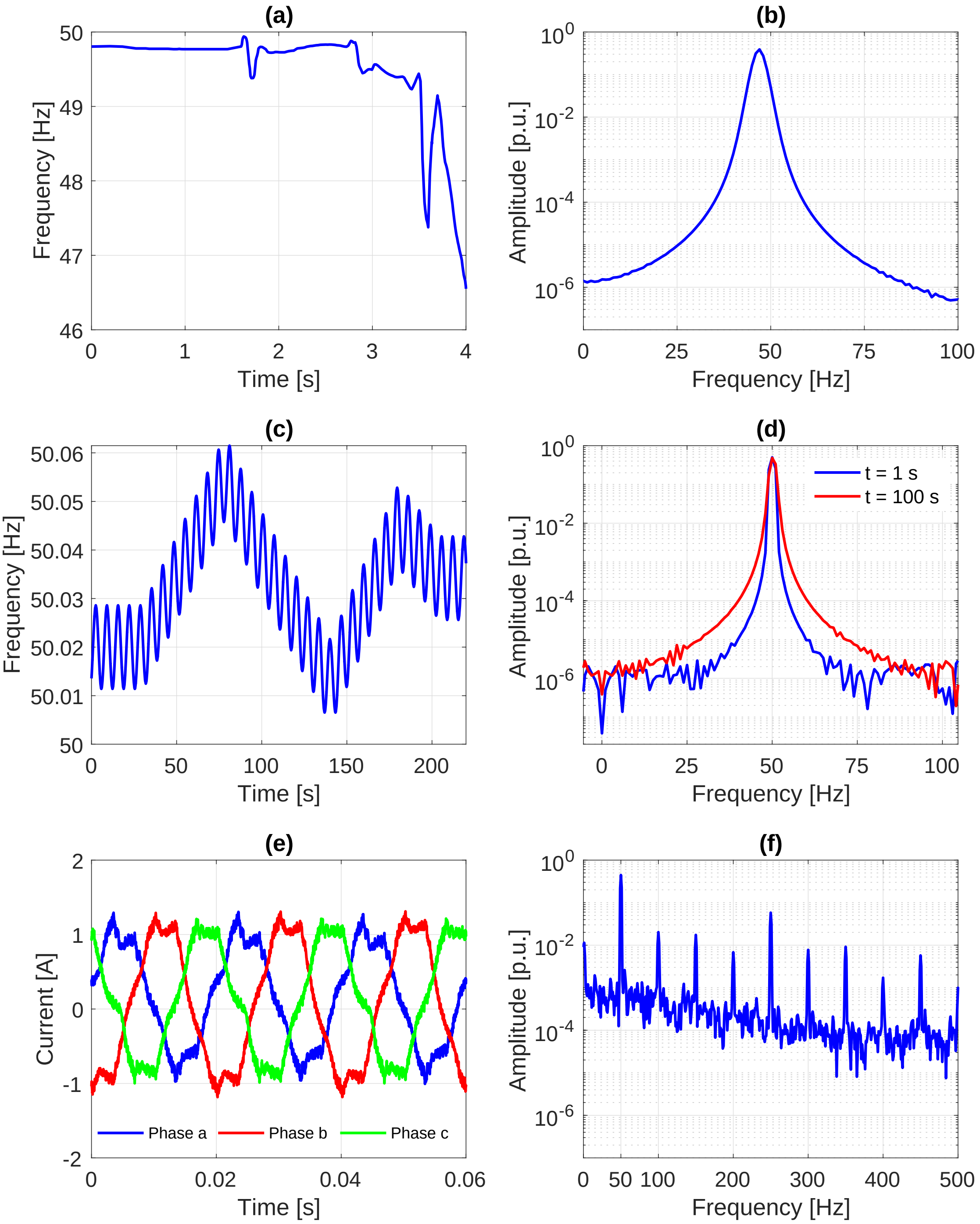

Figure 2.2 – Frequency estimated by PMUs during the Australian blackout on September 28, 2016 (a) and during the European inter-area oscillation on December 1, 2016 (c), as well as respective frequency domain spectra (b), (d). Time-domain three-phase current waveforms acquired at EPFL campus (e) and spectrum at phase a (f).

A clear example of these evolving power system dynamics happened in South Australia on September 2016, when the electrical grid faced a severe blackout because a strong windstorm hit the region while half of its power consumption was fed by wind generation [39]. Figure 2.2(a) shows the frequency as recorded by PMUs installed in that synchronous area. The frequency experienced a vast drop of almost 4 Hz in about 0.7 seconds, with an estimated Rate Of Change Of Frequency (ROCOF) of roughly -6.25 Hz/s.

Another example happened on December 2016, when an unexpected opening of a line in the French transmission network caused a significant voltage phase angle difference in the continental Europe electricity system and decreased the general damping, triggering a permanent oscillation [40]. As shown in Fig. 2.2(c), PMUs recorded undamped oscillations at 0.15 Hz.

Synchrophasor technology has been recently scaled-down to distribution networks to meet the increased automation requirements of medium voltage systems, creating further challenges [41, 42]. First, being the power flows smaller and the line distances shorter, the nodal voltage phase angle differences between adjacent buses are typically two orders of magnitude smaller than those across transmission grids, calling for increased synchrophasor estimation accuracy. Second, power quality issues in terms of distortion, unbalance and noise are more significant, particularly in the presence of converter-interfaced distributed generation integrated at the medium and low voltage levels. The installation of a Battery Energy Storage System (BESS) (720 kVA/500 kWh) in EPFL campus gave the opportunity to experimentally quantify the harmonic and inter-harmonic pollution in modern MV distribution networks [43, 44]. The BESS is interfaced with the 20 kV grid through a four-quadrant fully controllable DC/AC 720 kVA converter and a 0.3/21 kV 630 kVA step-up transformer. Figure 2.2(e) shows the distorted three-phase currents measured at the transformer that are characterized by 15% Total Harmonic Distortion (THD) and 18 dB Signal to Noise and Distortion ratio (SINAD) [6, 7].

From a theoretical perspective, it is worth investigating whether these operating conditions can be thoroughly described using traditional power system analysis tools that refer to the concept of phasor and assume signals to be in steady-state and characterized by narrow-banded spectra.

Typically, phasor parameters are determined using Fourier transform-based analysis: the frequency, amplitude, and phase of the phasor associated to the fundamental component can be inferred from the Discrete Fourier Transform (DFT) coefficients laying around the nominal system frequency [45]. However, during dynamic or heavily distorted events, the DFT may not allow for unequivocally identifying the parameters of the fundamental component [24].

To give an idea, Fig. 2.2(b) represents the spectrum of a dynamic signal affected by a decaying frequency ramp at -6.25 Hz/s, that mimics the evolution of the voltages before the blackout in South Australia. For the sake of frequency resolution and estimation accuracy, the DFT is computed over a window of 1 s, leading to a spectrum granularity of 1 Hz. The figure shows that only 32% of energy is transmitted in the range between 48 and 52 Hz and that the rest is spread well beyond the fundamental tone. This result demonstrates that an analysis limited to a narrow bandwidth surrounding the rated power system frequency would provide only a partial and inconsistent representation of the grid state. Figure 2.2(d) shows the spectrum of the signal taking place during the Pan-European inter-area oscillation, before and after the frequency ramp displayed in 2.2(c). Two main issues are evident: on the one hand, both spectra hinder the frequency modulation (evident in the time domain plot). On the other hand, the frequency ramp makes the energy spread over a wider bandwidth. Finally, Fig. 2.2(f) shows the DFT of the data acquired at the BESS installed at EPFL. It is evident that the entire observed spectrum is affected by harmonic and inter-harmonic components. Even in this case, the definition of synchrophasor as a narrow-band component might neglect a relevant portion of signal energy.

On top of that, different PMUs interpret reality differently: PMUs engineered by various manufacturers implement different synchrophasor estimation algorithms, based on arbitrary signal models. Therefore, PMUs may produce different interpretations when processing the samples relative to the same power system event. The conformity to an officially recognized standard is what ensures that the estimates from different PMUs end up within a given range of uncertainty. In this regard, the IEEE Std. C37.118 defines specific tests aimed at assessing the PMU accuracy under static and dynamic operating conditions. The standard has further defined two performance classes and related measurement requirements, to which PMUs must comply. P-class is meant for applications requiring fast response time, such as power system protection. M-class is meant for high accuracy measurements requiring resiliency against interfering spectral components.

Within this context, this Chapter aims at discussing and experimentally assessing what are the main challenges faced by modern synchrophasor estimation algorithms. First, Section 2.2 defines the nomenclature used in the manuscript. Then, Section 2.3 defines the synchrophasor model and highlights the inconsistencies that may arise from an ill-posed signal model to be used for synchrophasor estimation. Section 2.4 evaluates the synchrophasor model-dependency using synthetic data inspired by real events. The Section further assesses how different synchrophasor estimation techniques can influence the performance of the supplied power system applications via real-time simulation. Section 2.5 provides a discussion of the obtained results and demonstrates that PMUs shall not be regarded as black-boxes which provide unequivocal measurements.

2.2 Definitions

This Section aims at defining the specific technical nomenclature used in the manuscript.

According to the IEEE Standard for Synchrophasor Measurements for Power Systems C37.118.1 [19, 20] and the IEEE Standard for Synchrophasor Data Transfer for Power Systems C37.118.2 [21], the following definitions are used.

Synchrophasor
A phasor calculated from data samples using a standard time signal as the reference for the measurement. Therefore, the phasors from remote sites have a defined common phase relationship. A phasor is a complex equivalent of a sinusoidal wave quantity such that the complex modulus is the cosine wave amplitude, and the complex angle (in polar form) is the cosine wave phase angle.

Phasor Measurement Unit (PMU)
A device that produces synchrophasor, frequency, and rate-of-change-of-frequency (ROCOF) estimates from voltage and/or current signals and a time synchronizing signal.

Phasor Data Concentrator (PDC)
A function that combines and time-aligns phasor measurements from several PMUs.

Total Vector Error (TVE)
Euclidean distance between the true and estimated synchrophasors normalized with respect to the amplitude of the true synchrophasor.

According to the International Vocabulary of Basic and General Terms in Metrology (VIM) [46] and the Guide to the expression of uncertainty in measurement (GUM) [47], the following definitions are used.

Quantity
Property of a phenomenon, body, or substance, where the property has a magnitude that can be expressed as a number and a reference.

Value
Number and reference together expressing magnitude of a quantity.

Measurement
Process of experimentally obtaining one or more values that can reasonably be attributed to a quantity.

Measurand
Quantity intended to be measured.

Measured value
Value representing a measurement result.

Measuring instrument
Device used for making measurements, alone or in conjunction with one or more supplementary devices.

Measurement result
Set of values being attributed to a measurand together with any other available relevant information. A measurement result is only an estimate (approximation) of the true value of the measurand and thus is complete only when accompanied by a statement of the uncertainty of that estimate.

True value
Value consistent with the definition of a quantity, ideally obtained by a perfect measurement. The true value of a measurand is an ideal concept and is, in practice, unknowable. In a simulated environment this value is known.

Conventional value
Value attributed by agreement to a quantity for a given purpose. Estimate of a true value associated with small measurement uncertainty.

Reference value
Value used as a basis for comparison with quantities of the same kind. A reference value of a measurand can be a true value, in which case it is unknown, or a conventional value, in which case it is known.

Accuracy
Closeness of agreement between a measured value and a true value of a measurand.

Precision
Closeness of agreement between measured quantity values obtained by replicate measurements on the same or similar objects under specified conditions.

Error
Measured value minus a reference value. A measurement has imperfections that give rise to an error in the measurement result. Traditionally, an error is composed of a random component (that cannot be compensated) and a systematic component (that can be compensated).

Uncertainty
Parameter, associated with the result of a measurement, that characterizes the dispersion of the values that could reasonably be attributed to the measurand. The uncertainty of a measurement result reflects the lack of exact knowledge of the true value.

Stability
Property of a measuring instrument, whereby its metrological properties remain constant in time.

2.3 The Synchrophasor Model

As known, the phasor representation refers to the following single-tone static signal model:

$$x(t) = A_0 \cdot \cos\left(2\pi f_0 t + \varphi_0\right) = A_0 \cdot \cos\left(\Phi_0\right) \tag{2.1}$$

being A_0 the peak amplitude, φ_0 the initial phase (i.e., at time $t = 0$) and f_0 the frequency of the fundamental frequency component of the power system signal. Note that f_0 may be different from the nominal power system frequency f_N of 50 or 60 Hz. The equivalent phasor formulation is given by:

$$X = A_0 \cdot e^{j\Phi_0} \tag{2.2}$$

Note that (2.2) requires a transformation of the signal in (2.1) from the time domain to the frequency domain by means of the Fourier transform. This transformation can be achieved in practice using the DFT [45].

A generic voltage or current signal is rarely in steady-state though. It is rather characterized by time-variant parameters as a consequence of wide- and narrow-band disturbances. More generally, it can be identified with the following generic signal model [45, 48]:

$$x(t) = A_0(t)\left(1 + \varepsilon_{A_0}(t)\right) \cdot \cos\left(2\pi f_0(t)t + \varphi_0 + \varepsilon_{\varphi_0}(t)\right) + \eta(t) + \gamma(t) + \nu(t) \tag{2.3}$$

where:

- the fundamental tone amplitude $A_0(t)$ and frequency $f_0(t)$ are varying with respect to time, leading to a time-varying phase angle $\Phi_0(t)$;
- the time-varying term $\varepsilon_{A_0}(t)$ represents fundamental amplitude fluctuations (e.g., amplitude modulation);
- the time-varying term $\varepsilon_{\varphi_0}(t)$ accounts for fundamental phase and frequency fluctuations (e.g., phase modulation, frequency ramp);
- the term $\eta(t)$ models narrow-band disturbances (harmonic and/or inter-harmonic components):

  $$\eta(t) = \sum_h A_h(t)(1 + \varepsilon_{A_h}(t)) \cdot \cos\left(2\pi f_h(t)t + \varphi_h + \varepsilon_{\varphi_h}(t)\right) \qquad h = f_h/f_0, \quad h \in \mathbb{R} \tag{2.4}$$

  being $f_h(t)$ the harmonic/inter-harmonic frequency, $h = f_h/f_0$ the tone order, $A_h(t)$ the peak amplitude, φ_h the initial phase and the time-varying terms $\varepsilon_{A_h}(t)$ and $\varepsilon_{\varphi_h}(t)$ accounting for any amplitude and phase/frequency fluctuations;
- the term $\gamma(t)$ models dynamic wide-band disturbances, that are typically decaying DC transient components:

  $$\gamma(t) = A_{DC} e^{-t/\tau} \tag{2.5}$$

being A_{DC} the initial amplitude and τ the time constant characterizing the phenomena;

- the term $v(t)$ accounts for grid noise (e.g., thermal noise, corona effect, partial discharges).

For the sake of nomenclature, a power system signal in static operating conditions (i.e., when the time-varying terms $\varepsilon(t)$ and $\gamma(t)$ are null) can be represented with the following well-known signal model:

$$x(t) = A_0(t) \cdot \cos\left(2\pi f_0(t)t + \varphi_0\right) + \sum_h A_h(t) \cdot \cos\left(2\pi f_h(t)t + \varphi_h\right) + v(t) \tag{2.6}$$

Conversely, a power system is in dynamic operating conditions when at least one time-varying term ($\varepsilon(t)$ and/or $\gamma(t)$) is non-zero, and can be defined using the signal model in (2.3).

However, the generic power system signal model in (2.3) does not fit with the steady-state signal model in (2.1). The synchrophasor definition in the IEEE Std. C37.118 attempts to solve this inconsistency defining the following signal model and synchrophasor definition:

$$x(t) = A_0(t) \cdot \cos\left(2\pi f_0(t)t + \varphi_0\right) \tag{2.7}$$

$$X(t) = A_0(t) \cdot e^{j\Phi_0(t)} \tag{2.8}$$

According to the IEEE Std. C37.118, synchrophasors are measured with respect to a well-defined and common time reference, leading to the fact that phasors sensed by remote sites of a synchrophasor network share a common phase reference. To be more specific, the initial phase angle φ_0 refers to the phase offset from a cosine function pulsating at the nominal power system frequency (50 or 60 Hz) and locked to the UTC. It is worth observing that the synchrophasor phase $\Phi_0(t)$ takes into account both the frequency and initial phase. Having set a constant initial phase implies that the instantaneous phase variations are only due to the power system frequency variations and it avoids the possibility of having multiple couples of frequency and initial phase that produce the same instantaneous phase.

By definition, a PMU acquires a discrete time series of samples of the power system signal in (2.3), defined as follows:

$$x[n] := \{x(t) + \rho(t), \quad t = nT_s, \quad n = [1, \dots N] \in \mathbb{N}\} \tag{2.9}$$

where N is the number of samples acquired at each observation interval T that compose the considered observation window $N \cdot T_s$ being $T_s = F_s^{-1}$ the sampling time, and the term $\rho(t)$ accounts for wide-band measurement noise (intrinsic in the data-acquisition process). Given $x[n]$, the synchrophasor estimation algorithm embedded into the PMU attempts to retrieve the values of f_0, A_0, φ_0, and ROCOF associated to the fundamental component estimated within the window, with a given reporting rate F_r.

Although the synchrophasor concept has slightly relaxed the traditional steady-state requirement for defining a phasor, there is still much inconsistency among the synchrophasor model in (2.7) and the actual power system waveforms acquired by the PMU in (2.3). Indeed, the synchrophasor signal model accounts for the instantaneous amplitude and phase of the fundamental tone only and disregards any static and dynamic spurious contribution. Such assumption could work in static and lightly polluted operating conditions, i.e., when the DFT of the signal under analysis can be approximated by a term associated to the fundamental component, plus a restricted set of coefficients associated to existing harmonic or inter-harmonic contributions. In dynamic operating conditions, though, the model in (2.7) is still not entirely appropriate as it cannot account for rapid variations of signal parameters with a satisfying level of accuracy. Indeed, as shown in Fig. 2.2, during transients, the signal energy spreads over the entire frequency spectrum and cannot be approximated as a sequence of narrow-band components. If the signal under investigation cannot be approximated as periodic and band-limited, even the Fourier series representation loses its significance. Therefore, it might be hard and formally inconsistent to retrieve the fundamental tone synchrophasor in real-world scenarios.

Among the data estimated by a PMU, the parameter that is mainly sensitive to power system dynamics is the ROCOF [49, 50, 51, 52]. According to the IEEE Std. C37.118, the fundamental frequency and ROCOF are defined as the first and second time-derivative of the synchrophasor phase angle, respectively. However, most PMUs compute ROCOF as the finite difference between two consecutive frequency estimates. This approach, as well-known, amplifies the effects of measurement noise on the accuracy of the estimates [2, 3].

2.4 Synchrophasor Estimation Significance in Power System Applications

This Section aims at evaluating how different synchrophasor computation techniques can influence the uncertainty of the measurements, and, in turns, influence subsequent power system applications. The focus is on ROCOF measurements because this is the parameter whose estimation is the most sensitive to power system dynamics. Indeed, by definition, ROCOF can be seen as a predictive filter of frequency variations, whose output accounts for the variation of polarity and velocity. In this view, ROCOF may be employed in wide-area monitoring, protection and control applications, like load shedding [53], islanding detection [54], and distributed generation control [55]. However, a standard approach towards ROCOF measurement is still missing: most applications adopt estimation algorithms and signal models designed *ad hoc* to suitably meet the operating conditions and requirements [51].

The Section takes into account two state-of-the-art window-based synchrophasor estimators. The first one is based on a static synchrophasor model [56], the second one is based on a dynamic synchrophasor model [57]. The algorithms are also differentiated by the way they compute the ROCOF, i.e., a finite-difference between subsequent frequency measurements or as a state variable, respectively. Both algorithms prove to be compliant to the IEEE Std. C37.118. Therefore, one would expect the two methods to provide similar estimates when analyzing the same phenomenon.

The analysis makes reference to realistic operating conditions inspired by real-world networks: (i) the Hydro-Québec grid as representative of the frequency excursions and harmonic pollution typical of islanded grids [58]; (ii) the effect of large inter-area oscillations in the Pan-Europe transmission network (Fig. 2.2(c)) [40], and (iii) the islanding maneuver of an active distribution network characterized by reduced inertia [59].

Then, the analysis considers the feasibility of PMU-based ROCOF measurements to support power systems applications via real-time simulation. The target application is the Under Frequency Load Shedding (UFLS) strategy proposed in [1, 5], that exploits frequency and ROCOF measurements produced by PMUs as detectors of a large contingency.

The Section is structured as follows. Section 2.4.1 describes the adopted synchrophasor estimation algorithms and presents the considered ROCOF estimation techniques. Section 2.4.2 characterizes the algorithms' performance in terms of ROCOF error in synthetic datasets inspired by real-world experimental acquisitions. Section 2.4.3 assesses the influence of the adopted synchrophasor estimation algorithm on the UFLS outcome.

2.4.1 The Adopted Synchrophasor Estimation Algorithms

The proposed analysis takes into account two state-of-the-art window-based synchrophasor estimators, i.e., the Enhanced Interpolated DFT (e-IpDFT) [56] and the Compressive Sensing-based Taylor-Fourier Model (cs-TFM) [57]. Among other differences, the algorithms are differentiated by the way they compute the ROCOF: the e-IpDFT is a static approach and computes ROCOF as the incremental ratio between two consecutive frequency estimates. It is thus reasonable to expect that the ROCOF estimates are partially delayed and smoothed depending on the adopted reporting period. Conversely, the cs-TFM , that is a dynamic approach, directly computes the instantaneous ROCOF, along with the other state variables, as the second-order time-derivative of the phase. In general, a dynamic signal model enables the tracking of eventual time-varying trends, but at the same time suffers from a higher sensitivity to uncompensated disturbances [60].

The e-IpDFT adopts an enhanced version of the IpDFT to estimate the synchrophasor associated to the fundamental component of the power signal under analysis. Such technique, described in Algorithm 1, is specifically designed to mitigate the effects of long-range spectral leakage produced by the negative image of the fundamental component (further details are provided in Chapter 3, Section 3.2.3).

As described in Algorithm 1, the acquired signal $x[n]$ is first windowed with the Hanning function $w[n]$ to reduce the long-range spectral leakage effects, then the weighted signal DFT $X(k)$ is computed (line 1 of Alg. 1). The IpDFT technique applied to the highest DFT bins

Algorithm 1 The e-IpDFT synchrophasor estimator.

```
1: $X(k) = DFT\,[x(n) \cdot w(n)]$    ▷ Signal windowing and DFT computation
2: $\{\widehat{f}_0, \widehat{A}_0, \widehat{\varphi}_0\} = IpDFT\,[X(k)]$    ▷ Fundamental tone parameters estimation via IpDFT
3: $\widehat{X}_0^{+}(k) = X(k) - image\,[-\widehat{f}_0, \widehat{A}_0, -\widehat{\varphi}_0]$    ▷ Negative image compensation
4: $\{\widehat{f}_0, \widehat{A}_0, \widehat{\varphi}_0\} = IpDFT\,[\widehat{X}_0^{+}(k)]$    ▷ Enhanced fund. tone parameters estimation via IpDFT
5: $RO\hat{C}OF = [\hat{f}_0|_t - \hat{f}_0|_{t-1}]\,/\,T_r$ ▷ ROCOF estimation as frequency estimates' finite difference
```

provides a preliminary estimate of the fundamental parameters $\{\hat{f}_0, \hat{A}_0, \hat{\varphi}_0\}$ (line 2). These values enable the reconstruction of the tone negative image $\widehat{X}^{-}(k)$, that is subtracted from the original DFT bins, that now account only for the fundamental tone positive image $\widehat{X}^{+}(k)$ (line 3). In this reduced-leakage scenario, the IpDFT is applied again, leading to an enhanced estimation of the fundamental parameters (line 4). Finally, the ROCOF is estimated as the finite difference between two consecutive frequency estimations, divided by the reporting period T_r (line 5). This computation of the ROCOF is necessary since in this algorithm, based on a static signal model, the fundamental frequency is supposed to be constant and not a function of time.

The cs-TFM estimator adopts a formulation of the Taylor-Fourier Transform (TFT), that has been suitably modified and generalized in order to deal with multi-tone power system signals. Thanks to a Taylor series expansion truncated to the second derivative order, it is possible to include the fundamental frequency and ROCOF within the estimator state variables as the first and second time-derivative of the phase angle, respectively.

As shown in Algorithm 2, the first step of the cs-TFM method consists of applying a CS-based super-resolution technique to improve the frequency resolution associated with short observation intervals by almost one order of magnitude. Specifically, the DFT bins $X(k)$ are projected over the vector space spanned by matrix D_f, whose columns are designed to account for leakage effects over a super-resolved grid (line 1 of Alg. 2). The fundamental frequency is associated with the maximum bin of the super-resolved spectrum $\hat{f}_{max}$ (line 2). Then, the first four harmonic terms are included into the spectral support $\mathscr{S}$ (line 3), that is recovered through an Orthogonal Matching Pursuit (OMP) algorithm, i.e., a *greedy* selection routine that exploits the assumption that the signal spectrum is sparse and consists only of a limited number of narrow-band components. Given the recovered support $\mathscr{S}$, the TFM matrix M is constructed (line 4) and the corresponding dynamic synchrophasor coefficients p are computed as follows (line 5):

$$p = \{p^0, p^1, p^2\} = (M^{\dagger} M)^{-1} M^{\dagger} \cdot x(t) \tag{2.10}$$

where the superscript {0,1,2} denotes the derivative order, $M^{\dagger}$ is the conjugate transpose of M and the superscript {-1} denotes the inverse operator. The fundamental tone parameters are

Algorithm 2 The cs-TFM synchrophasor estimator.

```
$Y = D_f^{\dagger} \cdot X(k)$    ▷ Super-resolved spectrum computation
$\hat{f}_0 = \hat{f}_{max} = \max(Y)$    ▷ Fundamental frequency estimation as the maximum bin in $Y$
$\mathscr{S} = \{\hat{f}_0 \cdot [1,2,3,4]\}$    ▷ Spectral support computation including 4 harmonics
$M = TFM(\mathscr{S})$    ▷ TFM matrix computation
$p = (M^{\dagger}M)^{-1}M^{\dagger} \cdot x(t)$    ▷ Dynamic synchrophasor extraction
$\hat{f}_0, p \rightarrow \{\hat{A}_0, \hat{f}_0, \hat{\varphi}_0, RO\hat{C}OF\}$    ▷ Synchrophasor parameters estimation as state variables
```

extracted as:

$$\begin{aligned}
\hat{A}_0 &= |p^0|, & \hat{A}_0^1 &= 2\,\mathrm{Re}(p^1 \cdot e^{-j\hat{\varphi}_0}) \\
\hat{\varphi}_0 &= \angle p^0, & \varphi_0^1 &= \frac{\mathrm{Im}(p^1 \cdot e^{-j\hat{\varphi}_0})}{\hat{A}_0} \\
\hat{f}_0 &= \hat{f}_{max} + \frac{\hat{\varphi}^1}{2\pi}, & RO\hat{C}OF &= \frac{\mathrm{Im}(p^2 \cdot e^{-j\hat{\varphi}_0}) - \hat{A}_0^1 \cdot \hat{\varphi}_0^1}{2\pi \cdot \hat{A}_0}
\end{aligned} \tag{2.11}$$

For each algorithm, two window lengths are considered, as representative of P- and M-class PMUs. Specifically, three- and five-cycle windows are chosen, respectively, corresponding to 60 and 100 ms at the rated power system frequency of 50 Hz. Both estimators employ a sampling frequency of 5 kHz and a reporting rate of 50 frames per second (fps).

2.4.2 Experimental Validation using Real-World Datasets

This Section characterizes the performance of the considered algorithms (e-IpDFT and cs-TFM) in terms of ROCOF error (RFE) in datasets inspired by real-world experimental acquisitions, rather than in the IEEE Std. C37.118 test conditions [56, 57]. For each dataset, the results are presented by means of a figure showing the Cumulative Distribution Function (CDF) or the normalized Root Mean Squares Error (nRMSE) relative to RFEs and a Table providing further statistical performance metrics, i.e., the RFE mean value, standard deviation and 95th quantile (as the errors are not normally distributed). In the presence of small ROCOF variations, though, a reduced RFE is not enough to guarantee a sufficient resolution capability. As a consequence, also the Pearson's correlation coefficient between the estimated and ground-truth values is computed, that is a measure of the linear correlation between the two quantities. In this way, it is possible to assess whether the estimation technique operates as a linear predictor and the ROCOF estimates preserve the original information content. In particular, given a pair of variables (X,Y) characterized by standard deviations $(\sigma_X,\ \sigma_Y)$ the Pearson's correlation coefficient is calculated using:

$$\rho_{X,Y} = 100 \cdot \frac{cov(X,Y)}{\sigma_X \sigma_Y} \tag{2.12}$$

being *cov* the covariance operator. This value ranges from 0 to ± 100 %: a high value for ρ indicates that X can be expressed as a linear expansion of Y, meaning that the two variables are highly correlated.

Hydro-Québec grid

The first dataset is inspired by the Hydro-Québec grid. It is characterized by large frequency excursions and affected by several harmonic and inter-harmonic interferences [58, 61, 62].

The test waveform is inspired by the signal model proposed in [63], and is characterized by the following signal model:

$$x(t) = A_0 \cdot \cos\left(2\pi f_0 t + \varphi_0\right) + \sum_h A_h \cdot \cos\left(2\pi f_h t + \varphi_h\right) + \nu(t) \tag{2.13}$$

that accounts for a steady-state fundamental component affected by different disturbances, whose harmonic indexes and normalized amplitudes are reported in Table 2.1. For the sake of consistency with the other datasets, the system frequency and the relative interferences have been scaled to 50 Hz, instead of 60 Hz. Nine harmonics (up to 500 Hz), one inter-harmonic at 81.25 Hz, and one sub-harmonic at 12.15 Hz corrupt the signal. These spectral components are located outside the PMU passband [25, 75] Hz, and thus the PMU is expected to reject their injections in its final ROCOF estimates.

Moreover, two asymmetrical inter-modulation components, that differ in terms of normalized amplitude and deviation with respect to the system frequency are present. Since these components lay within the fundamental range [45, 55] Hz, it is reasonable to expect that the PMU cannot distinguish them as separate tones, but only measure their combined contribution [64]. In this regard, Fig. 2.3(c) presents the instantaneous frequency associated to the sum of fundamental and inter-modulation components. Given the model in (2.13), the instantaneous frequency is defined at each sampling time, i.e., at each 200 μs. The true ROCOF value (Fig. 2.3(d)) is defined as the incremental ratio between two consecutive frequency estimates at intervals of 20 ms. Finally, the measurement noise is reproduced by an uncorrelated white Gaussian variable, such that Signal to Noise Ratio (SNR) is equal to 60 dB.

The resulting signal is shown in Fig. 2.3(a): in the time-domain the waveform is characterized by a significant distortion level with THD and SINAD equal to 11.18% and 16.94 dB, respectively, as result of the interference components visible in the spectral representation (Fig. 2.3(b)).

This test presents two main challenges in terms of ROCOF measurements. First, the true ROCOF exhibits fast and irregular oscillations within a wide range of ±1.5 Hz/s. Second, the estimation of fundamental component parameters is affected by the spectral leakage caused by harmonic, sub- and inter-harmonic components.

Table 2.1 – Hydro-Québec dataset: model parameters

Component	Harm. Index	Norm. Amplitude
fundamental	1	1
inter-modulation	0.936	0.01
	1.082	0.005
harmonics	from 2 to 6	0.05
	from 7 to 10	0.02
inter-harmonic	1.625	0.075
sub-harmonic	0.243	0.02

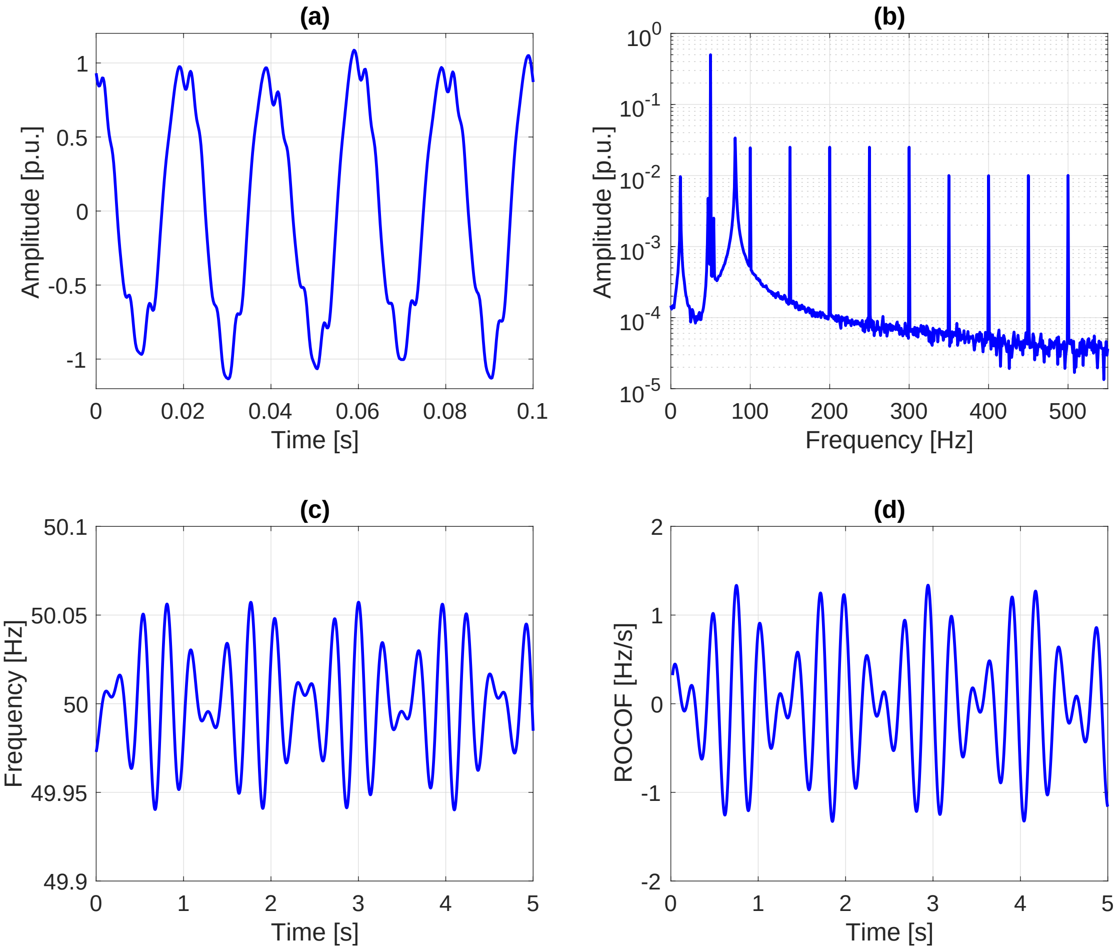

Figure 2.3 – Hydro-Québec dataset: simulated test waveform in time (a) and (b) frequency domain and ground-truth frequency (c) and ROCOF (d) associated to the signal fundamental component.

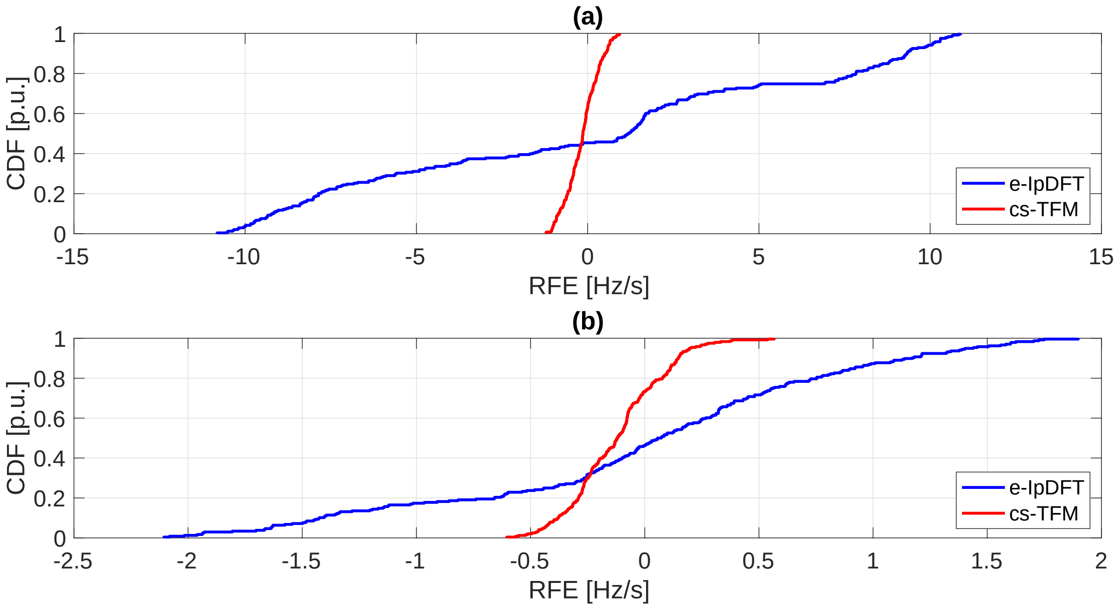

Figure 2.4 – Hydro-Québec dataset: CDF associated to the RFEs as produced by static (blue) and dynamic (red) signal model in P- (a) and M-class (b) configuration.

Table 2.2 – Hydro-Québec dataset: RFE statistical properties

Estimator	**Class**	**Mean**	**Std Dev**	**95%**	**Corr**
e-IpDFT	P	$-2.45 \cdot 10^{-2}$	6.76	10.51	0.77%
	M	$6.25 \cdot 10^{-4}$	0.89	2.03	50.31%
cs-TFM	P	$-1.51 \cdot 10^{-1}$	0.48	1.11	2.64%
	M	$1.20 \cdot 10^{-2}$	0.21	0.56	92.59%

As regards the P-class configuration, Fig. 2.4(a) shows that the e-IpDFT fails to reject the spectral leakage coming from the interfering tones, leading to errors up to 11 Hz/s. The cs-TFM, instead, provides better performance, although the obtained RFE still exceed 1 Hz/s. Nevertheless, the results in Table 2.2, demonstrate that, even if the cs-TFM guarantees a performance enhancement in terms of maximum error, the corresponding estimates do not provide any information regarding the ground-truth ROCOF, being the Pearson's correlation index limited to just 2.64%.

As regards M-class, Fig. 2.4b shows that enlarging the window length improves the overall performance. Still, the static estimator is characterized by significant errors of ± 2 Hz/s. The dynamic approach, instead, provides a better performance with RFE limited within ± 0.05 Hz/s. Together with an error reduction, the estimated values prove to be quite correlated with the ground-truth reference, with a correlation exceeding 92%.

Table 2.3 – European inter-area oscillation: non-linear fit model parameters

A	f	φ	k_A	f_A	k_φ	f_φ	R_1	R_2	R_3	R_4	R_5	R_6	R_7
[kV]	[Hz]	[rad]	[%]	[mHz]	[mrad]	[mHz]				[mHz/s]			
123.8	50.02	-1.80	13.6	153.1	56.4	152.6	-	2.28	-2.29	-2.05	2.53	-1.42	-
Time interval for R_i [s]							30.5	78.5	98.5	140.5	180.5	204.5	220.5

European inter-area oscillation

The second analysis refers to a real-world event, recorded on December 1, 2016, when an unexpected opening of a line in the French transmission network triggered an inter-area oscillation in the Continental Europe electricity system [40]. In particular, the test waveform derives from the estimates of a PMU employed by the grid operator of the city of Lausanne (Services industriels de Lausanne, SiL) [16]. The measurements refer to the 125 kV sub-transmission network, that is equipped with 15 P-class PMUs [16]. These devices are based on the e-IpDFT synchrophasor estimation algorithm [56].

Based on the PMU estimates of fundamental frequency, amplitude and initial phase, the time-domain waveforms are recovered as sampled at 5 kHz, through the non-linear fitting approach described in [11], whose details are provided in Chapter 5, Section 5.3.1. The method estimates the parameters of series of samples by fitting them to a specified signal model. For this dataset, the acquired signal is affected by simultaneous dynamic trends, that are modeled through the following non-linear model:

$$x(t) = A_0 \cdot \big(1 + k_A \cdot \cos(2\pi f_A t)\big) \cdot \cos\big(2\pi f_0 t + \varphi_0 + k_\varphi \cdot \cos(2\pi f_\varphi t) + R t^2\big) + \nu(t) \tag{2.14}$$

The signal is affected by an amplitude modulation characterized by a depth k_A equal to 13.6% and a frequency f_A equal to 153.1 mHz, and by a phase modulation characterized by a depth k_φ equal to 56.4 mrad and a frequency f_φ equal to 152.6 mHz. Frequency increasing and decreasing trends are modeled as a sequence of positive and negative linear ramps, characterized by a ramp parameter R_i, whose value varies within the range [-2.30, 2.55] mHz/s roughly every 30 s. Finally, a more realistic measurement noise scenario is modeled by adding white Gaussian noise with SNR equal to 60 dB. The parameters relative to model 2.14 are summarized in Table 2.3.

It is worth observing that, being in a simulated environment and based on the model 2.14, it is possible to define the true value of ROCOF at each sampling time. With respect to this reference value, it is possible to evaluate the ROCOF error (RFE).

As regards the P-class configuration, Fig. 2.5(a) shows that the two approaches provide nearly coincident performance, with an estimated error ranging within ±0.2 Hz/s. However, the results in Table 2.4 demonstrate that none of the considered estimation techniques provides a sufficient correlation with the ground-truth values.

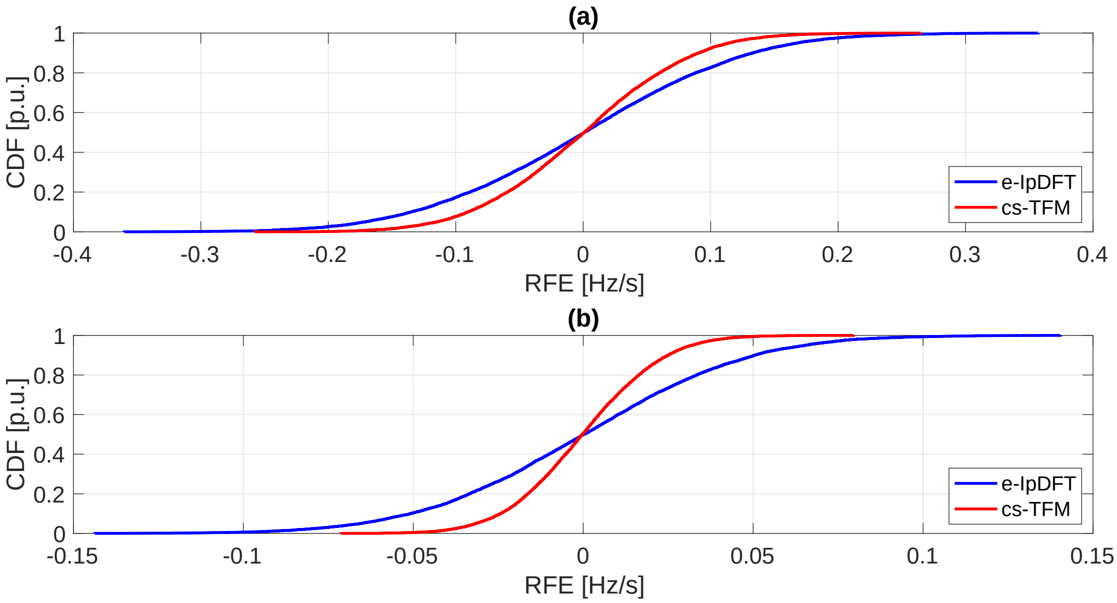

Figure 2.5 – European inter-area oscillation: CDF associated to the RFEs as produced by static (blue) and dynamic (red) signal model in P- (a) and M-class (b) configuration.

As regards M-class, Fig. 2.5(b) shows that the increased window length does not produce a remarkable performance enhancement. As regards the static approach, the RFE variation range is almost halved, with a maximum estimation error of 0.1 Hz/s. The dynamic approach, instead, provides a better performance with RFE limited within ±0.05 Hz/s. Nevertheless, despite this error reduction, the estimated values prove to be very poorly correlated with the ground-truth reference (just 29.19% in the best case).

A motivation could be found in the peculiar variation trend of the fundamental frequency. Both oscillatory and linear trends are characterized by time constants in the order of tens of seconds. The strict requirements in terms of reporting rate and latency force the PMUs to consider short observation periods where these phenomena can be hardly discriminated from steady-state conditions. In this sense, the employment of canonical PMUs for similar scenarios should probably require a close analysis of the most suitable estimation approaches, observation window lengths and reporting rates.

Table 2.4 – European inter-area oscillation: RFE statistical properties

Estimator	Class	Mean	Std Dev	95%	Corr
e-IpDFT	P	$2.51 \cdot 10^{-6}$	0.10	0.24	5.65%
	M	$2.80 \cdot 10^{-6}$	0.04	0.09	14.58%
cs-TFM	P	$9.68 \cdot 10^{-5}$	0.07	0.16	8.38%
	M	$-3.00 \cdot 10^{-6}$	0.02	0.04	29.19%

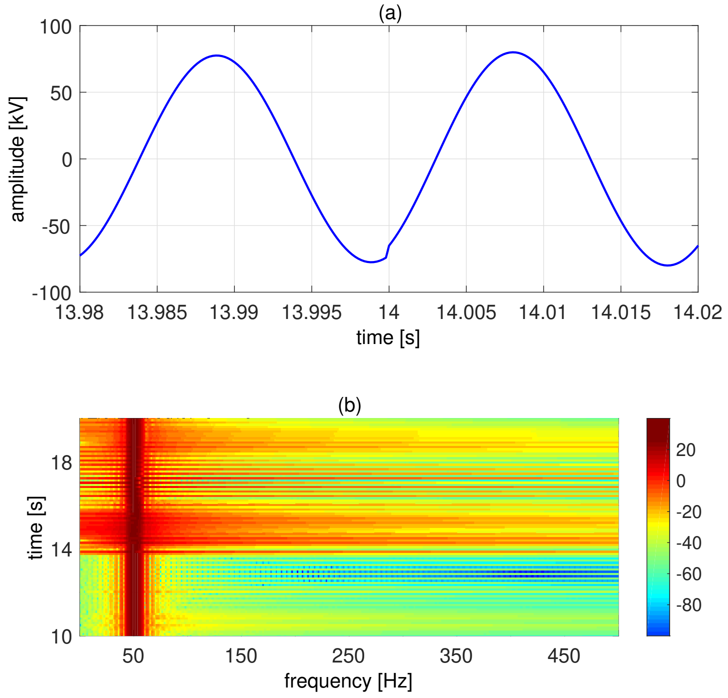

Figure 2.6 – Islanding maneuver: time-domain acquisition in correspondence of the islanding operation at 14 s (a) and the corresponding spectrogram expressed in dB (b).

Islanding maneuver

The third dataset consists of the waveforms acquired by an oscilloscope during an intentional islanding maneuver of an urban medium voltage grid, located in Imola, Italy, on August 13, 2009 [59]. In this regard, Fig. 2.6(a) represents the waveform portion of interest, where the islanding operation occurs around 14 s, whereas Fig. 2.6(b) shows the spectrogram (i.e. Short Time Fourier Transform as a function of time) computed over windows of 1024 samples. Before the islanding maneuver, the signal consists in the fundamental tone only. Once the operation has started, instead, the signal energy is no more limited around the fundamental tone, but spreads among over 500 Hz.

The signal parameters are extracted applying the non-linear fitting routine presented in [11] (details are provided in Chapter 5, Section 5.3.1). As reported in Table 2.5, the signal is modeled by means of a step change, characterized by a quasi-instantaneous variation of $k_A = 3.19\%$ and $k_\varphi = 0.148$ rad for amplitude and phase, respectively:

$$x(t) = A_0 \cdot (1 + k_A \cdot \chi(t-T)) \cdot \cos(2\pi f_0 t + \varphi_0 + k_\varphi \cdot \chi(t-T)) \tag{2.15}$$

where T represents the occurrence time and $\chi(\cdot)$ models a piece-wise step function, that is null at time $t \leq 0$, and is 1 elsewhere. The noise and distortion level is evaluated by computing the SNR, THD and SINAD indexes, that are equal to 46.24 dB, 2.03% and 33.49 dB, respectively.

Table 2.5 – Islanding maneuver: fitted waveform parameters

Segment	Amplitude [kV]	Frequency [Hz]	Phase [rad]
pre-islanding ($t < 14$ s)	77.66	50.07	1.032
post-islanding ($t \geq 14$ s)	80.14	50.07	0.884
SNR = 46.24 dB, THD = 2.31%, SINAD = 33.49 dB			

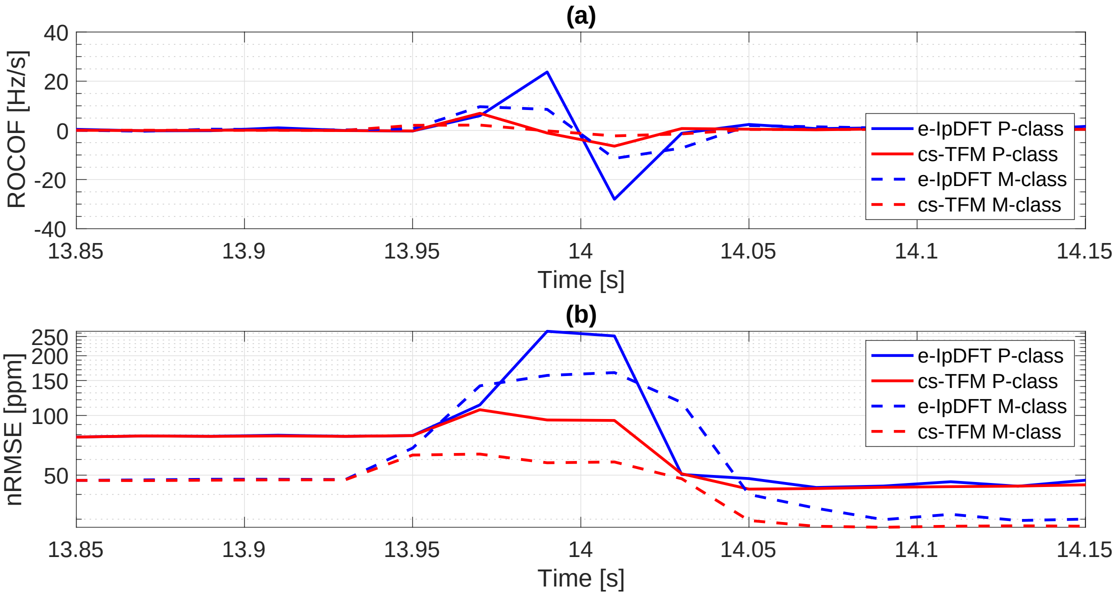

Figure 2.7 – Islanding maneuver: ROCOF (top) and nRMSE associated to static (blue) and dynamic (red) signal model in P- (solid line) and M-class (dashed line) configuration.

The adopted signal model does not account for frequency variations. Therefore, the corresponding ROCOF reference value is fixed at 0 Hz/s. Nevertheless, during a sudden step change, the performance evaluation based only on the RFE assessment does not provide any information regarding the estimator behavior during the transient. Therefore, the normalized root-mean-squared error (nRMSE) is evaluated, as proposed in [11]. At each reporting time, the synchrophasor estimation algorithms provide an updated estimate of amplitude, phase, frequency and ROCOF. Based on this information, the fundamental component trend is recovered in the time domain, and the root-mean-squared error with respect to acquired samples is computed. Finally, the obtained RMSE is normalized by the sample window energy. In this way, the new metric accounts for the portion of signal energy that has been neglected or misrepresented by algorithm estimates. This technique, works well in a controlled scenario, when it is possible to thoroughly evaluate the distribution of nRMSE values in the expected operating conditions.

In this regard, Table 2.6 reports the statistical description of the nRMSE distribution in terms of mean, standard deviation and maximum value for the two synchrophasor estimators. Figure 2.7 further shows the nRMSE error evolution with respect to time and the ROCOF estimates.

Table 2.6 – Islanding maneuver: nRMSE Statistical Distribution

Segment	Class	Mean [ppm]	Std Dev [ppm]	Max [ppm]
pre-islanding ($t < 14$ s)	P	81.94	1.34	85.70
	M	52.40	0.77	54.31
post-islanding ($t \geq 14$ s)	P	48.89	1.35	52.94
	M	29.98	0.69	32.07

As regards P-class configuration, Fig. 2.7 shows that both static and dynamic ROCOF estimates exhibit a rapid and significant increase, up to maximum values around 20 Hz/s. The similar increase of nRMSE suggests that a significant portion of signal energy has been neglected or misrepresented, demonstrating the lack of estimation reliability. Similar considerations can be made for the M-class configuration. A longer window allows for a more accurate ROCOF estimation, that is however still totally unreliable as shown by the large nRMSE values.

2.4.3 Behavior of Under Frequency Load Shedding Relays

As known, UFLS is a technique that minimizes the risk of uncontrolled system separation, loss of generation, or shutdown in case of large power system disturbances, after the primary frequency control reserve is exhausted [65, 66]. This Section considers the UFLS scheme proposed in [1, 5], that relies on PMU measurements of frequency and ROCOF to detect and clear large contingencies. The control action is scaled to the threshold level, i.e., larger ROCOF and frequency values correspond to larger amounts of loads to be shed or restored.

The results are obtained through the Opal-RT eMEGAsim PowerGrid Real Time Simulator (RTS) [67] implementing a detailed dynamic model of IEEE 39-bus power system integrating renewable energy resources [68, 69]. The total installed capacity is 10 GW, out of which 4 GW are provided by type-3 wind farms. The model is represented in Fig. 2.8, and further details are provided in Chapter 7 Section 7.3.2. The electrical grid is fully equipped with simulated PMUs, embedding the e-IpDFT and the cs-TFM synchrophasor estimators, for both P- and M-class of performance [70, 4]. The use of virtual PMUs within RTS takes into account the cumulative non-linear effect of synchrophasor estimation as a function of the network dynamic response and adopted control scheme.

The virtual PMUs are installed at each load bus and are characterized by sampling and reporting rate equal to 10 kHz and 50 fps, respectively. They measure the bus voltage synchrophasors, as well as frequency and ROCOF. These measurements are sent to the UFLS controller, that acts on the demand profile based on the UFLS strategy. In order to reproduce a plausible measurement scenario, the voltage waveforms are corrupted by additive white Gaussian noise resulting in SNR equal to 80 dB.

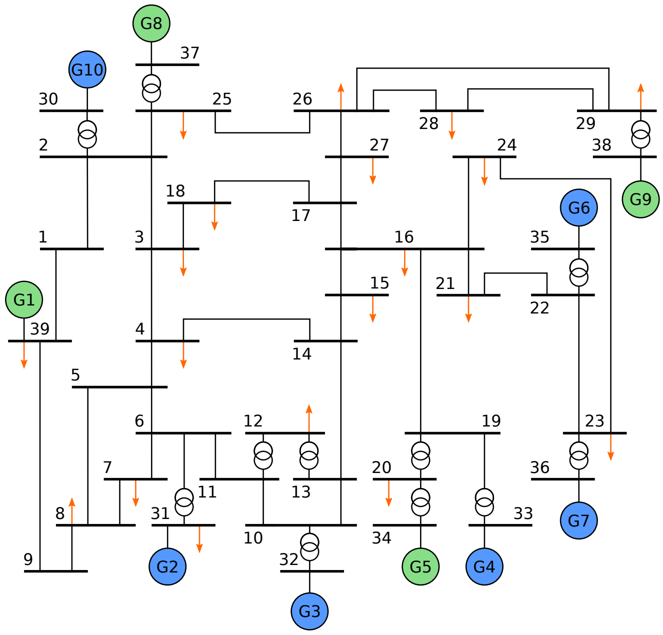

Figure 2.8 – Block diagram of the modified 39-bus power grid Opal-RT simulation model. The system is characterized by nominal voltage of 345 kV. The model consists in 6 synchronous generators (blue circles), 4 wind farms (green circles) and 19 loads (orange arrows). The total installed capacity is 10 GW.

For this analysis, the outage of three generators (G4, G6 and G7) is simulated, for a total tripped power of 1.5 GW. The outage occurs at t = 180 s and produces a noticeable step change that is followed by a long-term oscillating trend due to the grid inertia properties and the gradual load shedding and restoration (shown in Fig. 2.9).

The results are presented in Fig. 2.10, in terms of estimated ROCOF and of corresponding active profiles. For the sake of clarity, a single representative load for each class, i.e., load 16 for M-class and load 4 for P-class, is selected, but similar results hold in the rest of the nodes.

As regards ROCOF measurements, it is worth observing that the estimates of the two PMUs differ significantly in terms of both absolute value and polarity, in confirmation of the algorithm-dependency of PMU-based ROCOF measurements. As shown in the Fig. 2.10(a) and 2.10(c), right after the contingency, the cs-TFM estimates anticipate the e-IpDFT ones by one reporting period (i.e., 20 ms). This effect is due to the fact that cs-TFM adopts a dynamic signal model that allows for directly estimating the phase second-order time-derivative, whereas e-IpDFT adopts a static signal model and calculates ROCOF as the finite-difference between subsequent frequency measurements. This is particularly noticeable within the first 300 ms after the contingency. As UFLS starts to be triggered, this effect is less visible.

The corresponding active power is shown in Fig. 2.10(b) and 2.10(d). As regards M-class configuration, e-IpDFT sheds earlier whereas cs-TFM restores before. Although the cs-TFM estimates of ROCOF are anticipated by one reporting period, the e-IpDFT ones are character-

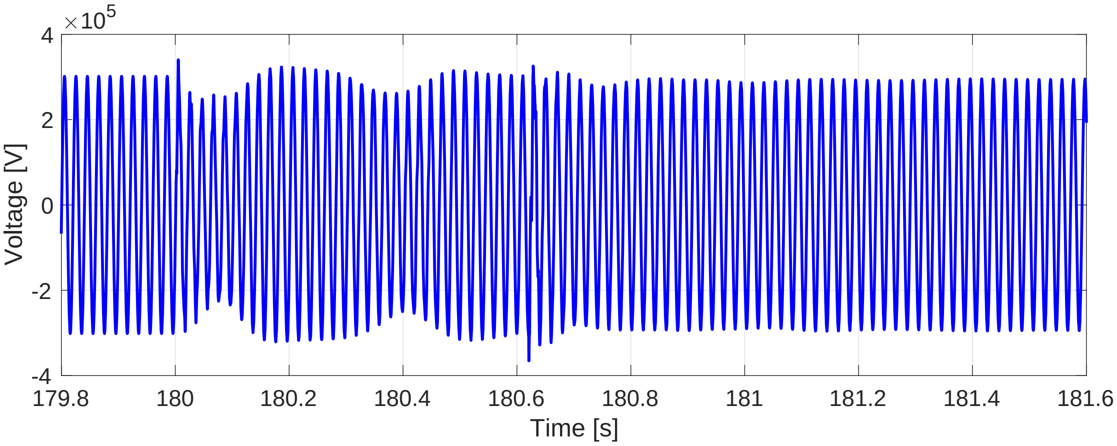

Figure 2.9 – Time-domain trend of the voltage waveform acquired by the PMUs at bus 26.

ized by higher ROCOF values. Therefore, it is reasonable to expect that the e-IpDFT estimates produce a larger amount of loads to be shed. As regards P-class configuration, given a shorter observation interval, on the one hand, control actions are taken earlier, on the other hand, the PMUs provide less accurate ROCOF measurements, leading to similar results for the two estimators. By extending the analysis to the entire grid, the performance difference can be characterized in terms of Expected Energy Not Served (EENS), defined as the expected amount of energy not being served to the demand during the UFLS and load restoration actions. The e-IpDFT always leads to higher EENS. In particular, the P-class configurations produces higher EENS values due to the larger amounts of shed loads caused by an overestimation of ROCOF, quantified in 16.8 MWh for e-IpDFT and 14.5 MWh cs-TFM, respectively. For M-class these values are reduced to 16.7 and 14 MWh, for e-IpDFT and cs-TFM respectively.

2.5 Discussion

After identifying the uprising operational challenges that modern power system operators are facing, the Chapter highlighted the importance of advanced and robust synchrophasor estimators for monitoring and control purposes, among others. Further, the main criticalities related to modern synchrophasor estimation algorithms were identified, along with the inconsistencies that may arise from an ill-posed formulation of the synchrophasor model.

Within this context, a set of simulation studies based on synthetic data inspired by real-scale events were used to evaluate the synchrophasor model-dependency. Specifically, signals characterized by heavy harmonic/inter-harmonic distortion, amplitude modulations, frequency ramps, and amplitude steps were considered. The obtained results experimentally validated that synchrophasor estimation algorithms guarantee enhanced accuracy, as long as the harmonic and inter-harmonic distortion within the measurement pass-band is reduced. Another critical condition is represented by transient events when the synchrophasor model loses its appropriateness, and a PMU-based approach towards situational awareness applica-

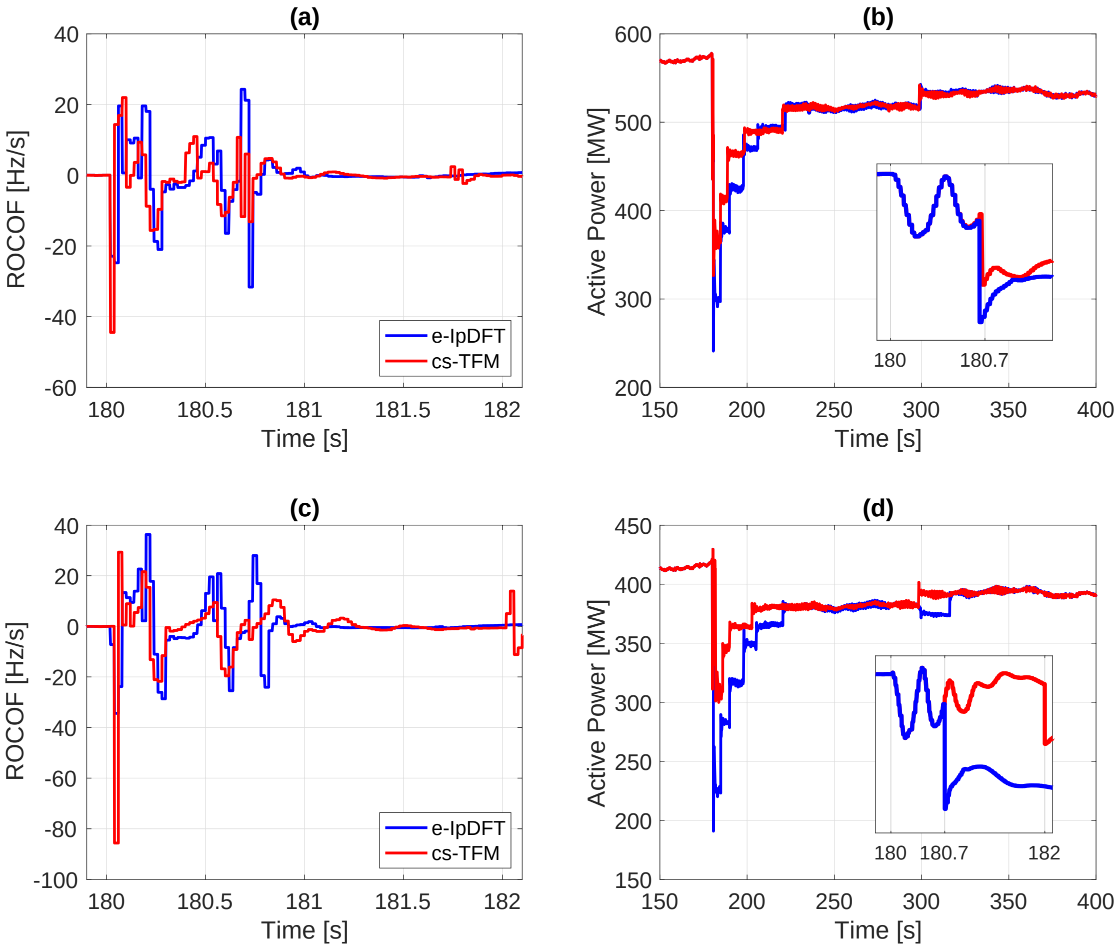

Figure 2.10 – PMU-based ROCOF measurements and corresponding active power profiles: (a) and (b) refer to load 4 and P-class configuration, whereas (c) and (d) refer to load 16 and M-class configuration.

tions might become questionable. Then, the Chapter proposed a real-time simulation-based study to assess how different synchrophasor estimation techniques can influence the performance of the supplied application in a reduced-inertia 10 GW-scale power system. In the proposed analysis, UFLS control schemes based on ROCOF estimations were implemented. In accordance with the previous results, the study proved that the control scheme performance depends on the adopted synchrophasor estimation technique and configuration.

To conclude, the basis for any reliable PMU-based control and protection application lies in the correct understanding of the rules governing the adopted synchrophasor estimation algorithm. That is why Chapters 3 and 4 thoroughly describe sophisticated synchrophasor extraction techniques, focusing on the adopted signal models, and characterize their performance under static and dynamic operating conditions. In practice, though, the only guarantee about PMU actual conduct is provided by their metrological calibration, presented in Chapter 5. Chapter 6 deals with technical aspects related to the actual deployability of synchrophasor networks, comprising time synchronization and data streaming. What if we get rid of the concept of synchrophasor? Chapter 7 proposes a new power system modeling approach that paves the way for developing new sensing infrastructures.

3 The Iterative-Interpolated Discrete Fourier Transform and its Application to Synchrophasor Estimation

Low-inertia grids are characterized by high shares of harmonic and inter-harmonic distortion, produced by the inverters that interface non-conventional generation assets to the electrical grid. These interfering tones largely compromise synchrophasor estimation and may jeopardize PMU-based protection and control strategies. Indeed, the IEEE Std. C37.118 does not require resiliency against inter-harmonic tones for P-class PMUs. In view of increasing synchrophasor technology reliability, the Chapter presents a single synchrophasor estimation algorithm that is simultaneously compliant with both P- and M-class of PMU performance. The method is integrated into an embedded device. The developed PMU complies with protection applications in terms of responsiveness and with measurement applications in terms of accuracy. The method, called iterative-Interpolated DFT (i-IpDFT), iteratively estimates and compensates the effects of the spectral interference produced by both a generic interfering tone, harmonic or interharmonic, and the negative image of the fundamental tone. The estimator adopts a window length of 60 ms and the 3-points IpDFT technique for cosine and Hanning window functions. Compliance with respect to the IEEE Std. C37.118 for P- and M-class is fully characterized.

The Chapter includes results of publications [8, 9].

3.1 Introduction and State of the Art

The IEEE Std. C37.118 [19] defines two performance classes to which PMUs must comply with. One of the main differences between P- and M-class requirements is represented by the Out-Of-Band Interference (OOBI) test. The latter, has been specifically designed for the M-class, to test the PMU capability to reject superposed interharmonics close to the 50 or 60 Hz main tone. These are defined as signals characterized by an amplitude that is 10% of the main tone and a frequency f_i in the bands [10, f_n-$F_r/2$] and [f_n+$F_r/2$, $2f_n$], being f_n the nominal power system frequency, F_r the PMU reporting rate and $f_i/f_n \notin \mathbb{N}$ [71].

Recently, the idea of a single PMU capable of satisfying both the P and M-class PMU requirements at the same time has become increasingly popular [72, 73]. The advantages are evident: from a cost perspective, an electrical utility interested to use PMUs to simultaneously supply monitoring and protection functionalities of situational awareness systems does not need to equip every measurement point with two different devices. From a measurement reliability perspective, the performance of fault management systems using PMU data to tune or back-up existing protection schemes, are not degraded by the presence of interharmonic tones [74]. In this respect, [72] proposes a hybrid P+M-class PMU design based on tunable trigger thresholds to switch between two different frequency-tracking filters. The technique self-switches from an M-class algorithm to a P-class one in case a transient event is detected. Conversely, [73] proposes a two-channel design that is conceived to comply with P- and M-class at once. The process implements in parallel two different Taylor Fourier Transform algorithms, not designed to meet P and M-class respectively: the first one produces accurate measurements of steady-state signals, while the second one is better suited to follow fast signal changes. In this case, the selection of the most appropriate output is implemented by a detector that identifies the presence of power system transients.

In this Chapter, a single algorithm designed to simultaneously fulfill the performance requirements of P- and M-class PMUs is proposed. That is to say that, for each operating condition defined in [19], the method is compliant with the most demanding specification of the joint P- and M-class requirements. The technique is hereafter called iterative Interpolated Discrete Fourier Transform (i-IpDFT) and demonstrates how it is possible to develop a DFT-based synchrophasor estimation algorithm capable of rejecting interharmonics, also when adopting relatively short window lengths (3 periods of a signal at f_n). The method represents an evolution of the one proposed in [56], conceived for P-class PMUs.

The i-IpDFT method iteratively finds and compensates the effects of the spectral interference produced by both an interfering tone and the negative image of the fundamental tone. Several algorithms that compensate the spectral interference generated by the image component of the main tone have been presented in the literature, the majority relying on the IpDFT [75, 56, 76, 77, 78]. Sine-fitting techniques [79], as well as compressive sensing [57] and lookup tables [80] have been investigated too. In [81] an IpDFT-based method that compensates the spectral interference generated by both the image component of the main tone and harmonic tones is presented. However, such investigation disregards interharmonic tones like those defined in the OOBI test.

The Chapter is structured as follows. Section 3.2 reviews the theoretical background about the 3-points IpDFT for cos^{α} windows and presents the effects of spectral leakage on the IpDFT performance. Section 3.3 formulates the i-IpDFT synchrophasor estimation algorithm, with a specific focus on the selection of the algorithm parameters. Section 3.4 assesses the algorithm performance in an offline simulation environment with respect to the testing conditions defined in [19]. Section 3.5 describes the implementation into an embedded hardware device, comprising a dedicated computational complexity analysis. Finally, Section 3.6 provides a discussion and some closing remarks.

3.2 The Interpolated DFT: advantages and limitations

The IpDFT is a technique that enables us to extract the parameters of a sinusoidal waveform by processing the highest DFT bins of the related DFT spectrum. In particular, the IpDFT enables the mitigation of the effects generated by incoherent sampling by [82, 83]:

- Applying suitably shaped window functions to reduce the *spectral leakage* effects;
- Interpolating the highest DFT bins of the spectrum to minimize the *spectral sampling* effects.

In the following of this Section the IpDFT technique is presented and the nomenclature is defined. More specifically, in Section 3.2.1 the family of $\cos^\alpha$ window functions is presented, with a particular focus on the cosine and the Hanning window. These two window types have been selected as they represent a good trade-off between the main-lobe width and the side-lobe levels. In Section 3.2.2 the IpDFT solution for these window functions is derived. Finally, in Section 3.2.3 the effects of spectral leakage on the IpDFT performance are discussed.

3.2.1 $\cos^\alpha$ Window Functions

The IpDFT solution can be analytically derived only for $\cos^\alpha$ windows[1] (also known as $\sin^\alpha$ windows) that are defined as follows [84]:

$$w_\alpha(n) = \sin^\alpha\left(\frac{\pi}{N}n\right),\ \ n \in [0, N-1],\ \ \alpha \in \mathbb{N} \tag{3.1}$$

being N the number of samples. Figure 3.1 shows three different $\cos^\alpha$ window functions obtained for $\alpha = \{0, 1, 2\}$. As it can be noted, the window spectrum depends upon α: as α decreases, the main lobe shrinks but the side lobes increase, whereas as α increases, the side lobes decrease but the main lobe becomes wider.

Generally, IpDFT algorithms were formulated for the so called Rife-Vincent class I windows, i.e., $\cos^\alpha$ windows characterized by a null or even value for α. The most elementary one is the rectangular ($\alpha = 0$), whose DFT is known as the Dirichlet kernel:

$$D_N(k) = e^{-j\pi k(N-1)/N}\frac{\sin(\pi k)}{\sin(\pi k/N)},\ \ k \in [0, N-1] \tag{3.2}$$

---

[1] The IpDFT can be also formulated for window functions not belonging to the $\cos^\alpha$ family. However, in this case the problem does not have a closed form analytical solution, although it is possible to use approximations of the numerically computed window spectrum.

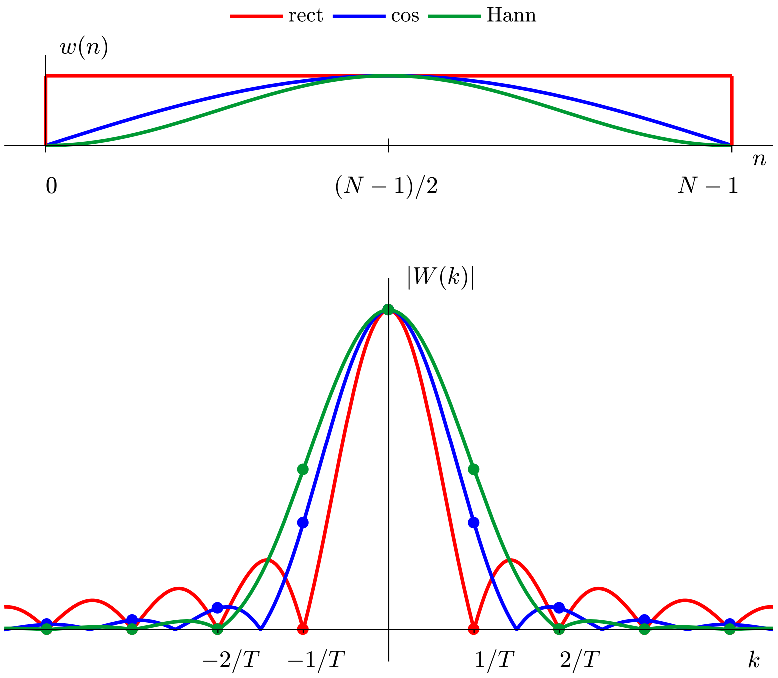

Figure 3.1 – Time (top) and frequency domain (bottom) representations of three different cos^α windows: the rectangular in red ($\alpha = 0$), cosine in blue ($\alpha = 1$) and Hanning in green ($\alpha = 2$).

This function is characterized by the narrowest main lobe among the $\cos^\alpha$ windows but at the same time it exhibits the highest side lobes.

In order to reduce the effects of spectral leakage generated by the side-lobe levels, IpDFT algorithms typically adopt bell-shaped windows, obtained by increasing the value of α in(3.1). The most common is the Hanning window ($\alpha = 2$) defined as:

$$w_H(n) = 0.5 \cdot (1 - \cos(2\pi n/N)), \; n \in [0, N-1] \tag{3.3}$$

and characterized by the following DFT:

$$W_H(k) = -0.25 \cdot D_N(k-1) + 0.5 \cdot D_N(k) - 0.25 \cdot D_N(k+1) \tag{3.4}$$

that is known for the good trade-off between the main-lobe width and side-lobe levels [83].

More recent studies have derived the analytical solution of the IpDFT problem for $\cos^\alpha$ windows in the case of an odd value for α [85]. In applications where the main lobe width plays a crucial role in identifying relatively nearby tones, like in synchrophasor estimation, the so-called cosine window, defined for $\alpha = 1$, is an extremely attractive solution as it represents a compromise between the rectangular and the Hanning window:

$$w_C(n) = \sin\left(\frac{\pi}{N} n\right), \; n \in [0, N-1] \tag{3.5}$$

Its DFT can be derived as follows:

$$W_C(k) = -0.5jD_N(k-0.5) + 0.5jD_N(k+0.5) \tag{3.6}$$

However, for an odd value for α, the window is a weighted sum of Dirichlet kernels modulated by non-integers of the frequency resolution, therefore an intrinsic limitation arises: as it can be seen from Fig. 3.1, the $W_C(k)$ zero-crossing do not happen for integer values of k. As a consequence, also with coherent sampling, the cosine window generates spectral leakage.

3.2.2 The Interpolated DFT

As known, the IpDFT is based on a static signal model that, in general, is assumed to contain a single unknown frequency component. In this respect, let us consider a finite sequence of N equally spaced samples $x(n)$ obtained by sampling an input continuous signal $x(t)$ with a sampling rate $F_s = 1/T_s$, being T_s the sampling time:

$$x(n) = A_0 \cos\left(2\pi f_0 n T_s + \varphi_0\right), \quad n \in [0, N-1] \tag{3.7}$$

where $\{f_0, A_0, \varphi_0\}$ are the signal frequency, amplitude and initial phase respectively. The signal is assumed to be windowed with a discrete function of N samples $w(n)$, being $T = N \cdot T_s$ the window length. The DFT $X(k)$ of the windowed input signal is:

$$X(k) \triangleq \frac{1}{B} \sum_{n=0}^{N-1} w(n) x(n) W_N^{kn}, \quad k \in [0, N-1] \tag{3.8}$$

where $B \triangleq \sum_{n=0}^{N-1} w(n)$ is the DFT normalization factor, and $W_N \triangleq e^{-j2\pi/N}$ is the so called twiddle factor. The DFT returns a sequence of N samples (also called bins) of the theoretical Discrete Time Fourier Transform (DTFT) that are uniformly spaced by the DFT frequency resolution $\Delta f = 1/T$. More specifically, based on the convolution theorem, the DFT of the windowed signal $x(n)$ exhibits a pair of scaled, shifted and rotated versions of the DFT of the window function (see Fig. 3.2): the so-called *positive image* (in blue), is shifted up to the tone frequency f_0, the so-called *negative image* (in red), is shifted down to $-f_0$:

$$X(k) = X_0^+(k) + X_0^-(k) \tag{3.9}$$

where:

$$\begin{cases} X_0^+(k) = A_0 e^{+j\varphi_0} W(k - f_0/\Delta_f) & \text{(3.10a)} \\ X_0^-(k) = A_0 e^{-j\varphi_0} W(k + f_0/\Delta_f) & \text{(3.10b)} \end{cases}$$

being $W(k)$ the DFT of the adopted window function.

As shown in Fig. 3.2, in case of incoherent sampling (i.e., when $f_0/\Delta f \notin \mathbb{N}$), the peak value of the continuous spectrum of the fundamental tone of a signal (highlighted in green) is located

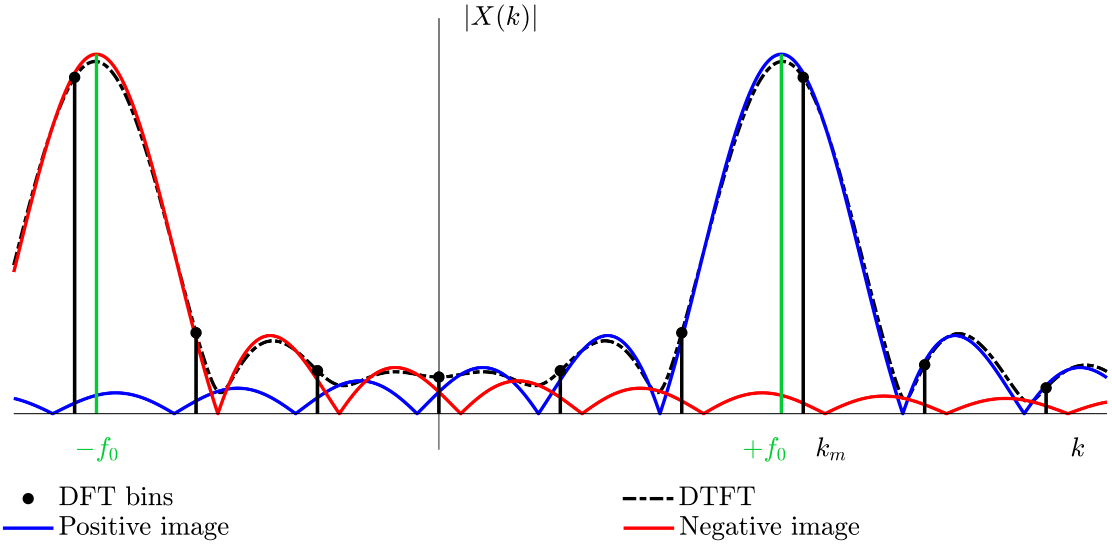

Figure 3.2 – DFT and DTFT of a steady-state single-tone signal that is incoherently sampled and the related positive and negative images.

between two consecutive DFT bins and the signal frequency can be expressed as:

$$f_0 = (k_m + \delta)\Delta f \tag{3.11}$$

being $-0.5 \leq \delta < 0.5$ a fractional correction term and k_m the index of the highest bin. The IpDFT problem lies in finding the correction term δ (and, consequently, the fundamental tone's parameters $\{f_0, A_0, \varphi_0\}$) that better approximates the exact location of the main spectrum tone.

The IpDFT problem solution has been originally provided as a 2-point interpolation scheme[82, 83]. More recently, multipoint interpolation schemes have demonstrated to inherently reduce the long-term spectral leakage effects, leading to more accurate interpolation results [76, 77]. In this respect, for the Hanning window, the fractional term δ can be computed by interpolating the 3 highest DFT bins as [76]:

$$\delta = 2\varepsilon \cdot \frac{|X(k_m+\varepsilon)| - |X(k_m-\varepsilon)|}{|X(k_m-\varepsilon)| + 2|X(k_m)| + |X(k_m+\varepsilon)|} \tag{3.12}$$

where $\varepsilon = \pm 1$ if $|X(k_m+1)| \gtrless |X(k_m-1)|$. The fundamental tone's amplitude and phase can then be computed as:

$$A_0 = |X(k_m)| \left| \frac{\pi\delta}{\sin(\pi\delta)} \right| \left| \delta^2 - 1 \right| \tag{3.13}$$

$$\varphi_0 = \angle X(k_m) - \pi\delta \tag{3.14}$$

Similarly, for the cosine window, δ can be obtained by interpolating the 3 highest DFT bins as

[85]:

$$\delta = 1.5\varepsilon \cdot \frac{|X(k_m+\varepsilon)| - |X(k_m-\varepsilon)|}{|X(k_m-\varepsilon)| + 2\,|X(k_m)| + |X(k_m+\varepsilon)|} \tag{3.15}$$

The fundamental tone's amplitude and phase can then be computed as (computational details are given in the next Paragraph):

$$A_0 = 4 \cdot \frac{\left|\delta^2 - 0.25\right|}{|\cos(\pi\delta)|} \cdot |X(k_m)| \tag{3.16}$$

$$\varphi_0 = \angle X(k_m) - \pi\delta \tag{3.17}$$

Solution of the IpDFT Problem using the Cosine Window

The analytical formulation of the IpDFT correction term δ for the cosine window given in (3.15) is derived from [85]. Regarding the tone's amplitude given in (3.16), no derivation was found in the existing literature.

If the number of samples N is sufficiently large, the following approximation is valid [45]:

$$e^{\pm j\frac{\pi}{2}(N-1)/N} \approx \pm j \tag{3.18}$$

Moreover, sine functions are approximated by their arguments in the case of small angles. The Dirichlet kernel evaluated in $k \pm 0.5$ can be then approximated as:

$$D_N(k \pm 0.5) = \mp j e^{-j\pi k(N-1)/N} \frac{\sin(\pi k \pm \pi/2)}{\sin(\pi(k \pm 0.5)/N)} \approx -\frac{jN}{\pi} e^{-j\pi k(N-1)/N} \frac{\cos(\pi k)}{k \pm 0.5} \tag{3.19}$$

Therefore, the DFT of the cosine window in (3.6) can be approximated as:

$$W_C(k) = -\frac{N}{2\pi} e^{-j\pi k(N-1)/N} \frac{\cos(\pi k)}{k^2 - 0.25} \tag{3.20}$$

The tone's amplitude A_0 corresponds to the modulus of the DTFT of the signal evaluated at frequency $f_0 = k_m + \delta$:

$$A_0 = |X(k_m + \delta)| \tag{3.21}$$

Its value can be formulated as a function of the highest amplitude DFT bin:

$$\frac{|X(k_m+\delta)|}{|X(k_m)|} \approx \frac{|W_C(0)|}{|W_C(-\delta)|} = 4 \cdot \frac{|\delta^2 - 0.25|}{|\cos(\pi\delta)|} \tag{3.22}$$

leading to (3.16). The approximation sign is used instead of equality, because the ratios might differ due to spectral leakage [45].

3.2.3 Spectral Leakage Effects on the IpDFT

The main assumptions behind the formulation of the IpDFT technique are the following [82]:

1. The input signal is characterized by time-invariant parameters;
2. The input signal is sampled with a sampling rate sufficiently higher than the highest signal's spectral component;
3. The DFT bins used to perform the interpolation are only generated by the positive image of the tone under analysis.

In order to satisfy the first two assumptions when applying the IpDFT to synchrophasor estimation, sampling rates in the order of few kHz and window lengths containing few periods of a signal at the rated power system frequency must be adopted respectively [45]. This choice causes the energy of the DFT spectrum to be concentrated in the lower frequency range and the positive and negative image of the main tone of the spectrum to be relatively close. In such conditions, in case of incoherent sampling, the tails of the negative image of the spectrum main tone (red curve in Fig. 3.2) leak into the positive frequency range and bias the DFT bins used to perform the interpolation (i.e., assumption 3 is not respected). This effect, also known as spectral interference has demonstrated to considerably corrupt the IpDFT estimations when applied to synchrophasor estimation [78]. To cope with these conditions, in [56] a technique that mitigates the effect of the spectral leakage produced by the negative image of the spectrum is presented. The method, called enhanced-IpDFT (e-IpDFT) is described in Algorithm 3, where the function *DFT* refers to (3.8), *IpDFT* refers to(3.11)-(3.14) and *image* to (3.10a) or (3.10b).

Algorithm 3 The e-IpDFT algorithm.

```
1: $X(k) = DFT\left[x(n) \cdot w(n)\right]$    ▷ Signal windowing and DFT computation
2: $\{\widehat{f}_0^0, \widehat{A}_0^0, \widehat{\varphi}_0^0\} = IpDFT\left[X(k)\right]$    ▷ Fundamental tone parameters computation via IpDFT
3: for $p = 1 \to P$    ▷ Interference compensation routine
4:     $\widehat{X}_0^{p-}(k) = image\left[-\widehat{f}_0^{p-1}, \widehat{A}_0^{p-1}, -\widehat{\varphi}_0^{p-1}\right]$    ▷ Fund. tone negative image reconstruction
5:     $\widehat{X}_0^{p+}(k) = X(k) - \widehat{X}_0^{p-}(k)$    ▷ Fund. tone positive image estimation
6:     $\{\widehat{f}_0^p, \widehat{A}_0^p, \widehat{\varphi}_0^p\} = IpDFT\left[\widehat{X}_0^{p+}(k)\right]$    ▷ Fund. tone parameters computation via IpDFT
7: end for
```

The technique starts with the computation of the DFT spectrum $X(k)$ (line 1 in Alg. 3), that can be performed with any DFT computation method. Then, a preliminary estimation of the main tone parameters is obtained by applying the IpDFT to $X(k)$ (line 2). These values are used to estimate the main tone's negative image $\widehat{X}_0^-(k)$ (line 4), as in (3.10b), that is then subtracted from $X(k)$, to return an estimation of the main tone's positive image (line 5). The IpDFT is applied to the resulting spectrum, where the spectral interference produced by the negative image is considerably reduced (line 6). The compensation of the spectral interference produced by the negative image of the fundamental tone, can be iterated a predefined number of times P, leading to more accurate estimates as P increases (see Section 3.3.2). The method proposed in [56] can be summarized by defining a single function *eIpDFT* that accounts for lines 2-7 of Algorithm 3:

$$\{\widehat{f}_0, \widehat{A}_0, \widehat{\varphi}_0\}|_P = eIpDFT\,[X(k)] \tag{3.23}$$

The method presented in [56] does not account for the spectral interference produced by tones other than the fundamental one. As a consequence, it produces incorrect results in presence of interfering tones that are relatively close to the main one, such those defined in the OOBI test.

3.3 The Iterative-Interpolated DFT for Synchrophasor Estimation

This Section aims at presenting the i-IpDFT, that represents an enhancement of the method proposed in [56] as it takes into account the effects of the spectral interference generated by both the negative image of the main tone and a generic interfering one. More specifically, Section 3.3.1 defines the synchrophasor estimation algorithm, whereas Section 3.3.2 and 3.3.3 propose a procedure to tune the algorithm parameters.

3.3.1 The i-IpDFT Algorithm Formulation

Let us consider a steady-state discrete signal composed of two tones, a fundamental and an interfering tone (not necessary harmonic, i.e., $f_i / f_0 \in \mathbb{R}$), both unknown:

$$x(n) = A_0 \cos\left(2\pi f_0 n T_s + \varphi_0\right) + A_i \cos\left(2\pi f_i n T_s + \varphi_i\right) \tag{3.24}$$

As shown in Fig. 3.3, its DFT spectrum can be modeled as the sum of the positive (in blue) and negative (in red) images of the fundamental (solid line) and interfering (dashed line) tones:

$$X(k) = X_0(k) + X_i(k) = X_0^+(k) + X_0^-(k) + X_i^+(k) + X_i^-(k) \tag{3.25}$$

The proposed i-IpDFT algorithm iteratively estimates and compensates the effects of spectral leakage generated by an interfering tone and by the negative image of the main tone, such that the IpDFT is applied to a DFT spectrum that is only composed of the positive image of the main tone $X_0^+(k)$. The pseudo-code of the proposed i-IpDFT is reported in Algorithm 4, whereas Fig. 3.4 illustrates the spectra processed during successive steps of the method.

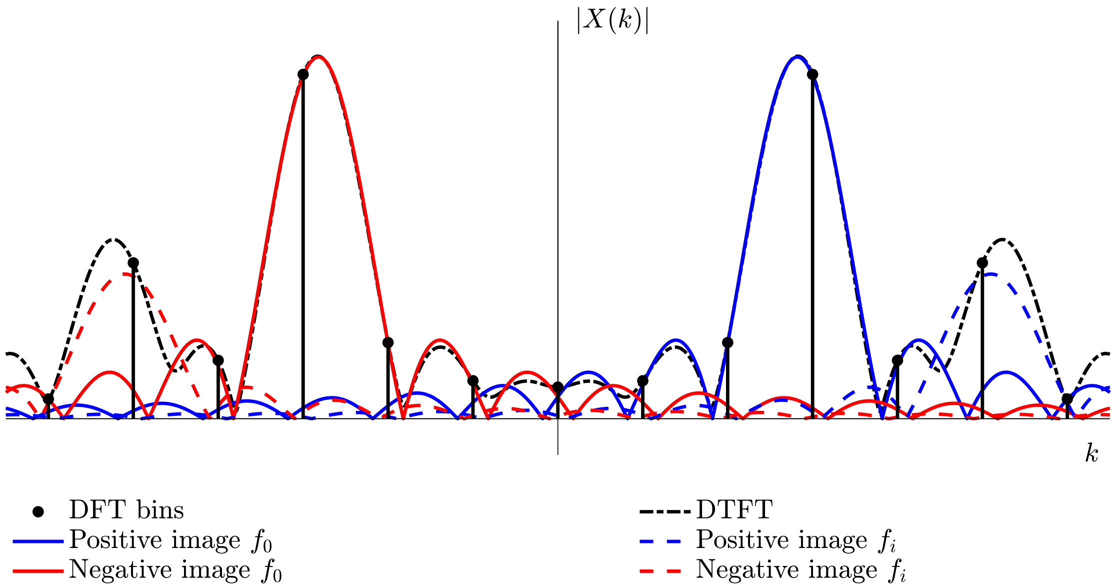

Figure 3.3 – DFT and DTFT of a steady state signal composed of a main tone and an interharmonic one and the related positive and negative images.

Algorithm 4 The i-IpDFT algorithm.

```
$X(k) = DFT\,[x(n)\cdot w(n)]$    ▷ Signal windowing and DFT computation
$\{\widehat{f}_0^0, \widehat{A}_0^0, \widehat{\varphi}_0^0\}|_P = eIpDFT\,[X(k)]$    ▷ Fund. parameters computation via e-IpDFT
$\widehat{X}_0^0(k) = image\,[\widehat{f}_0^0, \widehat{A}_0^0, \widehat{\varphi}_0^0] + image\,[-\widehat{f}_0^0, \widehat{A}_0^0, -\widehat{\varphi}_0^0]$    ▷ Fund. spectrum reconstruction
if $\sum|X(k) - \widehat{X}_0^0(k)|^2 > \lambda\cdot\sum|X(k)|^2$    ▷ Interference detection
    for $q = 1 \rightarrow Q$    ▷ Interference compensation routine
        $\{\widehat{f}_i^q, \widehat{A}_i^q, \widehat{\varphi}_i^q\}|_P = eIpDFT\left[X(k) - \widehat{X}_0^{q-1}(k)\right]$    ▷ Inter. param. computation via e-IpDFT
        $\widehat{X}_i^q(k) = image\,[\widehat{f}_i^q, \widehat{A}_i^q, \widehat{\varphi}_i^q] + image\,[-\widehat{f}_i^q, \widehat{A}_i^q, -\widehat{\varphi}_i^q]$    ▷ Inter. spectrum reconstr.
        $\{\widehat{f}_0^q, \widehat{A}_0^q, \widehat{\varphi}_0^q\}|_P = eIpDFT\,[X(k) - \widehat{X}_i^q(k)]$    ▷ Fund. param. computation via e-IpDFT
        $\widehat{X}_0^q(k) = image\,[\widehat{f}_0^q, \widehat{A}_0^q, \widehat{\varphi}_0^q] + image\,[-\widehat{f}_0^q, \widehat{A}_0^q, -\widehat{\varphi}_0^q]$    ▷ Fund. spectrum reconstr.
    end for
else
    break
end if
```

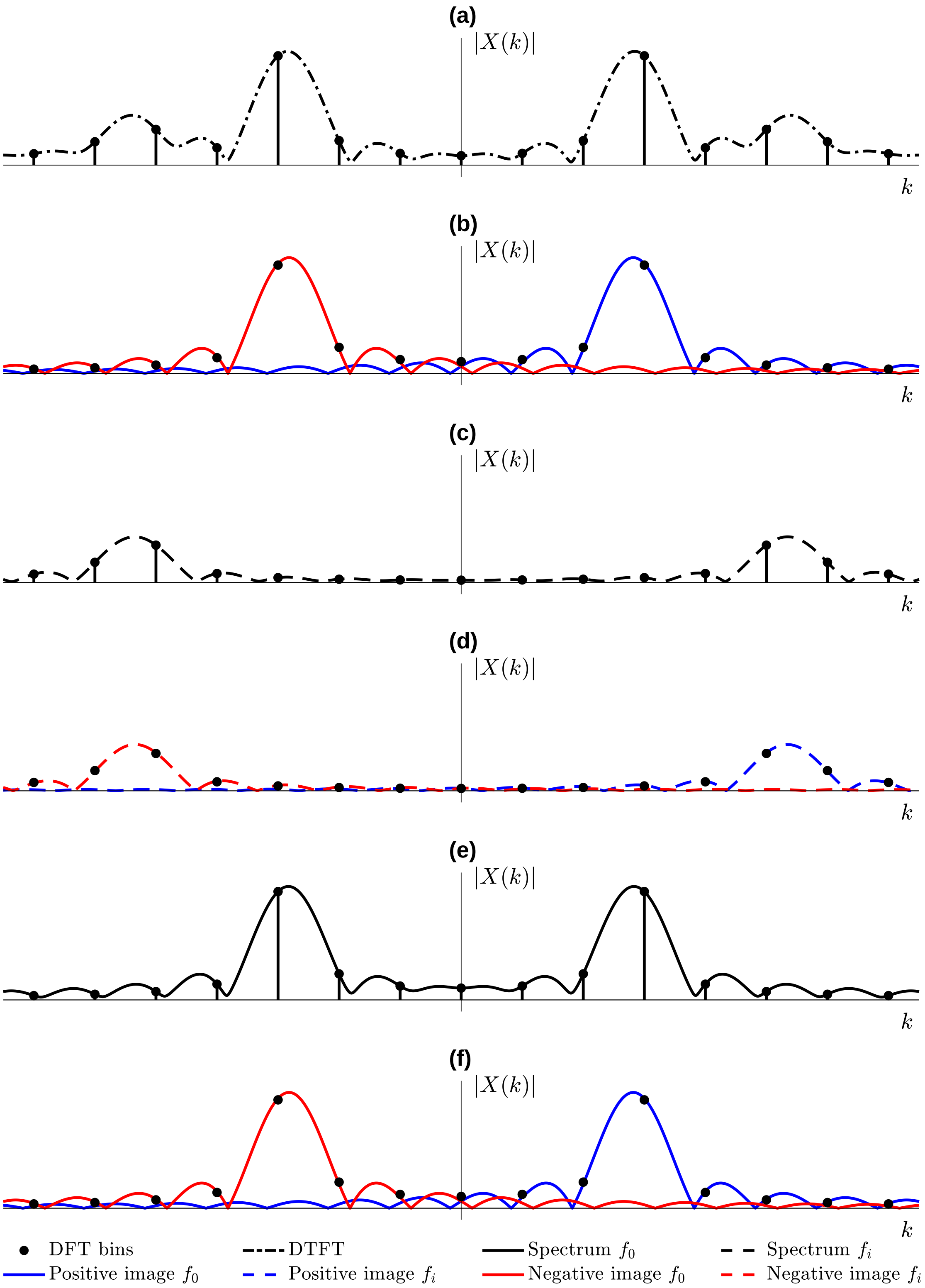

Figure 3.4 – Spectra processed at different steps of Algorithm 4: $X(k)$ in line 1 (a); $\widehat{X}_0(k)^0$ in line 3 (b); $X(k)-\widehat{X}_0^{q-1}(k)$ in line 4 and 6 (c); $\widehat{X}_i^q(k)$ in line 7 (d); $X(k)-\widehat{X}_i^q(k)$ in line 8 (e); $\widehat{X}_0^q(k)$ in line 9 (f).

The first steps (lines 1-2 in Alg. 4) of the i-IpDFT algorithm exactly correspond to the e-IpDFT technique in Algorithm 3. Although in presence of an interfering tone the estimated main tone parameters might be largely biased, they can be used to approximate the positive and the negative image of the fundamental tone (line 3, Fig. 3.4(b)). The latter are then subtracted from the original DFT bins to produce a spectrum $X(k)-\widehat{X}_0(k)$ that accounts for any spurious contribution perturbing the fundamental tone of the signal (line 4, Fig. 3.4(c)).

In case an interfering tone is detected, the procedure that estimates and compensates its spectral interference must be activated. Otherwise the method stops and returns the parameters $\{\widehat{f}_0^0, \widehat{A}_0^0, \widehat{\varphi}_0^0\}$ estimated at line 2. If an interfering tone is present, the spectral energy of $X(k)-\widehat{X}_0^0(k)$ weighted by the spectral energy of $X(k)$, exceeds a certain threshold λ (see Section 3.3.3 for further details):

$$E_n = \frac{E[X(k)-\widehat{X}_0^0(k)]}{E[X(k)]} = \frac{\sum\limits_{k=0}^{K} |X(k)-\widehat{X}_0^0(k)|^2}{\sum\limits_{k=0}^{K} |X(k)|^2} > \lambda \tag{3.26}$$

where K is the total number of computed DFT bins. In such a case, the e-IpDFT is applied to $X(k)-\widehat{X}_0^{q-1}(k)$, to estimate the parameters $\{\widehat{f}_i^q, \widehat{A}_i^q, \widehat{\varphi}_i^q\}$ of the detected interharmonic tone (line 6). The latter, are used to evaluate both the positive and negative image of the interharmonic tone (line 7, Fig. 3.4(d)), that are then subtracted from the original DFT bins, obtaining the spectrum $X(k)-\widehat{X}_i^q(k)$ that does not contain the interfering tone (line 8, Fig. 3.4(e)). Finally, the e-IpDFT is applied to such spectrum leading to an enhanced estimation of the main tone parameters $\{\widehat{f}_0^q, \widehat{A}_0^q, \widehat{\varphi}_0^q\}$ (line 8, Fig. 3.4(f)).

The whole procedure can be iterated a predefined number of times Q, leading to more and more accurate estimates as Q increases (see Section 3.3.2). The presented i-IpDFT algorithm can be formulated for any window function, number of IpDFT interpolation points, window length and sampling frequency. Even though it has been formulated for a single interfering component, it can be easily extended to consider more than one interfering component. In this respect, it is worth mentioning that the amount of DFT bins to be calculated at line 1 depends on the highest frequency component that has to be compensated.

Finally, the Rate-Of-Change-Of-Frequency (ROCOF) is computed by means of a classical backward first-order approximation of a first-order derivative:

$$ROCOF(n) = \left|\widehat{f}_0(n) - \widehat{f}_0(n-1)\right| \cdot F_r \tag{3.27}$$

where $\widehat{f}_0(n)$ and $\widehat{f}_0(n-1)$ represent the fundamental frequency estimations at two successive reporting times.

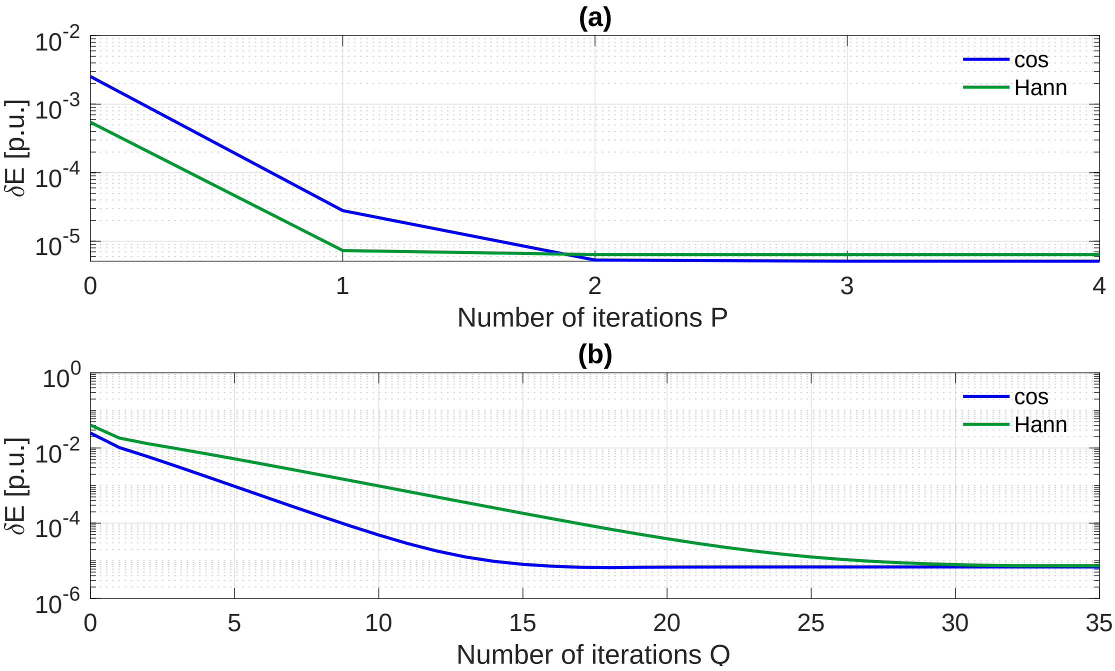

Figure 3.5 – Error in estimating the IpDFT correction term δ with the e-IpDFT technique as a function of P (a), and with the i-IpDFT as a function of Q (b) for the cosine (blue) and the Hanning (green) window functions. $F_s = 50$ kHz, $T = 60$ ms, SNR = 80 dB. In (a) single-tone signal at $f_0 = 47.5$ Hz. In (b) signal at $f_0 = 47.5$ Hz plus an interfering tone at $f_i = 20$ Hz.

3.3.2 On the Tuning of the Number of Iterations P and Q

The performance of the i-IpDFT algorithm are mainly influenced by two parameters, and in what follows a procedure to select them is presented:

- P: the number of iterations of the compensation of the spectral interference generated by the negative image of the tone under analysis (see Algorithm 3);
- Q: the number of iterations of the iterative routine to compensate the interfering tone (see Algorithm 4).

The effects of P can be evaluated when applying the e-IpDFT technique to a single-tone signal that is incoherently sampled. In this respect, Fig. 3.5(a) shows the accuracy in estimating the IpDFT correction term δ as a function of P, when analyzing a signal at 47.5 Hz with a sampling rate of 50 kHz and a window length of 60 ms. In order to emulate more realistic conditions, the signal is characterized by an 80 dB Signal-to-Noise Ratio (SNR) [48]. As it can be noted, in this specific case, the effect of the compensation becomes negligible after $P = 2$ iterations both for the Hanning and the cosine windows. In general this is not always the case and the number of iterations gets higher as the relative distance between the positive and negative images gets smaller. Nevertheless, due to its good trade-off between the overall algorithm performance and computational complexity, in the following the results will be presented for $P = 2$.

The effects of the overall number of iterations Q are evaluated when applying the i-IpDFT algorithm to a signal corrupted by an interharmonic tone. In particular, the case of a signal characterized by a main tone at 47.5 Hz and an interharmonic tone at 20 Hz is presented (similar results hold for all combinations of f_0 and f_i in the OOBI range). Again, an 80 dB SNR is considered [48]. Fig. 3.5(b) shows the error in estimating the correction term δ with the i-IpDFT technique (F_s = 50 kHz, T = 60 ms) as a function of Q. For the cosine window the effects of the compensation become negligible after Q = 16 iterations, whereas for the Hanning window after Q = 28 iterations. This result is explained by the fact that the narrower main lobe of the cosine window allows to detect (and therefore compensate) the interharmonic tone with a smaller number of iterations. As a consequence, the i-IpDFT results are presented for Q = 16 and Q = 28 for the cosine and Hanning window respectively.

3.3.3 On the tuning of the threshold λ

The threshold λ must be set so that the iterative compensation (i.e., lines 5-10 of Algorithm 4) is activated only in presence of an interharmonic tone. Furthermore, the proposed technique can turn out to be extremely useful to compensate the spectral leakage generated by an harmonic tone when using the cosine window, which has demonstrated to generate spectral leakage also with coherent sampling.

In general, the normalized spectral energy E_n can contain contributions generated by an interfering tone (e.g., harmonic or interharmonic) as well as any spurious component generated by a dynamic event that is wrongly captured by the DFT (e.g., steps in amplitude and in phase or amplitude and phase modulations). In this respect, Fig. 3.6 shows the variability of E_n by means of a boxplot representation for the various testing conditions dictated by [19]. Fig. 3.6 shows that, when the main tone is corrupted by a 10% harmonic or interharmonic component, the values of E_n are relatively higher than all the other testing conditions. Therefore, in the following the value of λ is set to $3.3 \cdot 10^{-3}$, in order to activate the algorithm only in presence of interfering components higher than 10% of the fundamental tone.

Even if not required by [19], dedicated simulations to assess the influence of lower interharmonic amplitudes on the i-IpDFT performance are carried out. Specifically, A_i is varied within the interval [1, 10]%A_0. As it can be seen from Fig. 3.6, the threshold $\lambda = 3.3 \cdot 10^{-3}$ enables the correct identification of interharmonic tones characterized by A_i above 8% for the cosine window and 9% for the Hanning one. Consequently, a correct behavior of the algorithm takes place and the errors are below the limits dictated by [19]. Below such amplitudes, given that the iterative compensation in not activated, the i-IpDFT cannot identify and correct the interharmonic tone. Therefore, the errors exceed the limits dictated by [19]. Even though a lower value of λ would enable the detection of interfering tones characterized by smaller amplitudes, it would not enable the distinction between an interfering tone (to be eliminated from the signal spectrum) and a dynamic behavior (not to be eliminated).

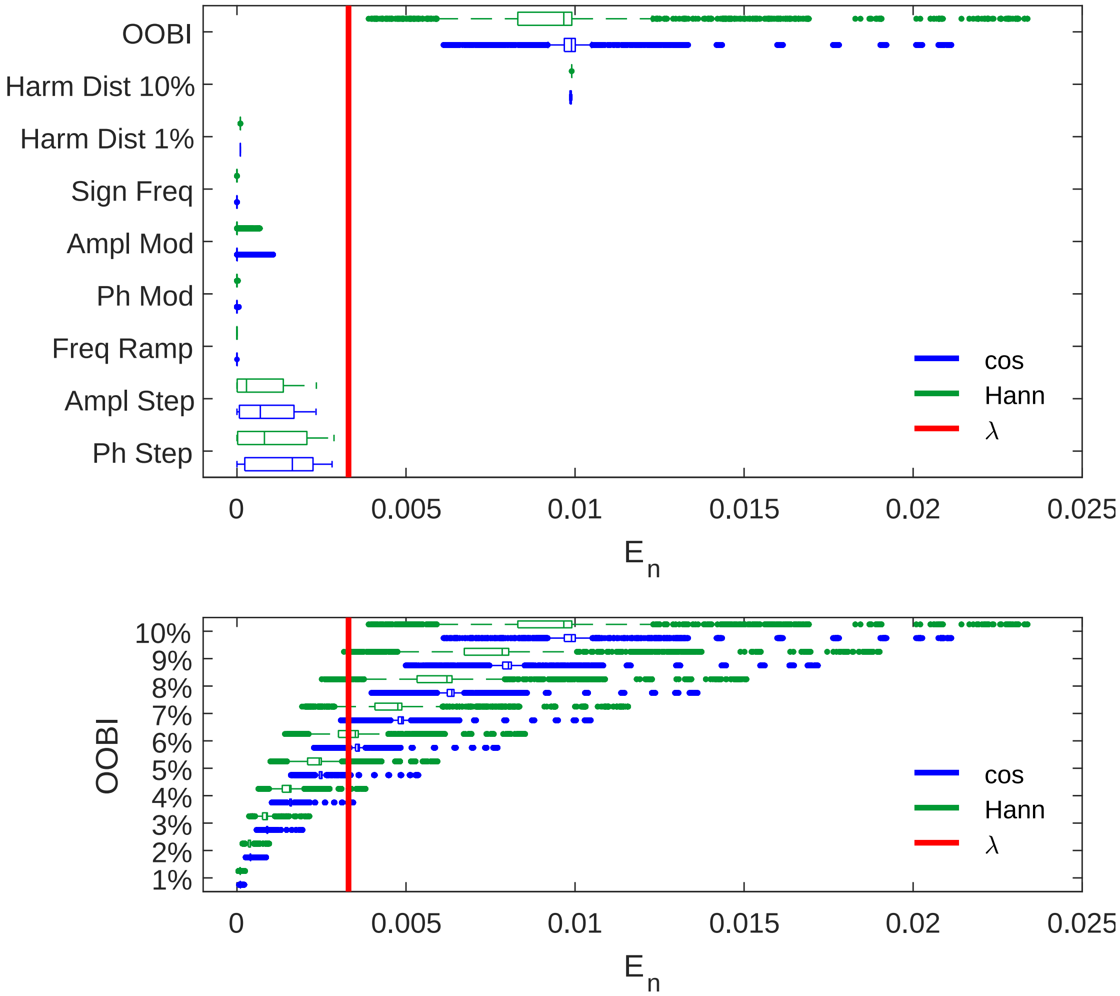

Figure 3.6 – Boxplot representation of E_n for the cosine (blue) and Hanning (green) window function in all operating conditions indicated in [19] (a) and in the OOBI test when changing A_i in the range $[1,10]\%A_0$ (b). The red line represents the selected threshold $\lambda = 3.3 \cdot 10^{-3}$. $F_s =$ 50 kHz, $f_n = 50$ Hz, $T = 60$ ms, SNR = 80 dB.

3.4 Performance Characterization with respect to the IEEE Std. C37.118

This Section presents the numerical validation of the i-IpDFT algorithm, that is carried out in a simulation environment, by making reference to the static (Section 3.4.1) and dynamic (Section 3.4.2) performance requirements dictated by the IEEE Std. C37.118 [19, 20] and following the testing procedures described in the IEEE Guide C37.242 [86]. In order to limit the number of tests, the nominal frequency and the reporting rate have been fixed to 50 Hz and 50 frames-per-second (fps) respectively. For each test, the results are presented by means of three graphs showing the maximum Total Vector Error (TVE), Frequency Error (FE) and ROCOF Error (RFE) as a function of the independent variable of the specific test, together with the maximum limit allowed by [19] for both P- and M-class PMUs. TVE, FE and RFE, are computed as [19]:

$$\mathrm{TVE} = \frac{|\hat{p}-p|}{|p|}; \quad \mathrm{FE} = |\hat{f}-f|; \quad \mathrm{RFE} = |\hat{R}-R| \tag{3.28}$$

where p, f and R represent the synchrophasor, frequency and ROCOF associated to the fundamental component and the hat denotes the estimated values. Moreover, two tables summarize the maximum obtained TVE, FE and RFE and the maximum limit allowed by [19] in all tests. Although [19] does not provide any guidelines regarding the noise, additive white Gaussian noise with zero mean and variance corresponding to SNR in the range [60, 80] dB is added to the reference signals, in order to simulate more realistic conditions [48]. For the sake of clarity, since the trend of errors is similar for any value of SNR, the graphs refer to SNR of 80 dB, whereas the tables include the maximum obtained errors for both 60 and 80 dB.

As reported in Table 3.1, the i-IpDFT algorithm results are shown for both the Hanning (green lines) and cosine windows (blue lines), using a sampling rate of 50 kHz and a window containing 3 periods of a signal at the nominal power system frequency. This is the shortest observation interval that enables us to distinguish between the fundamental and the interfering tone, and to fulfill jointly the P and M-class requirements. The time-stamp of the synchrophasor is referred to the center of the applied window. The synchrophasors are estimated at overlapping observation windows, that are shifted by the PMU reporting time, i.e.,

Table 3.1 – i-IpDFT parameters.

Parameter	**Variable**	**Value**
Nominal system frequency	f_n	50 Hz
Window type	-	Cosine and Hanning
Window length	T	60 ms ($3/f_n$)
Sampling rate	F_s	50 kHz
PMU reporting rate	F_r	50 fps
DFT bins	K	11 (cos) and 8 (Hann)
Iterations compensation fund. image	P	2
Iterations compensation interference	Q	16 (cos) and 28 (Hann)
IpDFT interpolation points	-	3

20 ms. For the cosine function, the first 10 DFT bins of the spectrum are computed, in order to be able to compensate the effects of any interfering component up to the 3^{rd} harmonic. For the Hanning function, this value can be reduced to 7 bins taking advantage of the fact that harmonic components do not determine spectral leakage for this specific window. The 3-points IpDFT is used to estimate the fractional correction term δ. It is worth pointing out that the parameters reported in Table 3.1 are kept constant during all tests, and that such configuration enables the simultaneous compliance to P- and M-class in all operating conditions defined in [19].

3.4.1 Static Operating Conditions

In accordance with the IEEE Std. C37.118 specifications, the static tests are intended to assess the algorithm estimation accuracy in steady-state conditions. The results of the i-IpDFT are presented in Fig. 3.7-3.9 and Table 3.2.

The first test, known as signal frequency, considers the following signal model:

$$x(t) = A_0 \cdot \cos(2\pi f_0 t + \varphi_0) \tag{3.29}$$

where A_0 is fixed to its nominal values, φ_0 is set to zero, whereas f_0 varies within [45, 55] Hz with an incremental step of at least 1 Hz. In order to provide more exhaustive results, in this analysis f_0 is incremented by steps of 0.1 Hz. Since the fundamental frequency is not synchronized with the sampling rate, this test enables us to characterize also the estimation accuracy as a function of the initial phase. According to the IEEE Std. C37.118, TVE and FE limits are equal to 1% and 5 mHz respectively for both performance classes, whereas the RFE is limited to 0.4 and 0.1 Hz/s for P- and M-class, respectively.

As shown in Fig. 3.7, the i-IpDFT errors are not influenced by the fundamental tone frequency, nor by the adopted window function. The compensation of the spectral leakage introduced by the negative image of the fundamental tone enables accurate synchrophasor estimates in the whole PMU pass-band. As it can be noted from Table 3.2, when the wideband noise level is 60 dB, in case of using the Hanning window, the RFE is 0.126 Hz/s, being 0.1 Hz/s the maximum limit allowed by [19]. Nevertheless, in the same conditions, for the cosine window the RFE is below such limit.

The harmonic distortion test, considers the following signal model:

$$x(t) = A_0 \cdot \cos(2\pi f_0 t + \varphi_0) + A_h \cdot \cos(2\pi h f_0 t + \varphi_h) \tag{3.30}$$

where the fundamental component is characterized by nominal amplitude, frequency and initial phase set to zero, whereas the harmonic distortion is produced by a single component whose amplitude A_h corresponds to a Total Harmonic Distortion (THD) level of either 1 or 10%. For this analysis, the harmonic order h is varied from 2 to 50. For the sake of generality, the harmonic initial phase is also varied within [0, π] rad, with an incremental step of $\pi/10$.

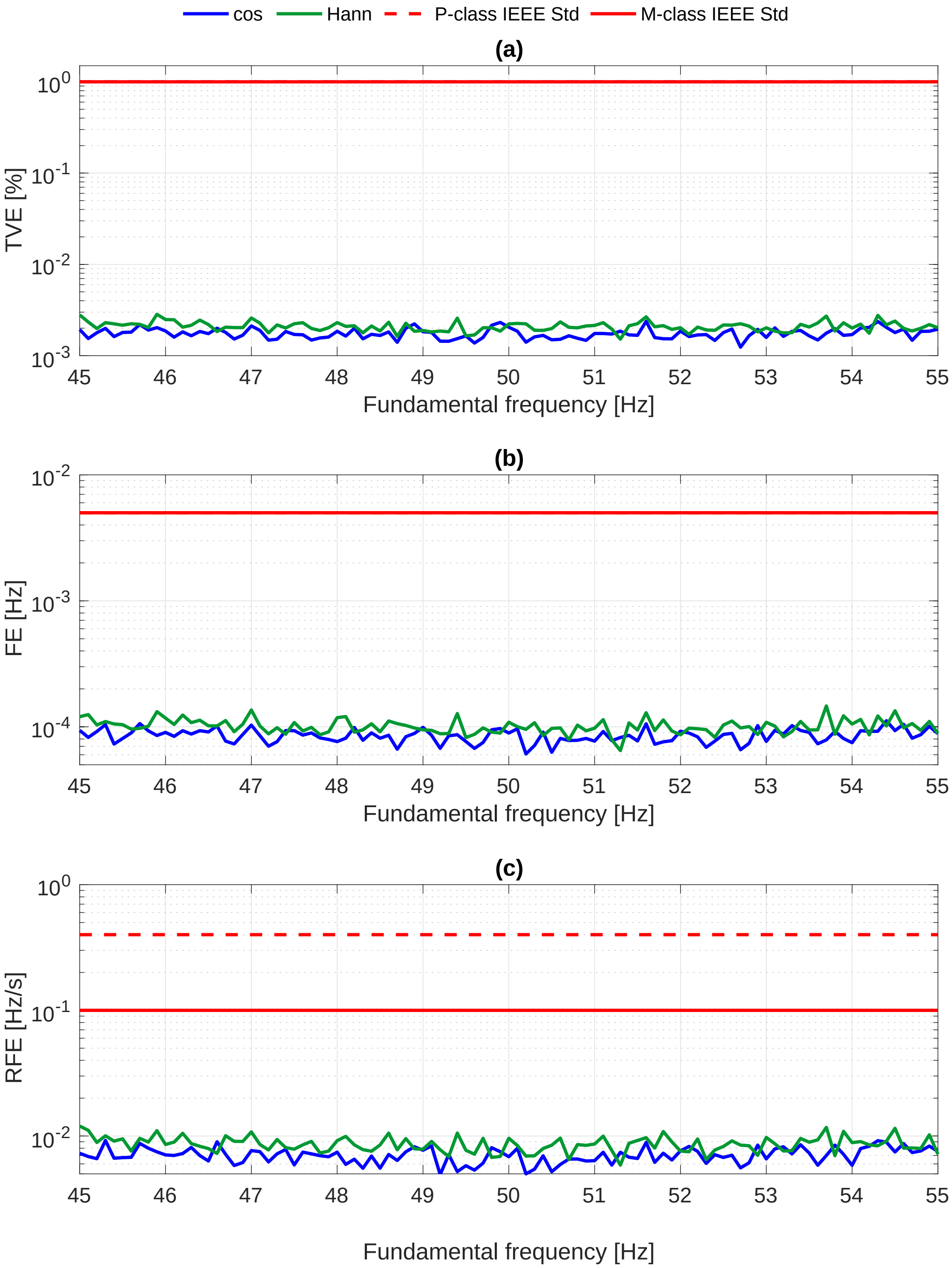

Figure 3.7 – Signal frequency test: worst-case TVE (a), FE (b) and RFE (c) as a function of the signal fundamental frequency, with cosine (blue) and Hanning (green) window functions. The dashed and solid red lines represent the IEEE Std. C37.118 performance requirements for P- and M-class, respectively.

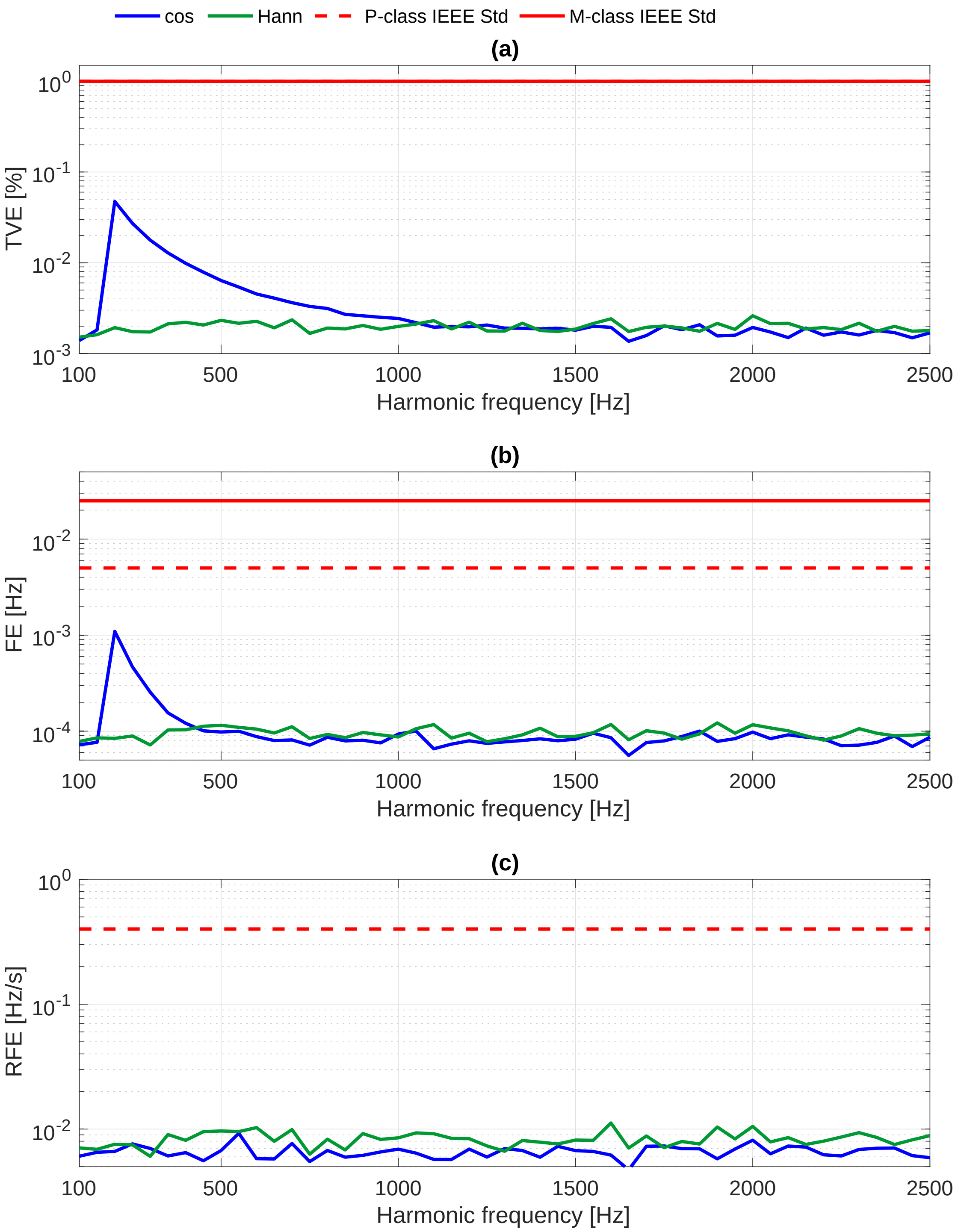

Figure 3.8 – Harmonic distortion test: worst-case TVE (a), FE (b) and RFE (c) as a function of the harmonic component frequency, with cosine (blue) and Hanning (green) window functions. The dashed and solid red lines represent the IEEE Std. C37.118 performance requirements for P- and M-class, respectively.

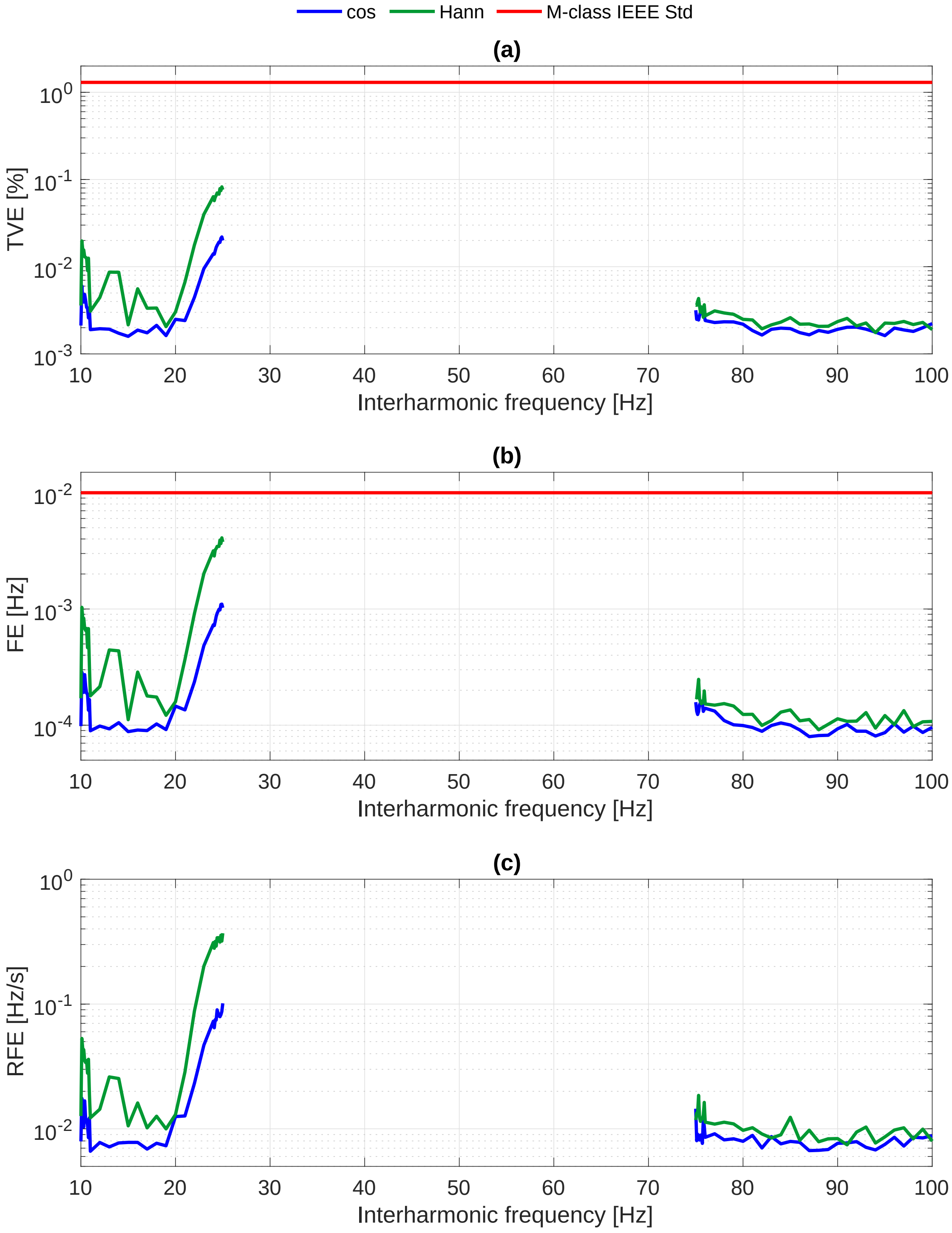

Figure 3.9 – OOBI test: worst-case TVE (a), FE (b) and RFE (c) as a function of the interharmonic component frequency, with cosine (blue) and Hanning (green) window functions. The solid red line represents the IEEE Std. C37.118 performance requirement for M-class.

Table 3.2 – Compliance with respect to static signals: maximum TVE, FE and RFE for the i-IpDFT and maximum limit allowed by [19].

		TVE [%]						**FE [mHz]**						**RFE [Hz/s]**					
		IEEE Std		i-IpDFT				IEEE Std		i-IpDFT				IEEE Std		i-IpDFT			
		P	M	cos		Hann		P	M	cos		Hann		P	M	cos		Hann	
				SNR [dB]		SNR [dB]				SNR [dB]		SNR [dB]				SNR [dB]		SNR [dB]	
				60	80	60	80			60	80	60	80			60	80	60	80
Sign Freq		1	1	0.024	0.002	0.03	0.003	5	5	1.3	0.1	1.5	0.1	0.4	0.1	0.095	0.009	0.126	0.012
Harm Dist 1%		1	1	0.108	0.094	0.028	0.003	5	25	5.4	4.7	1.3	0.1	0.4	-	0.086	0.009	0.112	0.011
Harm Dist 10%		1	1	0.055	0.047	0.026	0.003	5	25	2	1.1	1.2	0.1	0.4	-	0.085	0.009	0.124	0.011
OOBI	f_0=47.5 Hz	-	1.3	0.056	0.022	0.108	0.082	-	10	2.7	1.1	5.6	4.1	-	-	0.217	0.101	0.513	0.369
	f_0=50 Hz	-	1.3	0.026	0.003	0.033	0.004	-	10	1.3	0.1	1.7	0.2	-	-	0.104	0.009	0.153	0.013
	f_0=52.5 Hz	-	1.3	0.043	0.004	0.044	0.011	-	10	2.1	0.2	2.2	0.6	-	-	0.143	0.022	0.150	0.032

In this way, the effect of phase displacement between the harmonic and the fundamental component is also evaluated. According to the IEEE Std. C37.118, the TVE is limited to 1% for both classes, the FE is limited to 5 and 25 mHz for P- and M-class, respectively, whereas the RFE limit is defined for P-class only and is equal to 0.4 Hz/s.

As it can be seen in Fig. 3.8, in case the Hanning window is adopted, the errors are invariant with respect to the harmonic order, due to the fact that both the fundamental and the harmonic tone are coherently sampled. On the contrary, for the cosine window the two tones are not coherently sampled, therefore the effects of spectral leakage are significant, worsening the i-IpDFT results especially for lower harmonic orders. Indeed, as reported in Table 3.2, in case $A_h = 1\% A_0$ the FE exceeds the 5 mHz limit dictated by [19] when SNR = 60 dB, and is below such limit for higher SNR. It is worth mentioning that, in case $A_h = 10\% A_0$, for the second and third harmonic the weighted energy E_n exceeds the threshold λ, activating the strategy that compensates the detected harmonic tone, leading to smaller errors even for the cosine window. For higher harmonic order, the errors are rather invariant.

The OOBI test relies on the following signal model:

$$x(t) = A_0 \cdot \cos(2\pi f_0 t + \varphi_0) + A_i \cdot \cos(2\pi f_i t + \varphi_i) \tag{3.31}$$

where the interfering component has an amplitude A_i corresponding to a Total Inter-Harmonic Distortion (TIHD) of 10%, and its frequency f_i varies within [10, 25] and [75, 100] Hz. As indicated in the IEEE Guide C37.242 [86], the interharmonic frequency should increase logarithmically, in order to provide more tests nearby the PMU pass-band. Therefore, this analysis considers an incremental step of 0.1 Hz for f_i next to 10, 25 and 75 Hz, and a step of 1 Hz for f_i within [11, 24] and [76, 100] Hz. The fundamental amplitude and initial phase are fixed to 1 pu and 0 rad, respectively, whereas the fundamental frequency varies within [47.5, 50, 52.5] Hz. In this way, it is possible to evaluate how different frequency deviations and phase-shifts between fundamental and interfering components affect the algorithm estimation accuracy. It is interesting to observe that, for this test, the IEEE Std. C37.118 does not introduce requirements for P-class nor for RFE. The compliance to class M, instead, requires TVE and FE not to exceed 1.3% and 10 mHz, respectively.

Figure 3.9 shows the maximum obtained errors among the 3 considered fundamental frequencies. The TVE and FE are within the limits required by [19] for every combination of interharmonic and fundamental frequencies, for both cosine and Hanning window. Even though [19] does not define any specific limit for the RFE, the obtained results show the capability of estimating the ROCOF with similar performance as in the harmonic distortion test. To be more precise, the most challenging condition is when the two tones have frequencies that are close together and their images are not detectable due to short-term spectral leakage. In case $f_0 = 47.5$ Hz, this occurs for $20 \leq f_i \leq 25$ Hz whereas in case $f_0 = 52.5$ Hz, this occurs for 75 $\leq f_i \leq 80$ Hz.

3.4.2 Dynamic Operating Conditions

After assessing the steady-state compliance, the dynamic tests enable us to investigate the estimation accuracy in the presence of time-varying test conditions. The results of the i-IpDFT are presented in Figures 3.12-3.15 and Table 3.3.

The measurement bandwidth tests are performed by applying sinusoidal amplitude and phase modulated signals to the fundamental tone. The amplitude modulation test relies on the following signal model:

$$x(t) = A_0 \cdot (1 + k_m \cdot \cos(2\pi f_m t)) \cdot \cos(2\pi f_0 t + \varphi_0) \tag{3.32}$$

where the fundamental amplitude and frequency are fixed to their nominal values, the initial phase is set to zero, whereas k_m and f_m account for modulation depth and frequency, respectively. In particular, k_m is set equal to 0.1, and f_m is varied within [0.1, 2] Hz for P-class and [0.1, 5] Hz for M-class, with an incremental step of 0.2 Hz. Similar considerations can be made for the phase modulation test, whose signal model is defined as follows:

$$x(t) = A_0 \cdot \cos(2\pi f_0 t + \varphi_0 + k_m \cdot \cos(2\pi f_m t - \pi)) \tag{3.33}$$

where the modulation depth k_m is equal to $\pi/18$ rad, whereas the modulation frequency f_m varies between 0.1 and 2 or 5 Hz for P- and M-class, respectively. Again, the fundamental amplitude and frequency are fixed to their nominal values and the initial phase is set to zero. In the measurement bandwidth scenario, the IEEE Std. C37.118 requires TVE not to exceed 3% for both performance classes, FE not to exceed 60 and 300 mHz for P- and M-class, respectively, and RFE not to exceed 2.3 and 14 Hz/s for P- and M-class, respectively.

As it can be seen in Fig. 3.10 for amplitude and Fig. 3.11 for phase modulation results, the errors are always well within the limits required by [19]. Nevertheless, the errors increase with the modulating frequency. This effect can be explained by considering the Fourier series decomposition of the signal model. In the frequency domain, the fundamental component is represented by a single tone centered at f (and its imaginary counterpart). In this context, an amplitude modulation produces two additional tones centered at $f - f_A$ and $f + f_A$, respectively and the same holds for phase modulation where the two tones are centred at $f - f_\varphi$ and $f + f_\varphi$. Accordingly, the modulation test can also be seen as the response to a couple of interfering terms within the synchrophasor pass-band. In this regard, as long as the modulation frequency and depth are limited, the interference contribution is negligible. Conversely, larger values of frequency and depth may produce a significant distortion of fundamental tone, which is reflected by a degradation of solution accuracy.

For the frequency ramp test, the following signal model is adopted:

$$x(t) = A_0 \cdot \cos(2\pi f_0 t + \varphi_0 + k_r \cdot \pi t^2) \tag{3.34}$$

where the quadratic phase term corresponds to a linear contribution in frequency.

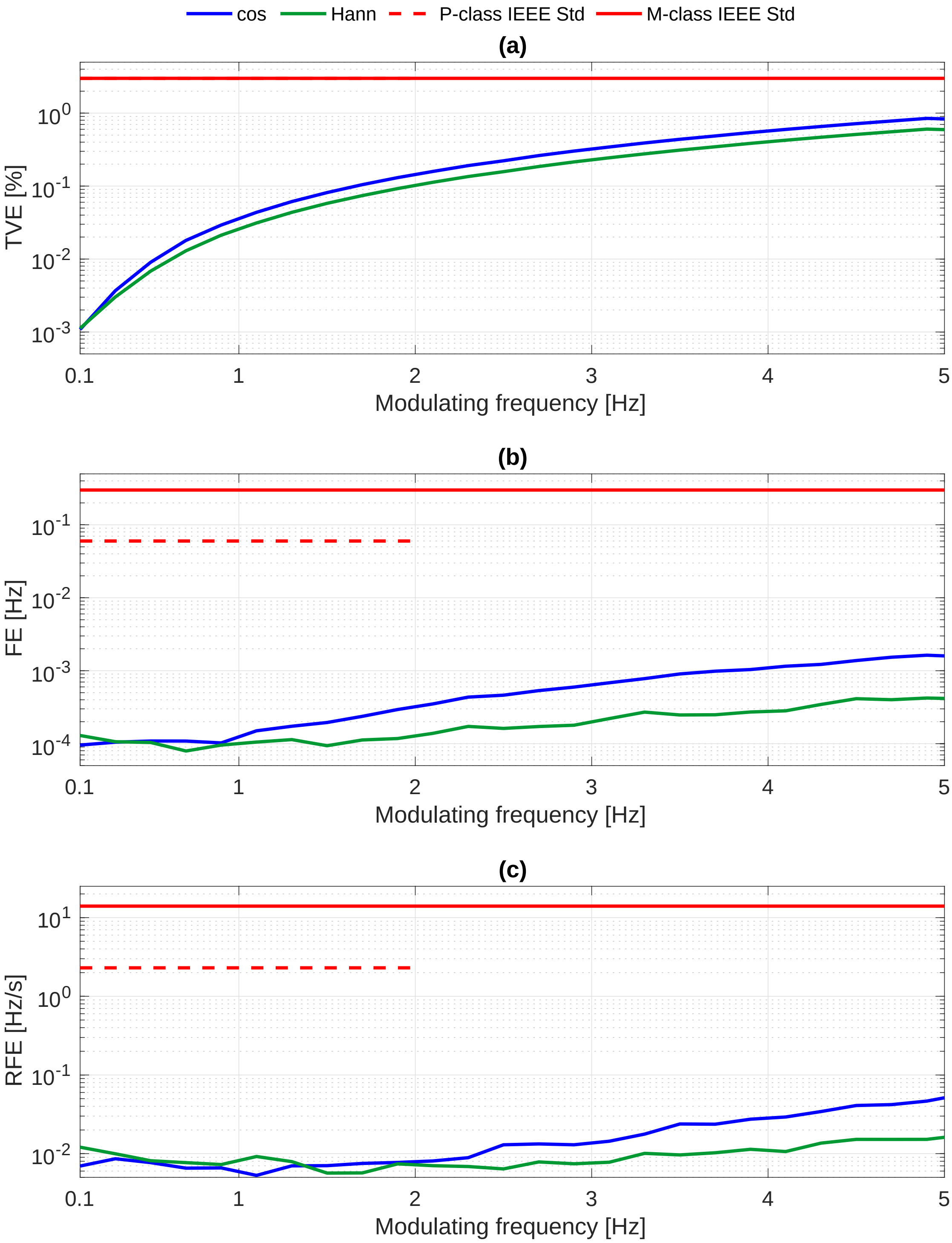

Figure 3.10 – Amplitude modulation test: worst-case TVE (a), FE (b) and RFE (c) as a function of the modulation frequency, with cosine (blue) and Hanning (green) window functions. The dashed and solid red lines represent the IEEE Std. C37.118 performance requirements for P- and M-class, respectively.

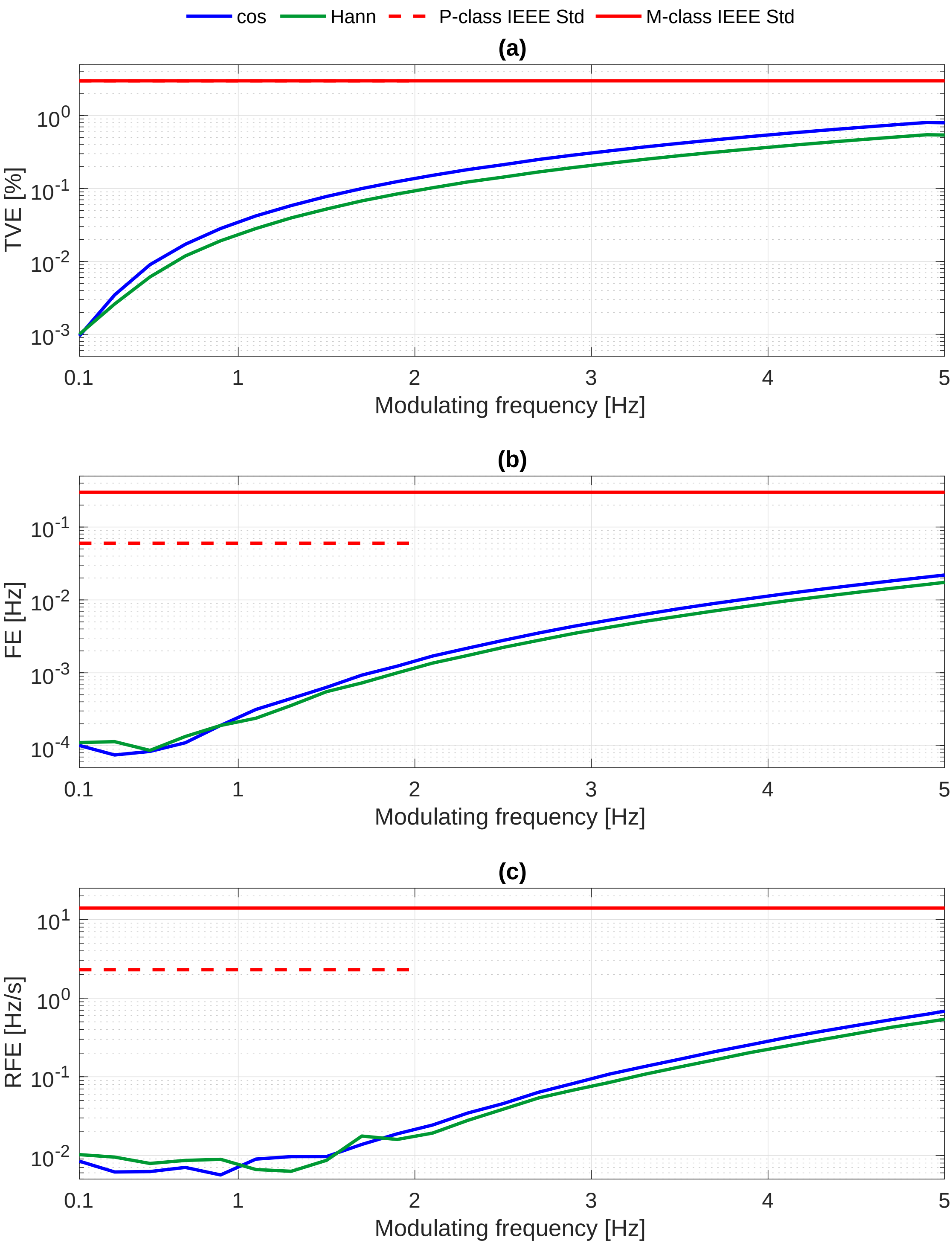

Figure 3.11 – Phase modulation test: worst-case TVE (a), FE (b) and RFE (c) as a function of the modulation frequency, with cosine (blue) and Hanning (green) window functions. The dashed and solid red lines represent the IEEE Std. C37.118 performance requirements for P- and M-class, respectively.

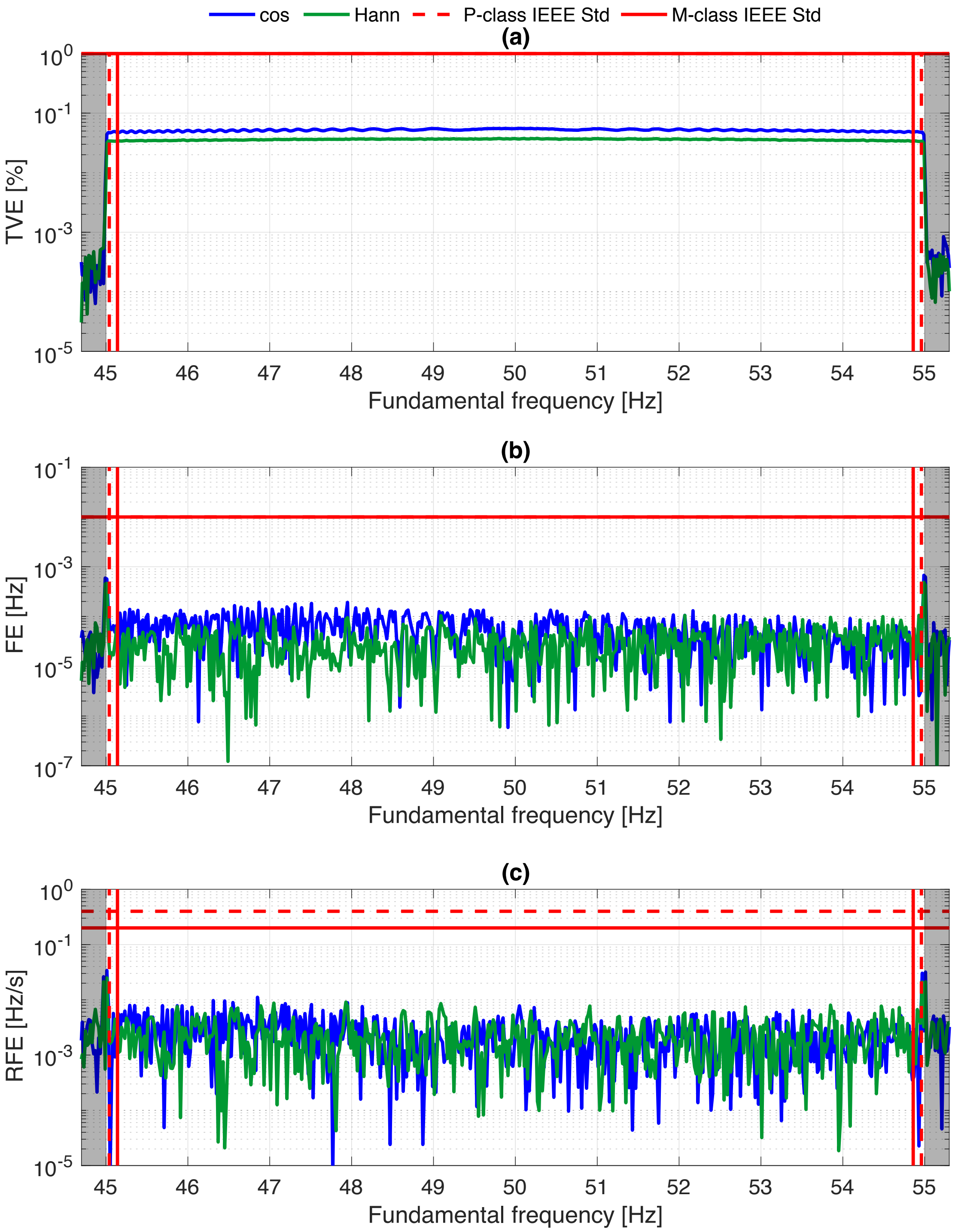

Figure 3.12 – Frequency ramp test (positive): worst-case TVE (a), FE (b) and RFE (c) as a function of the modulation frequency in the range [45, 55] Hz, with cosine (blue) and Hanning (green) window functions. The gray areas correspond to the initial and final steady-state conditions. The horizontal dashed and solid red lines represent the IEEE Std. C37.118 performance requirements for P- and M-class, respectively. The vertical red lines delineate the exclusion intervals: $2/F_s = 0.04$ s for P-class (dashed lines) and $7/F_s = 0.14$ s for M-class (solid lines). Similar results hold for negative frequency ramp.

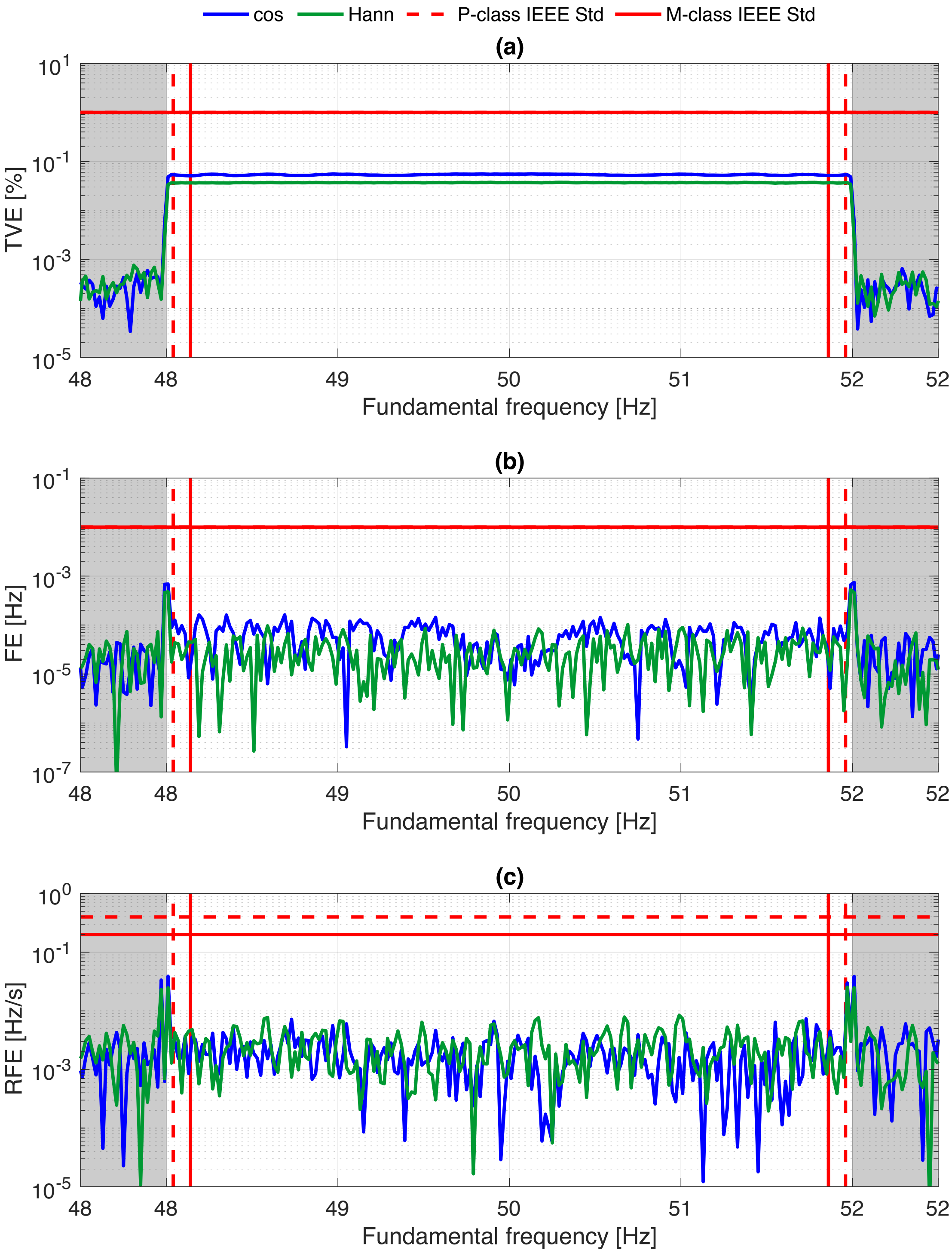

Figure 3.13 – Frequency ramp test (positive): worst-case TVE (a), FE (b) and RFE (c) as a function of the modulation frequency in the range [48, 52] Hz, with cosine (blue) and Hanning (green) window functions. The gray areas correspond to the initial and final steady-state conditions. The horizontal dashed and solid red lines represent the IEEE Std. C37.118 performance requirements for P- and M-class, respectively. The vertical red lines delineate the exclusion intervals: $2/F_s = 0.04$ s for P-class (dashed lines) and $7/F_s = 0.14$ s for M-class (solid lines). Similar results hold for negative frequency ramp.

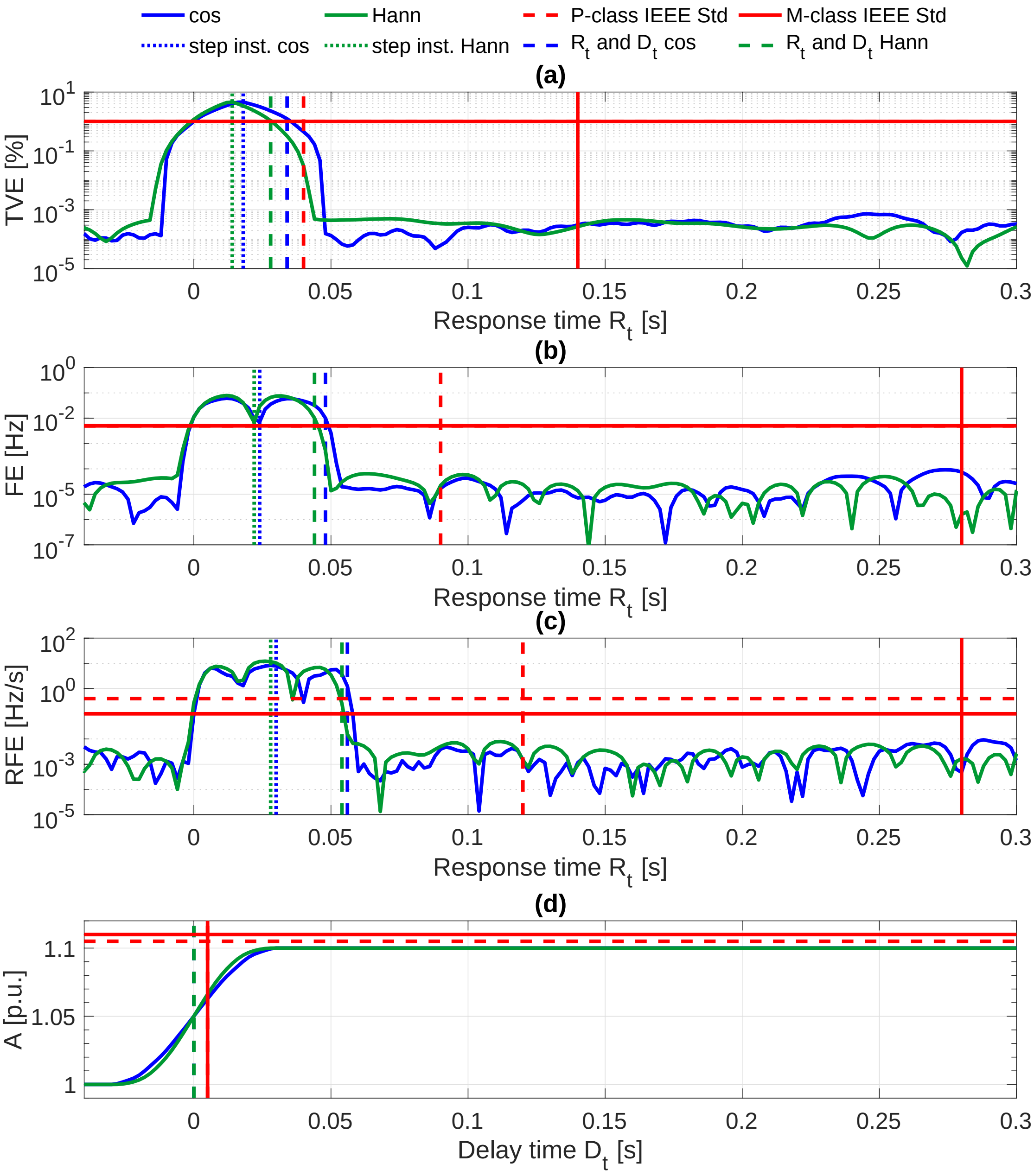

Figure 3.14 – Amplitude step test (positive): TVE (a), FE (b) and RFE (c) as a function of the response time R_t and estimated amplitude as a function of the delay time D_t (d), with cosine (blue) and Hanning (green) window functions. In (a), (b) and (c) time $t = 0$ corresponds to the instant when the measurement leaves the accuracy limit, to which the curves for the two windows are aligned. The vertical dotted lines indicate the instant when the step change is applied; the vertical dashed lines indicate the estimation response time R_t; the vertical dashed and solid red lines indicate the response time limits for P- and M-class, respectively. In (d) time $t = 0$ corresponds to the instant when the step change is applied. The vertical dashed lines indicate the estimation delay time D_t; the vertical red line indicates the delay time limit for both classes. The dashed and solid red lines represent the IEEE Std. C37.118 performance requirements for P- and M-class, respectively. Similar results hold for negative step test.

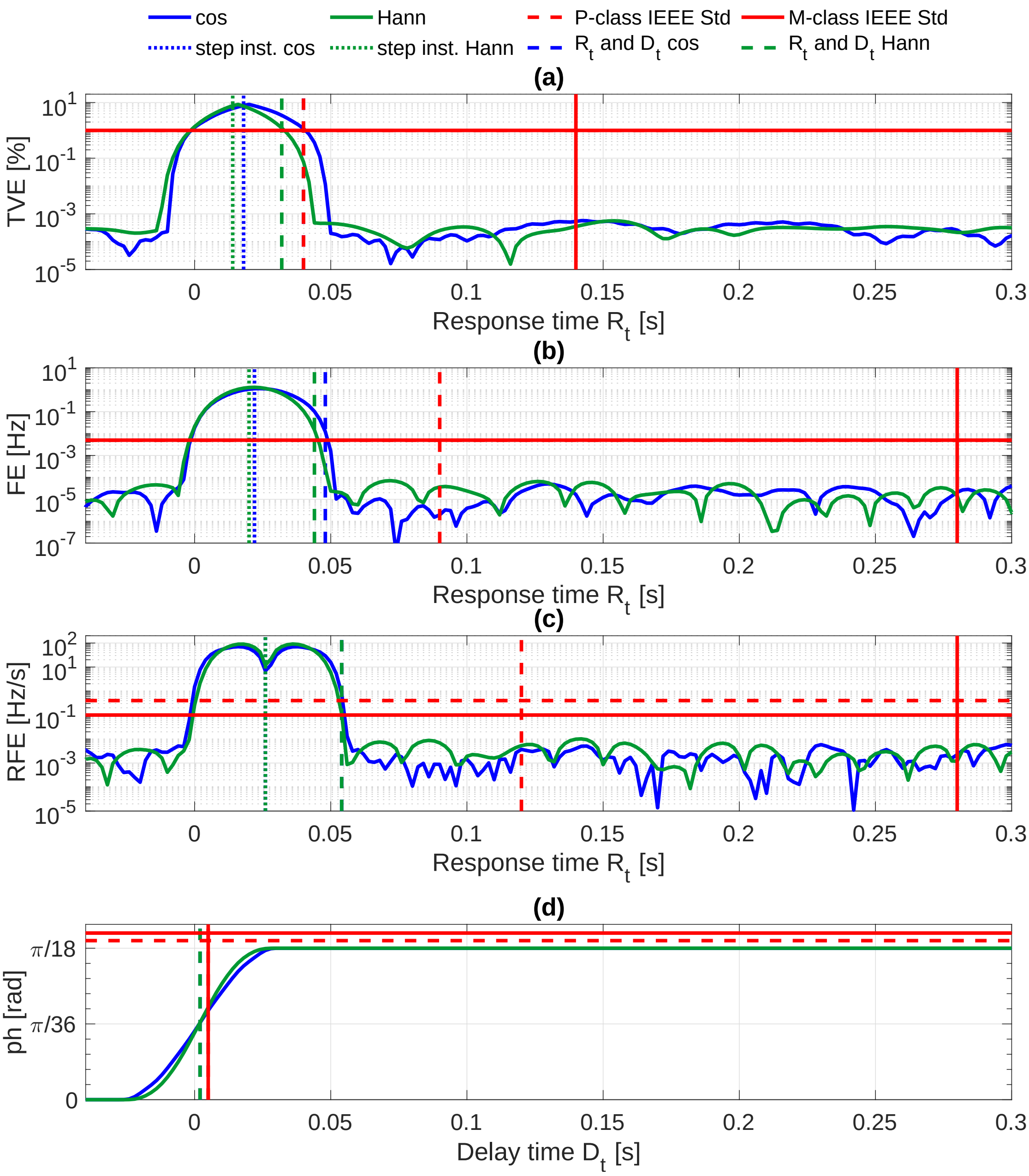

Figure 3.15 – Phase step test (positive): TVE (a), FE (b) and RFE (c) as a function of the response time R_t and estimated phase as a function of the delay time D_t (d), with cosine (blue) and Hanning (green) window functions. In (a), (b) and (c) time $t = 0$ corresponds to the instant when the measurement leaves the accuracy limit, to which the curves for the two windows are aligned. The vertical dotted lines indicate the instant when the step change is applied; the vertical dashed lines indicate the estimation response time R_t; the vertical dashed and solid red lines indicate the response time limits for P- and M-class, respectively. In (d) time $t = 0$ corresponds to the instant when the step change is applied. The vertical dashed lines indicate the estimation delay time D_t; the vertical red line indicates the delay time limit for both classes. The dashed and solid red lines represent the IEEE Std. C37.118 performance requirements for P- and M-class, respectively. Similar results hold for negative step test.

In this context, k_r accounts for the rate of change of frequency, measured in Hz/s. The fundamental frequency is varied within the range [48, 52] Hz for P-class and [45, 55] Hz for M-class, with a rate of change of ±1 Hz/s. In terms of accuracy, the IEEE Std. C37.118 limits the TVE and FE to 1% and 10 mHz, respectively for both performance classes, and the RFE to 0.4 and 0.2 H/s for P- and M-class, respectively.

As shown in Fig. 3.12 for the [45, 55] Hz range and 3.13 for the [48, 52] Hz range, the i-IpDFT errors fully satisfy the requirements. The errors are also comparable with those obtained during the signal frequency test even within the exclusion intervals. It is worth pointing out that the figures show the positive frequency ramps, but similar results hold for the negative ramps.

As final test, the algorithm performance is characterized during an instantaneous step change of signal amplitude or phase. In this way, it is possible to evaluate the algorithm responsiveness to a transient event. The signal model of the amplitude step test is defined as:

$$x(t) = A_0 \cdot (1 + k_t \cdot \chi(t - T_t)) \cdot \cos(2\pi f_0 t + \varphi_0) \tag{3.35}$$

where k_t and T_t account for the step size and occurrence time, respectively, whereas $\chi(\cdot)$ models a piece-wise step function:

$$\chi(t) = \begin{cases} 0 & \text{if } t < 0 \\ 1 & \text{if } t \geq 0 \end{cases} \tag{3.36}$$

For this analysis, k_t and T_t are set to 0.1 and 1.5 s, respectively.

Similarly, the phase step signal model is:

$$x(t) = A_0 \cdot \cos(2\pi f_0 t + \varphi_0 + k_t \cdot \chi(t - T_t)) \tag{3.37}$$

where the step size k_t corresponds to $\pi/18$ rad, and the step occurrence time T_t is set equal to 1.5 s. In this case, the IEEE Std. C37.118 requirements regard the algorithm response time, defined as the time to transit between two steady-state measurements, before and after the step change. Specifically, the response time is determined as the difference between the time instants when the measurement accuracy exceeds and reenters within a given limit (i.e., TVE ≤ 1%, FE ≤ 5 mHz, RFE ≤ 0.4 Hz/s for P-class and RFE ≤ 0.1 Hz/s for M-class). This requirement is particularly stringent for P-class: the response time should not exceed 40, 90 and 120 ms for TVE, FE and RFE, respectively. For M-class the limit is more relaxed: 140 ms for TVE and 280 ms FE and RFE. The IEEE Std. C37.118 defines two additional performance indexes to characterize the algorithm during step conditions. The delay time is defined as the amount of time the stepped parameter takes to achieve a value that is halfway between the starting and ending steady-state values, and is limited to 5 ms. The maximum overshoot is defined as a maximum percentage of the step magnitude that the signal can reach before it settles to the final steady-state value, and is limited to 5 and 10% for P- and M-class, respectively. In order

Table 3.3 – Compliance with respect to dynamic signals: maximum TVE, FE and RFE for the i-IpDFT and maximum limit allowed by [19].

	TVE [%]						**FE [mHz]**						**RFE [Hz/s]**					
	IEEE Std		i-IpDFT				IEEE Std		i-IpDFT				IEEE Std		i-IpDFT			
	P	M	cos		Hann		P	M	cos		Hann		P	M	cos		Hann	
			SNR [dB]		SNR [dB]				SNR [dB]		SNR [dB]				SNR [dB]		SNR [dB]	
			60	80	60	80			60	80	60	80			60	80	60	80
Ampl Mod	3	3	0.846	0.847	0.604	0.604	60	300	2.2	1.6	1.6	0.4	2.3	14	0.106	0.051	0.123	0.016
Ph Mod	3	3	0.805	0.806	0.547	0.547	60	300	21.9	22	17.9	17.4	2.3	14	0.725	0.683	0.568	0.540
Freq Ramp	1	1	0.058	0.055	0.044	0.038	10	10	1	0.2	0.9	0.2	0.4	0.2	0.088	0.011	0.083	0.011
	TVE Response time [s]						**FE Response time [s]**						**RFE Response time [s]**					
	IEEE Std		i-IpDFT				IEEE Std		i-IpDFT				IEEE Std		i-IpDFT			
	P	M	cos		Hann		P	M	cos		Hann		P	M	cos		Hann	
			SNR [dB]		SNR [dB]				SNR [dB]		SNR [dB]				SNR [dB]		SNR [dB]	
			60	80	60	80			60	80	60	80			60	80	60	80
Ampl Step	0.04	0.14	0.034	0.034	0.028	0.028	0.09	0.28	0.048	0.048	0.044	0.044	0.12	0.28	0.056	0.056	0.054	0.054
Ph Step	0.04	0.14	0.040	0.040	0.032	0.032	0.09	0.28	0.048	0.048	0.044	0.044	0.12	0.28	0.054	0.054	0.054	0.054
	Delay time [s]						**Max Overshoot [%]**											
	IEEE Std		i-IpDFT				IEEE Std		i-IpDFT									
	P	M	cos		Hann		P	M	cos		Hann							
			SNR [dB]		SNR [dB]				SNR [dB]		SNR [dB]							
			60	80	60	80			60	80	60	80						
Ampl Step	0.005	0.005	0.002	0.002	0.002	0.002	5	10	0	0	0	0						
Ph Step	0.005	0.005	0.002	0.002	0.002	0.002	5	10	0	0	0	0						

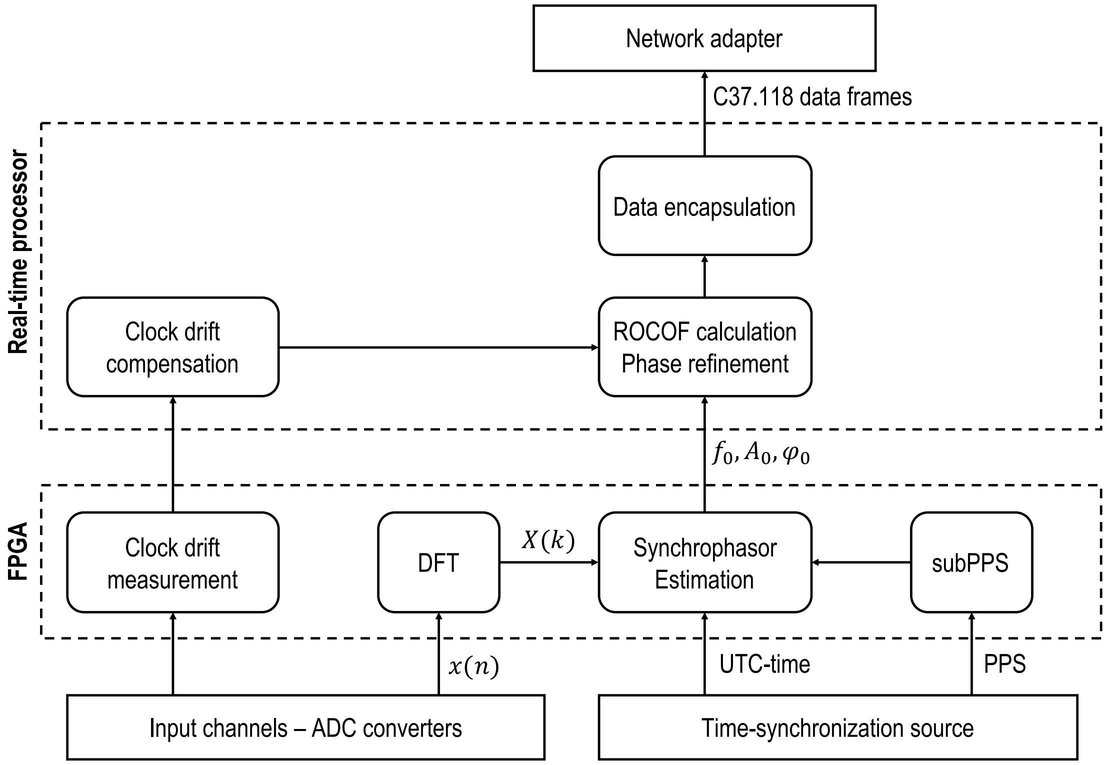

Figure 3.16 – High level design of the proposed PMU architecture.

to perform this analysis, it is necessary to compute the interleaved time-domain trend of TVE, FE and RFE. To this end, in this analysis the reporting rate is set equal to the sampling rate, producing a new estimate for each acquired sample.

Regarding the amplitude and phase steps (see Fig. 3.14 and 3.15 for the positive step cases), the errors are represented as a function of the measured response time. Moreover, the estimated amplitude (A) and phase (ph) are represented as a function of the delay time. The results show that, during positive steps, the errors return below the limits within the allowed response times without any violation of the overshoot limit (similar results hold for the negative step cases).

3.5 Embedded Hardware Implementation

The i-IpDFT has been fully integrated into an hardware platform that embeds all the key features of a PMU, i.e., (i) synchrophasor estimation, (ii) time synchronization, (iii) data acquisition, and (iv) data streaming. This Section describes all implementation details, except for the time synchronization part that is thoroughly described in Chapter 6, Section 6.1. The i-IpDFT adopts an observation interval of 60 ms and is based on the Hanning window function.

The hardware of the developed PMU is based on the National Instruments compactRIO (cRIO) system, an embedded industrial controller with a real-time processor, a user-programmable Field Programmable Gate Array (FPGA) and reconfigurable IO modules [87]. A high level overview of the proposed design is shown in Fig. 3.16. As it can be seen, the three most significant processes, i.e., (i) signal acquisition, (ii) PMU time synchronization and (iii) synchrophasor estimation, run at the FPGA level. This choice guarantees that all operations are governed by the FPGA on-board clock that provides hardware-timed speed and reliability, which are essential features for PMUs. Also, thanks to their intrinsic parallelism, FPGAs are particularly efficient when solving recursive problems.

Overall, the workload is higher than the one of the e-IpDFT procedure presented in [56] because of the computational complexity of the proposed iterative routine to compensate interfering tones. Nevertheless, the possibility to share FPGA resources when implementing iterative algorithms, such as the i-IpDFT, enables a considerable reduction the overall FPGA occupation and the possibility to fit the proposed i-IpDFT in an embedded device. The problem that has to be carefully addressed is the time needed to complete the synchrophasor estimation. In this context, the PMU measurement reporting latency is defined as the time delay between the instant a specific event occurs in the power system and the instant the same event is reported by the PMU. According to the IEEE Std. C37.118 [19], this value is a function of the PMU performance class and reporting rate F_r. In particular, for P-class PMUs the allowed latency is of 2 reporting periods, whereas for M-class ones this value is relaxed to 5 periods. Having fixed F_r to 50 fps, these values correspond to 40 and 100 ms respectively. As in the previous Section 3.4, in order to demonstrate that the proposed design is P+M compliant, the most stringent requirement of 40 ms is taken as reference. In the proposed design, an observation interval T of 60 ms is adopted and the time-stamp of the synchrophasors is referred to the center of the applied window. Therefore, the windowing of the signal already accounts for 30 ms, leaving only 10 ms of time budget to the processing unit. In the proposed architecture, the PMU is expected to monitor 3 voltages and 3 currents, for a total of 6 measured synchrophasors, leading to a time budget of roughly 1.6 ms for each channel in case of estimating them in series.

The target platform is the cRIO-9039 controller, integrating (i) a 1.91 GHz quad-core Intel Atom E3845 processor characterized by 16 GB solid state drive nonvolatile data storage and 2 GB DDR3L memory, and (ii) a reconfigurable Xilinx Kintex-7 325T FPGA with an on-board clock frequency of 40 MHz, 407600 flip-flops, 203800 look-up tables (LUTs), 16020 kbits of block RAM and 840 DSP slices [88].

The synchronization to the UTC reference can be achieved using three different time dissemination technologies, i.e., the Global Positioning System (GPS), the Precision Time Protocol (PTP) and the White Rabbit. Thorough details in terms of operating principle and hardware implementation are provided in Section 6.1.

The sampling of the voltage and current waveforms is realized by means of two parallel 24-bits delta–sigma converters, module NI 9225 and 9227 respectively, characterized by a sampling rate F_s of 50 kHz and an input range of 300 V_{RMS} for the voltage and 5 A_{RMS} for the current [89, 90]. They are equipped with built-in anti-aliasing filters with a pass-band of 0.453 F_s and a stop-band starting at 0.547 F_s. In particular, the design accounts for 3 voltage and 3 current channels, enabling the sensing of a 3-phase system. The sampling process of the waveforms is free-running and the UTC-time synchronization is achieved *a posteriori*. At the moment of actual deployment into the electrical grid, the A/D converters should be interfaced with the high voltage signals through dedicated instrument transformers.

The i-IpDFT has been fully implemented at the FPGA level, to take advantage of the intrinsic parallelism, the calculation speed and the overall determinism offered by this fabric. A parallel process measures the eventual drift of the ADC sampling clock. This value, together with the estimated synchrophasors is transferred to the real-time processor through dedicated Direct Memory Access (DMA) channels. This is a common practice to timely share information among the two parts of the cRIO. At the real-time processor level the synchrophasor phase and frequency are corrected for the ADC clock drift and the ROCOF is computed as the finite difference between two consecutive frequency estimates as described in (3.27). The data are then encapsulated according to the protocol specified in the IEEE Std. C37.118.2 and streamed out through one of the two available Ethernet adapters to the phasor data concentrator.

The whole software, including real-time processor and FPGA, is programmed with NI LabVIEW programming language.

3.5.1 FPGA Design and Resources Allocation

This Section describes the implementation of Algorithm 4 into the target FPGA. Table 3.4 presents the FPGA compilation results for each step of the estimation process, considering a single input channel. The results are presented in terms of used number of flip-flops, LUTs, blocks of RAM (one block of RAM can store up to 32 kbits of data) and DSP blocks (one DSP block contains a 18 × 25 multiplier). Also, the execution time of each function is reported. The results are obtained using a standard Xilinx Vivaldo compiler.

The Free-Running Sampling Process

As shown in Fig. 3.16, at the FPGA level, a sub PPS square waveform (hereafter called subPPS) is derived from the UTC-PPS signal and is locked to it. The subPPS is characterized by a frequency corresponding to the PMU reporting rate F_r that, in the proposed design, is 50 fps. The signal acquisition, the synchrophasor estimation, and the synchrophasor time-stamping are triggered by the rising edge of such subPPS. However, there is no guarantee that the sampling process is locked to such subPPS signal: there must be an *a posteriori* time refinement.

Specifically, two delays have to be compensated. The first one results from the fact that the sampling frequency might drift from its nominal value, due to oscillator degradation or environment conditions variation (such as temperature). This frequency drift is measured over observation windows of M samples, with $M >> N$ (such as few seconds windows). If the sampling process was uniform, such window would account for an ideal amount of time MT_s. In real operating conditions, the actual difference between the time instant when the last sample is acquired t_{M-1} and the time instant when the first sample is acquired t_0, might differ from the ideal delay. The clock drift is defined as the normalized difference between these two delays:

$$f_D = \frac{(t_{M-1} - t_0) - MT_s}{MT_s} \tag{3.38}$$

Every time the clock drift is updated, the DFT frequency resolution $\Delta f = 1/T$ can be adequately compensated as:

$$\Delta f_c = \Delta f (1 - f_D) \tag{3.39}$$

and therefore the frequency estimation improved $\hat{f}_{0,c}$.

The second delay is due to the possible offset between the two clocks. Indeed, in ideal operating conditions, i.e., if the sampling process was locked to the subPPS, the time delay between the rising edge of the subPPS t_{subPPS} and the time instant when the first sample of the related window is acquired t_0 would be exactly zero. In real operating conditions, there could be a delay that would result in bad initial phase estimations. This time delay is measured at every subPPS and compensated by updating the estimated phase as follows:

$$\hat{\varphi}_{0,c} = \hat{\varphi}_0 + 2\pi \hat{f}_c (t_0 - t_{subPPS}) \tag{3.40}$$

FPGA Design of the Iterative-Interpolated DFT

The FPGA receives a continuous stream of samples $x(n)$ from the ADC input channels. Then, the same four-stages pipeline architecture proposed in [56] is adopted. As shown in Fig. 3.17, based on the subPPS rising edge the samples from each input channel are filled into a dedicated memory until the number of samples N contained in the observation window is collected (signal buffering). Once the memory is completely filled in, a flag activates the next processing stage, i.e., the synchrophasor estimation (SE).

Having set the window length to 60 ms, 8 DFT bins have to be calculated in order to account for the frequency contributions in the range [10, 100] Hz. In this configuration, the first bin refers to the DC component, the second last bin refers to the second harmonic, and the last bin is needed for the three-points interpolation around 100 Hz. Although a recursive approach like the Modulated Sliding DFT (MSDFT) could reduce the time for computing the DFT, the developed code uses the canonical DFT, in view of its straightforward implementation. Indeed, as the amount of bins to be calculated is little (only 8), the computational burden is limited. In particular, the Hanning windowing weights are pre-computed for each bin in terms of real

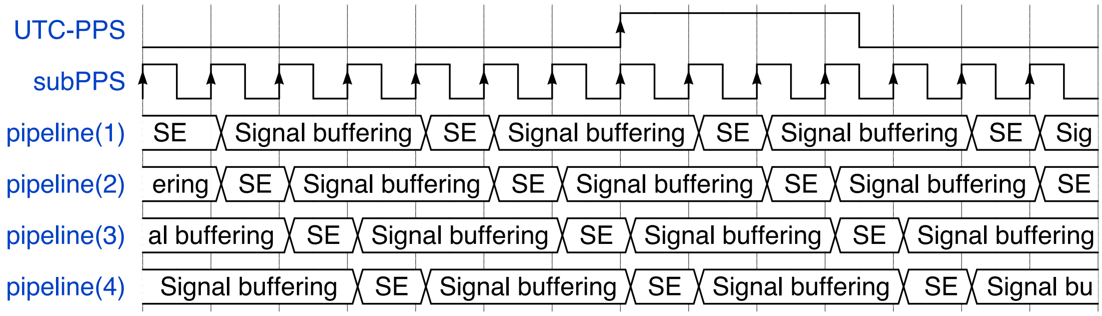

Figure 3.17 – Digital timing diagram of the proposed PMU architecture. SE stands for Synchrophasor estimation. Adapted from [56].

Table 3.4 – FPGA compilation results. The latency refers to the computation of 1 channel.

Function	Configuration	line Alg. 4	Flip-Flops	LUTs	RAM	DSP	Latency
DFT	1 bin		433	166	0	0	0.3 ms
	8 bin	1	503	251	0	0	0.3 ms
IpDFT	3-point		1’576	2’179	0	15	1.8 μs
e-IpDFT	P = 1	6	8’493	14’329	0	142	6.4 μs
	P = 2	2, 8					10.9 μs
λ		4	487	245	0	0	7.9 μs
Spectrum		3, 7, 9	2’974	2’838	0	80	2.6 μs
i-IpDFT	Q = 28	2 - 13	36’159	64’749	0	551	0.75 ms
	Q = 0						42.2 μs

and imaginary components according to:

$$\mathrm{Re}\{H(k,n)\} = w(n)\cdot\cos(2\pi kn/N), \qquad \mathrm{Im}\{H(k,n)\} = w(n)\cdot\sin(2\pi kn/N), \tag{3.41}$$

and stored in dedicated memories inside the FPGA, resulting into 16 memories (8 for the real and 8 for the imaginary component). This solution, besides sacrificing occupation of RAM blocks inside the FPGA, saves execution time. The DFT computation of the 8 bins results into 16 parallel N consecutive multiply-and-accumulate operations, which are quite fast and optimized at the FPGA level:

$$\mathrm{Re}\{X(k)\} = \frac{1}{B}\sum_{n=0}^{N-1} x(n)\cdot\mathrm{Re}\{H(k,n)\} = \frac{1}{B}\sum_{n=0}^{N-1} x(n)\cdot[w(n)\cdot\cos(2\pi kn/N)] \tag{3.42}$$

$$\mathrm{Im}\{X(k)\} = \frac{1}{B}\sum_{n=0}^{N-1} x(n)\cdot\mathrm{Im}\{H(k,n)\} = \frac{1}{B}\sum_{n=0}^{N-1} x(n)\cdot[w(n)\cdot\sin(2\pi kn/N)] \tag{3.43}$$

As reported in Table 3.4, in view of the possibility to execute each computation in parallel, the latency for computing 1 DFT, roughly 300 μs per bin corresponds to the latency for computing

Table 3.5 – Final FPGA allocation and latency for a 6-channels PMU.

FPGA allocation				**Latency [ms]**		
Flip-Flops	**LUTs**	**RAM**	**DSP**		**1 ch**	**6 ch**
63’165	90’984	51	596	Q = 28	1.20	7.20
15.5%	44.6%	9.4%	71.0%	Q = 0	0.34	2.04

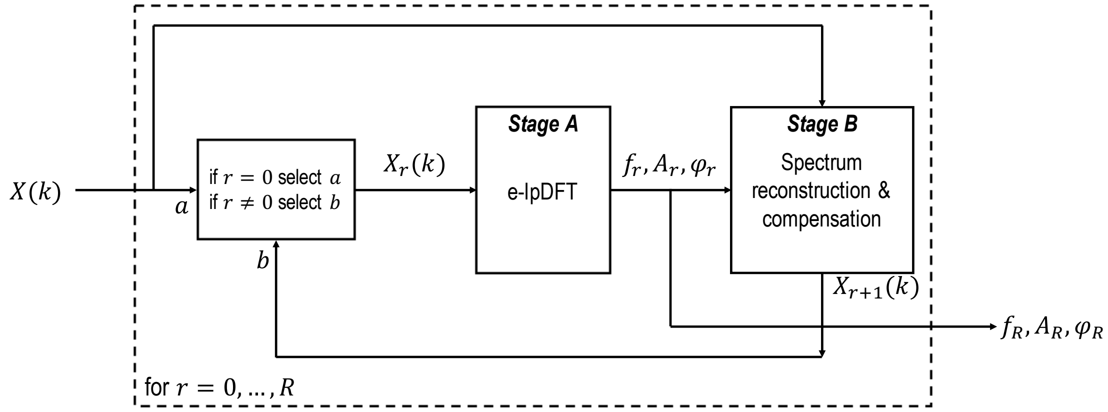

Figure 3.18 – Block diagram of the FPGA implementation.

8 DFT bins. Also, replicating the calculation 8 times, leads to a negligible raise in complexity.

The calculated DFT samples $X(k)$ are then transferred the process that estimates the synchrophasors. By taking a close look at Algorithm 4, it is possible to notice that the code is composed of a recursive two-stage routine that first estimates the signal parameters via e-IpDFT (line 2, 6, 8) and then, based on these estimates, reconstructs the signal DFT spectrum (line 3, 7, 9).

This feature has been exploited in order to efficiently allocate FPGA resources, as shown in Fig. 3.18. In particular, the code is composed of two consecutive stages that are repeated recursively a predefined number of times R. Specifically, Stage A refers to the e-IpDFT that, at each iteration r, processes the input samples $X_r(k)$ and returns the estimated parameters $\{f_r, A_r, \varphi_r\}$. Stage B reconstructs spectrum relative to the estimated parameters and subtracts it from the original DFT bins $X(k)$. The result is a new spectrum $X_{r+1}(k)$ that will be processed at the next iteration. Indeed, at the first iteration $r = 0$, Stage A processes the original DFT bins $X(k)$. At the next iterations it processes the outcome of Stage B.

The iterations relative to an even value for r refer to the fundamental tone. In particular, according to Algorithm 4, Stage A can be identified with lines 2 and 8 and Stage B with lines 3 and 9. When r is odd, instead, the interfering tone is being estimated and Stage A refers to line 6, whereas Stage B refers to line 7.

The procedure is repeated a predefined number of times R. In order to account for $Q = 28$

iterations of the routine to compensate the interfering tone, the loop accounts for $R = 2Q + 1$, corresponding to a total of 57 iterations.

The synchrophasors are finally pushed to the real-time processing units through dedicated DMA channels.

As shown in Table 3.5, such a two-stage structure enables the efficient allocation of the FPGA resources. The overall FPGA occupation reaches 54 % and the final time needed to estimate the synchrophasor of a single input channel is of roughly 1.2 ms. Such a value enables the estimation of the 6 channels in series, one after the other, leading to a total latency 7.2 ms, compliant with the IEEE Std. C37.118 regulations for P-class PMUs. The choice of estimating the synchrophasors in sequence, although enlarging the overall time delay, keeps the same amount of allocated FPGA resources independently of the processed number of channels.

It is worth to point out that such a long latency is needed only when an interfering tone is detected. Indeed, in case the compensating iterative routine is not activated, the time to estimate the synchrophasors is limited to 46 μs per channel. By adding the time to compute the DFT bins, this leads to 346 μs per channel and 2 ms for 6 channels.

3.6 Discussion

The Chapter presented an IpDFT-based synchrophasor estimation algorithm, called i-IpDFT. The limits of the IpDFT technique when estimating the parameters of a signal corrupted by an interharmonic tone were discussed and a technique that is resilient against the spectral leakage generated by any interfering tone was developed. A sensitivity analysis meant to characterize the dependence upon the adopted window function and upon the algorithm's parameters was conducted. The performance with respect to all the operating conditions introduced for P and M-class PMUs in [19] was assessed.

The proposed i-IpDFT algorithm satisfies all the accuracy requirements defined in [19] for P and M-class PMUs simultaneously. In particular, the i-IpDFT fulfils the OOBI test constraints. In such an operating condition, the maximum TVE is 0.1 % (being 1.3 % the maximum limit allowed by [19]) and the maximum FE is 5.6 mHz (being 10 mHz the maximum limit [19]).

Finally, the integration of the proposed algorithm into an embedded device demonstrated the prospective deployability of the proposed architecture into real-scale synchrophasor networks. The measurement reporting latency of the developed PMU is of 7.2 ms when the an interfering tone is detected and 2 ms otherwise.

4 Reduced Leakage Synchrophasor Estimation based on the Hilbert Transform

The key point to improve PMU responsiveness is reducing the observation interval adopted for the synchrophasor estimation. However, the accuracy of DFT-based algorithms may be compromised by short windows due to the spectral leakage effect. To overcome this limitation, the Chapter proposes a joint application of the Hilbert Transform (HT) and of the Interpolated DFT (IpDFT) technique for synchrophasor estimation. Specifically, the HT enables the suppression of the spectral leakage generated by the negative image of the tones under analysis, whereas the IpDFT limits the effects of spectrum granularity. The iterative IpDFT (i-IpDFT) is adopted to deal with the presence of harmonic and interharmonic tones. The proposed estimator adopts a window length of 40 or 60 ms and the 3-points IpDFT technique with the Hanning window function. The estimation accuracy and responsiveness with respect to the IEEE Std. C37.118 are assessed, demonstrating that the algorithm guarantees compliance with all the requirements for both P- and M-class, with the only exception of 1% harmonic distortion and phase step tests.

The Chapter includes results of publication [10].

4.1 Introduction and State of the Art

The previous Chapter 3 has discussed the stringent requirements in terms of PMU accuracy dictated by the IEEE Std. C37.118 [19], that have pushed the development of highly-sophisticated algorithms for synchrophasor estimation. In view of a PMU practical application, though, also latency limits have to be taken into account [91]. In particular, the IEEE Std. C37.118 requires the maximum latency to not exceed two or five times the reporting period for P- and M-class, respectively, i.e., not to exceed some tens of milliseconds. To this end, any possible delay contribution has to be minimized, starting from the computational complexity and delay introduced by the adopted synchrophasor estimation algorithm.

As already discussed in the previous Chapter 3, traditional DFT approaches suffer from several uncertainty contributions, due to the stationarity assumption, the finite-grid resolution and spectral leakage [84]. Enlarging the window length, mitigates these effects. However, the longer the window length, the higher the group delay introduced by the synchrophasor estimation process. Conversely, a shorter window might result in a too scarce frequency resolution and an intractable distortion level. In case of short windows, the main contribution to estimation errors is represented by the interference introduced by the negative image of the tone under analysis. Typically, DFT-based synchrophasor estimation algorithms adopt a minimum window length equal to three cycles of a signal at the rated power system frequency, corresponding to 60 ms at 50 Hz.

In this context, the Hilbert Transform (HT) might represent a promising and effective solution to shorten the observation interval. Given the acquired waveform, in ideal conditions the HT produces a complex-valued signal, also known as analytic signal, whose spectrum consists only of positive frequency components. In practical applications, this largely mitigates the effects of spectral leakage generated by the negative image of the tone under analysis. Having limited the spectral interference, shorter window lengths might be adopted.

Within this context, the Chapter proposes a synchrophasor estimation algorithm that is based on the joint application of the HT and the IpDFT and accounts for both leakage suppression and finite resolution compensation. In more details, the proposed technique consists in two steps. First, the analytic signal associated to the acquired waveform is computed by means of the HT. Then, the iterative IpDFT (i-IpDFT) is applied to estimate the fundamental amplitude, frequency and initial phase. The algorithm, hereafter called HT-IpDFT, enables the accurate estimation of synchrophasors in all operating conditions considered by the IEEE Std. C37.118 [19] for P- and M-class PMUs, while adopting a window length up to only 40 ms at 50 Hz, corresponding to a frequency resolution of 25 Hz.

It is worth noticing that the HT has been previously applied to the analysis of power signals, because of the capability to extract an instantaneous envelope of the signal under analysis [92]. This peculiar property is typically employed, in combination with singular value decomposition [93] or wavelet transform [94], for a nearly real-time monitoring of power quality indices. In [95], the HT is applied to the autocorrelation of the acquired power signal to design a P-class PMU.

The Chapter is organized as follows. Section 4.2 introduces the mathematical formulation of the HT, and discusses its possible implementations. Section 4.3 describes the main stages of the proposed HT-IpDFT algorithm and defines the criteria for setting the parameters. Section 4.4 thoroughly characterizes the estimation accuracy in all the static and dynamic test conditions indicated by the IEEE Std. C37.118. Section 4.5 concludes the Chapter with a discussion and final remarks.

4.2 The Hilbert Transform: advantages and limitations

The HT $\mathscr{H}(\cdot)$ is defined as a convolution operator with the function $1/\pi t$ [96]:

$$\tilde{x}(t) = \mathscr{H}[x(t)] = \frac{1}{\pi}\int_{-\infty}^{+\infty} \frac{x(\tau)}{t-\tau} d\tau \tag{4.1}$$

It should be noticed that the integrand function presents a singularity in $\tau = t$, thus (4.1) does not have a closed-form solution. In this regard, an approximation can be obtained by applying the Cauchy Principal Value method as follows [97]:

$$\mathscr{H}[x(t)] \simeq \frac{1}{\pi} \lim_{\varepsilon \longrightarrow 0^+} \left[\int_{-\infty}^{t-\varepsilon} \frac{x(\tau)}{t-\tau} d\tau + \int_{t+\varepsilon}^{+\infty} \frac{x(\tau)}{t-\tau} d\tau \right] \tag{4.2}$$

In this way, it is possible to define the HT of some basic and frequently employed functions [98], e.g., $\mathscr{H}[\cos(t)] = \sin(t)$.

In addition to the convolution operator formulation, the HT can be also interpreted as a linear phase-shift filter, characterized by a frequency response $H(\cdot)$ defined as follows:

$$H(\omega) = -j \cdot sgn(\omega) \tag{4.3}$$

where ω and j represent the considered angular frequency and the imaginary unit, respectively. Accordingly, the HT filter exhibits a Hermitian symmetric trend with respect to the DC frequency, i.e., it keeps unaltered the spectral component magnitudes, while producing a phase shift equal to $-sgn(\omega) \cdot \pi/2$.

In this context, let us introduce the analytic signal $\hat{x}(t)$:

$$\hat{x}(t) = x(t) + j \cdot \mathscr{H}[x(t)] = x(t) + j \cdot \tilde{x}(t) \tag{4.4}$$

defined as a complex-valued quantity, with the original signal and the HT output as real and imaginary component, respectively. From (4.3) and (4.4), it can be observed that the spectral representation of the analytic signal does not consist of negative frequency components, but only of (doubled) positive frequency components. It is thus reasonable to expect that the DFT of the analytic signal is less affected by long-range spectral leakage effects. In order to demonstrate this generic property, let us consider the specific case of $x(t)$ being a real sinusoid:

$$x(t) = A_0 \cos(\omega_0 t + \varphi_0) \tag{4.5}$$

As it is well known, its spectral representation consists of two bins centered at $\pm\omega_0$:

$$\mathscr{F}[x(t)] = A_0/2 \cdot [\delta(\omega - \omega_0)e^{j\varphi_0} + \delta(\omega + \omega_0)^{-j\varphi_0}] \tag{4.6}$$

being $\mathscr{F}(\cdot)$ the Fourier Transform (FT) operator and δ the Dirac function. Conversely, the HT of $x(t)$ is:

$$\mathscr{H}[x(t)] = \tilde{x}(t) = A_0 \sin(\omega_0 t + \varphi_0) \tag{4.7}$$

and the resulting analytic signal is:

$$\hat{x}(t) = A_0 \cos(\omega_0 t + \varphi_0) + j \cdot A_0 \sin(\omega_0 t + \varphi_0) = A_0 e^{j(\omega_0 t + \varphi_0)} \tag{4.8}$$

The spectral representation of $\hat{x}(t)$ can be derived from its FT:

$$\mathscr{F}[\hat{x}(t)] = A_0 \cdot \delta(\omega - \omega_0) e^{j\varphi_0} \tag{4.9}$$

demonstrating that the spectral representation of the analytic signal does not consist of imaginary components, but only of (doubled) real components.

It should be noticed that the removal of the negative frequency components does not correspond to a loss or alteration of the original information content. From a mathematical point of view, the analytic signal can be considered as a generalization of the concept of phasor representation. Given a phasor model, we are able to provide an instantaneous estimate of the signal amplitude, frequency and phase, under the assumption that such quantities are time-invariant. The analytic signal, instead, allows for tracking the time-variations of the signal parameters [99].

In this context, Fig. 4.1(a) compares the DFT absolute values of three different signals: a real-valued cosine signal $x(t)$, the corresponding analytic signal $\hat{x}(t)$, and a DFT pure tone $w(t)$ (usually referred to as DFT kernel) with the same amplitude, frequency and initial phase:

$$x(t) = A_0 \cdot \cos(2\pi f_0 t + \varphi_0) \tag{4.10}$$

$$\hat{x}(t) = x(t) + j \cdot \mathscr{H}[x(t)] = x(t) + j \cdot \tilde{x}(t) \tag{4.11}$$

$$w(t) = A_0/2 \cdot \left(\cos(2\pi f_0 t + \varphi_0) + j \cdot \sin(2\pi f_0 t + \varphi_0)\right) = A_0/2 \cdot \exp^{j \cdot (2\pi f_0 t + \varphi_0)} \tag{4.12}$$

More precisely, the signal under investigation is characterized by A_0, f_0 and φ_0 equal to 1 pu, 52.5 Hz and 0 rad, respectively, while the sampling rate is 50 kHz. In this case, the window length consists of three nominal cycles, i.e. 60 ms, corresponding to a frequency resolution of 16.67 Hz. This window length has been selected in order to enhance the graphical representation of spectral leakage effects, but similar results hold for any window length. For the sake of a clearer comparison, both the analytic and pure tone signals have been halved, therefore the DFT peak values coincide.

Due to incoherent sampling, all the spectral representations are affected by spectral leakage. Nevertheless, it is interesting to observe how the analytic signal presents only the lobe associated to the positive frequency component. In this regard, Fig. 4.1(b) presents the point-wise deviation of real-valued and analytic signal DFTs with respect to the complex exponential reference. It should be noticed that the suppression of the negative frequency component is nearly perfect: the remainder spurious contribution is in the order of some parts per mil-

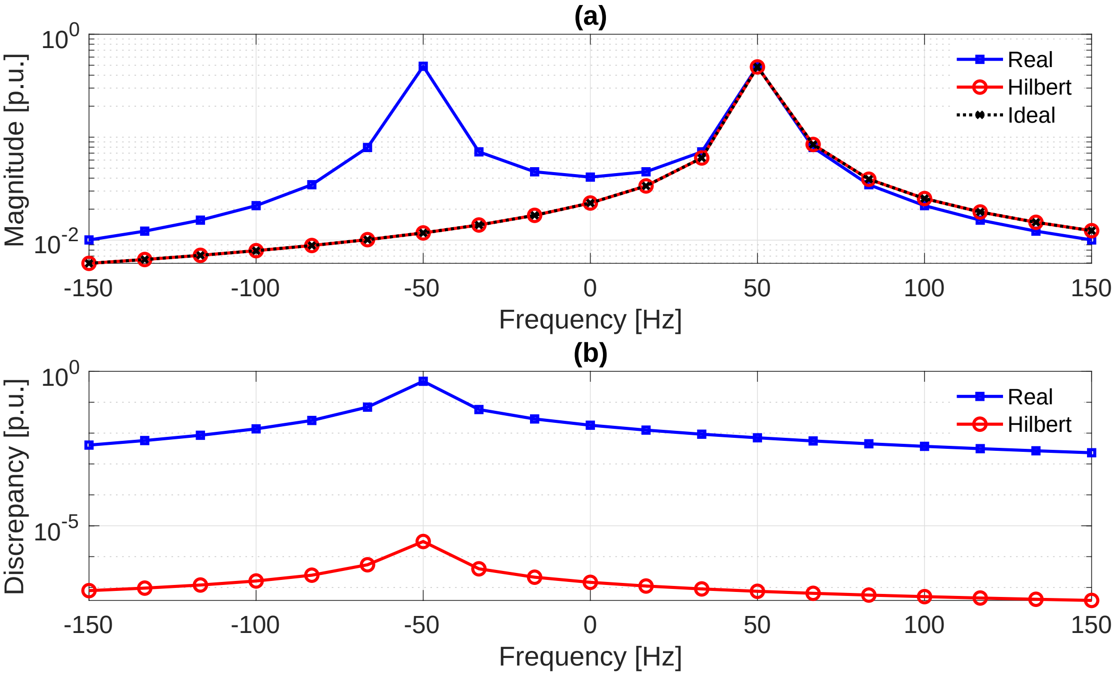

Figure 4.1 – DFT modules of a real-valued cosine signal (blue, squares), the corresponding analytic signal (red, circles), and the ideal DFT kernel (black, crosses) (a). Discrepancy between the DFT module of real-valued and analytic signal with respect to ideal DFT kernel (b).

lion, probably due to the limited spectral resolution given by the finite number of samples employed in this example. Based on this property, it is reasonable to expect that DFT-based algorithms might provide accurate estimates also on restricted window lengths, i.e shorter than 60 ms.

The HT computation represents an open issue. Indeed, we cannot know in advance the exact signal model, thus an approximation of the HT should rely exclusively on the acquired time-series $x[n]$. In this context, two are the possible solutions. On one side, frequency-based methods apply a weighing function to the signal DFT, to approximate (4.3), and retrieve the analytic signal through the inverse DFT [100, 96]. Such methods can be easily implemented, but are affected by the typical DFT limitations, e.g., stationarity constraint and truncation effects: in the presence of dynamic trends, it is reasonable to expect that the signal DFT accounts only for an average representation of the parameter variations. Conversely, time-based methods approximate (4.3) by means of a cascade of Infinite Impulse Response (IIR) filters [101]. These methods can operate in nearly real-time conditions, even if that requires an accurate characterization and compensation of filter contributions in terms of magnitude gain and phase delay. Moreover, the employment of digital filters does not require the computation of both direct and inverse DFT, and better preserves the original signal dynamics [102]. For this reason, a time-based method that employs two different filter banks is considered.

4.3 The Hilbert Transform for Synchrophasor Estimation

This Section describes the main steps of the proposed HT-IpDFT algorithm, and how it achieves accurate synchrophasor estimates by jointly using the HT and the IpDFT techniques. Specifically, Section 4.3.1 defines the synchrophasor estimation algorithm, Section 4.3.2 and 4.3.3 discuss the theoretical and experimental criteria that condition the choice of the method's parameters.

4.3.1 The HT-IpDFT Algorithm Formulation

The proposed algorithm is organized in three sequential stages. In the first stage, the acquired signal passes through a bank of two parallel HT filters, characterized by high reconstruction accuracy and high responsiveness, respectively. An event detection block determines which filter output has to be propagated to the following stage. If a transient event is detected, the best option is represented by the fast HT filter, capable of promptly responding to rapid variations. Otherwise, the accurate HT filter is preferable, because of its reduced distortion effect. In the third stage the actual synchrophasor estimation process takes place through a procedure based on the three-points i-IpDFT. The algorithm's details are given in the next paragraphs, whereas the pseudo-code of the proposed HT-IpDFT is reported in Algorithm 5.

Filtering Stage

The two filters approximate the HT properties and both rely on a two-stage cascade of IIR filter, whose parameters and performance indices are reported in Table 4.1 where a sampling frequency of 50 kHz is assumed. The filters are complex filters, i.e., with a complex valued impulse response, that provide the analytic signal of the input signal. The same transition width of 50 Hz is set, thus guaranteeing a flat pass-band response within the range [25, 75] Hz, that corresponds to the pass-band of a PMU with a nominal fundamental frequency of 50 Hz and a reporting rate of 50 fps. The filter order is set equal to 61 and 21 for the accurate and fast

Table 4.1 – HT Filter Parameters

Parameter	Accurate Filter	Fast Filter
filter order	61	21
stages number	2	2
transition width [Hz]	50	50
pass-band ripple [dB]	$8.37{\cdot}10^{-10}$	$8.86{\cdot}10^{-6}$
group delay [ms] at 50 Hz	4.6	5.7
round-off noise [dB/Hz] at 50 Hz	-89.3	-99.8
multipliers number	32	12
adders number	61	21
states number	65	25

Algorithm 5 The HT-IpDFT algorithm.

```
1. Filtering Stage: Analytic signal computation through HT filters
$\hat{x}_{fast}(n) = \mathscr{H}_{fast}[x(n)]$    ▷ Fast HT filtering
$\hat{x}_{acc}(n) = \mathscr{H}_{acc}[x(n)]$    ▷ Accurate HT filtering
2. Event Detection Stage: Selection of the appropriate HT filter output
if $x(t) - B[x(n)] > \beta$    ▷ Butterworth low-pass filtering
    $\hat{x}(n) = \hat{x}_{fast}(n)$    ▷ If a transient event is detected, select the fast HT filter
else
    $\hat{x}(n) = \hat{x}_{acc}(n)$    ▷ In static operating conditions, select the accurate HT filter
end if
3. Synchrophasor Estimation Stage: Estimation of the fundamental tone parameters
$X(k) = DFT\,[\hat{x}(n) \cdot w(n)]$    ▷ Hanning windowing and DFT computation
$\{\widehat{f}_0^0, \widehat{A}_0^0, \widehat{\varphi}_0^0\} = IpDFT\,[X(k)]$    ▷ Fundamental tone parameters estimation via IpDFT
$\widehat{X}_0^{0+}(k) = image\,[\widehat{f}_0^0, \widehat{A}_0^0, \widehat{\varphi}_0^0]$    ▷ Fund. tone positive image reconstruction
if $\sum |X(k) - \widehat{X}_0^{0+}(k)|^2 > \lambda \cdot \sum |X(k)|^2$    ▷ Interference detection
    for $q = 1 \to Q$ and $E_n > \lambda$    ▷ Interference compensation routine
        $\{\widehat{f}_i^q, \widehat{A}_i^q, \widehat{\varphi}_i^q\} = IpDFT\left[X(k) - \widehat{X}_0^{q-1+}(k)\right]$    ▷ Inter. param. computation via IpDFT
        $\widehat{X}_i^{q+}(k) = image\,[\widehat{f}_i^q, \widehat{A}_i^q, \widehat{\varphi}_i^q]$    ▷ Inter. tone positive image reconstruction
        $\{\widehat{f}_0^q, \widehat{A}_0^q, \widehat{\varphi}_0^q\} = IpDFT\left[X(k) - \widehat{X}_i^{q+}(k)\right]$    ▷ Fund. param. computation via IpDFT
        $\widehat{X}_0^{q+}(k) = image\,[\widehat{f}_0^q, \widehat{A}_0^q, \widehat{\varphi}_0^q]$    ▷ Fund. tone positive image reconstruction
    end for
else
    break
end if
```

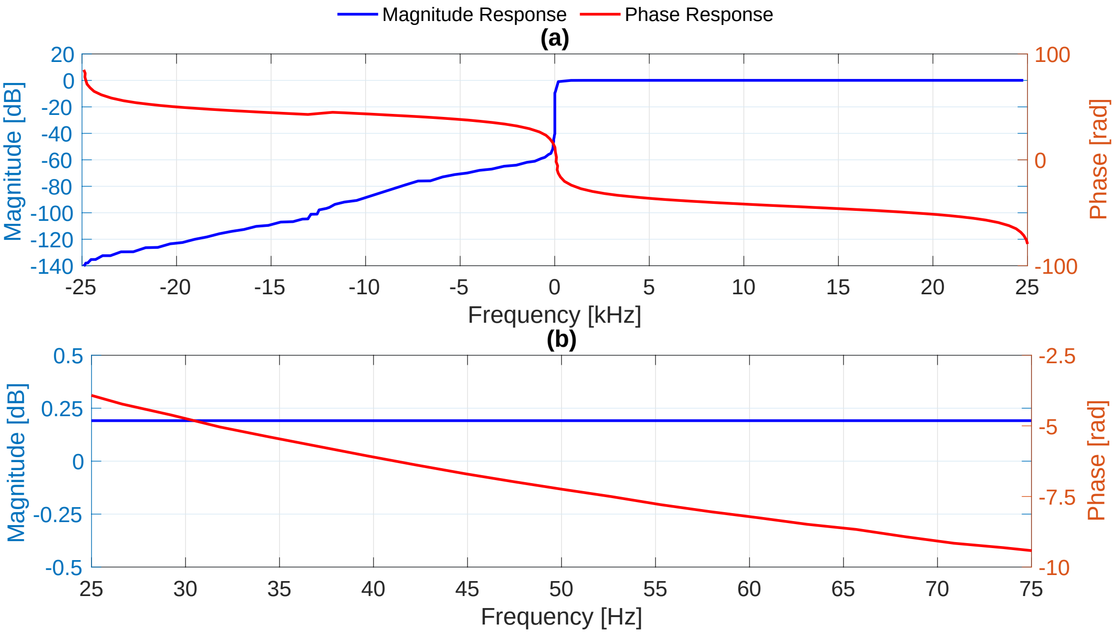

Figure 4.2 – Frequency response of the accurate HT filter for a sampling rate of 50 kHz, over the acquisition (a) and the PMU pass-band (b).

solution, respectively: these values enable the minimization of the pass-band ripple and the power density of the round-off noise.

The filter performance is evaluated in terms of pass-band ripple, group delay, power spectral density of round-off noise and computational complexity. The pass-band ripple accounts for the deviation from unity gain in the filter pass-band. The accurate solution is characterized by a ripple lower than $8.5 \cdot 10^{-10}$ dB, whereas the fast solution provides a ripple in the order of $8.9 \cdot 10^{-6}$ dB. The group delay, instead, quantifies the time delay between the input and output of the filter cascade. Since IIR filters are characterized by group delays varying with the frequency of the test signal, in Table 4.1 the value related to the nominal fundamental frequency (50 Hz) is reported. In particular, a group delay of 4.6 and 5.7 ms is measured for accurate and fast solution, respectively. The round-off noise is produced by the quantization and truncation error within the filter cascade, due to the finite precision arithmetic. In line with the group delay analysis, the focus is on the noise power within the bandwidth of interest. In particular, at 50 Hz the accurate solution is characterized by a noise power spectral density in the order of -90 dB/Hz, whereas the fast solution guarantees an even lower noise power, around -100 dB/Hz, thanks to the reduced number of coefficients. Finally, the computational complexity of the designed filters is evaluated. In particular, the number of multipliers, adders and filter internal states, necessary to implement the filter cascades is identified. The accurate solution proves to be more demanding than the fast solution. Indeed, a better approximation of the peculiar HT frequency response is achieved at the price of higher number of states and operations.

The main disadvantage of IIR filters is typically represented by their non-linear phase response. Nevertheless, the present analysis focuses on a restricted bandwidth, i.e [10, 150] Hz, where the filter response can be reasonably considered as almost linear and thus can be properly compensated. Once characterized the filter response as a function of frequency, it is possible to determine the amplitude and phase correction based on the estimated value of the fundamental frequency. Figure 4.2(a) represents the magnitude and phase response of the accurate HT filter over the entire acquisition bandwidth. It is worth observing that the magnitude response (blue line) is nearly equal to 0 dB for the positive frequency components, whereas it decreases from -60 up to -140 dB in the negative frequency domain. In accordance with (4.3), the phase response (red line) produces a shift of $\pi/2$ for the negative frequency components and -$\pi/2$ for the positive frequency ones. In this way, it is reasonable to expect that a significant rejection of the long-range interference can be achieved. A detailed view of the trend over the PMU pass-band [25, 75] Hz is provided in Fig. 4.2(b). Both magnitude and phase response are not equal to their ideal values, i.e. 0 dB and -$\pi/2$, respectively. Nevertheless they exhibit a nearly linear trend that can be compensated, once the frequency of the fundamental component has been estimated. Similar trends can be obtained on varying the filter order (e.g., from 61 to 21) or the sampling rate (e.g., from 50 to 10 kHz). Once designed the filter frequency response, the magnitude gain and phase delay within the range of interest [10, 150] Hz is modeled by means of a smoothing spline approximation. In this regard, the goodness of fit is guaranteed by the fact that the models present a coefficient of determination r^2 equal to 1, and the square root of the variance of the residuals is equal to $2.31{\cdot}10^{-4}$ and $8.82{\cdot}10^{-6}$ for the accurate and fast solution, respectively.

Event Detection Stage

The selection between accurate and fast HT Filter outputs is carried out by an event detection block that relies on a simple feedback operation inspired by [103, 104]. First, the input signal is processed through a Butterworth third-order low-pass filter $B[\cdot]$. The cut-off frequency is set equal to 3 kHz, in order to include within the filter pass-band any harmonic term up to 50^{th} order. As shown in Fig. 4.3(a), the stop-band is characterized by an attenuation of -20 dB. Then, the point-wise difference between the original and filtered version of the input signal is computed: if it exceeds the expected level of variability β (due to measurement noise and filter distortion) a transient event is detected.

In order to define the threshold level, a heuristic procedure is carried out and the distribution of the discrepancy values is evaluated in the test conditions indicated by the IEEE Std. C37.118 with a test duration of 5 s, a sampling frequency of 50 kHz, and a signal-to-noise ratio of 80 dB. In this regard, it should be noticed that the most challenging among the considered scenarios is taken into account, as it is characterized by the highest noise level and the poorest time resolution. As it can be seen in Fig. 4.3(b), in the presence of amplitude and phase steps (AS and PS, respectively) the discrepancy presents some outliers that can be used to detect the occurrence of a step change with a delay of less than 10 samples. In the

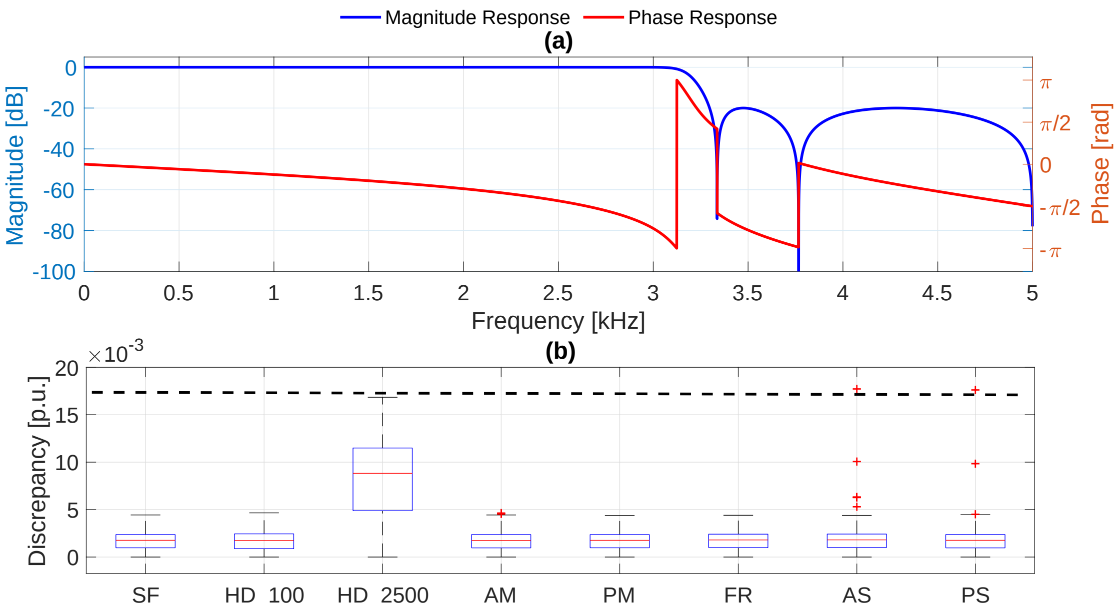

Figure 4.3 – Event Detection Block: magnitude and phase response (wrapped to the range [-π, +π]) of the low-pass filter (a), boxplot representation of the discrepancy value distributions in different IEEE Std. C37.118 tests with respect to selected threshold level (b).

presence of abrupt variations (e.g., an amplitude step change), the filter output presents a slower transition, due to the finite impulse response and the limited pass-band. As a consequence, the discrepancy value is expected to exceed its typical variability depending on the test signal characteristics, the SNR and the sampling frequency. Based on this analysis, the event detection threshold (black dashed line) is set equal to $17.5{\cdot}10^{-3}$ p.u., larger than the maximum discrepancy obtained during high-order harmonic distortion (HD-2500), but lower than the outliers produced by amplitude and phase step. Due to its non-linear dependence by the test conditions, the event detection process might be improperly triggered in the presence of high-order harmonic tones. Nevertheless, the presence of a single harmonic tone whose amplitude and frequency are equal to 0.1 pu and 2500 Hz is rather unrealistic in practice, as it would imply a carryover of 10% of the signal energy at high frequency. Furthermore, it is worth noticing that this kind of interference does not produce significant distortion effects on the DFT bins interested by the interpolation process. Therefore, even in case of erroneous detection, also the fast HT filter guarantees a sufficient level of estimation accuracy (as shown by TVE and FE results in Sec. 4.4.2).

Synchrophasor Estimation Stage

Once computed the analytic signal $\hat{x}(t)$, the fundamental tone parameters are estimated through an approach based on the IpDFT. Specifically, the i-IpDFT is applied to the event detection block output, similarly to what described in Algorithm 4 of Chapter 3. However, since the DFT of the analytic signal results in only positive images, the compensation of the negative image is omitted, largely simplifying the estimation process.

As it can be seen in Algorithm 5, the method starts by computing the DFT bins related to the analytic signal (line 8 of Alg. 5). By considering the analytic signal $\hat{x}(t)$, we would expect to deal with spectra containing the positive frequency components only. However, since the HT filter is only an approximation of the ideal transform, residual distortion contribution might still be present, and should be suitably mitigated, in particular when a relatively short window length is employed. In order to limit the possible spectral leakage effect, the signal is windowed with the Hanning function. Then, the three-point IpDFT is applied to the selected HT output in order to estimate the amplitude, frequency and initial phase of the fundamental component (line 9). Based on this preliminary estimate, the fundamental component contribution is computed (line 10), and then it is subtracted from the original spectrum in order to verify whether the resulting DFT bins still contain spurious narrow-band components. It is worth pointing out that only the positive image of the spectrum is computed, as the DFT bins related to the analytic signal ideally consist of only positive frequencies. An energy thresholding process is applied, and if the energy content E_n is larger than a predefined threshold λ (line 11), the iterative compensation routine is triggered (line 12-17). Otherwise, the estimates obtained via the first IpDFT (i.e., in line 9) are validated as the final HT-IpDFT outcomes. Conversely, if the threshold is exceeded, a peak search identifies the plausible bin associated to the interfering component and a new three-point interpolation is performed (line 13). Once identified the spurious component parameters (line 14), they are subtracted from the original DFT bins and a new fundamental estimation is performed (line 15).

The whole procedure can be iterated a predefined number of times Q, leading to more and more accurate estimates as Q increases (see the next Paragraph). The presented HT-IpDFT algorithm can be formulated for any window function, number of IpDFT interpolation points, window length and sampling frequency. In the present case, this compensation routine is applied only to inter-harmonic and harmonic components whose frequency does not exceed 150 Hz. In fact, higher-frequency components do not produce significant distortion effects within the DFT bins associated to the fundamental component.

Finally, as suggested by the signal processing models in the IEEE Std. C37.118, the HT-IpDFT computes ROCOF as the incremental ratio between two consecutive frequency estimates [19]:

$$ROCOF(n) = \left|\widehat{f}_0(n) - \widehat{f}_0(n-1)\right| \cdot F_r \tag{4.13}$$

where $\widehat{f}_0(n)$ and $\widehat{f}_0(n-1)$ represent the fundamental frequency estimations at two successive reporting times.

4.3.2 On the Tuning of the Number of Iterations Q

In order to guarantee feasibility and efficiency of the routine that compensates for the spectral leakage introduced by interfering tones, two stop criteria are introduced. More specifically, the

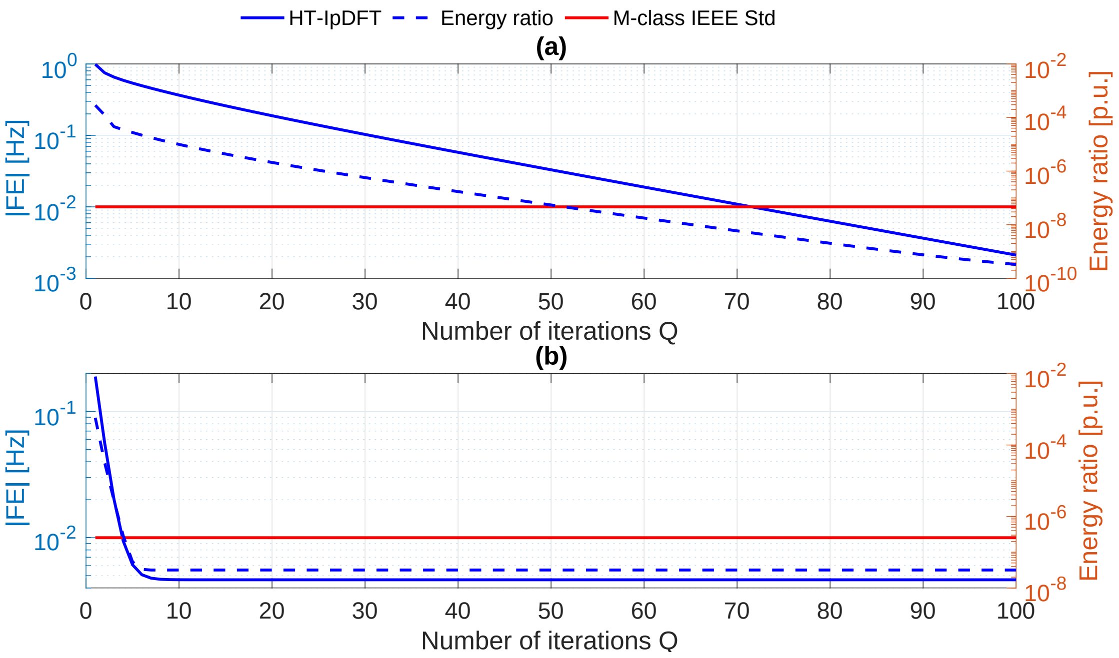

Figure 4.4 – FE (solid line) and energy ratio E_n (dashed line) with the HT-IpDFT technique as a function of the iteration number Q. In (a), f_0 = 52.5 Hz and f_i = 75 Hz; in (b), f = 50 Hz, f_i = 10 Hz. The red line represents the performance requirement for M-class OOBI test in [19]. F_s = 50 kHz, T = 40 ms, SNR = 80 dB.

routine stops when the incremental ratio between two consecutive values of the ratio between the residual and original spectrum energy E_n is negligible, i.e. lower than 10^{-10}, or when the iteration number exceeds the maximum limit Q equal to 100. As in (3.26), the residual energy is defined as follows:

$$E_n = \frac{E[X(k) - \widehat{X}_0^0(k)]}{E\,[X(k)]} = \frac{\sum_{k=0}^{K} |X(k) - \widehat{X}_0^0(k)|^2}{\sum_{k=0}^{K} |X(k)|^2} \tag{4.14}$$

Figure 4.4 represents FE and E_n as a function of the iteration number Q in two significant cases of the OOBI test, with a two-cycle window, as well the FE limit of 10 mHz introduced by the IEEE Std. C37.118 for the OOBI test. The upper graph (a) considers one of the worst-cases, where f_0 and f_i are set equal to 52.5 and 75 Hz, respectively. As a consequence, the distance between fundamental and inter-harmonic component is less than a single bin on the considered frequency axis. In this challenging scenario, FE and E_n decade monotonically but slowly: 72 iterations are necessary to obtain a FE compliant with M-class requirement. In the lower graph (b), instead, the fundamental and inter-harmonic frequency are set equal to 50 and 10 Hz, respectively. Since the deviation between f_0 and f_i is relevant, it is reasonable to expect that the interference effect is reduced. In fact, FE achieves the compliance with the standard limit after just four iterations. In a similar way, the residual energy E_n rapidly decreases and

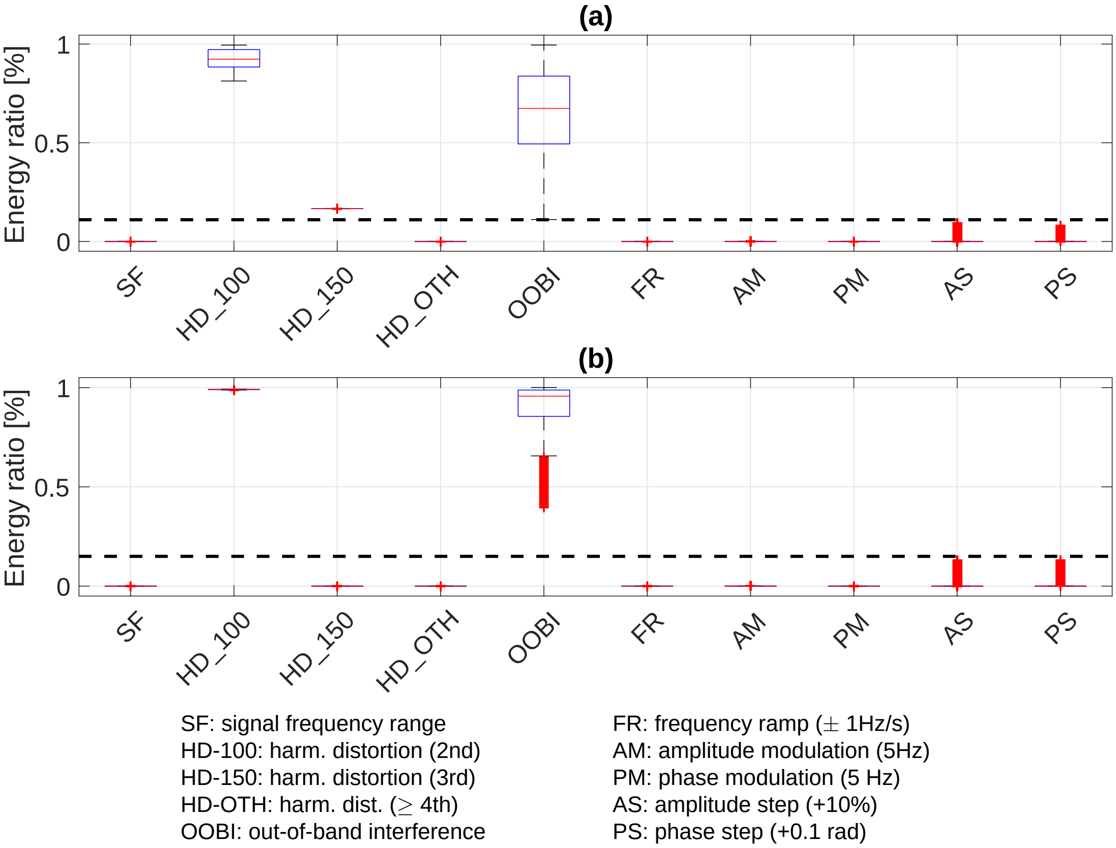

Figure 4.5 – Boxplot representation of E_n in all operating conditions indicated in [19] with window length equal to two (a) and three cycles (b). The dashed line represents the selected threshold λ (0.11% two-cycles, 0.15% three-cycles). $F_s = 50$ kHz, $f_n = 50$ Hz, SNR = 80 dB.

becomes constant just after 7 iterations. This example proves how the double stop criterion represents an optimal trade-off between computational efficiency and estimation accuracy.

4.3.3 On the tuning of the threshold λ

In order to define the most suitable detection threshold λ, a heuristic procedure to determine the distribution of E_n in the test conditions indicated by the IEEE Std. C37.118 is conducted, with a sampling frequency of 50 kHz and a SNR of 80 dB. In this regard, Fig. 4.5 shows the box-plot associated to the different test conditions for window length equal to 40 and 60 ms, respectively. For this analysis, interfering component amplitudes are set equal to 0.1 pu, i.e. the maximum value required by the IEEE Std. It is interesting to observe that the threshold value is nearly coincident in the considered two cases (0.11% for two-cycles, 0.15% for three-cycles) and enables us to discriminate between the presence of spurious components with frequency lower than 150 Hz, whereas higher-order harmonics (HD-OTH) or dynamic test conditions do not trigger the iterative routine.

In both the configurations, the OOBI test is characterized by a significantly large variability, due to the wide range of frequencies interested by the interfering tones, i.e. [10, 25] Hz and [75, 95] Hz. As regards the third-order harmonic, it is worth noticing that it exceeds the threshold only in two-cycle configuration. In this case, the reduced frequency resolution and the Hanning windowing produce the tails of the harmonic component to interfere with the tails of the fundamental one. In the tree-cycle configuration, instead, the enhanced frequency resolution guarantees a complete separation between the two spectral contributions, as confirmed by the energy ratio distribution that coincides with the one produced by the higher-order harmonic components. The energy ratio might assume high values (close to the detection threshold) also in the presence of transient events, like amplitude and phase step changes. Nevertheless, in this case, the event detection block is triggered and the compensation routine is not activated.

4.4 Performance Characterization with respect to the IEEE Std. C37.118

In this section, the estimation accuracy of the HT-IpDFT algorithm in terms of TVE, FE and RFE is thoroughly characterized. For this analysis, the static (Section 4.4.1) and dynamic (Section 4.4.2) test conditions dictated by the IEEE Std. C37.118 [19, 20] are reproduced following the test procedures indicated in the IEEE Guide C37.242 [86]. In order to approximate a more realistic operating scenario, the measurement noise is simulated by means of an additive white Gaussian component, varying the SNR between 60 and 80 dB. For each test condition, the results are presented by means of two graphs, showing the maximum TVE and FE as a function of the independent variable of the specific test, and the limits allowed by [19] for P and M performance class. Also, for each group of tests, two tables report the maximum TVE, FE and RFE provided by each HT-IpDFT configuration as a function of the test condition. The figures show the results for SNR 80 dB, whereas the tables include the results at 60 dB.

Table 4.2 summarizes the parameters for the HT-IpDFT. In particular, the nominal power system frequency is 50 Hz, and the results are shown for a window length containing two (blue lines) and three cycles (green lines), i.e., 40 and 60 ms respectively at 50 Hz. Unless otherwise specified, the sampling frequency F_s is fixed to 50 kHz and the reporting rate F_r is set equal

Table 4.2 – HT-IpDFT parameters.

Parameter	Variable	Value
Nominal system frequency	f_n	50 Hz
Window type	-	Hanning
Window length	T	40 ms (2 cycles) and 60 ms (3 cycles)
Sampling rate	F_s	50 kHz
PMU reporting rate	F_r	50 fps
DFT bins	K	8 (2 cycles) and 11 (3 cycles)
Iterations compensation interference	Q	100
IpDFT interpolation points	-	3

to 50 fps. The synchrophasors are estimated at overlapping observation windows and the time-stamp is referred to the center of the observation interval. In order to compensate the effects of any interfering component up to the third harmonic, for the 2 cycles configuration the first 6 bins of the spectrum are computed (150 Hz/25 Hz = 6). Including the DC and the bin next to the third harmonic, this results in 8 total DFT bins. For the 3 cycles estimator, this value is augmented to 11. The number of iterations of the compensation routine Q is upper limited to 100, but its actual value depends on the amplitude and frequency of the interfering tone. The 3-points IpDFT is used to estimate the fractional correction term δ. For each test condition, a signal waveform $x[n]$ with an overall duration of 5 s is reproduced (except for the modulation and frequency ramp tests where the duration is increased up to 20 s). It is worth pointing out that the parameters reported in Table 4.2 are kept constant during all tests: such configuration enables the simultaneous fulfillment of the P and M-class compliance.

4.4.1 Static Operating Conditions

According to [19], three cases are taken into account as regards the steady state tests (see Figures 4.6-4.8 and Table 4.3):

- Signal frequency: single-tone signals in the frequency range $45 \leq f_0 \leq 55$ Hz (Fig. 4.6);
- Harmonic distortion: signals distorted by a single 1% or 10% harmonic in the frequency range $100 \leq f_h \leq 2500$ Hz (Fig. 4.7)
- OOBI: signals characterized by a fundamental frequency f_0 of 47.5, 50 and 52.5 Hz, distorted by single 10% interharmonic in the frequency range $10 \leq f_i \leq 25$ Hz and 75 $\leq f_i \leq 100$ Hz (Fig. 4.8).

Regarding the signal frequency test (see Fig. 4.6), in terms of TVE the main error source is represented by the additive noise rather than the window length. In the worst-case, the TVE does not exceed 0.01%, i.e., it is negligible if compared with the limit required by [19] equal to 1%. As regards FE, instead, it is worth observing that the window length significantly affects the estimation accuracy: passing from two to three cycles, the error is nearly halved. Nevertheless, the worst-case FE keeps strictly lower than the limit of 5 mHz. In terms of RFE, when the SNR is limited to 80 dB the two- and three-cycle configuration provide a maximum error of 21 and 15 mHz/s, respectively, within the limit of 100 mHz/s. For lower SNR, the limit is violated reaching RFE up to 220 mHz/s.

Regarding the harmonic distortion test (see Fig. 4.7), the worst-case TVE satisfies the performance requirement of 1% in all the considered configurations, not exceeding a maximum value of 0.19%. Conversely, the worst-case FE varies significantly as a function of the distortion level. Given a THD equal to 10%, the frequency error keeps lower than 4 mHz, being 5 mHz the limit dictated by [19]. However, limiting the distortion level to 1%, the worst-case FE becomes larger than 80 mHz for a two-cycle window length. In this case, the frequency resolution is too scarce to suitably identify an interfering component with reduced amplitude. As a consequence, the iterative compensation routine might not be successful, and the resulting frequency estimates are gravely distorted. As regards RFE, [19] defines a limit of 400 mHz/s. If the THD is set equal to 10%, the worst-case performance is 270 and 137 mHz/s for two- and three-cycle configuration, respectively. If the THD is set equal to 1%, instead, the HT-IpDFT produces a maximum RFE of 360 and 101 mHz/s for two- and three-cycle configuration, respectively.

Regarding the OOBI test, Fig. 4.8 presents the worst-case TVE and FE as a function of the inter-harmonic frequency, obtained with a fundamental frequency of 52.5 Hz, proving that the HT-IpDFT is compliant with the requirements of [19] in terms of both TVE (1.3%) and FE (10 mHz) in all the considered configurations. As in the previous test, the three-cycle configuration guarantees a significant performance enhancement, due to the fact that a larger window length corresponds to a finer frequency resolution, a reduced short-range interference, and thus a better capability of compensating the spurious tones. If f_{ih} is lower than 15 Hz, the frequency resolution of the two-cycle configuration does not allow for discriminating between DC and inter-harmonic contributions. As a consequence, the iterative compensation routine is non-optimal and produces a TVE and FE equal to 0.02% and 7 mHz, in the worst-case. Within [15, 25] Hz, the two- and three-cycle configurations provide comparable results: TVE and FE do not exceed 0.05% and 1 mHz, respectively. Finally, if f_i varies within [75, 95] Hz, the three-cycle configuration guarantees a performance enhancement by almost one order of magnitude, with a maximum TVE of 0.004% and a FE lower than 0.2 mHz.

4.4.2 Dynamic Operating Conditions

Regarding the dynamic conditions (see Figures 4.9-4.12 and Table 4.4), three cases are analyzed according to [19]:

- Measurement bandwidth: signals characterized by phase and amplitude modulations, being $0.1 \leq f_m \leq 5$ Hz the modulating frequency (Fig. 4.9 and 4.10);
- Frequency ramp: signals characterized by positive and negative frequency ramps in the frequency range $48 \leq f_0 \leq 52$ Hz and $45 \leq f_0 \leq 55$ Hz at a rate of ± 1 Hz/s (Fig. 4.11);
- Amplitude and phase steps: signals characterized by positive and negative amplitude (± 10 %) and phase ($\pm\pi/18$) steps (Fig. 4.12).

As regards amplitude modulation, in the worst case, TVE is equal to 0.37%, whereas FE is lower than 11.1 mHz, while the IEEE Std. C37.118 requires TVE and FE not to exceed 3% and 60 mHz, respectively. Fig. 4.9 represents the worst-case TVE and FE as a function of the modulation frequency f_m. It is worth noticing that the estimation accuracy does not depend significantly on the window length. Amplitude, phase and frequency errors are mainly due to the mismatch between the static signal model employed by interpolated DFT and the time-varying trend of

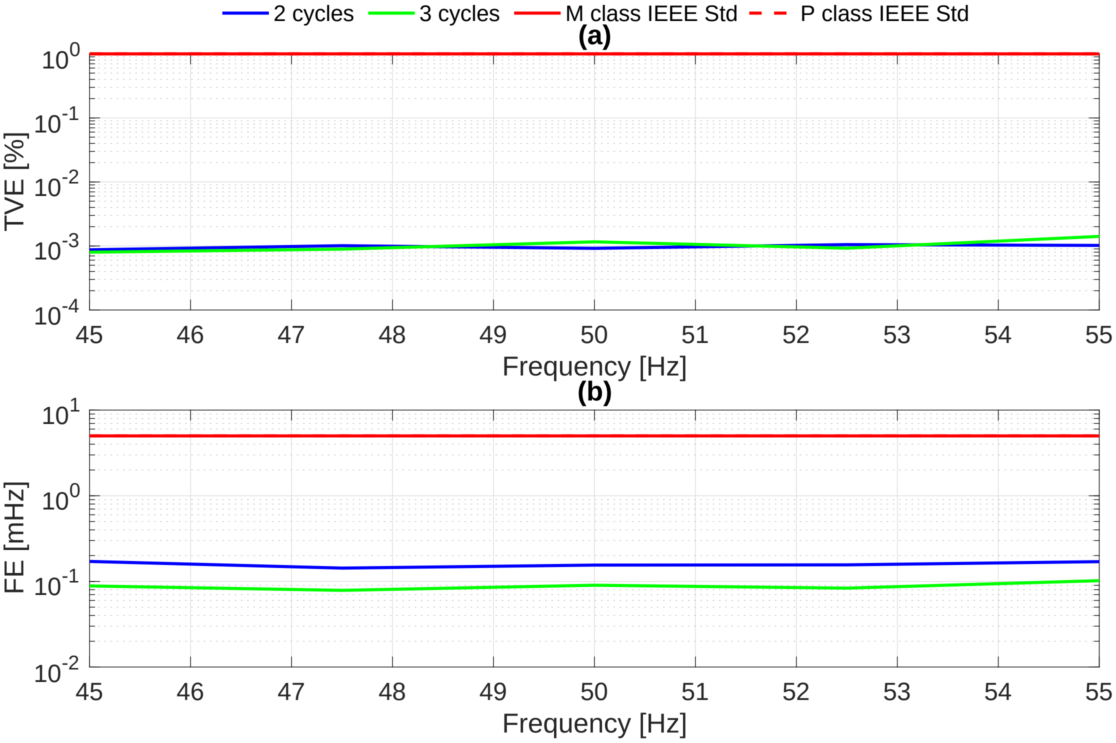

Figure 4.6 – Signal frequency test: worst-case TVE (a) and FE (b) as a function of the signal fundamental frequency, with 2 (blue) and 3 cycles (green) window. The dashed and solid red lines represent the IEEE Std. C37.118 performance requirements for P- and M-class.

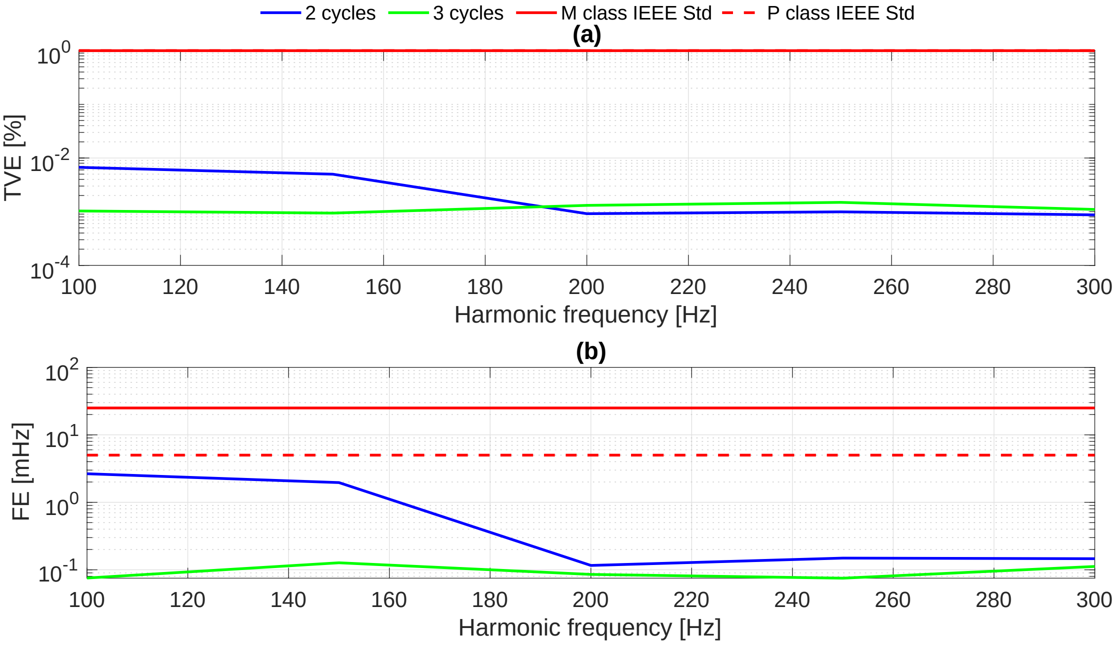

Figure 4.7 – Harmonic distortion test: worst-case TVE (a) and FE (b) as a function of the harmonic component frequency, with 2 (blue) and 3 cycles (green) window. The dashed and solid red lines represent the IEEE Std. C37.118 performance requirements for P- and M-class.

Table 4.3 – Compliance with respect to static signals: maximum TVE, FE and RFE for the HT-IpDFT and maximum limit allowed by [19].

		TVE [%]						**FE [mHz]**						**RFE [Hz/s]**					
		IEEE Std		HT-IpDFT				IEEE Std		HT-IpDFT				IEEE Std		HT-IpDFT			
		P	M	2 cycles		3 cycles		P	M	2 cycles		3 cycles		P	M	2 cycles		3 cycles	
				SNR [dB]		SNR [dB]				SNR [dB]		SNR [dB]				SNR [dB]		SNR [dB]	
				60	80	60	80			60	80	60	80			60	80	60	80
Sign Freq		1	1	0.01	0.001	0.01	0.001	5	5	1.97	0.17	1.04	0.10	0.4	0.1	0.22	0.02	0.14	0.01
Harm Dist 1%		1	1	0.19	0.187	0.01	0.001	5	25	84.7	83.4	1.03	0.13	0.4	-	0.36	0.27	0.10	0.01
Harm Dist 10%		1	1	0.01	0.007	0.01	0.001	5	25	2.60	0.36	1.07	0.13	0.4	-	0.27	0.10	0.14	0.02
OOBI	f_0=47.5 Hz	-	1.3	0.03	0.025	0.01	0.008	-	10	5.78	5.28	1.25	0.95	-	-	0.45	0.42	0.08	0.06
	f_0=50 Hz	-	1.3	0.02	0.020	0.01	0.007	-	10	6.10	4.99	1.37	0.88	-	-	0.46	0.40	0.09	0.06
	f_0=52.5 Hz	-	1.3	0.05	0.022	0.02	0.009	-	10	6.08	5.13	1.41	1.03	-	-	0.53	0.48	0.11	0.08

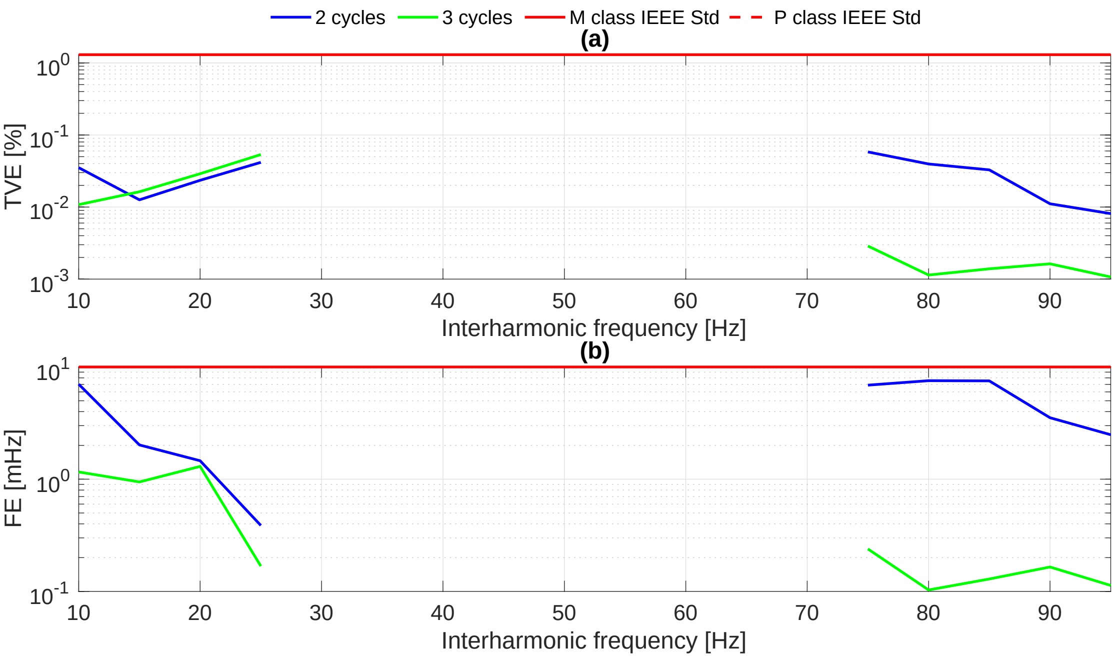

Figure 4.8 – OOBI test: worst-case TVE (a) and FE (b) as a function of the interharmonic component frequency, with 2 (blue) and 3 cycles (green) window. The solid red line represents the IEEE Std. C37.118 performance requirement for M-class.

the modulated signal. In terms of RFE, the worst-case performance is equal to 350 and 330 mHz/s for two- and three-cycle configuration, respectively (being the limit 2.3 Hz/s).

Similar considerations can be made for the phase modulation test: in the worst-case, TVE and FE are equal to 0.49% and 15.7 mHz, respectively. During a phase modulation, both signal frequency and phase are varying. Because of this duality (inherent in the synchrophasor phase angle definition), the possible sources of uncertainties are two. Nevertheless, as shown also in Fig. 4.10, the proposed algorithm proves to be compliant with the requirements in [19] for both class M and P in all the considered configurations. As regards RFE, the worst-case performance is equal to 350 and 180 mHz/s for two- and three-cycle configuration.

As regards the frequency ramp test, the results in Table 4.4 show that the HT-IpDFT is compliant with the IEEE Std. C37.118 limits in all the considered configurations. In particular, TVE and FE do not exceed 0.03% and 3.7 mHz. As shown in Fig. 4.11, the estimation accuracy does not depend on the polarity of the linear ramp: nearly coincident results are obtained for k_r equal to +1 or -1 Hz/s. As already mentioned for measurement bandwidth tests, the algorithm performance does not vary significantly when varying the window length: the error descends from the inconsistency of the IpDFT static signal model, rather than on the frequency resolution. In this case, the RFE presents a worst-case performance of 270 and 160 mHz/s for two- and three-cycle configuration, respectively, being the limit 200 mHz/s. When the SNR il limited to 80 dB the errors are limited to 40 mHz/s.

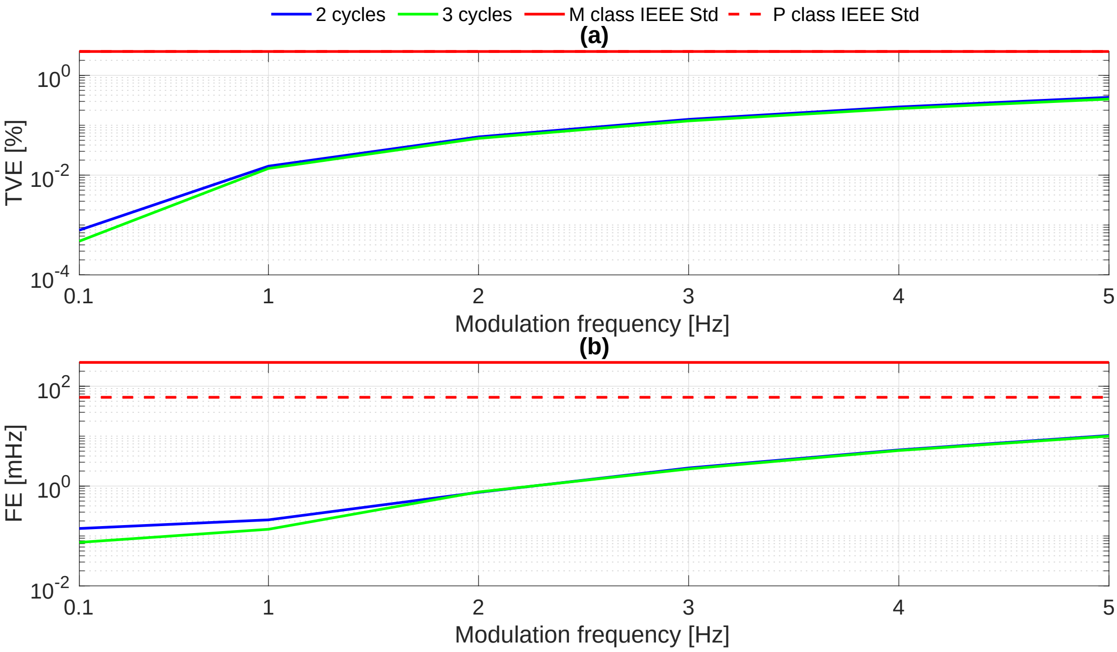

Figure 4.9 – Amplitude modulation test: worst-case TVE (a) and FE (b) as a function of the modulation frequency, with 2 (blue) and 3 cycles (green) window. The dashed and solid red lines represent the IEEE Std. C37.118 performance requirements for P- and M-class.

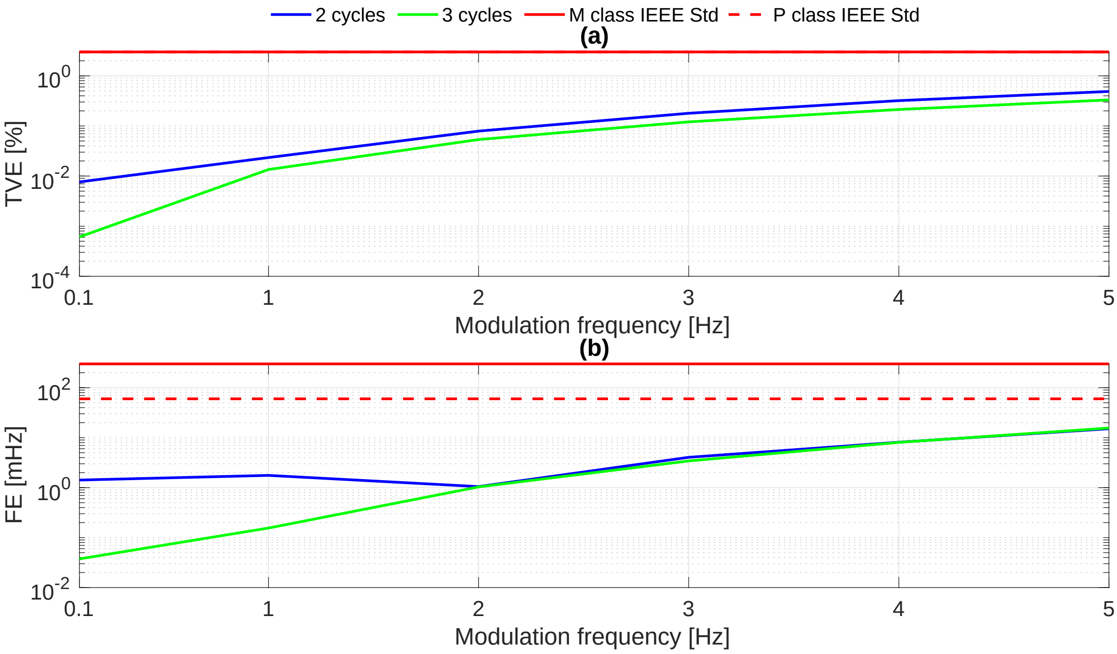

Figure 4.10 – Phase modulation test: worst-case TVE (a) and FE (b) as a function of the modulation frequency, with 2 (blue) and 3 cycles (green) window. The dashed and solid red lines represent the IEEE Std. C37.118 performance requirements for P- and M-class.

Table 4.4 – Compliance with respect to dynamic signals: maximum TVE, FE and RFE for the HT-IpDFT and maximum limit allowed by [19].

	TVE [%]						**FE [mHz]**						**RFE [Hz/s]**					
	IEEE Std		HT-IpDFT				IEEE Std		HT-IpDFT				IEEE Std		HT-IpDFT			
	P	M	2 cycles		3 cycles		P	M	2 cycles		3 cycles		P	M	2 cycles		3 cycles	
			SNR [dB]		SNR [dB]				SNR [dB]		SNR [dB]				SNR [dB]		SNR [dB]	
			60	80	60	80			60	80	60	80			60	80	60	80
Ampl Mod	3	3	0.37	0.362	0.30	0.268	60	300	11.1	10.3	10.7	10.0	2.3	14	0.35	0.18	0.33	0.26
Ph Mod	3	3	0.49	0.488	0.37	0.341	60	300	15.7	15.1	15.2	15.1	2.3	14	0.31	0.11	0.18	0.08
Freq Ramp	1	1	0.03	0.025	0.03	0.026	10	10	3.73	1.48	2.01	1.41	0.4	0.2	0.27	0.04	0.16	0.01
	TVE Response time [s]						**FE Response time [s]**						**RFE Response time [s]**					
	IEEE Std		HT-IpDFT				IEEE Std		HT-IpDFT				IEEE Std		HT-IpDFT			
	P	M	2 cycles		3 cycles		P	M	2 cycles		3 cycles		P	M	2 cycles		3 cycles	
			SNR [dB]		SNR [dB]				SNR [dB]		SNR [dB]				SNR [dB]		SNR [dB]	
			60	80	60	80			60	80	60	80			60	80	60	80
Ampl Step	0.04	0.14	0.024	0.024	0.036	0.036	0.09	0.28	0.062	0.061	0.056	0.056	0.12	0.28	0.074	0.074	0.081	0.081
Ph Step	0.04	0.14	0.036	0.036	0.071	0.071	0.09	0.28	0.094	0.094	0.124	0.121	0.12	0.28	0.112	0.112	0.140	0.140

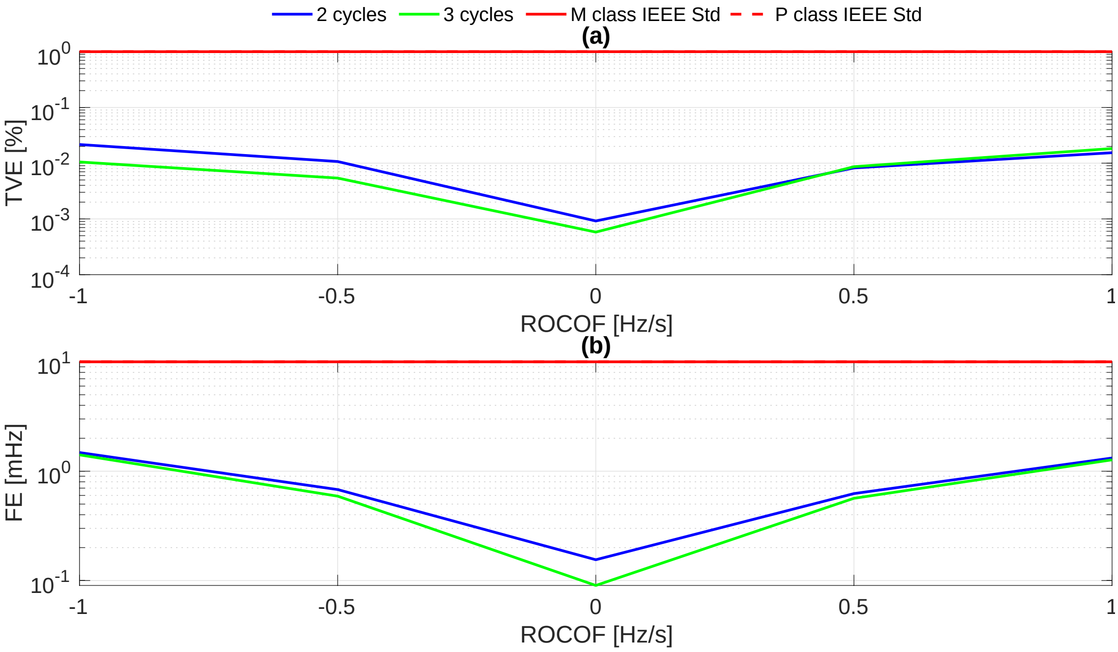

Figure 4.11 – Frequency ramp test: worst-case TVE (a) and FE (b) as a function of the ROCOF with 2 (blue) and 3 cycles (green) window. The dashed and solid red lines represent the IEEE Std. C37.118 performance requirements for P- and M-class.

As regards the step tests, F_r is set equal to F_s, producing a new estimate in correspondence with each acquired sample, therefore interleaved estimates. In Fig. 4.12a and 4.12b, the solid blue and green lines represent TVE and FE as a function of time. The error trends obtained with two and three cycles have been aligned with respect to $t = 0$, i.e., the time instant when the performance index exceeds the corresponding threshold (dashed black line). The dashed lines indicate the step occurrence time T_t in the two configurations. For the amplitude step, both TVE and FE are characterized by a response time lower than the class P limit (dashed red line). As reported in Table 4.4, the worst-case response time is equal to 36 and 62 ms for TVE and FE, respectively. For the phase steps, the responsiveness of the HT-IpDFT degrades as the window length is increased: the 3 cycles configuration is not compliant with none of the P-class requirements. Conversely, the two-cycle configuration fulfills both TVE requirements, whereas the worst-case FE response time exceeds the limit by less than 5 ms. It is important to notice that all the considered configurations are compliant with the requirements of class M.

The reason for such a performance deterioration can be found in the filter frequency response. Given the limited order, the fast HT filter is characterized by a step response with a reduced settling time, but a non-negligible ringing effect: the cosine argument exhibits a damped oscillation that can be interpreted as either a phase or frequency modulation. In fact, the synchrophasor estimation algorithm is unable to discriminate between these contributions, due to the ambivalent definition of synchrophasor phase angle depending on both fundamental frequency and phase [52, 105]. Therefore, the same damped oscillation is noticeable in TVE

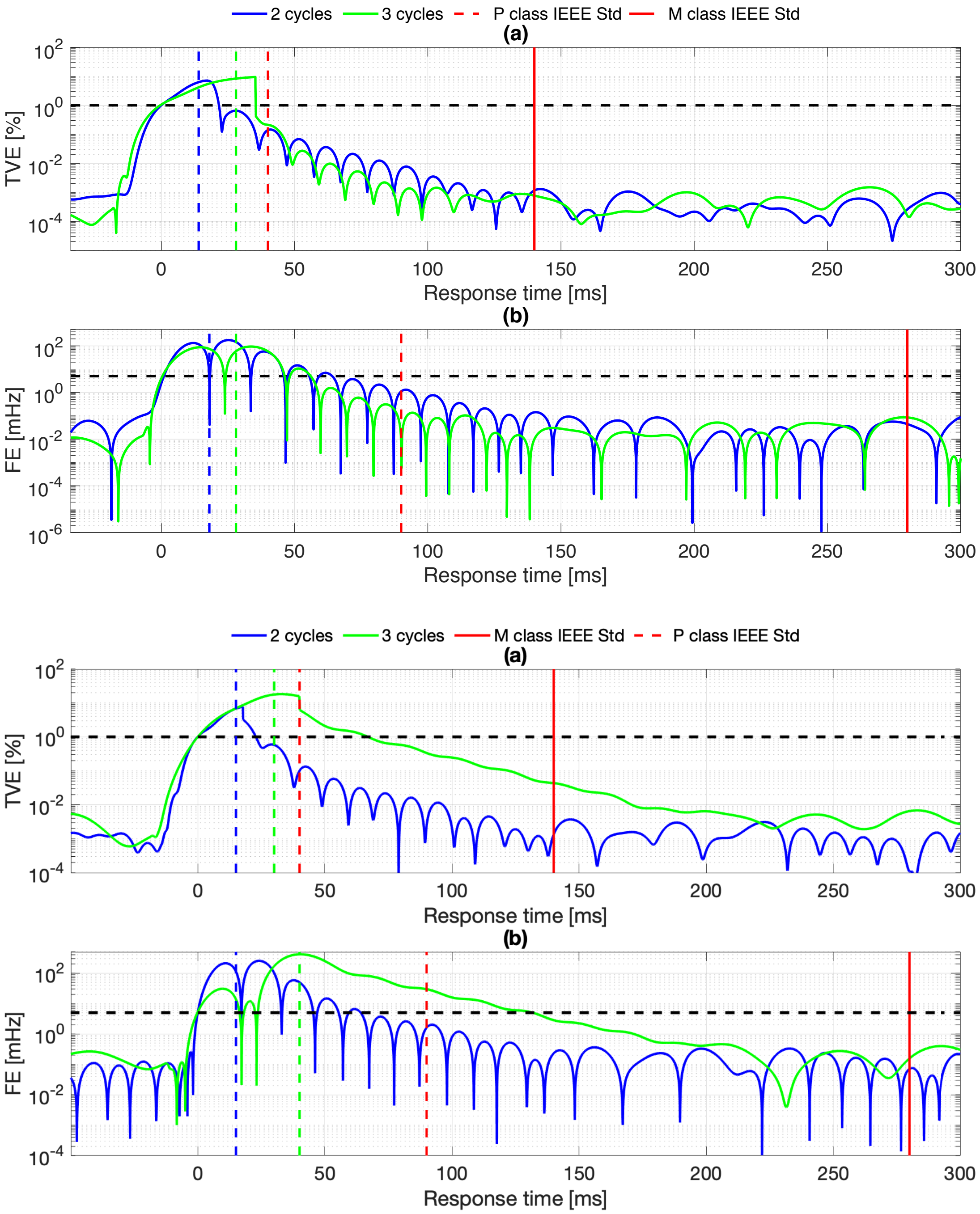

Figure 4.12 – Compliance with respect to positive amplitude (top) and phase (bottom) step signals: TVE (a) and FE (b) as a function of the response time with 2 (blue) and 3 cycles (green) window. The dashed and solid red lines represent the IEEE Std. C37.118 performance requirements for P- and M-class. Time $t = 0$ corresponds to the instant when the measurement leaves the accuracy limit, to which the curves for the two windows are aligned. The vertical dashed lines indicate the instant when the step change is applied; the vertical dashed and solid red lines indicate the response time limits for P- and M-class, respectively. Similar results hold for negative step test.

Table 4.5 – HT-IpDFT Computational Complexity

		Parameter	**Value**
		Q	≤100
		K	8 (2 cycles) 11 (3 cycles)

	$+\|-\|\times$	$:\|exp\|sin\|\angle$	$funct$
(A) Dirichlet kernel	10	8	
(B) Hanning window	7	0	3 × (A)
(C) Image compensation	5	1	K × (B)
(D) 3p-IpDFT	20	6	
(E) 3p-IpDFT (+ comp)	21	6	
HT-IpDFT (single tone)	3 K + 4	0	(C) + (D)
HT-IpDFT (OOBI com.)	3 K + 7	0	(2Q+2) × (C) + (Q+1) × (D) + Q × (E)

and FE trends in the bottom plot in Fig. 4.12, whereas in the amplitude step test, this trend was restricted to only the TVE.

4.4.3 Computational Complexity

In order to assess the practicality of a future integration of HT-IpDFT into an embedded hardware device, the computational complexity of the proposed algorithm is evaluated. In this context, Table 4.5 summarizes the number of arithmetic operations required to produce each step of the HT-IpDFT, in case the energy ratio threshold for the iterative compensation is exceeded or not. Nevertheless, it is worth pointing out that the main barrier to the actual implementation of the proposed algorithm is represented by the filtering stage. The latter should account for a dedicated design to make the filtering efficient, fast and computationally effective.

Taking as reference a Field Programmable Gate Array (FPGA)-based device, a differentiation between simple (like additions, multiplications) and complex operations (like exponential, trigonometric operators) is carried out. Also, some function calls are defined (like the call of a sub-routine or an algorithm). In Table 4.5, the operation count is parameterized with respect to the number of considered DFT bins K, and the iteration number Q, according to the values presented in Table 4.2.

4.5 Discussion

The Chapter presented a synchrophasor estimation algorithm based on the joint application of the HT and IpDFT, called HT-IpDFT. By considering the analytic signal representation, the HT is able to mitigate the spectral leakage caused by the negative frequency components and thus to achieve accurate synchrophasor measurements while reducing the window length. In this way, it is possible to produce high-accuracy estimates of synchrophasor, frequency, and ROCOF associated to the fundamental component, as well as minimizing the measurement reporting latency.

The Chapter further described the theoretical principles and the implementation details of the proposed HT-IpDFT algorithm, providing a preliminary analysis of its computational requirements and discussing the most suitable setting of the algorithm parameters. Then, its metrological performance in terms of estimation accuracy and response time in all the test conditions indicated by the IEEE Std. C37.118 was characterized. The proposed IpDFT-based approach guarantees the compliance with all the IEEE Std. C37.118 requirements for both P and M-class, with the only exception of harmonic distortion (1%) and phase step tests.

Based on the obtained results, the employment of Hilbert Transform represents a promising solution for synchrophasor estimation, as it allows for a relaxation of the reporting latency constraints if compared to the i-IpDFT presented in Chapter 3. However, from the practical implementation point of view, the filtering stage may represent a barrier in terms of computational complexity.

5 Advanced Calibrator for the Metrological Characterization of PMUs

Type-testing of highly accurate PMUs is particularly challenging, as the calibration platform should be characterized by even lower levels of uncertainty. Indeed, since state-of-the-art synchrophasor estimators exhibit TVEs in the order of $0.0x\%$*, PMU calibrators should provide the reference synchrophasors with TVE limited to* $0.00x\%$*. In this context, the Chapter describes the hardware and software architecture of an advanced PMU validation system that successfully meets this requirement. The calibrator consists of a forward path, used to generate the reference waveforms, and a return path, introduced to re-acquire the waveforms and estimate their reference parameters through a non-linear least-squares fitting algorithm. The two actions are suitably synchronized to a highly stable timing source. The uncertainty contributions due to generation, acquisition, and synchronization are experimentally characterized. Furthermore, the fitting algorithm solution accuracy, robustness, and uniqueness are analyzed within the whole range of tests defined by the IEEE Std. C37.118 as well as in off-standard test conditions.*

The Chapter includes results of publications [11, 12].

5.1 Introduction and State of the Art

The IEEE Std. C37.118 [19] indicates the accuracy requirements for a PMU operating in static and dynamic conditions in terms of Total Vector Error (TVE), Frequency Error (FE) and Rate-Of-Change-Of-Frequency Error (RFE). As for any other measurement device, compliance certification is performed by comparing the PMU under test against a reference system of values provided by a PMU calibrator. More specifically, the synchrophasors measured by the PMU under test are compared to reference synchrophasors computed by the PMU calibrator, whose accuracy is expected to be at least one order of magnitude better than the PMU under test. In this regard, the IEEE Guide C37.242 [86] and the test suite specification (TSS) for synchrophasor measurements [106] describe the details of test and calibration procedures.

The recent literature is proposing synchrophasor estimation algorithms characterized by a TVE in the order of $0.0x\%$ in steady-state test conditions [25]. For instance, two examples have been presented in the previous Chapters 3 and 4: considering signals affected by 80 dB of noise and a window length of 60 ms, the Iterative Interpolated DFT (i-IpDFT) and the Hilbert Transdorm IpDFT (HT-IpDFT) are characterized by a maximum TVE of $0.0x\%$ and $0.x\%$ in static and dynamic operating conditions, respectively. As a consequence, a rigorous metrological characterization of PMUs implementing those algorithms requires a validation system whose accuracy is at least one order of magnitude better. That is to say that the PMU calibrator should be characterized by a TVE in the order of $0.00x\%$ in steady-state test conditions and $0.0x\%$ in distorted or dynamic test conditions [107].

In this context, several versions of PMU calibrators have been recently developed by national metrological institutes [108, 109, 110, 111, 112, 113, 114, 115], research laboratories [116, 117, 118, 11, 12] and manufacturing companies [119, 120]. The reference grade is represented by the calibration systems of the National Institute of Standards and Technology (NIST), Washington, DC and of the Swiss Federal Institute of Metrology (METAS), Bern, CH. Indeed, these two prototypes are capable of performing the IEEE Std. C37.118 compliance verification with a TVE in the order of 0.05% in static test conditions, while the uncertainty on the synchrophasor phase angle is limited to 300 μrad. In general, the design of state-of-the-art PMU calibrators is well-established and consists of three main stages:

1. A generation stage that generates the test waveforms and feeds them to the PMUs under test;
2. An acquisition stage that simultaneously re-acquires the same test waveforms and processes them in order to define the reference synchrophasor, frequency and ROCOF;
3. A synchronization stage that triggers both the generation and acquisition stage, and guarantees that the calibrator estimates are aligned to the UTC.

Inevitably, each of the three stages introduces uncertainty contributions in the calibration procedure, whose sum results into the overall calibration uncertainty, that must be metrologically characterized.

Within this framework, the Chapter presents the hardware and software architecture of a PMU calibrator that is able to reproduce all the test conditions defined by the IEEE Std. C37.118, as well as user defined scenarios. The TVE associated to the reference synchrophasors is in the order of $0.00x\%$ in static and $0.0x\%$ in dynamic conditions. The calibrator consists of a forward path, to generate the reference waveforms, and a return path, to re-acquire the waveforms and estimate their reference parameters through a non-linear least-squares (NL-LSQ) fitting algorithm. The two actions are suitably synchronized to a highly stable timing source.

The Chapter is structured as follows. Section 5.2 presents the design principles of the hardware and software architecture of the proposed PMU calibrator. Section 5.3 studies the accuracy and the conditions for the uniqueness of the solution of the adopted NL-LSQ algorithm. Section 5.4 evaluates the power quality of the generated test waveforms and metrologically characterizes the magnitude, phase and frequency uncertainty associated with the reference synchrophasors. Section 5.5 reports the performance of the proposed PMU calibrator in the IEEE Std. C37.118 tests as well as in off-standard test conditions. Finally, Section 5.6 provides a discussion and some closing remarks.

5.2 Architecture of the proposed PMU Calibrator

The Section presents the hardware and software architecture of the proposed PMU calibrator, shown in Fig. 5.1. The validation system consists of the following elements:

i. The GPS-receiver guarantees the alignment with the absolute time reference;

ii. The rubidium atomic clock enhances the short-term variability of the internal time-base;

iii. The time-synchronization board receives from the atomic clock a pulse-per-second (PPS) and a 10 MHz trigger signal and employs them to align the different hardware modules;

iv. The generation board with three digital-to-analog converters (DACs) that are capable to reproduce three-phase waveforms compliant with IEEE Std. C37.118 specifications based on user defined parameters;

v. The acquisition board whose analog-to-digital converters (ADCs) re-acquire the waveforms fed to the PMU under test, and sends them to the waveform analysis unit;

vi. The waveform analysis unit processes the acquired samples via a NL-LSQ algorithm and extracts the *reference values* of synchrophasor, frequency and ROCOF;

vii. The voltage and current amplifier scales up the generation output range;

viii. N PMUs under test estimate the synchrophasors associated to the test waveforms and encapsulate synchrophasor measurements into C37.118 data frames;

ix. The telecom switch routes C37.118 data frames to the PDC;

x. The Phasor Data Concentrator (PDC) gathers the *measured values* of synchrophasor, frequency and ROCOF by the N PMUs under test;

xi. The error assessment unit compares the *measured* and the *reference* synchrophasors, and produces a test report containing the PMU calibration results for each PMU under test.

The validation system is based on the National Instruments PXI architecture (National Instruments, Austin, TX) [121]. The choice is motivated by the fact that PXI enables hardware multidevice synchronization thanks to dedicated timing and triggering technologies. Indeed, PXI architecture guarantees high precision shared timing and synchronization within the different modules, leading to highly accurate measurements.

The core element is represented by a NI PXI 1042Q chassis [122], coupled with three operating modules: the NI PXI-8110 embedded controller [123], the NI PXI-6682 synchronization board [124], and the NI PXI-6289 data acquisition (DAQ) board [125]. The internal trigger is provided by the FS725 rubidium oscillator (Stanford Research Systems, Sunnyvale, CA) [126], disciplined by the GPS 169-PCI Radio Clock board (Meinberg, Bad Pyrmont) [127]. This

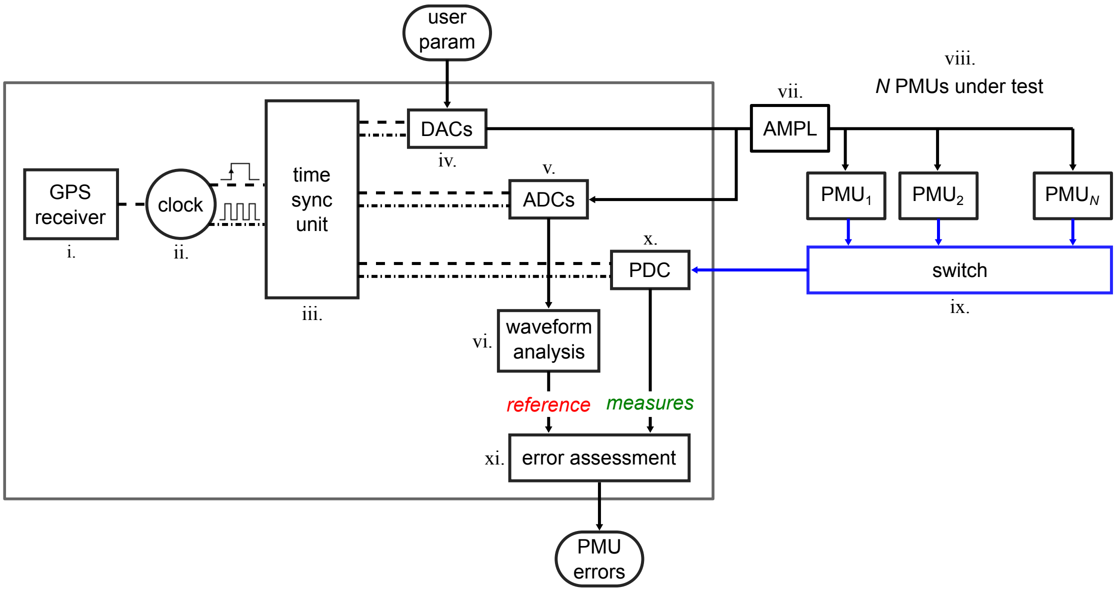

Figure 5.1 – Hardware architecture of the proposed validation system. Generation (DACs) and acquisition (ADCs) boards are aligned to UTC through the same synchronization board, that is disciplined by a GPS-receiver and a Rubidium atomic clock in order to enhance the stability of the internal time-base. The PMU calibrator integrates a PDC for PMU latency assessment.

peculiar synchronization scheme enables exploiting the advantages of both time-sources: the rubidium oscillator provides a reduced short-term variability on the 10 MHz time-base signal, whereas the GPS clock guarantees the alignment with respect to UTC and minimizes the long-term variability. The NI PXI-6289 DAQ board enables the generation and simultaneous re-acquisition of the three-phase waveforms provided to the PMU under test. In the generation stage, the PMU calibrator employs three 16-bits DACs with an output range of ±10 V and a sampling frequency of 100 kHz. The test waveforms are defined according to the IEEE Std. C37.118 specifications, but can also reproduce user-defined operating conditions. In the acquisition stage, the three-phase waveforms are digitized by a multiplexed 18-bits ADC with an input range of ±10 V and a sampling frequency of 25 kHz. According to the IEEE Std. C37.118 specifications, the typical voltage for testing PMUs is 70 Vrms [106]. In order to meet this requirement, the DAC output is amplified by means of an Omicron CMS 356 precision transformer (OMICRON electronics GmbH, Austria) [128], whose amplitude output is limited to 300 Vrms and 32 A.

The generated waveforms are fed to N PMUs under test that can be simultaneously calibrated. The PMUs independently estimate the synchrophasors' parameters based on their own synchrophasor estimation technique, window length and reporting time. Each PMU encapsulates the measured values into C37.118 data frames, and sends this information to the PDC through a common data switch. The PDC, whose details are given in Chapter 6 Section 6.2, gathers the estimates provided by the PMUs under test, and aligns them based on their time-stamp. In this way, it is possible to compare reference and measured values associated to the same time-stamp and accordingly determine the uncertainty associated to the devices under test. Moreover, the PDC can be used to evaluate the PMU measurement reporting latency and response time, as the PDC time-tags the data frames arrival time. The IEEE Std. C37.118 requires to quantify response time and reporting latency with an accuracy not lower than 2 ms and 100 μs, respectively. As soon as the waveform generation begins, a counter estimates the clock ticks elapsed until each packet arrives. In this way, the reporting latency can be characterized with the resolution of the internal time-base, i.e., 100 ns. It is worth mentioning that the communication network latency is negligible in the proposed PMU calibrator, being the packets streamed over a 0.5 meter Ethernet cable through a passive data switch. Therefore the difference between the data frame arrival time and the data frame time stamp represents the PMU measurement reporting latency.

5.3 Non-linear Least-Squares for Reference Synchrophasor Estimation

This Section describes the proposed non-linear least-squares algorithm used to estimated the reference synchrophasors in the calibration architecture. The solution uniqueness is studied in Section 5.3.2, and the dependence upon the algorithms parameters in Section 5.3.3. The analysis is conducted on simulated and real waveforms, respectively.

5.3.1 Reference Synchrophasor Estimation Algorithm

In the proposed architecture, a non-linear least-squares (NL-LSQ) fitting algorithm is employed to process the acquired waveform and determine the reference synchrophasors. The proposed PMU calibrator considers the mathematical model of a generic time-variant noiseless power signal affected by disturbances, defined as follows:

$$x(t) = A_0(1+\varepsilon_A(t)) \cdot \cos(2\pi f_0 t + \varphi_0 + \varepsilon_\varphi(t)) + \eta(t) \tag{5.1}$$

where A_0, f_0 and φ_0 are the amplitude, frequency and initial phase of the fundamental component, $\varepsilon_A(t)$ and $\varepsilon_\varphi(t)$ account for amplitude and phase modulations, and $\eta(t)$ is the contribution of harmonic or inter-harmonic components or transient events not related to the fundamental component. Such signal model can reproduce any test condition of the IEEE Std. C37.118, as well as other realistic operating conditions, like transient phenomena.

During the validation process, the user sets the parameters in (5.1) to reproduce the desired test conditions. Along with all the values, the user sets the fundamental component parameters:

$$\mathscr{P} = \{A_0, f_0, \varphi_0\} \tag{5.2}$$

Then, the system generates the corresponding waveforms, feeds them to one or more devices under test and simultaneously re-acquires a discrete time-series of samples, defined as follows:

$$x[n] := \{x(t) + \rho(t) \quad | \quad t = nT_s,\, n = [1, \dots N_m] \in \mathbb{N}\} \tag{5.3}$$

where N_m is the number of samples that compose $x[n]$, $\rho(t)$ accounts for wide-band disturbances (e.g., additive uncorrelated noise) and T_s is the sampling step.

Given $x[n]$, the PMU calibrator estimates the signal parameters triplet:

$$\hat{\mathscr{P}} = \{\hat{A}_0, \hat{f}_0, \hat{\varphi}_0\} \tag{5.4}$$

by solving the following NL-LSQ problem:

$$\text{argmin}_{\hat{\mathscr{P}}} \|x[n] - \hat{x}[n]\|_2^2 \qquad \text{s.t.} \qquad \hat{\mathscr{P}} \in \mathscr{S} \tag{5.5}$$

where $\hat{x}[n]$ is the time-series of the power signal reconstructed from the solution $\hat{\mathscr{P}}$, and $\mathscr{S}$ defines a specific region of feasible values for A_0, f_0 and φ_0. Based on these results, the synchrophasor associated to the fundamental component is defined as:

$$X(t) = A_s e^{j\Phi_s}, \qquad A_s = \frac{\hat{A}_0}{\sqrt{2}}, \qquad \Phi_s = 2\pi \hat{f}_0 t + \hat{\varphi}_0 \tag{5.6}$$

where A_s is equal to the root-mean-squared (RMS) magnitude, and Φ_s is the synchrophasor phase angle that accounts for both fundamental frequency and initial phase. Such reference synchrophasor is compared with the output of the PMU under test.

The calibrator accuracy is assessed by comparing the estimated reference synchrophasors $\hat{\mathscr{P}}$ with respect to the ideal true synchrophasors:

$$\mathscr{P}^{id} = \{A_0^{id}, f_0^{id}, \varphi_0^{id}\} \tag{5.7}$$

In steady-state conditions, $\mathscr{P}^{id}$ can be inferred by the measurements provided by high-accuracy hardware instrumentation, i.e., a multimeter for the reference amplitude and a time counter for the reference phase and frequency. In non-sinusoidal tests, the accuracy level of the hardware instrumentation is no more guaranteed, therefore, the estimated reference values are compared with the parameters set by the user and included in the ideal mathematical model $\mathscr{P}$.

The objective function defined in (5.5) is strictly non-convex, so it cannot provide a closed-form solution and presents multiple minima. In order to overcome this limitation, the problem is solved through an iterative optimization procedure based on the well-known Levenberg-Marquardt algorithm [129], that is characterized by noticeable accuracy provided that the initial guess is precise enough. In calibration context, the generated waveform model is predefined for each test and the nominal waveform parameters are known a priori. Therefore, it is possible to take advantage of this knowledge and to use the entire waveform model as initial condition, resulting in a very accurate estimation algorithm. It is worth pointing out that the proposed NL-LSQ algorithm introduces a single constraint: as the cardinality of $\hat{\mathscr{P}}$ is equal to three, $x[n]$ must consist of at least three samples.

Starting from an initial guess $\mathscr{P}^*$, the estimated values $\hat{\mathscr{P}}$ are iteratively updated solving (5.5) until the energy of the residual is comparable with the expected noise level. By varying the initial guess $\mathscr{P}^*$, the optimization procedure might produce different solutions. In the context of PMU calibration, the initial guess can be trivially set equal to the values set by the user $\mathscr{P}$.

5.3.2 Solution Uniqueness

A thorough study of the objective function enables the definition of a specific range of values for the initial guess $\mathscr{P}^*$ which ensures the solution uniqueness. This preliminary analysis is performed on simulated waveforms in nominal steady-state conditions, but similar results hold for all the test conditions defined by the IEEE Std. C37.118. Let us consider a time-series:

$$x[n] = A_0 \cdot \cos(2\pi f_0 n T_s + \varphi_0) \tag{5.8}$$

Let us assume the amplitude equal to 1 p.u., the instantaneous frequency 50 Hz, and the initial phase 0 rad. A sampling frequency of 5 kS/s is adopted, and the observation interval length consists of three cycles at the nominal frequency, i.e., 60 ms at 50 Hz. Equation (5.5) is solved numerically while varying $\mathscr{P}^*$ in a plausible range of the parameters space, close to the ideal values $\mathscr{P}^{id} = \{1, 50, 0\}$, that in a simulated environment are known a priori. In particular, A_0^* is varied in the range [0.8, 1.2] p.u., f_0^* in the range [45, 55] Hz, and φ_0^* around $\pm\pi/2$ rad.

The influence of $\mathscr{P}^*$ on the solution of the NL-LSQ algorithm is studied through a Monte Carlo analysis. In particular, the combined effect of the three initial guess values A_0^*, f_0^* and φ_0^* on the solution convergence to the ideal values $\mathscr{P}^{id}$ is studied. For each parameter, the range is divided in 21 uniformly spaced values. Then, the Monte Carlo analysis is performed on a total of 9261 possible combinations of initial guess, and the optimization problem is solved for each of them. A trial is considered successful if the the solution $\hat{\mathscr{P}}$ deviates from the ideal $\mathscr{P}^{id}$ of less then 0.001%. According to this success criterion, as shown in Fig. 5.2, the convergence area is limited between 0.9 to 1.1 p.u. in terms of A_s and between $\pi/2$ and $3/2\pi$ rad in terms of Φ_s, that corresponds to limiting f_0^* between 48 to 52 Hz and φ_0^* between $\pm\pi/4$. In this range a convergence probability equal to 99.82% is determined, with a confidence interval of 99%. In this regard, it is reasonable to assume that the fitting algorithm converges to the minimum $\hat{\mathscr{P}}^{min}$ when setting the user defined generation parameters $\mathscr{P}$, even if the hardware generation stage introduces a non negligible uncertainty on the initial guess $\mathscr{P}^*$.

5.3.3 Dependence on Algorithm Parameters

This Section analyses the influence on the solution accuracy of the algorithm parameters, i.e., the observation interval length N_m, the generation rate F_{DAC} and the acquisition rate F_{ADC}.

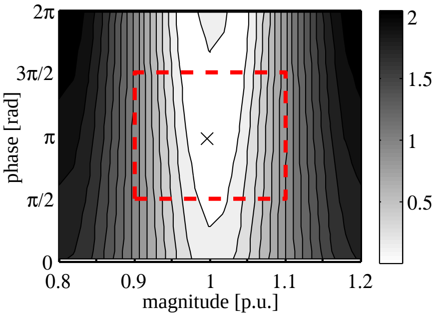

Figure 5.2 – Objective function trend. Within the assumed variation range for the initial guess $\mathscr{P}^*$ (red rectangle), the optimization problem proves to be nearly convex, and the global minimum $\hat{\mathscr{P}}^{min}$ (cross) is the best possible approximation of $\mathscr{P}^{id}$.

Table 5.1 – Magnitude (MU) and phase uncertainty (PU) while varying the observation interval

T [ms]	N_m	**MU [V]**		**PU [rad]**		**TVE [%]**
		μ	σ	μ	σ	
60	6000	$-1.82 \cdot 10^{-4}$	$1.85 \cdot 10^{-6}$	$-3.14 \cdot 10^{-3}$	$1.93 \cdot 10^{-7}$	$9.27 \cdot 10^{-5}$
100	10000	$-1.82 \cdot 10^{-4}$	$1.47 \cdot 10^{-6}$	$-3.14 \cdot 10^{-3}$	$1.49 \cdot 10^{-7}$	$6.61 \cdot 10^{-5}$
200	20000	$-1.81 \cdot 10^{-4}$	$1.05 \cdot 10^{-6}$	$-3.14 \cdot 10^{-3}$	$1.09 \cdot 10^{-7}$	$4.77 \cdot 10^{-5}$
1000	100000	$-1.81 \cdot 10^{-4}$	$6.02 \cdot 10^{-7}$	$-3.14 \cdot 10^{-3}$	$4.45 \cdot 10^{-8}$	$2.46 \cdot 10^{-5}$

Observation interval length

Given the acquisition rate F_{ADC}, the observation interval length considered by the NL-LSQ algorithm determines the number of analyzed samples N_m. For this analysis, let us consider a single-tone signal in steady-state conditions at a sampling frequency of 100 kS/s, that is generated and simultaneously re-acquired. The signal consists of a fundamental component whose amplitude, frequency and initial phase are equal to 9 V, 50 Hz and 0 rad, respectively. Four different values of N_m are considered, i.e., 6000, 10000, 20000 and 100000, that correspond to 3, 5, 10 and 50 cycles of a nominal fundamental component at 50 Hz. The test length depends on N_m, and is scaled in order to account for 248 consecutive observation intervals, partially overlapped to reproduce a reporting rate equal to 50 fps. For each interval, the NL-LSQ estimates the reference synchrophasors $\hat{\mathscr{P}}$.

Table 5.1 reports the estimation uncertainty associated to magnitude A_s (MU) and phase Φ_s (PU) in terms of mean μ and standard deviation σ. The worst case TVE associated to the NL-LSQ algorithm is computed by considering a conservative error range of $\pm 3\sigma$ on both synchrophasor magnitude and phase. As expected, the TVE decreases as the observation interval length increases following a $1/\sqrt{N_m}$ trend [130]. In practice, the IEEE Std. C37.118 does not impose any constraint on response time or computational load of the PMU calibrator. Nevertheless, in the following, an observation interval of 60 ms is considered, since it is a common value adopted by PMUs and still ensures a TVE lower than 10^{-4}%.

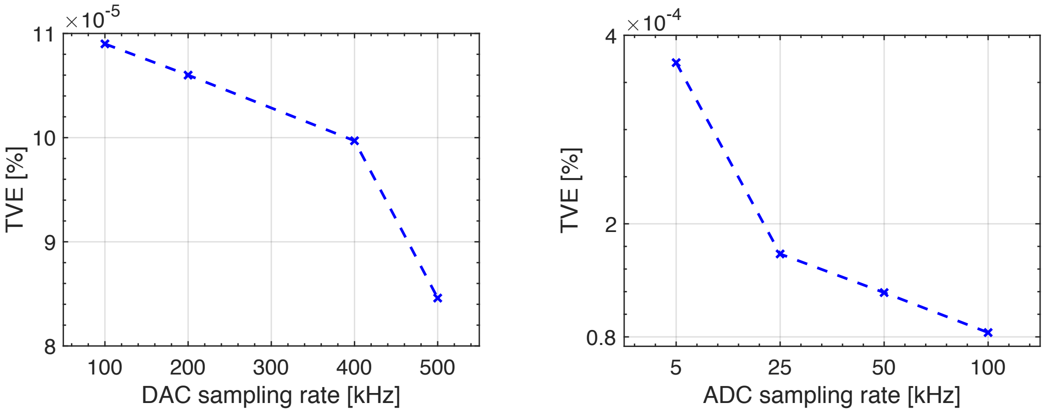

(a) TVE as a function of the DAC sampling rate. (b) TVE as a function a of the ADC sampling rate.

Figure 5.3 – TVE while varying generation and acquisition parameters.

Generation and re-acquisition stage

The PMU calibrator can generate the reference waveforms up to the maximum rate of 500 kS/s, enabling a better approximation of a nearly continuous-time waveform. Since no reconstruction filter is employed, the distortion introduced by the DAC stage is studied through a zero-order hold model. In order to evaluate how the generation rate F_{DAC} affects the solution accuracy, the generation rate is varied in the range [100, 500] kHz, whereas the observation interval length and acquisition rate F_{ADC} are fixed to 60 ms and 100 kHz, respectively. As shown in Fig. 5.3a, at the maximum generation rate, F_{DAC} = 500 kS/s, the magnitude attenuation is 0.01 ppm at 50 Hz, resulting in a nearly negligible contribution to overall uncertainty.

In a similar way, the PMU calibrator re-acquires the reference waveforms up to the maximum rate of 100 kS/s. As shown in Fig. 5.3b, the worst case TVE decreases as F_{ADC} increases in the range [5, 100] kS/s, resulting in a TVE of $9 \cdot 10^{-5}$ at 100 kS/s (in accordance with Table 5.1). This proves that the actual bottleneck for the solution accuracy is represented by the acquisition stage, whereas the generation stage (if synchronous with the fundamental frequency) provides a negligible uncertainty contribution.

5.4 Metrological Characterization in Steady-State Conditions

This Section provides a rigorous metrological characterization of the test waveforms in steady-state conditions. First, the power quality is analyzed, in terms of noise and distortion (Section 5.4.1) and the frequency response of the adopted amplifier in characterized (Section 5.4.2). Then, the test waveform accuracy is assessed in terms of magnitude, phase and frequency uncertainty (Section 5.4.3). Finally, the steadiness of the estimated reference values due to synchronization issues is evaluated (Section 5.4.4).

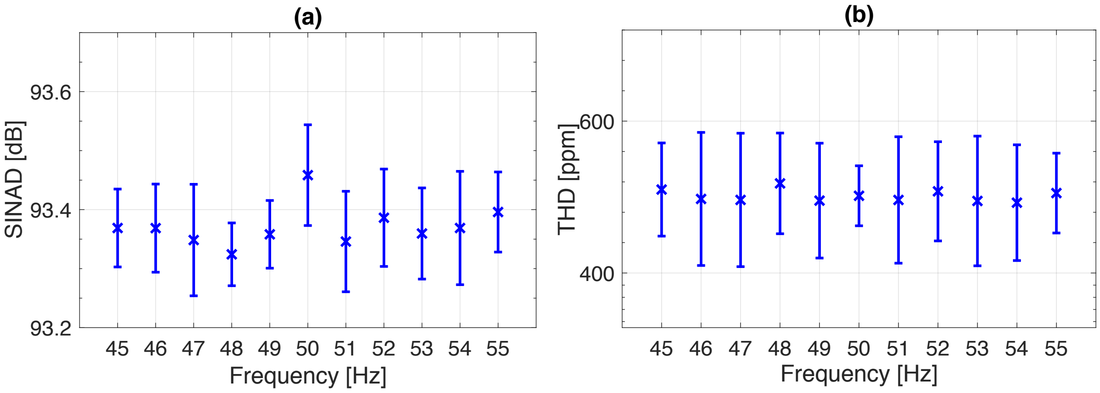

Figure 5.4 – SINAD (a) and THD (b) as a function of the fundamental frequency. The cross represents the mean value μ, whereas the bold line determines a confidence interval of three standard deviations $\pm 3\sigma$.

5.4.1 Power quality of the generated waveforms

Non-idealities inherent in DAC and ADC stages introduce a non-negligible amount of noise and distortion that, in general, may limit the accuracy of reference values estimation. This contribution cannot be included in the model (5.1), but can be experimentally quantified with sufficient accuracy using the acquired waveforms. In particular, this Section characterizes the uncorrelated noise in terms of signal-to-noise and distortion (SINAD) ratio and evaluates the effect of narrow-band components by computing the total harmonic distortion (THD) index over the first 50 harmonics. The Section further verifies that the generated test waveforms are perfectly balanced three-phases signals.

For this analysis, let us consider a test waveform in steady-state conditions, where the signal amplitude and initial phase are set to 9 V and 0 rad, respectively, whereas the signal frequency varies in the range [45, 55] Hz. Generation and acquisition stage adopt a sampling frequency of 100 and 25 kHz, respectively. For each test, a sample record of 5 s is acquired and is divided into 248 observation intervals of 60 ms, partially overlapped to achieve a reporting rate of 50 fps. Then, the SINAD and the THD associated to each observation interval are determined, and a statistical description of these two indices in terms of mean μ and confidence interval of three standard deviations 3σ is provided. In particular, once detected the spectrum highest peak, the Enhanced Interpolated DFT (e-IpDFT) algorithm estimates the fundamental frequency and amplitude (whose details are provided in Chapter 3, Section 3.2). The SINAD is defined as the ratio between the fundamental energy and the remainder signal energy, expressed in dB, whereas THD is the ratio between the RMS sum of the harmonic tones (up to 50th order) and the amplitude of the fundamental tone. At the same time, the symmetrical components' method is used to decompose the three-phase signal into its direct, inverse and homopolar sequence. For each 60 ms observation interval, the energy of inverse and homopolar sequences is normalized by the energy of corresponding direct sequence.

Table 5.2 – Power quality indices of the generated test waveforms in the IEEE Std. C37.118

Test	SINAD [dB]	SFDR [dB]	VUF [ppm]
Sign Freq	93.38	110.23	1.51
Harm Dist	20.04	19.96	3.11
OOBI	20.04	19.94	2.05
Meas Band	93.22	109.88	3.98
Freq Ramp	93.34	108.54	4.70
Step	93.33	109.36	2.54

As shown in Fig. 5.4, in the considered frequency range, SINAD keeps around 93.4 dB, which corresponds to an equivalent number of 15 bits, whereas THD varies between 4 and $6.5 \cdot 10^{-4}\%$. Both these experimental results confirm that the waveforms are affected by nearly negligible levels of additive noise and distortion. In this regard, it should be noticed that the IEEE Std. C37.118 requires THD and possible distortions coming from interfering components not to overcome 0.02% [19].

As regards the unbalance associated to inverse and homopolar sequences has been quantified in some ppm of the direct sequence over the whole range [45, 55] Hz, whereas the EN Std. 50160 limits the unbalance ratio to 2% for distribution networks [131]. Accordingly, it is reasonable to say that the proposed system generates test waveforms that adequately approximate a balanced three-phase grid.

This power quality analysis is repeated in all the set conditions provided by the IEEE Std. C37.118. Specifically, for each test three performance indices are measured: the SINAD ratio to evaluate the incidence of noise and distortion, the spurious free dynamic range (SFDR) to determine the ratio between the RMS amplitude of the fundamental and the highest interfering component, and the voltage unbalance factor (VUF) to quantify the entity of the indirect sequence. As reported in Table 5.2, SINAD ratio keeps unaltered around 93 dB, except for harmonic and out-of-band distortion tests, where SINAD is equal to 20 dB due to the presence of an interfering component. As regards SFDR, in all the test conditions the index is equal to almost 110 dB, i.e., the noise floor is at least five order of magnitude lower than the fundamental component. Only in the presence of harmonic or out-of-band distortion, SFDR almost reaches 20 dB. Finally, the VUF analysis shows that the mean energy ratio between inverse and direct sequence does not exceed 5 ppm. It is thus reasonable to say that the proposed system satisfies the IEEE Std. C37.118 requirements in terms of power quality of the generated waveforms, in both static and dynamic test conditions.

5.4.2 Frequency response of the amplifier

The accuracy and stability of the amplifier stage still represents an open issue for power system applications and their uncertainty contributions might largely exceed the target performance

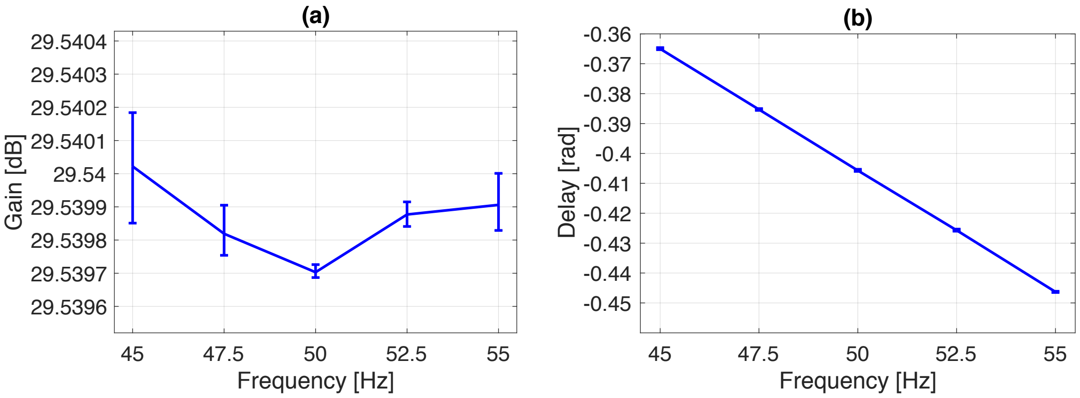

Figure 5.5 – Frequency response of the adopted amplifier in terms of magnitude gain and phase delay in dB and rad, respectively. The vertical bar represents the measurement variability (ranging from minimum to maximum value) over an observation interval of 2 s.

[132, 133]. Nevertheless, their frequency response can be carefully characterized and compensated, in order to mitigate the propagation of uncertainty to the final estimation of the reference values. To this end, Fig. 5.5 presents the magnitude and phase response and the relative uncertainty variation range as a function of fundamental frequency for the adopted amplifier. For this analysis, the uncertainty is quantified as the interval between the minimum and maximum measured value, as shown by the vertical bars in Fig. 5.5. Based on the knowledge of this response function, it is possible to suitably define the waveform parameters in order to obtain the desired amplifier output in terms of waveform amplitude and phase. In particular, it is interesting to observe that the magnitude gain is nearly constant with a variation range of 0.0002 dB, whereas the phase response presents a linear trend that can be modeled and compensated as a first-order filter response.

5.4.3 Accuracy of the generated waveforms

In this Section the reference estimates $\hat{\mathscr{P}}$ resulting from the NL-LSQ processing on the re-acquired waveforms are compared with the ideal values $\mathscr{P}^{id}$ provided by high-accuracy hardware instrumentation. Based on these ground-truth values, the proposed analysis aims at identifying the cumulative effect of generation, acquisition and processing stages on the final estimation uncertainty of the synchrophasors. It should be noticed that the present analysis considers only steady-state test signals, in the absence of interfering tones, as the performance of hardware instrumentation is no more guaranteed otherwise [126, 134, 135]. Nevertheless, it is reasonable to say that similar results are obtained in the other test conditions, as the generation procedure is exactly the same and does not depend on the model of the test signal.

For each parameter configuration, a three-phase time-series with an overall duration of 5 s is acquired, and divide it into 248 consecutive observation intervals of 60 ms, partially overlapped by 40 ms in order to reproduce a reporting rate equal to 50 fps. Generation and acquisition stage adopt a sampling frequency of 100 and 25 kHz, respectively. Assuming a normal distribution, the discrepancy between estimated $\hat{\mathscr{P}}$ and ideal values $\mathscr{P}^{id}$ is described in terms of mean μ and standard deviation 3σ. The first one constitutes a systematic contribution and can be compensated in the system's software, whereas the second one is a random contribution and represents the actual uncertainty of the measurement process. At the moment of comparing the PMU estimates with the calibrator reference values, the systematic errors are subtracted by the PMU errors as they are fixed offsets.

Magnitude Uncertainty

The uncertainty on the synchrophasor magnitude is evaluated by comparing the system estimates, with the measurements provided by the 3458A Digital Multimeter (Keysight Technologies, Santa Rosa, CA) with a resolution of 8.5 digits, corresponding to an absolute uncertainty of ± 1 μV. As shown in Fig. 5.6, the instrument is triggered by a clock signal derived from the same rubidium atomic clock as the PMU calibrator. The AC Voltage modality is adopted with synchronous sub-sampling technique. An input range of ± 10 V and an acquisition time window of 1 s are adopted, and the measurement is repeated 5 times. In this way, a single measurement is produced for each test but the effect of time jitter and measurement noise is reduced, and guaranteeing an accuracy of 10 ppm in the frequency range from 1 Hz to 10 MHz [136, 134].

In Fig. 5.7, the fundamental amplitude and initial phase are set equal to their nominal values, i.e. 9 V and 0 rad, whereas the fundamental frequency is varied from 45 to 55 Hz with an incremental step of 1 Hz. In (a) the mean error that accounts for the constant uncertainty contribution is shown, whereas in (b) the 3σ range as representative of the random uncertainty contribution is considered. In the observed frequency range, the MU keeps rather stable and does not exceed 12 μV. The accuracy performance slightly degrades, as the fundamental frequency decreases, e.g. 45 Hz. This is due to the fact that a lower fundamental frequency corresponds to a lower number of periods in the fixed observation interval of 60 ms, resulting in a degradation of the NL-LSQ accuracy. By varying the signal amplitude, Fig. 5.8 shows that the most accurate estimates are obtained when the signal covers the entire input range of the ADC stage, nevertheless, the percentage MU does not exceed $1 \cdot 10^{-4}$% even when operating with only 10% of the available 18 bits (i.e. $A = 0.9$ V). In the signal model (5.1), the fundamental frequency and initial phase are fixed to 50 Hz and 0 rad, respectively, and three amplitude values are considered, namely 9, 4.5 and 0.9 V, that correspond to 100, 50 and 10% of the nominal value.

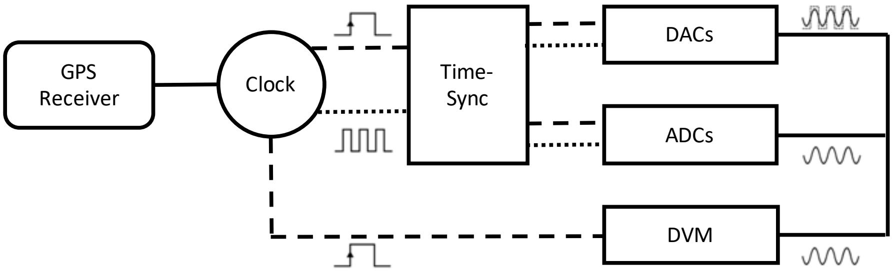

Figure 5.6 – Measurement setup for the assessment of magnitude uncertainty. The generated waveforms are simultaneously sent to the ADC stage and to the digital multimeter (DVM). The synchronization between the two measurement chains is guaranteed by the same trigger provided by the atomic clock.

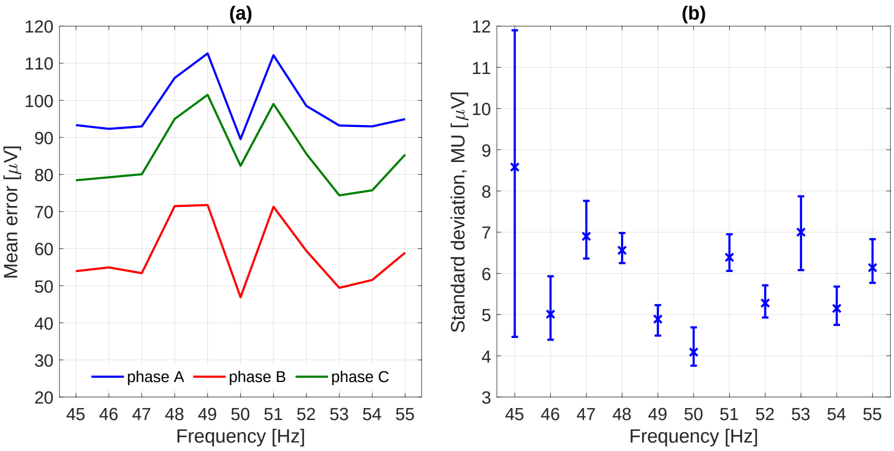

Figure 5.7 – Magnitude estimation error as a function of the fundamental frequency for the three phases, in terms of mean (a) and standard deviation (b). In (b) the cross represents the mean standard deviation among the three phases, whereas the bold line represents the standard deviation variability, ranging from minimum to maximum value.

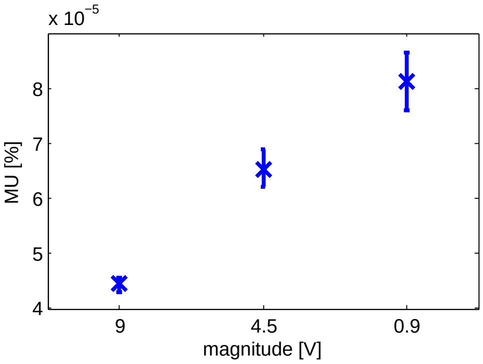

Figure 5.8 – Normalized magnitude uncertainty as a function of the fundamental amplitude. The cross represents the mean standard deviation among the three phases, whereas the bold line represents the standard deviation variability, ranging from minimum to maximum value.

Phase Uncertainty

Given the synchrophasor model in (5.6), the phase angle Φ_s accounts for both fundamental frequency and initial phase. In this context, a deviation from the nominal system frequency produces a rotation of the synchrophasor associated to the fundamental component, and can be interpreted as a contribution to the overall phase angle. As a consequence, the definition of the ground-truth value of the synchrophasor phase angle requires the simultaneous measurement of two quantities, i.e. the fundamental frequency and the initial phase. The adopted measurement test-bed is equipped with a time-counter device capable of measuring both frequency and phase, but only one at time. For this reason, in defining the ground-truth Φ_s, a two-step approach is needed. First, the fundamental frequency is measured through the SR620 counter (Stanford Research Systems, Sunnyvale, CA), with an acquisition time window of 1 s, and an accuracy in the order of 10 nHz [135]. As in the previous paragraph, the synchronization between the validation system and the analog instrument is guaranteed by the trigger signal provided by the atomic clock (see Fig. 5.9). Then, the ground-truth value of fundamental initial phase is defined by processing the same acquired waveform with the e-IpDFT algorithm, over the entire waveform duration of 5 s. By limiting the uncertainty contributions due to spectral leakage, the algorithm is expected to provide an accuracy in the order of hundreds nrad given a SINAD around 90 dB [56]. The proposed approach is repeated separately on each phase of the generated three-phase waveform.

In the first case, the fundamental amplitude and initial phase are fixed to 9 V and 0 rad, respectively, and the fundamental frequency is varied in the range [45, 55] Hz, with an incremental step of 1 Hz. In this context, Fig. 5.10 shows the mean and standard deviation of the PU, that exhibits a rather symmetrical trend: the uncertainty increases as the fundamental frequency deviates from its nominal value. In the considered frequency range, the worst-case performance corresponds to a maximum PU of 0.8 μ rad. By varying the signal initial phase in the range [0, π] rad, Fig. 5.11 shows that PU variations are almost negligible and limited to 0.5 μrad.

Frequency and ROCOF Uncertainty

The stability of the generated waveform frequency is assessed by comparing the system estimates with the measurements provided by the SR620 counter. This test is performed by generating single-tone steady state signals characterized by frequencies in the range [45, 55] Hz. In all the test conditions, the measured frequency deviates from the value set by the user by some tens of nHz, i.e., comparable with the instrument resolution. This experimental validation, enables the relaxation of one of the constraints of the optimization problem (5.1). Indeed, being the generated frequency so close to the value set by the user, it is reasonable to assume the fundamental frequency as a known parameters of the the problem.

The frequency associated to the fundamental component can be also defined as the first time-derivative of the synchrophasor phase angle. Therefore, based on the PU characterization, the

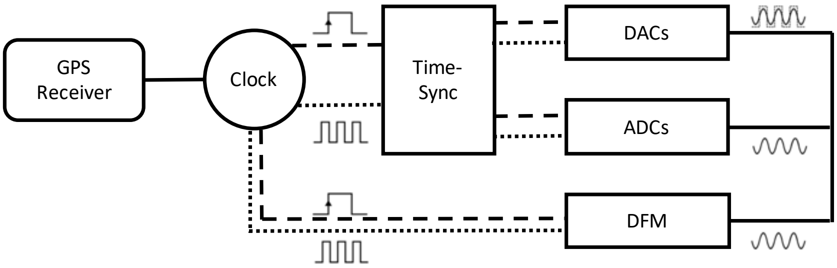

Figure 5.9 – Measurement setup for the assessment of phase and frequency uncertainty. The generated waveforms are simultaneously sent to the ADC stage and to the counter (DFM). The synchronization between the two measurement chains is guaranteed by the same trigger provided by the atomic clock.

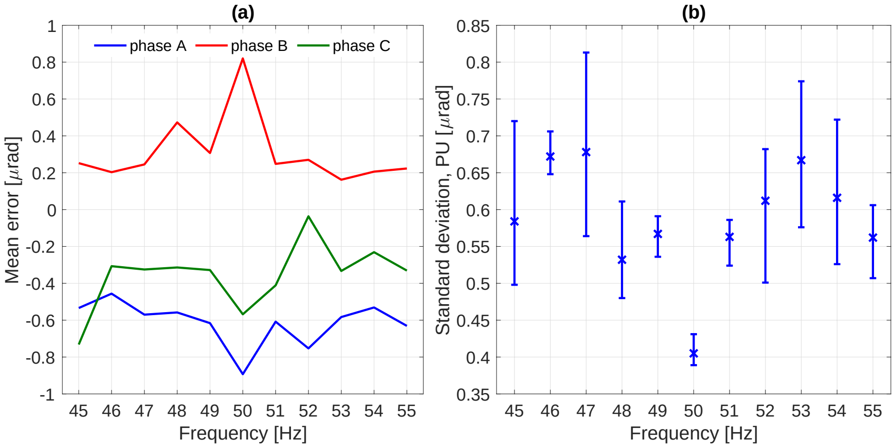

Figure 5.10 – Phase estimation error as a function of the fundamental frequency for the three phases, in terms of mean (a) and standard deviation (b). In (b) the cross represents the mean standard deviation among the three phases, whereas the bold line represents the standard deviation variability, ranging from minimum to maximum value.

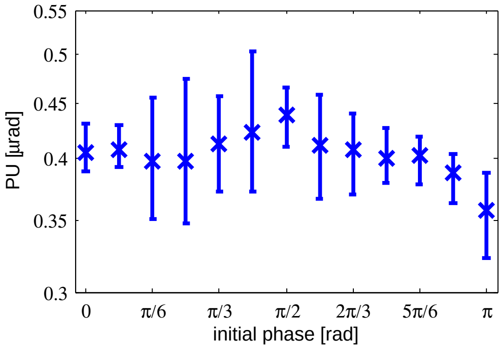

Figure 5.11 – Phase uncertainty as a function of the fundamental initial phase. The cross represents the mean value μ, whereas the bold line determines a confidence interval of three standard deviations $\pm 3\sigma$.

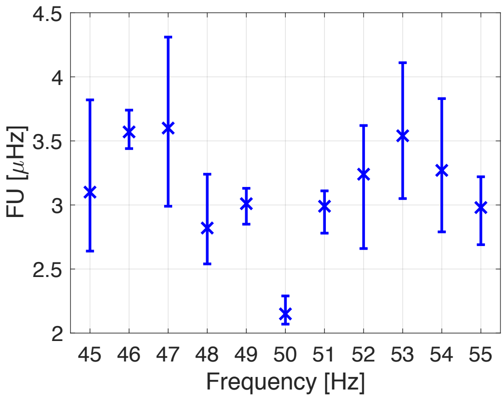

Figure 5.12 – Frequency uncertainty as a function of the fundamental frequency. The cross represents the mean standard deviation among the three phases, whereas the bold line represents the standard deviation variability, ranging from minimum to maximum value.

confidence interval for the estimation of the fundamental frequency can be evaluated. The synchrophasor phase angle depends on both fundamental frequency and initial phase. In order to provide a more conservative evaluation of this uncertainty contribution, the entire PU is considered as frequency uncertainty only (FU), whereas the initial phase error is assumed null. In this regard, Fig. 5.12 evaluates the FU as a function of the fundamental frequency. For this analysis, the amplitude and initial phase are set equal to 9 V and 0 rad, respectively, and the fundamental frequency is varied within the range [45, 55] Hz. At 50 Hz, the FU is limited to 2.3 μHz. In the rest of the range the trend is rather symmetric: the estimation accuracy degrades as the fundamental frequency deviates from its nominal value. The worst-case performance is obtained at 47 Hz, with FU nearly equal to 4.3 μHz.

The ROCOF uncertainty (RFU) directly descends from the FU. Coherently with the IEEE Std. C37.118 formulation, ROCOF is defined as the difference between two consecutive frequency estimates, divided by the reporting time (20 ms). In this context, the worst-case RFU can be computed as 2·FU/20 ms. In the considered frequency range, the worst-case RFU is equal to 0.22 mHz/s, whereas, a maximum uncertainty of 0.15 mHz/s is noticed at 50 Hz.

Total Vector Error

The combination of the ±3σ errors on both magnitude A_s and phase Φ_s, results into the worst case TVE provided by the calibrator. For this analysis, a three-phase waveform in steady-state test conditions is considered, by setting the fundamental amplitude and initial phase equal to their nominal values, 9 V and 0 rad, respectively, while varying the fundamental frequency from 45 to 55 Hz, with an incremental step of 1 Hz. As shown in Fig. 5.13, the worst-case TVE among the three phases does not exceed 5×10^{-4}%.

The same analysis is repeated in the entire spectral bandwidth associated to possible har-

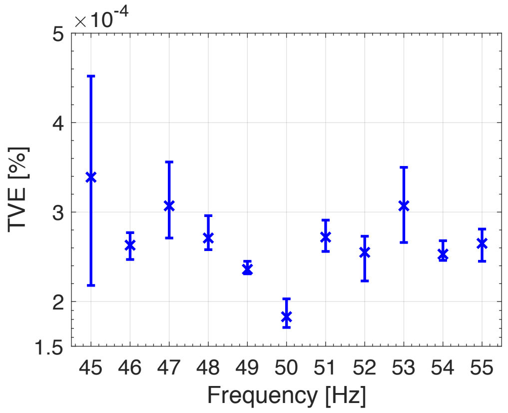

Figure 5.13 – TVE as a function of the frequency in the range provided for the fundamental component, i.e. from 45 to 55 H. The cross represents the mean standard deviation among the three phases, whereas the bold line represents the standard deviation variability, ranging from minimum to maximum value.

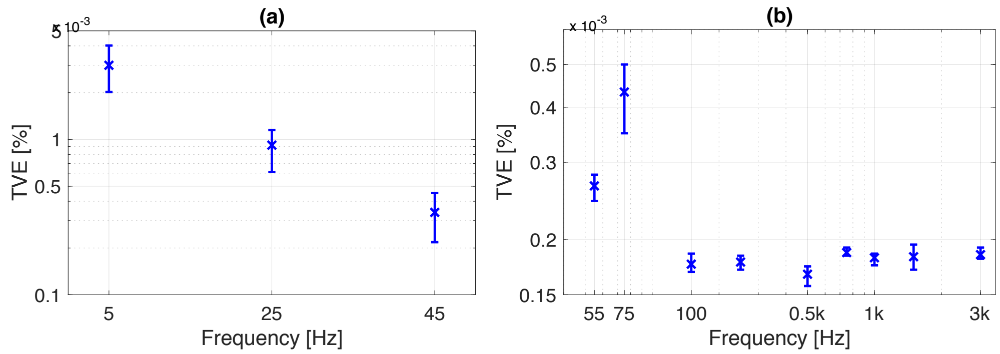

Figure 5.14 – TVE as a function of the frequency in the range provided for harmonic and interharmonic components, i.e. from 5 to 25 Hz (a) and from 75 to 3000 Hz (b). The cross represents the mean standard deviation among the three phases, whereas the bold line represents the standard deviation variability, ranging from minimum to maximum value.

monic and interharmonic disturbances, in order to take into account also distorted operating conditions. In this regard, Fig. 5.14 represent the worst-case TVE measured in the range [5, 25] and [75, 3000] Hz. In order to provide a term of comparison, in both the graphs the TVE associated to the nearest extreme of the fundamental frequency bandwidth [45, 55] is included. For frequencies higher than 75 Hz, the TVE is rather stable around 2×10^{-4}%, i.e. the same accuracy level measured at the nominal frequency of 50 Hz. At lower frequencies the perfromance degrades up to a worst-case TVE in the order of 5×10^{-3}%, due to the fact that lower frequency corresponds to lower number of periods in a given observation interval.

5.4.4 Stability issues

In the presence of repeated validations, an aspect to be considered is the consistency and steadiness of the estimated reference values. Some uncertainty sources might introduce uncompensated contributions and thus produce erroneous estimates of the reference magnitude and phase. In particular, this Section focuses on two synchronization issues: first, the atomic clock jitter that may increases the phase noise; second, the synchronization delay between generation and acquisition that results in imprecise definition of the reference initial phase.

Timing uncertainty

The internal timing reference is provided by the rubidium atomic clock, disciplined by the GPS receiver. On the one hand, the GPS receiver provides a PPS signal, characterized by a noticeable long-term stability, and guarantees the alignment with respect to UTC. On the other hand, the rubidium atomic clock provides a 10 MHz time-base signal, with reduced short-term variability, that can be used to synchronize all the modules connected to the PXI chassis. It is worth pointing out that the rubidium atomic clock derives the time-base signal directly from the PPS signal received from the GPS receiver. Thus, if considering observation interval lengths not lower than 1 s, the two signals can be assumed perfectly synchronized and locked in phase.

The long-term stability of the PPS signal has been evaluated at METAS laboratories, by comparing the PPS signal provided to the PXI with the UTC-CH. For this analysis, the SR620 counter is employed in time interval modality with an accuracy of 100 ps [135]: the PPS derived form UTC-CH starts the counter, while the PPS routed out by the PXI stops the counter. Fig. 5.15 presents the time deviation measured over an observation interval of 48 hours. An average deviation in the order of hundreds ns can be noticed, that represents a systematic contribution due to the length of the antenna cable (25 m) and can be compensated. Conversely, the standard deviation constitutes the actual contribution to the overall phase uncertainty. The PPS uncertainty is not larger than 12 ns, corresponding to an estimation error on the synchrophasor phase of 4 μrad considering a fundamental frequency of 50 Hz.

The short-term stability of the 10 MHz time-base signal has also been evaluated at METAS laboratories. The phase noise as a function of the frequency offset with respect to the signal carrier frequency has been measured. Fig. 5.16 compares three different configurations: the first one consists of the PXI in free-running mode (blue circles), in the second one the PXI time-base is disciplined by the GPS receiver only (red crosses), the third one considers the proposed hardware configuration, with the rubidium atomic clock, disciplined by the GPS receiver (green squares). It is interesting to observe how the employment of the GPS receiver only produces a reduced enhancement in the long-term stability. Conversely, the rubidium atomic clock guarantees a reduction of the phase noise by almost 30 dBc/Hz in the entire considered range.

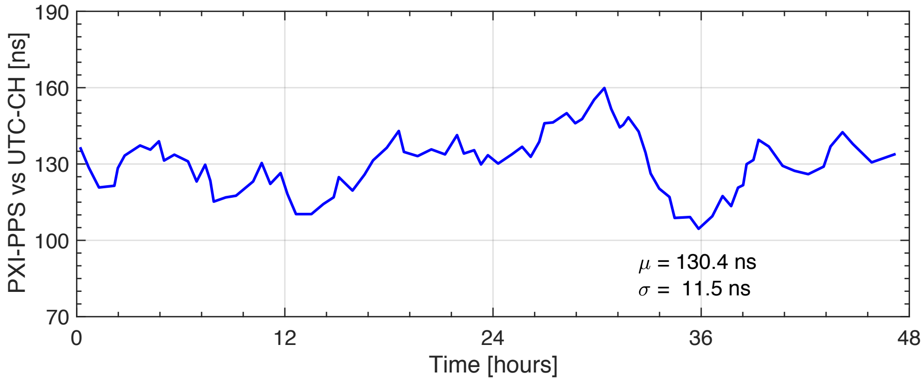

Figure 5.15 – Time deviation between the PPS signal provided to the PXI (PXI-PPS) and the PPS signal derived from UTC-CH over an observation interval of two days.

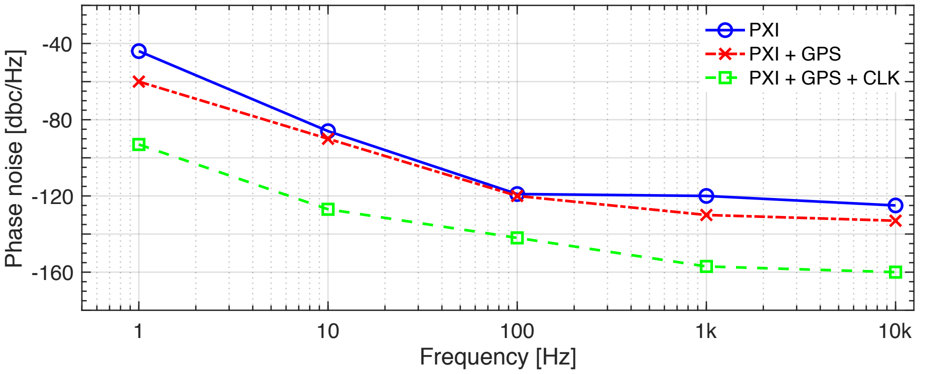

Figure 5.16 – Phase noise obtained with three different configurations: free-running PXI (blue), PXI disciplined by GPS receiver (red), PXI disciplined by atomic clock and GPS receiver (green).

Integrating the phase noise curve between 1 Hz to 20 MHz, we can also calculate the equivalent RMS phase jitter affecting the 10 MHz time-base signal. In the proposed hardware configuration, the employment of the rubidium atomic clock enables us to limit the jitter in the order of 1 ps, that corresponds to a phase uncertainty in the order of hundreds prad, thus negligible if compared with the PPS contribution.

Synchronization uncertainty

Within the proposed architecture, an imprecise internal synchronization of the hardware modules might be translated into a phase discrepancy between generated and acquired waveforms. Indeed, the internal time-base and the trigger signals are propagated in a non-ideal and non-deterministic way, that produces a non-negligible jitter between the PXI boards. In particular, the lack of synchronization between generation and acquisition stages produces an initial phase displacement between the waveform acquired and processed by the PMU

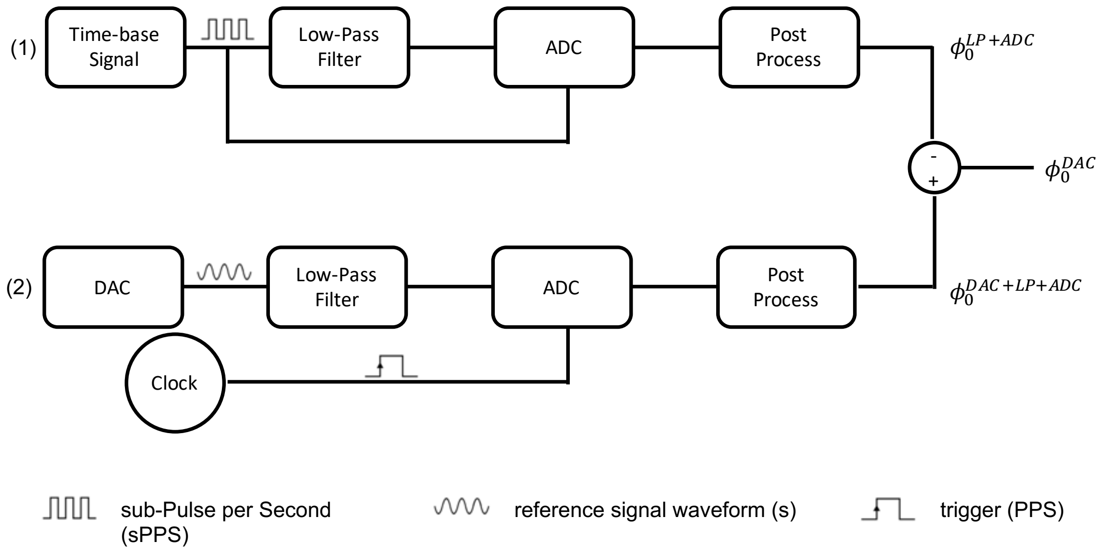

Figure 5.17 – Measurement setup for the assessment of the initial phase displacement due to imprecise synchronization between generation and acquisition stage. In (1), the uncertainty due to low-pass filter and acquisition stages is evaluated. In (2), the uncertainty due also to generation stage is determined. The subtraction provides the single DAC contribution.

under test and the reference values provided by the validation system. The variability of this phenomenon is characterized by means of a two-step processing technique, inspired by [107].

Fig. 5.17 provides a block scheme of the architecture used to analyze this phenomenon. In particular, the block diagram consists of two parallel processing schemes. The upper one is related to the phase uncertainty of the acquisition stage only, whereas the lower one accounts for both generation and acquisition stage. From their subtraction, the initial phase contribution related to the generation stage only can be evaluated.

In the upper scheme, from the 10 MHz time-base a square logic waveform is derived, i.e., a transistor–transistor logic (TTL) signal with a duty cycle of 50%, with a given fundamental frequency f. In the following, this signal is referred to as sub-PPS (sPPS), as it is perfectly locked to the PPS signal provided by the GPS antenna. Then, an analog passive low-pass filter with a cut-off frequency of nearly 725 Hz is applied to the signal (the filter consists of a resistor of 10 kΩ and a capacitor of 0.022 μF). In this way, even though the filtering stage introduces a systematic phase contribution, it limits the sPPS spectral bandwidth. Thus, the filtered waveform can be acquired without noticeable aliasing. For this analysis, a sampling frequency of 25 kHz is adopted, considering an experiment duration of 5 s. The ADC is triggered with the sPPS itself. The acquired time-series is divided into 200 observation intervals of 1 s, partially overlapped in order to reproduce a reporting rate of 50 fps. First, the mean value is removed in order to mitigate the spectral contributions caused by DC and low frequency. Then, the initial phase of the fundamental component is estimated by means of the e-IpDFT algorithm. By repeating this analysis on each observation interval, it is possible to determine the statistical distribution of the sPPS initial phase, in terms of mean and standard deviation, and thus characterize the uncertainty contribution due to low-pass filtering (LP) and acquisition (ADC) stages, φ_0^{LP+ADC}.

In the lower scheme, in a second moment, the validation system is employed to generate a sinusoidal waveform s in steady-state test conditions, with the same fundamental frequency f as in the upper scheme. For this analysis, amplitude and initial phase are set equal to 9 V and 0 rad, respectively. Then, the same analog low-pass filter is applied, the ADC is triggered with the PPS signal provided by the GPS antenna. In this sense, the uncertainty on the trigger event is comparable to the one of the upper scheme, as sPPS and PPS are locked by construction. As in the upper scheme, the acquired time-series is divided into 200 observation intervals of 1 s, with a reporting rate of 50 fps. The e-IpDFT algorithm is used to estimate the initial phase in each observation interval, and thus derive its statistical distribution in terms of mean and standard deviation. In this way, the lower scheme accounts for the uncertainty contribution due to generation (DAC), low-pass filtering (LP), and acquisition (ADC) stages, $\varphi_0^{DAC+LP+ADC}$.

Finally, the difference between lower and upper scheme estimates is computed. The resulting distribution accounts only for the generation uncertainty φ_0^{DAC}. Indeed, the contributions due to low-pass filtering and acquisition are perfectly equivalent in upper and lower schemes, as the corresponding synchronization signals (sPPS and PPS) are directly derived by the same timing reference.

Figure 5.18a represents the time-domain trend of sPPS and s, in blue and red line, respectively, when the fundamental frequency is set equal to 50 Hz. It is interesting to observe how the LP filtering stage has limited the actual bandwidth of the TTL signal, characterized by smoothed transitions and damped oscillations. To a first approximation, the signals seem synchronized as their zero-crossing locations are nearly coincident. Nevertheless, the proposed analysis is intended to determine the non-negligible delay introduced by the internal synchronization between DAC and ADC stages. Figure 5.18b presents the DFT of the acquired sPPS and s. For the sake of clarity, the observed bandwidth is limited to 300 Hz and the DFT coefficients have been normalized and expressed in p.u.. Given a frequency resolution of 1 Hz, it is reasonable to assume that the leakage contributions are almost negligible. Also the odd harmonic terms included in the sPPS spectrum do not introduce significant distortions in the fundamental tone estimation. Figure 5.19 presents the standard deviation of φ_0^{DAC} as a function of sPPS frequency, when varying the frequency of sPPS and s waveforms within the range [10, 500] Hz. It is worth pointing out that due to hardware limitations only frequency values that are integer dividers of 10 MHz can be adopted. It is interesting to observe how the synchronization uncertainty ranges from 1.1 to 4.6 μrad, i.e., it is comparable with the timing uncertainty.

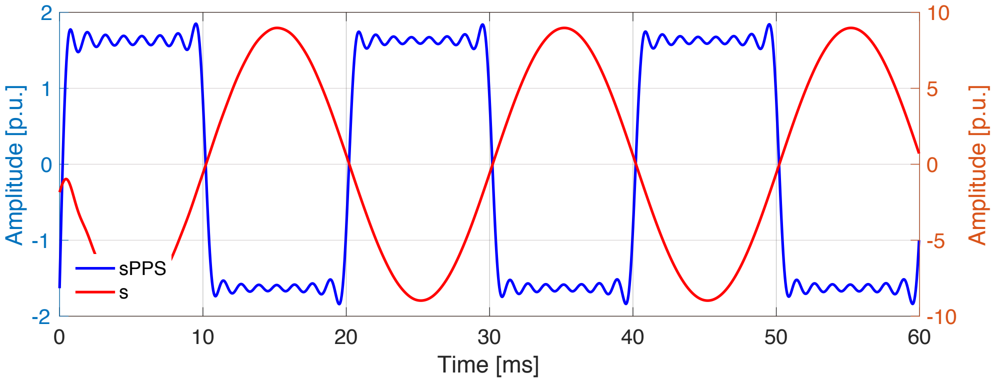

(a) Time domain.

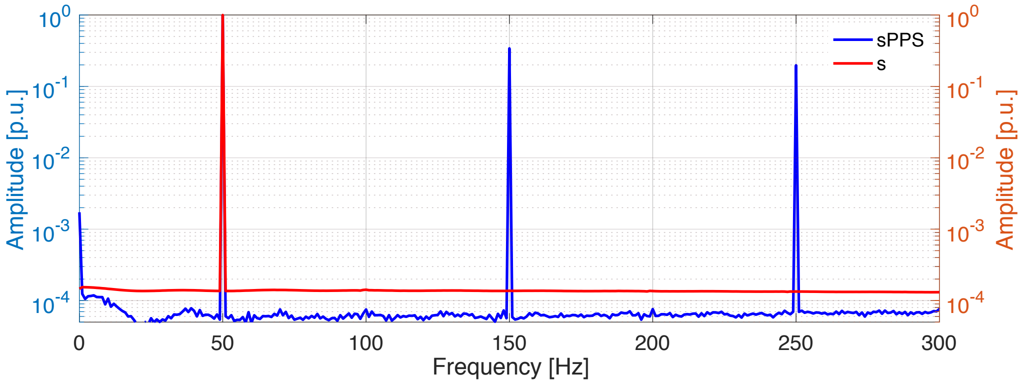

(b) Frequency domain via DFT.

Figure 5.18 – Initial phase characterization routine: detail of the signals sPPS (blue) and s (red), as acquired in the upper and lower scheme in Fig. 5.17.

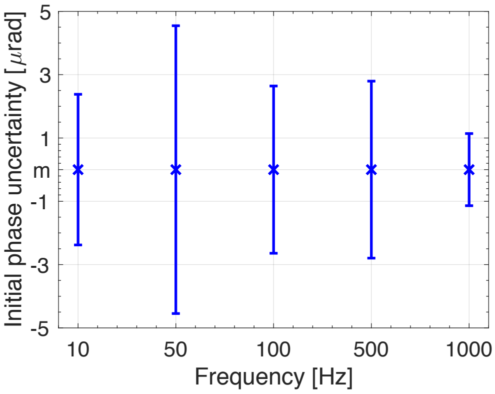

Figure 5.19 – Initial phase uncertainty due to DAC initial phase contribution as a function of sPPS and s frequency. The cross represents the mean value μ, whereas the bold line determines a confidence interval of three standard deviations $\pm 3\sigma$.

Table 5.3 – Calibration performance in IEEE Std. C37.118 tests

Test	**TVE [%]**	**FE [Hz]**	**RFE [Hz/s]**
Nominal	$2.03 \cdot 10^{-4}$	$2.29 \cdot 10^{-6}$	$2.29 \cdot 10^{-4}$
Sign Ampl	$1.84 \cdot 10^{-3}$	$2.02 \cdot 10^{-5}$	$2.02 \cdot 10^{-3}$
Sign Freq	$3.56 \cdot 10^{-4}$	$4.31 \cdot 10^{-6}$	$4.31 \cdot 10^{-4}$
Harm Dist	$1.74 \cdot 10^{-4}$	$4.19 \cdot 10^{-6}$	$4.19 \cdot 10^{-4}$
OOBI	$4.02 \cdot 10^{-4}$	$1.50 \cdot 10^{-6}$	$1.50 \cdot 10^{-4}$
Meas Band	$3.57 \cdot 10^{-2}$	$1.34 \cdot 10^{-3}$	$1.34 \cdot 10^{-1}$
Ampl Mod	$2.53 \cdot 10^{-5}$	$6.40 \cdot 10^{-2}$	$6.40 \cdot 10^{-3}$
Ph Mod	$2.52 \cdot 10^{-2}$	$1.34 \cdot 10^{-3}$	$1.34 \cdot 10^{-1}$
Freq Ramp	$9.17 \cdot 10^{-2}$	$4.86 \cdot 10^{-3}$	$4.86 \cdot 10^{-1}$
Step	$4.24 \cdot 10^{-4}$	$7.19 \cdot 10^{-6}$	$7.19 \cdot 10^{-4}$

5.5 Metrological Characterization According to IEEE Std. C37.118 and in Off-Standard Conditions

In this Section, the system performance is characterized in all the test conditions provided by the IEEE Std. C37.118 (Section 5.5.1), as well as in off-standard operating conditions (Section 5.5.2). As the reference values for synchrophasor magnitude, phase, frequency and ROCOF cannot be measured through multimeter or counter during dynamic tests, they are set equal to the parameter values set by the user in the generation stage.

For each test, the parameters of signal model (5.1) are set in order to reproduce the desired test condition. Generation and acquisition stage adopt a sampling frequency of 100 and 25 kHz, respectively. Then, a three-phase time-series of 5 s is acquired and is divided it into 248 consecutive observation intervals of 60 ms, with a reporting rate of 50 fps. For each window, the NL-LSQ algorithm estimates the corresponding magnitude A_s and phase Φ_s of the fundamental component synchrophasor. Finally, the synchrophasor magnitude and phase uncertainty $\pm 3\sigma$ are evaluated, and the corresponding worst-case TVE, FE and RFE, are computed.

5.5.1 IEEE Std. C37.118 Test Conditions

The accuracy of the proposed PMU calibrator has been experimentally validated in all the test conditions dictated by the IEEE Std. C37.118, and the results are reported in Table 5.3.

The table is divided into three parts, corresponding to three different classes of test conditions. The upper part accounts for nominal steady-state conditions, with fundamental amplitude, frequency and initial phase set to 9 V, 50 Hz and 0 rad, respectively. In this case, TVE is in the order of $2 \cdot 10^{-4}$% and FE does not exceed 2.3 μHz.

In the middle part, the M-class requirements for the steady-state compliance verification are considered. First, the calibration accuracy is evaluated as a function of the fundamental tone parameters. For this analysis, the fundamental amplitude is varied from 10 to 120% of its nominal value, and the fundamental frequency from 45 to 55 Hz. In these tests, TVE and FE are limited to $1.85{\cdot}10^{-3}$% and 20.5 μHz, respectively. Then, the effect of harmonic and inter-harmonic distortion is considered. In particular, an interfering tone is added, whose amplitude is equal to 10% of fundamental amplitude. In these tests, a maximum TVE of $4.05{\cdot}10^{-4}$% and a maximum FE of 4.2 μHz are reported.

The lower part presents the performance of the proposed system in the M-class requirements for the dynamic compliance verification. In the measurement bandwidth test, a simultaneous modulation of amplitude (AM) and phase (PM) is applied, with a modulation frequency of 5 Hz and a modulation depth of 0.9 pu and 0.1 rad, respectively. The accuracy of AM and PM applied separately is also reported. The maximum TVE is around $3.6{\cdot}10^{-2}$%, and the maximum FE does not exceed 1.35 mHz. For the frequency ramp test, a test waveform of 10 s is reproduced, and the fundamental frequency is varied between 45 and 55 Hz with a linear rate of 1 Hz/s. In this test, the worst-case performance corresponds to a maximum TVE of $9.2{\cdot}10^{-2}$% and a maximum FE of 4.9 mHz. Finally, the performance under step changes is evaluated. In particular, variations of ±0.9 pu and $\pm\pi/10$, in terms of amplitude and phase. In this case, a maximum TVE of $4.24{\cdot}10^{-4}$% and a maximum FE of 7.2 μHz are obtained.

The step change tests are intended to evaluate the PMU response time and reporting latency. In more detail, the response time is defined as the time interval between the instants when the PMU measurement accuracy exceeds and respects again given limit (TVE $\leq$ 1%, FE $\leq$ 5 mHz). The reporting latency, instead, is the maximum time interval between the time stamp of the PMU measurement, and the time when the data becomes available at the PMU output. In this regard, the IEEE Std. C37.118 requires to quantify response time and reporting latency with an accuracy not lower than 2 ms and 100 μs, respectively. As regards the response time, the proposed system can be easily employed to carry out an interleaved analysis, where the waveform parameters are kept constant and the only step occurrence time is varied with a resolution given by the adopted sampling rate, i.e., 40 μs at 25 kHz. As regards the reporting latency, instead, the PDC integrated within the calibration platform characterizes the reporting latency with the resolution of the internal time-base, i.e., 100 ns.

5.5.2 Off-Standard Test Conditions

In addition to the canonical tests provided by the IEEE Std. C37.118, the proposed system is also capable of reproducing user-defined test conditions, that better approximate typical power system operating conditions. A single constraint has to be satisfied: the user-defined signal model has to be a special case of (5.1). This Section, focuses on two specific cases, i.e., a voltage unbalanced three-phase waveform and a load inrush event, which typically can occur in networks characterized by fast dynamics and high volatility of renewable energy resources.

Voltage unbalance

The voltage characteristics of European public distribution systems are regulated by EN Std. 50160 [131]. In terms of voltage unbalance, EN Std. 50160 considers ratio between the average RMS value of negative and positive phase sequence, computed over an observation interval of 10 minutes. Under normal operating conditions, during a week, this ratio shall not exceed 2%. Accordingly, the following three-phase waveform is generated:

$$\begin{aligned} x_A(t) &= 9.18 \cdot \cos(2\pi 50 t + 0) \\ x_B(t) &= 9.00 \cdot \cos(2\pi 50 t + 2.1287) \\ x_C(t) &= 8.82 \cdot \cos(2\pi 50 t - 2.0951) \end{aligned} \tag{5.9}$$

in order to reproduce a voltage unbalance of 2%.

As reported in Table 5.4, the worst case results among the three phases are comparable with those obtained in steady state conditions. The maximum TVE is $3.70{\cdot}10^{-4}$% and the maximum FE is 3.80 μHz.

Load inrush

As shown in Fig. 5.20, a load inrush event produces a current waveform with a rapidly increasing amplitude, followed by an exponentially-decaying trend. The test signal model is defined as follows:

$$\begin{aligned} x(t) &= A_0 \cdot \sin(2\pi f_0 t + \varphi_0) + \eta \qquad (5.10) \\ \eta(t) &= \left(\frac{A_T}{1 + e^{-k(t-T_T)}} \right) \cdot e^{-\frac{t-T_T}{\tau}} \sin(2\pi f t + \varphi) \end{aligned}$$

where the current inrush event is modeled by the additive term $\eta(t)$. The parameters A_T and T_T determine the transient amplitude and occurrence time, respectively, whereas τ is the time-constant of the exponential decay. For this analysis, the fundamental amplitude, frequency and initial phase are set equal to 1 p.u., 50 Hz and 0 rad, respectively. The current inrush occurs at T_T = 0.495 s with k = 10000, and we set A_T, τ and ϕ equal to 6 p.u., 0.087 and 1.53 rad, respectively.

Table 5.4 shows that also in the presence of a severe transient event, like a current inrush, the PMU calibrator is capable of providing accurate estimates of the reference synchrophasors, with a maximum TVE in the order of 0.25% and a maximum FE not exceeding 22 μHz.

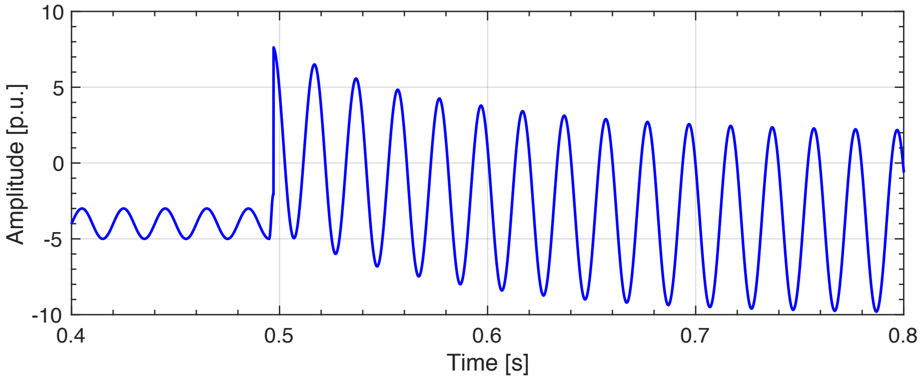

Figure 5.20 – Detail of a current in-rush event, as reproduced by the proposed PMU calibrator.

Table 5.4 – Calibration performance in off-standard tests

Test	**TVE [%]**	**FE [Hz]**	**RFE [Hz/s]**
Voltage unbalance	$3.69 \cdot 10^{-4}$	$3.80 \cdot 10^{-6}$	$3.80 \cdot 10^{-4}$
Load inrush	$2.53 \cdot 10^{-1}$	$2.19 \cdot 10^{-5}$	$2.19 \cdot 10^{-3}$

5.6 Discussion

The Chapter presented a highly accurate PMU calibrator, that is suitable for the performance assessment of PMUs characterized by TVE in the order of $0.0x$%. The system is capable of reproducing all the tests indicated by the IEEE Std. C37.118, as well as user-defined test conditions.

The Chapter first assessed the robustness of the adopted synchrophaseor estimation algorithm based on NL-LSQ. Specifically, the range of initial conditions that guarantees the uniqueness of the solution was determined, and the algorithm performance was evaluated on varying the operating parameters, i.e., the observation interval length and the sampling rate employed by the generation and acquisition stages.

Then, the test waveform accuracy was characterized in terms of power quality of the generated test waveforms, frequency response of the adopted voltage and current amplifier and uncertainty associated to the magnitude, phase and frequency estimates. The analysis was conducted using high-accuracy hardware instrumentation. In nominal conditions, the worst case TVE is in the order of $5 \cdot 10^{-4}$%. Also, the uncertainty contributions related to the timing reference provided by the atomic clock (4 μrad) and the internal synchronization between generation and acquisition stage (4.6 μrad) were discussed.

Finally, the performance of the proposed calibrator was evaluated in the IEEE Std. C37.118 tests as well as in off-standard conditions. This final analysis was performed taking as reference the parameter values set by the user in the generation stage. In the steady-state compliance tests, worst-case TVE and FE are limited to $1.85 \cdot 10^{-3}$% and 20.5 μHz, respectively. In the dynamic compliance tests, instead, the calibrator exhibits a TVE and FE not larger than $9.2 \cdot 10^{-2}$% and 4.9 mHz, respectively.

6 Real-Time and Low Latency Synchrophasor Networks

Synchrophasor technology is the leading edge of timing use for power systems. On the one hand, PMUs must be coupled with an appropriate time dissemination technique to correctly phase align phasors from different locations of an electrical grid. On the other hand, PMUs cannot be adopted for mission-critical or real-time automated actions, unless relying on a low-latency telecommunication infrastructure. Within this context, the Chapter focuses on the key concepts of time and latency. First, innovative time dissemination technologies for highly accurate synchrophasor phase measurement are introduced. Specifically, the White Rabbit protocol is considered, that is an evolution of the Precision Time Protocol (PTP), and its implementation into a dedicated PMU is described. In order to assess the influence of the time synchronization technique on the synchrophasor estimation, the White Rabbit is compared with respect to two state-of-the-art dissemination techniques: the Global Positioning System (GPS) and the PTP. Then, the architecture of a low latency and time deterministic Phasor Data Concentrator (PDC) is presented. The developed PDC is aimed at minimizing the delay introduced by the concentration point without decreasing the data completeness. The performance of the proposed PDC is experimentally validated in terms of reliability, determinism and reduction of the overall latency in two real PMU installations adopting different telecom infrastructures. The first one is based on optical fiber links, the second one adopts a 4G LTE wireless infrastructure.

The chapter includes results of publications [13, 14, 15, 16, 17].

6.1 Time Dissemination Techniques for PMUs

Synchrophasor technology represents one of the primary time-dependent applications used in modern power systems, as Phasor Measurement Units (PMUs) require an accurate and reliable time source to correctly phase align synchrophasors relative to geographically-distant substations [19, 137]. Typically, PMUs rely on the time reference made available by the Global Positioning System (GPS) that represents an optimal trade-off between performance and installation cost [138]. To improve timing redundancy and reliability, and given the potential vulnerability of GPS [139], mission-critical applications should use multiple timing sources, for instance deployable over the legacy power system telecommunication infrastructure [137]. In case the sky is not accessible and the telecommunication infrastructure is already available, there exist different network-based alternatives to substitute or support the GPS, for instance the Precision Time Protocol (PTP) [140] or synchronous-Ethernet based systems like the White Rabbit (WR) Time Protocol [141, 142, 143, 144, 145].

The IEEE Std. C37.118 requires a maximum uncertainty in the synchrophasor time jitter of 1 μs [19], good-enough to correctly serve transmission applications. Distribution PMUs, requiring and increased level of accuracy, expect a lower level of uncertainty, in the order of tens of ns [41, 137]. Indeed, modern PMUs embed synchrophasor estimation algorithms exhibiting phase accuracies of few μrad, corresponding to 10 ns if considering a power system at 50 Hz. The GPS provides an uncertainty in the order of 100 ns when coupled with commercial receivers, whereas the PTP is characterized by an uncertainty of 1 μs. Therefore, these time references could negatively affect the phase estimation performance of the relative PMUs. Conversely, the WR achieves the sub-nanosecond, assuming only fiber interconnections and dedicated switches.

The purpose of this section is to assess the influence of the adopted time dissemination technique on the phase estimation accuracy. Specifically, the phase uncertainty of a PMU whose timing block integrates the GPS, the PTP and the WR technology is characterized. The phase stability is experimentally validated on the short, medium and long term, and the results are presented by means of the Allan deviation [146]. To carry out this analysis three PMUs are used, that are based on the same hardware and on the same synchrophasor estimation algorithm, whereas time reference is varied. Therefore, it is plausible to say that any discrepancy on the phase estimation accuracy comes from the adopted time synchronization module.

The Section includes results of publications [13, 15, 14] and is structured as follows. Section 6.1.1 describes state-of-the-art time dissemination techniques for PMU applications. Section 6.1.2 illustrates the operating principles of the WR protocol as well as its applicability to synchrophasor networks. Section 6.1.3 illustrates the implementation details of the developed WR-synchronized PMU. Section 6.1.4 assess its performance.

6.1.1 State of the Art: Satellite and Network-based Time Synchronization

Time synchronization is a key factor in any PMU-based monitoring systems [137]. The IEEE Std. C37.118 [19] defines the phase of a synchrophasor as the instantaneous phase angle relative to a cosine function at the nominal power system frequency, synchronized to Coordinated Universal Time (UTC). In that sense, any uncertainty in the time synchronization Δt linearly translates in a phase uncertainty $\Delta\varphi$, depending on the instantaneous frequency f of the signal:

$$\Delta\varphi = 2\pi f \Delta t + \varepsilon_{alg} + \varepsilon_{acq} \tag{6.1}$$

where ε_{alg} and ε_{acq} account for two additional uncertainty sources, i.e., the phase error introduced by the adopted synchrophasor estimation algorithm and the phase noise produced by the acquisition process (including the measurement chain from the sensor to the PMU analog input), respectively. Since these errors come from independent devices, these two contributions are assumed statistically independent and uncorrelated, and the focus mainly on the synchronization uncertainty. The same standard further requires that synchrophasor measurements are reported by PMUs at a specific reporting rate, with the first frame within the second at the UTC-second rollover.

From the IEEE Std. C37.118 it is possible to infer the maximum uncertainty on the synchrophasor time-jitter to be limited to 1 μs [19]. Indeed, this value is indirectly determined by the requirement for a maximum Total Vector Error (TVE) of 1%, corresponding to a phase uncertainty of 0.01 rad in case the TVE is only influenced by the phase error. When time is the only source of error, this corresponds to 31 μs at 50 Hz. A reliable time source should be characterized by an uncertainty at least 10 times better, giving some allowance for sources of error other than synchronization, leading to the recommended time uncertainty of 1 μs. However, it is well-established that PMUs operating in distribution networks are expected to meet more stringent accuracy requirements, at least two orders of magnitude lower than those met by transmission PMUs (TVE lower than 0.01%) [41]. Therefore, the uncertainty contribution coming from the timing unit should be reduced to the order of tens of ns [137].

In the following, two time dissemination technologies that are currently being used for PMU applications are described: (i) satellite and (ii) network-based synchronization systems, making reference to their functional features and performance. Their applicability to synchrophaosor technology and their vulnerability to timing-attacks is discussed [137].

Satellite-based Time Synchronization Systems

The operation principle of satellite systems is based on the time measurement of synchronizing signals between satellites and terrestrial receivers. The satellites are equipped with atomic clocks, daily monitored and controlled to be highly synchronized and traceable to the UTC time. The receivers are equipped with an internal clock, and are able to determine the actual UTC time by collecting and processing messages from several satellites. GPS receivers are often used as primary absolute timing source for most of time dissemination techniques. To correctly lock satellites, the GPS receiver requires a clear view of the sky. Indeed, being in an enclosed space such as a high rise urban environment, reduces the number of tracked satellites and determines signal reflections and wakening, resulting in a degradation of the time information accuracy [147].

Regarding security, the GPS signals can be easily spoofed, jammed or meaconed with inexpensive electronics resulting into complex and potentially dangerous time attacks [148, 139, 149, 150]. Among different types of attacks, GPS spoofing is the most malicious and difficult to detect [151]. It is achieved by superimposing a fake signal with a higher signal-to-noise ratio, which would enable an attacker to manipulate the GPS clock. With particular reference to the GPS-based PMUs, a spoofing attack can cause the GPS receiver of a PMU to compute an erroneous clock offset, resulting in an erroneous time stamp calculation, which introduces an error in the PMU's phase measurement. The failure to deliver data to concentrators and applications within acceptable latency periods causes data gaps that could corrupt early warning information about dynamic grid conditions.

As known, PMU applications generally rely on the GPS that provides an uncertainty in the order of $\pm$ 100 ns when coupled with commercial GPS-receivers (e.g., [56]), although modern units can nowadays reach uncertainty lower than $\pm$50 ns. In such scenario, a dedicated GPS receiver must be installed at every PMU location, and the same applies to Phasor Data Concentrators (PDC) in case time-stamping functionalities are implemented at data collection.

Packed-Switched Synchronization Messaging Protocols

Typically, synchrophasor networks use the Ethernet network protocol as physical layer to transfer data. The protocol, introduced by the IEEE Std. 802.3, represents a well-established and very high-performance solution, that is capable of supporting the high-throughput of synchrophasor data streams [152]. The Ethernet protocol also integrates various standards that enable the time synchronization of the network nodes with different levels of accuracy. In other words, the same telecom infrastructure used for seamless data transfer could be exploited for disseminating the time information.

The Network Time Protocol (NTP) has been proposed to synchronize the clocks of a distributed system over the Internet [153]. However, the average uncertainty provided by the NTP is in the range of few milliseconds that does not fulfill the PMU requirements. The Precision Time Protocol (PTP) was introduced by the IEEE Std. 1588 in order to provide time accuracies beyond those attainable using NTP, thanks to a technique called hardware time-stamping [140]. The most recent PTP version 2 (PTPv2) provides 1 μs uncertainty, measured as the deviation of each node with respect to the UTC.

The core element of the PTP is the exchange of time-tagged messages in a peer-to-peer link between master and slave clocks, used to calculate the link delay between the two clocks. Specifically, at time t_1 the master node sends a *Sync* message, that is received at time t_2 by the slave. Similarly, at time t_3, the slave node sends a message, received at time t_4 by the master. Knowing these four time-stamps, the one-way delay between the two clocks can be estimated as:

$$\delta = (t_2 - t_1 + t_4 - t_3)/2 \tag{6.2}$$

The slave node accounts for this offset when adjusting its clock time with respect to the one of its master clock. The PTP assumes that all network nodes are equipped with PTP-aware routers or switches, implementing the so-called hardware-assisted time-stamping, a technique to measure and compensate for the time spent by messages in queuing at their own ports.

The first limitation of the PTP is that it assumes that the one-way delay is exactly half of the two-way delay, which, due to link asymmetry is true only as long as the cable is very short. The second limitation is that the final PTP uncertainty is limited by the precision and resolution of the master and slave clocks to measure the time when sending or receiving messages, typically of 100 ppm. The third limitation is that these clocks are typically free-running oscillators, without any guarantee of synchronism between oscillators at different nodes. This results in uncontrolled time drift between masters and slaves. The higher the exchange rate of PTP messages, the lower the time drift, the higher the bandwidth needed for PTP-related traffic.

The security of PTP (as well as WR) against cyber-attacks is studied in [154] by using a so-called delay-box that introduces a malicious offset of a few microseconds in the slave clock. Nevertheless, the attack can be counteracted by using redundant and disjoint communication paths or using the GPS as a redundant time source.

An extended profile for the use of PTP in power system applications is specified in IEEE Std. C37.238-2017 [155], whereas the IEC/IEEE Std. 61850-9-3-2016 [156] specifies a PTP profile allowing compliance with the highest synchronization classes of IEC Std. 61850-5 [157] and IEC Std. 61869-9 [158]. The profile has been integrated in power system applications in [159]. With a specific reference to PMUs, the protocol has been integrated into synchrophasor networks to distribute the time [160, 161].

6.1.2 The White Rabbit Time Synchronization Protocol

Recently, the WR protocol, also known as PTP version 3 (PTPv3), has been developed and used at CERN to align the clocks of their accelerator complex [141, 143, 144, 145]. The protocol enables the synchronization of thousands of devices connected in a network spanning several kilometers through already existing Ethernet-based networks. The uncertainty, measured as the deviation of each node with respect to the UTC, achieves the sub-nanosecond, assuming only fiber interconnections. Moreover, the protocol features a reliable and deterministic data delivery. The project is open source [162].

These features make the WR an appropriate time synchronization protocol for smart grids applications [144, 163, 145]. Indeed, the uncertainty on 1 ns exceeds the one of synchrophasor needs. Also, the superior determinism with respect to PTP is good for the overall reliability of mission-critical applications. This technology represents an appropriate alternative or complement to the GPS with particular focus on the cases when (i) the sky is not accessible (e.g., urban areas), (ii) the telecommunication infrastructure is already available, and (iii) the typical length between two PMUs is less than 10 km (e.g., sub transmission or power

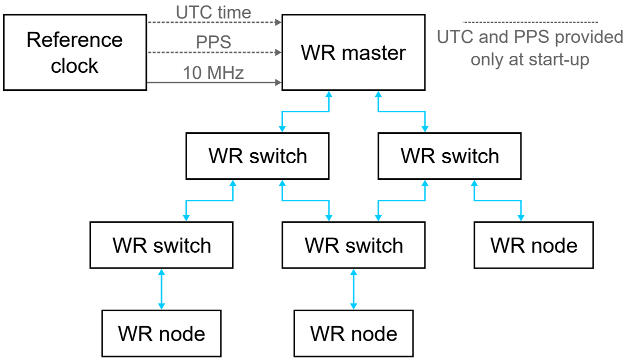

Figure 6.1 – The WR network architecture.

distribution networks). It is worth mentioning that recent studies have demonstrated the stability of the WR protocol over fiber links up to 950 km [164, 165]. Further studies have addressed the problem of temperature-related hardware delays [166].

The White Rabbit Network Architecture

Figure 6.1 shows the layout of a typical WR network, that is composed of WR nodes and WR switches, interconnected by fiber links. Data-wise it is a standard Ethernet switched network, i.e., there is no hierarchy: any node can talk to any other node in the network. Regarding time synchronization, there is a hierarchy, that goes from the top, i.e., from the WR master, down to other WR switches and consequent nodes. The WR switch, key element of any WR network, is similar to a standard Ethernet switch, but it is also able to precisely distribute the WR master clock over the network thanks to a technique called precise phase measurement [167].

The uppermost switch in the hierarchy, also called grand-master, receives the absolute clock from an NTP source (e.g., the NTP daemon running on a computer), together with the pulse-per-second (PPS) and the 10 MHz from an external reference (e.g., a GPS receiver or a Cesium clock). At start-up, the WR switch uses the NTP and the PPS to determine the absolute UTC time. Then, it calculates the time using only the 10 MHz signal. After the switch has completed the rebooting routine, i.e., few minutes after powering it on, the NTP service and the PPS are not needed anymore and the grand-master switch could be potentially disconnected from these sources. The accuracy of the round-trip time measurement is mostly determined by the accuracy of the 10 MHz source. The grand-master switch then distributes the time information to further WR nodes via intermediate WR switches. It is worth pointing out that the subsequent switches do not have to be connected to a 10 MHz source.

In the power system context, it is reasonable to expect that the grand-master WR switch is located in a safe location, such as the control room of the network operator. To guarantee reliability, the grand-master switch as well as the 10MHz sources should be powered via an uninterruptible power source (UPS). It is also reasonable to expect that the grand-master switch is rebooted only if needed, few times over the lifetime of the synchrophasor network, for instance at the same time of rebooting the central phasor data concentrator (PDC) or updating PMUs firmware.

Finally, the security of WR against delay-attacks is studied in [154], and countermeasures for this type of attack are proposed.

The White Rabbit Synchronization Scheme

The WR is based on existing standards, namely Ethernet (IEEE Std. 802.3) [152], Synchronous Ethernet (SyncE) [168], IEEE Std. 1588 (PTPv2) [140] and adopts a technique called Precise Phase Measurement. The combination of these technologies, further described in this section, enables to achieve the sub-nanosecond uncertainty [169].

The WR is an extended version of the PTP protocol, therefore, the same principles described for calculating the one-way transmission delays hold. However, in a WR network, PTP messages are managed not only by the grand master clock, but also by the WR switches. This method prevents PTP messages to be exchanged between long links from the master to a far side slave, reducing the unavoidable jitter introduced by each switch. Also, the number of messages between master and slaves is reduced, reducing the PTP-related throughput and allowing more bandwidth for mission-critical data exchange.

Typical PTP implementations use free-running oscillators in each node, resulting in growing time drifts between master and slaves, that is maintained between specific bounds by a dedicated time stamping mechanism. The same holds for WR protocol, but with smaller bounds. The problem of oscillator drifting is further mitigated by the SynchE protocol, a technique to transfers the frequency over the Ethernet physical layer, in order to lock all the network nodes to beat at exactly the same rate. Every WR switch uses the clock recovered by the data link to sample the incoming data. Then, it uses an embedded PLL-based oscillator, locked to the recovered clock, for transmission. This procedure ensures high level jitter elimination. Since it acts on the physical layer, its accuracy is independent of data transmission (packet delay or traffic load). The technology has been proven to be able to transfer very accurate timing over long distances [168, 142].

The accumulation of phase noise degrades the performance of network-based synchronization protocols. To this end, every WR switch is equipped with a phase measurement module based on phase/frequency detectors that periodically measures the phase difference between the recovered clock and the master clock [170]. The calculated phase difference is transmitted to a slave node for further compensation of the round-trip link delay with sub-nanosecond uncertainty.

6.1.3 Integration Schemes of Time References into a Dedicated PMU

In order to compare the performance of the time synchronization techniques under investigation, three PMUs based on the same synchrophasor estimation algorithm and the same hardware are developed. The only difference among the three is the adopted technique to synchronize to the absolute time reference: the so-called GPS-PMU is based on the GPS time dissemination technique, the PTP-PMU is based on PTPv2 whereas the WR-PMU is based on the WR protocol. The main features of the three devices are very similar to those of the PMU described in Chapter 3, Section 3.5: any difference or similarity is illustrated in this section, with a focus on all implementation details that condition time accuracy.

To limit any discrepancy introduced by the synchrophasor estimation process, the three PMUs are based on the same synchrophasor estimation algorithm described in Chapter 3, i.e., the Iterative Interpolated DFT, hereafter called i-IpDFT.

The hardware platform of the three devices is based on the National Instruments compactRIO (cRIO) system, an embedded industrial controller with a real-time processor, a user-programmable Field Programmable Gate Array (FPGA) and reconfigurable IO modules [87]. It is worth to point out that in the designed architecture, the three main processes, i.e., (i) PMU time synchronization, (ii) signal acquisition and (iii) synchrophasor estimation, run at the FPGA level. The sampling of the voltage and current waveforms is realized by means of two parallel 24-bits delta–sigma converters, module NI 9225 and 9227, characterized by a sampling rate F_s of 50 kHz and an input range of 300 $\mathrm{V_{RMS}}$ and 5 $\mathrm{A_{RMS}}$, respectively [89, 90].

The Synchrophasor Estimation Algorithm

The developed PMUs adopt the i-IpDFT algorithm to estimate the synchrophasors, whose details are discussed in Chapter 3. The frequency $\hat{f}_0$, amplitude $\hat{A}_0$, phase angle $\hat{\varphi}_0$ and the Rate-of-Change-of-Frequency (ROCOF) associated to the fundamental tone of the power system signal under analysis are estimated using a technique that is specifically designed to mitigate the effects of long-range spectral leakage produced by the negative image of the fundamental component, and possible interfering tones.

The parameters of the adopted i-IpDFT are reported in Table 6.1. In particular, the algorithm adopts the Hanning window function and a 2-points interpolator to estimate the synchrophasors. The number of iterations to compensate the spectral interference produced by the negative image of the fundamental component is set to 2. Conversely, as the tests proposed in this Section are aimed at assessing the steady-state accuracy of single tone signals, the routine that compensates the effects of interfering tones is deactivated, setting Q equal to 0. It is also worth mentioning that the higher the observation interval over witch synchrophasors are measured, the higher the accuracy of the estimates. In the current implementation, the observation interval T can be equal to 60 ms, as representative of P-class and equal to 100 ms, that is a value typical of M-class PMUs.

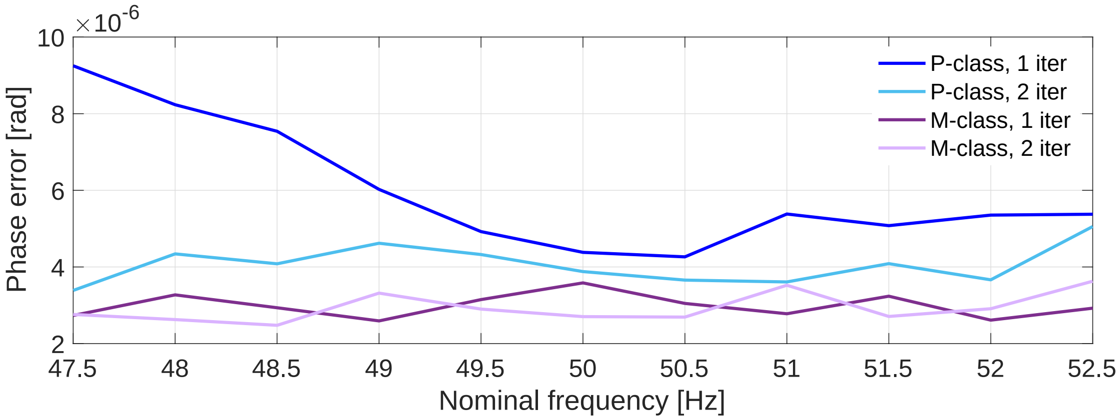

Figure 6.2 – Phase estimation error as provided by e-IpDFT as a function of the fundamental frequency, for P and M synchrophasor estimation and when the iteration number P of the compensation process is set equal to 1 and 2. The additive white Gaussian noise produces a signal-to-noise ratio of 85 dB.

In this regard, Fig. 6.2 compares the phase estimation errors obtained with a P-class and an M-class algorithm, and with P equal to 1 and 2. The test is performed with simulated waveforms in steady-state test condition. Specifically, the amplitude and the initial phase are equal to 1 pu and 0 respectively, the frequency varies between 47.5 and 52.5 Hz, i.e., within the PMU pass-band considering the nominal frequency at 50 Hz and the reporting rate of 50 fps. In order to reproduce measurement noise coherent with the signals experimentally acquired in Section 6.1.4, the waveforms are corrupted by an additive uncorrelated white Gaussian noise, whose variance is scaled to reproduce an overall signal-to-noise ratio (SNR) of 85 dB. In this context, it is interesting to observe that for P-class configuration the second iteration provides a significant performance enhancement in case of non-nominal frequency values, with a phase error not exceeding 5 μrad. For the M-class configuration, already with P equal to 1 the phase error does not exceed 4 μrad.

Table 6.1 – i-IpDFT parameters.

Parameter	Variable	Value
Nominal system frequency	f_n	50 Hz
Window type	-	Hanning
Window length	T	60 ms and 100 ms
Sampling rate	F_s	50 kHz
PMU reporting rate	F_r	50 fps
DFT bins	K	8
Iterations compensation fund. image	P	2
Iterations compensation interference	Q	0
IpDFT interpolation points	-	2

Considering the uncertainty balance in (6.1), it is possible to quantify ε_{alg} and ε_{acq} of the test-bed. The synchrophasor estimation uncertainty ε_{alg} is constant in the considered spectral bandwidth and lower than 5 μrad, whereas the measurement noise exceeds the quantization noise of the acquisition module and thus makes negligible its uncertainty contribution ε_{acq}.

The Free-Running Sampling Process

As discussed in Section 3.5, regardless of the adopted time dissemination technique, the sampling process of the waveforms is free-running and the UTC-time synchronization is achieved *a posteriori*. Specifically, at the FPGA level, a sub PPS square waveform (subPPS) is derived from and locked to the UTC-PPS signal, and is characterized by a frequency corresponding to the PMU reporting rate F_r. The signal acquisition, the synchrophasor estimation, and the synchrophasor time-stamping are triggered by the rising edge of such subPPS. Because there is no guarantee that the sampling process is locked to such subPPS signal, the PMU performs an *a posteriori* time refinement, compensating for two delays (implementation details are provided in Section 3.5): first, the ADC clock drift due to oscillator degradation or environment conditions variation; second the offset between the ADC clock and the subPPS.

GPS Time Synchronization

The GPS-PMU is based on the cRIO-9068 controller [171], embedding a reconfigurable Xilinx Zynq 7020 FPGA with an on-board clock frequency of 40 MHz, 106400 flip-flops, 53200 look-up tables (LUTs), 4480 kbits of block RAM and 220 DSP slices (each one characterized by a 25 X 18 multiplier, an adder and an accumulator). The UTC-GPS signal is acquired by means of the NI 9467 GPS time-stamping and synchronization module [172], that is directly coupled with the on-board FPGA clock. This enables to timestamp each tick of the 40 MHz clock with real-world time, accurate to within ± 100 ns. That is to say that the NI GPS module provides a continuous time reference characterized by a time polling resolution corresponding to the FPGA clock. The subPPS is locked to the UTC-GPS.

The GPS module is coupled with a Trimble's Bullet III GPS receiver, an active GPS antenna with a high-gain preamplifier (35 dB) and dual passband filters [173]. The preamplifier enables preserving the GPS signal even for long cable lengths, whereas the filters improve rejection to interfering radio signals and reliability. The antenna is mounted on the rooftop of DESL laboratory with a full-sky visibility and is coupled to the module via a 30-meters RG-213 shielded cable. The latter, introduces un unavoidable propagation delay of 5.05 ns/m, leading to 151.5 ns (suitably compensated).

PTP Time Synchronization

The PTP-PMU is based on the cRIO-9039 controller, characterized by a reconfigurable Xilinx Kintex-7 FPGA with an on-board clock frequency of 40 MHz, 407600 flip-flops, 203800 look-up

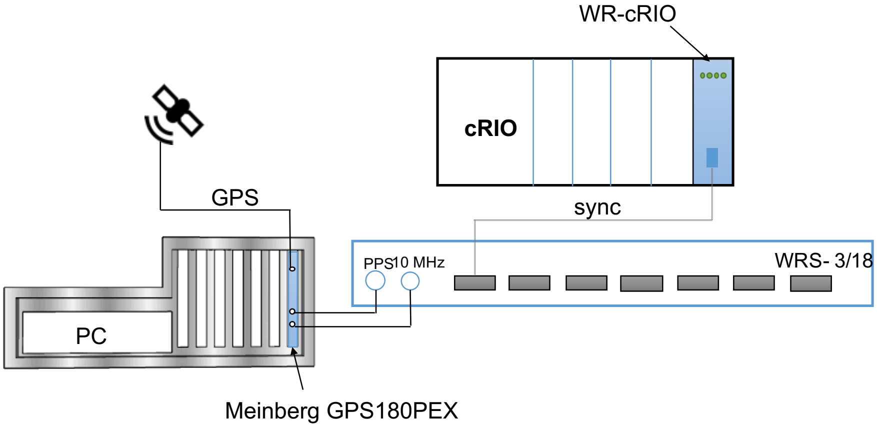

Figure 6.3 – The experimental WR network composed of a Meinberg GPS180PEX card, a WR switch and a NI-cRIO integrating the WR-cRIO module (i.e., a WR-PMU).

tables (LUTs), 16020 kbits of block RAM and 840 DSP slices [88]. The PTP distribution is achieved thanks to the NI TimeSync library, that synchronizes the timekeeping clocks of the cRIO. The so-called hardware time-stamping enables to discipline the FPGA clock directly via the UTC-PTP reference. This enables to timestamp each tick of the 40 MHz clock with real-world time, accurate to within ± 1 μs. The TimeSynch library provides a continuous time reference, however, since the FPGA clock is locked to the UTC-PTP, the resolution of time stamps corresponds to 25 ns.

The UTC-PTP reference signal is acquired by connecting point-to-point the three-speed RJ-45 Gigabit Ethernet Port to a PTP master clock. The latter is the Network Time Server NTS 100 manufactured by Tekron [174]. The clock receives the absolute time by a Trimble's Bullet III GPS receiver, whose characteristics have been already discussed [173].

White Rabbit Time Synchronization

The WR-PMU setup is shown in Fig. 6.3, and is based on the same hardware platform as the GPS-PMU, i.e., cRIO-9068 [171]. The WR-UTC signal is provided by the NI WR cRIO module, a standalone WR node which can be coupled with the NI cRIO platforms to integrate the WR protocol [175]. The module is equipped with a Xilinx Spartan-6 FPGA and can be used in all operation modes defined by the WR protocol, i.e., grand-master, master or slave. Depending on the selected operation mode, a different configuration of input and outputs shall be adopted. A user programmable HDSUB-15 I/O module is provided, that can acquire the 10 MHz and PPS inputs (in case of operating the node in grand-master mode) or any sort of external trigger, as well as generate reference clock, PPS outputs or generic triggers. The module is also equipped with a Small Form-factor Pluggable (SFP) cage, for disseminating WR messages over optic fiber transceivers. In particular, when operated in slave mode, such cage is used to connect the module to its master WR switch and to retrieve the time information.

In the developed PMU, the module is operated in slave mode, and is connected point-to-point to a WR switch operated in grand-master mode. The switch is manufactured by Seven Solutions [176]. Ethernet frames are exchanged through 18 ports equipped with SFP sockets, connected directly to a Xilinx Virtex-6 FPGA characterized by very low latency. An ARM CPU running Linux helps with less time-sensitive processes like remote management and keeping the frame filtering database in the FPGA up to date. The clocking resources block contains PLLs for cleaning up and phase-compensating the system clock, as well as for generating the frequency-offset clock. The WR switch provides deterministic delivery and a reliable communication using redundant network topology. It allows many hops (14 tested keeping sub-nanosecond accuracy).

The NTP service, used to determine the absolute time and date at reboot, is provided by a Windows machine connected point-to-point to the RJ-45 management port of the WR switch via an Ethernet cable. The computer is equipped with a Meinberg 180 PEX card that disciplines the system time as well as the NTP service [177]. The card is coupled with an active GPS receiver, mounted on the rooftop of DESL laboratory, via a 30-meters RG-213 shielded cable. The card compensates for the delay introduced by the cable. The card further generates reference PPS and 10 MHz signals, that are fed to the WR switch.

Due to hardware limitations, the UTC-WR polling is limited by the module's FPGA clock running at 50 kHz, therefore, the WR cRIO does not provide a continuous time reference. Also, the UTC-WR reading introduces a deterministic delay, that needs to be compensated.

To retrieve the UTC-WR from the WR cRIO, a trigger is generated, and is characterized by a frequency of 50 kHz, i.e., the maximum value attainable in the WR cRIO FPGA. The procedure illustrated in Algorithm 6 is implemented to trigger the UTC-WR acquisition, to freeze the time, and to acquire it. Specifically, when the state is *Wait for Node Start*, the trigger is generated and the WR cRIO acquires the reference time. The UTC-WR is frozen and acquired in the next states. Then the node is set in *Idle* mode until the next trigger. The time acquisition process is not continuous but the UTC-WR is updated in a discrete manner, determined by the trigger period T_{trig} of 20 μs. This lower bound is limited by the FPGA integrated in the NI cRIO, characterized by a finite and deterministic time polling resolution, not appropriate for PMU applications.

To overcome this hardware limitation, an additional internal free-running clock is implemented. Such clock is disciplined by the FPGA clock and is implemented at every tick, i.e., every 25 ns. As long as the UTC-WR is not updated, the free-running clock governs the PMU time. Every time the UTC-WR is acquired, the free-running clock is overwritten by the updated reference time.

As it is known, the FPGA clock could drift even in the short interval between two consecutive triggers, biasing the attainable sub-nanosecond accuracy. Therefore, every time the UTC-WR is acquired, the deviation between the free-running clock and the UTC-WR is computed, and this error is used by a PI controller to condition the free-running clock.

Algorithm 6 Retrieving the WR time.

```
while True
    Go to normal operation
    Start
    while $T_{trig}$
        Wait for node start
    end
    Read UTC-WR
    Idle
end
```

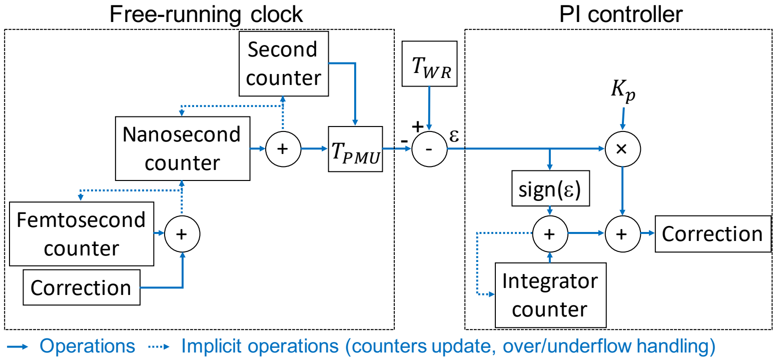

Figure 6.4 – The structure of the internal clock regulated by the PI controller.

The structure of the free-running clock and its PI controller is shown in Fig. 6.4: the PMU time is made of the second and nanosecond counters and the correction $\gamma(n)$ is added to a femtosecond counter at each tick. The PMU time is therefore corrected only when this counter has an overflow or an underflow. The tuning of the PI controller has been done empirically: the proportional coefficient K_p has been chosen to average the error entering the PI controller over a period of 10 ms, which gives a very low jitter. The integrator is built as a counter that is incremented or decremented according to the sign of the error. Its resolution has been set to 1 fs (i.e. the highest possible), which allows to compensate the steady-state error without introducing additional jitter. The implemented internal clock is explained in Algorithm 7. It is worth noting that, due to hardware limitations, there is a delay in acquiring the UTC-WR. However, the use of the FPGA makes this delay time-deterministic (in the order of few μs) and, therefore, enables the free-running clock to compensate for it (see Fig. 6.5).

In addition to greater resolution, the internal free-running clock also has much less jitter than the WR time, as shown in Table 6.2. The calculation of jitter is done by computing the time steps of the WR time T_{WR} and the PMU clock T_{PMU} (i.e., WR time together with the internal free-running clock) between two successive triggers T_{trig}. The standard deviation is then computed with 1000 samples. Results show that T_{WR} is characterized by 2.89 ns jitter, whereas T_{PMU} improves the jitter up to 0.42 ns. The performance of this implementation, characterized by the jitter, is appropriate for a PMU application.

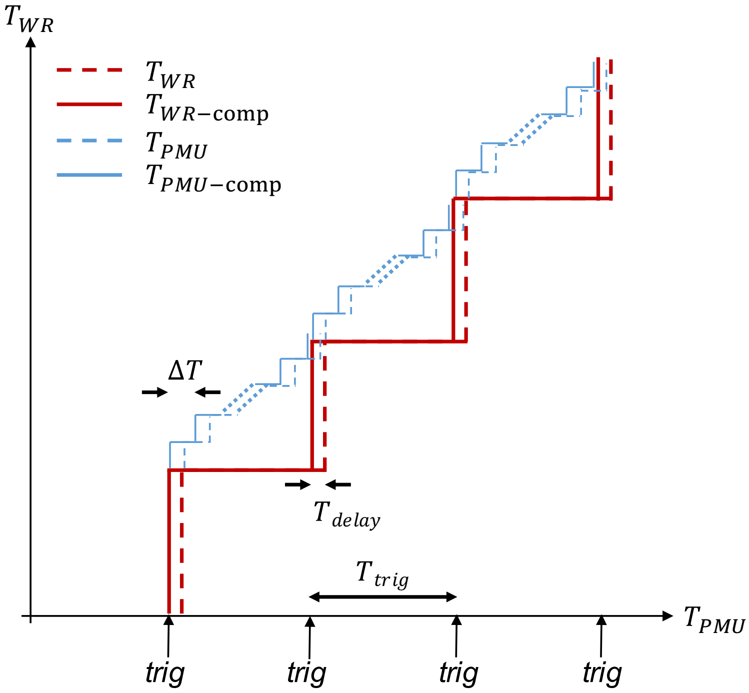

Figure 6.5 – The structure of the internal conditioned clock together with the T_{WR}.

Table 6.2 – Performance of T_{WR} and T_{PMU}.

	T_{WR}	T_{PMU}
Jitter [ns]	2.89	0.42

Algorithm 7 Internal free-running clock.

```
if $T_{WR}(n) \neq T_{WR}(n-1)$
    $\varepsilon(n) = T_{WR}(n) - T_{PMU}(n)$
    $\gamma(n) = K_p \varepsilon(n) + \sum_0^n sign(\varepsilon(k))$
end
$T_{PMU}(n) = T_{PMU}(n) + \Delta T + \gamma(n)$
```

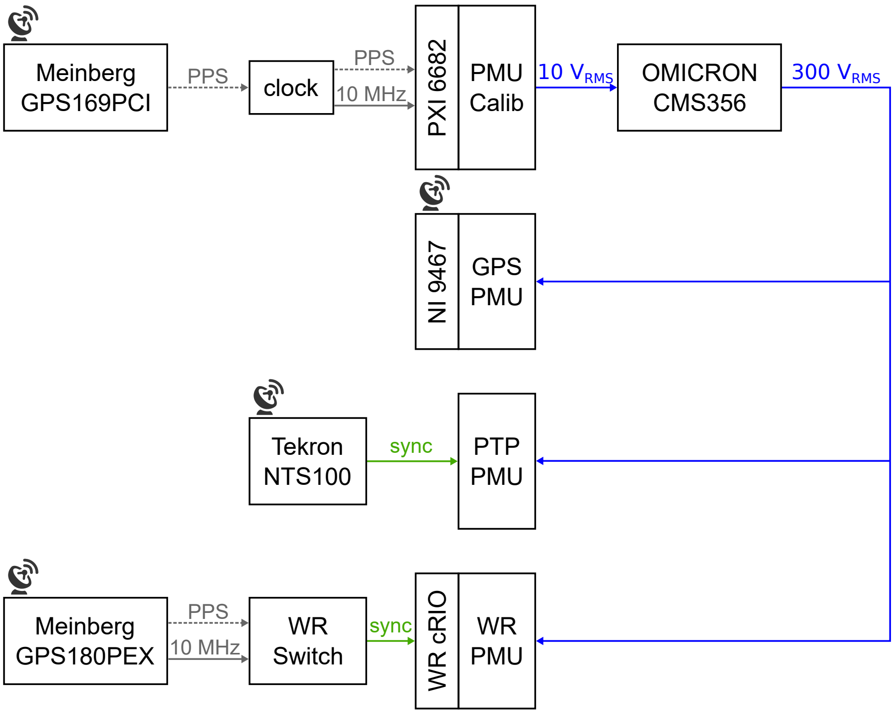

Figure 6.6 – Measurement setup for the performance assessment. The PMU calibrator generates user-defined test waveforms, that are amplified up to 300 V by the CMS 356 OMICRON amplifier, and then supplied to the three considered PMUs, relying on GPS, PTP and WR time dissemination.

6.1.4 Performance Assessment

The performance of the described PMUs is assessed using the test-bed illustrated in Fig. 6.6, i.e., by means of the dedicated PMU calibrator described in Chapter 5 that enables the validation of the conformity of the PMU under test with respect to the IEEE Std. C37.118 [19]. The calibrator, generates reference signals whose true parameters are known with a TVE in the order of 10^{-4}%, obtained in case of static signals.

The forward path of the calibrator generates a set of static reference waveforms characterized by a sampling rate of 500 kHz, peak amplitude of 10 V, 0 rad phase and frequency varying in the range [47.5, 52.5] Hz (i.e., the PMU passband considering a nominal frequency at 50 Hz and the reporting rate of 50 fps). These signals are amplified by a CMS-356 OMICRON precision voltage and current amplifier, characterized by an amplification gain of 30, and simultaneously acquired by the three PMUs under test. The final waveforms are characterized by a signal-to-noise-ratio (SNR) of 85 dB. It is worth pointing out that, as highlighted in Fig. 6.6, the master clocks of the three PMUs and the one of the PMU calibrator use separate GPS receivers, thus guaranteeing the non correlation among the various absolute times.

As known, the uncertainty requirements are expressed in terms of TVE, Frequency Error (FE), and ROCOF Error (RFE). However, the analysis of amplitude and phase error separately provides a deeper understanding about eventual error sources. More specifically, every inaccuracy related to a poor time-synchronization of the PMU under test, expresses itself in a phase error. Also, since the synchrophasor estimation algorithm and the hardware platform are identical for the three PMUs, the time synchronization protocol mainly affects the phase estimation.

For each PMU configuration and for each nominal frequency the phase estimation accuracy is evaluated over a test duration of 24 hours. The results are presented by means of two performance indicators. First, Cumulative Distribution Function (CDF) of the unbiased normalized phase errors is evaluated[1]. Second, the stability of the adopted time dissemination technology is quantified computing the Allan deviation [146].

To this end, the M-sample variance is considered, defined as:

$$\begin{aligned}\sigma^2(\tau) &= \frac{1}{M-1}\left[\sum_{m=0}^{M-1}\delta_{\varphi}^2(m,\tau) - \frac{1}{M}\left(\sum_{m=0}^{M-1}\delta_{\varphi}(m,\tau)\right)^2\right]\\ \delta_{\varphi}(m,\tau) &= \frac{\varphi(mT_r+\tau)-\varphi(mT_r)}{\tau}\end{aligned} \tag{6.3}$$

where $\varphi(mT_r)$ is the phase estimate associated to mT_r time instant, expressed as a function of the reporting period T_r, M is the sample number for the variance computation, and τ is the time deviation between two consecutive phase estimates. The Allan variance refers to the specific case where M and T_r are set equal to 2 and τ, respectively, and the Allan deviation is its square root [146]. The phase estimation accuracy is evaluated over different time intervals, varying τ between 10^1 to 10^4 s.

The analysis has been conducted by coupling for several days the three devices with the PMU calibrator and in the following paragraphs, the results are obtained for three different scenarios. The first two paragraphs are meant to evaluate the performance during normal operating conditions and refer to P- and M-class PMUs, respectively. The third paragraph instead refers to P-class PMUs during the worst-case condition that has been recorded over various tests and is meant to assess the maximum phase uncertainty that can be introduced by GPS, PTP and WR synchronization schemes.

Normal Operating Conditions, P-class

The first test compares the phase estimation accuracy of P-class PMUs obtained in normal operating conditions as a function of the fundamental frequency. Specifically, Fig. 6.7a, 6.8a and 6.9a present the phase error CDFs for 50, 47.5 and 52.5 Hz, respectively.

Independently from the fundamental frequency values, the WR enables us to keep the normalized phase error within ±15 μrad, whereas PTP and GPS might exceed 30 μrad. It is also

---

[1] The phase errors are normalized by their mean value calculated in the considered observation interval. By doing so, the analysis focuses on the standard deviation of the phase error. Indeed, any absolute phase discrepancy can be properly compensated at the PMU output.

worth observing that the GPS tends to outperform the PTP and this performance discrepancy becomes more evident, as non-nominal test conditions are taking place, when the sampling rate is not locked to the fundamental frequency.

In the same test conditions, Fig. 6.7b, 6.8b and 6.9b evaluate the Allan deviation as a function of the time interval τ. Coherently with the previous results, the WR is characterized by the lowest variability, whereas PTP and GPS provide comparable performance. For instance, at 50 Hz the WR Allan deviation decreases from 0.5 μrad up to 0.7 nrad, when the time interval is enlarged from 10^1 up to 10^4 s. This performance enhancement provided by the WR time dissemination becomes more significant as τ increases, particularly when asynchronous sampling conditions are considered.

Normal Operating Conditions, M-class

Given a fundamental frequency of 50 Hz, Fig. 6.10a and 6.10b show the CDF and the Allan deviation for the M-class configuration, respectively. The choice of limiting the analysis to a synchronous sampling condition enables us to limit the uncertainty coming from the synchrophasor extraction process and focus primarily on the stability of the time synchronization source.

As expected, the M-class configuration provides better performance than the P-class one, leading to errors roughly 1 μs lower for every considered timing technology. As shown in Fig. 6.10a the distribution of the errors is in this case sharper and less disperse than the results presented previously. As regards the Allan deviation, the WR still provides enhanced stability, over any of the considered time intervals.

Worst-Case Operating Conditions, P-class

In the third scenario, the worst-case performance associated to each time dissemination is extracted and compared in order to experimentally determine the accuracy limit provided by GPS, PTP and WR-PMUs. As in the previous section, the analysis is limited to coherent sampling, i.e., keeping the fundamental frequency to the nominal value of 50 Hz.

As shown in Fig. 6.11a, the three PMUs are characterized by different trends of the distribution of the absolute phase error. As expected, the PTP-PMU is characterized by the most disperse distribution, with a standard deviation of 26 μrad. The GPS and PTP-PMUs are characterized by non-symmetric tails and a non-null mean value, because the time evolution of the phase errors is characterized by a non-symmetric trend with respect to the respective mean value. The WR-PMU instead always reports a symmetric behavior, thus leading to a balanced CDF. Finally, the WR-PMU exhibits the sharpest CDF trend with a standard deviation of 8 μrad, demonstrating once again that such synchronization technique is the most deterministic one.

In general, the results in Fig. 6.11a reflect the accuracy specification of the adopted time

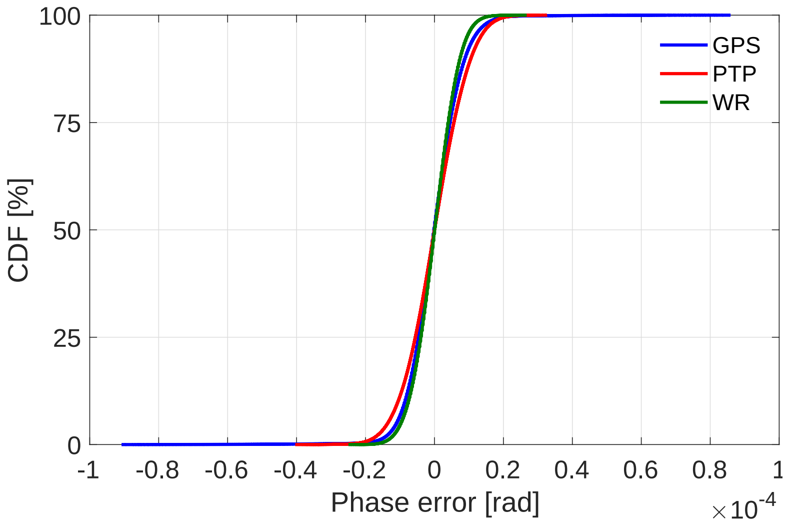

(a) Phase error CDF at 50 Hz.

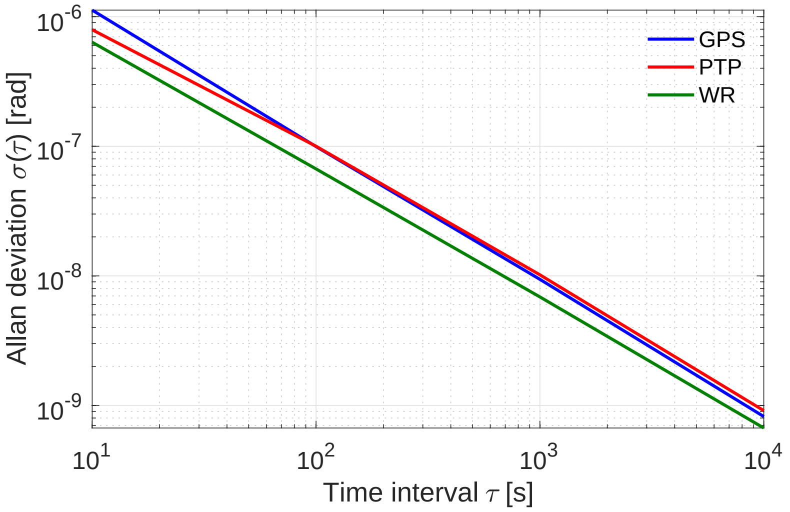

(b) Phase error Allan deviation at 50 Hz.

Figure 6.7 – P-class: phase error cumulative distribution functions (top) and phase error Allan deviation as a function of the time interval τ (bottom) as provided by GPS (blue), PTP (red) and WR (green) PMUs over a 24-hour test. The test waveform consists of a single fundamental tone whose amplitude, frequency and phase are set equal to 300 V, 50 Hz, and 0 rad, respectively.

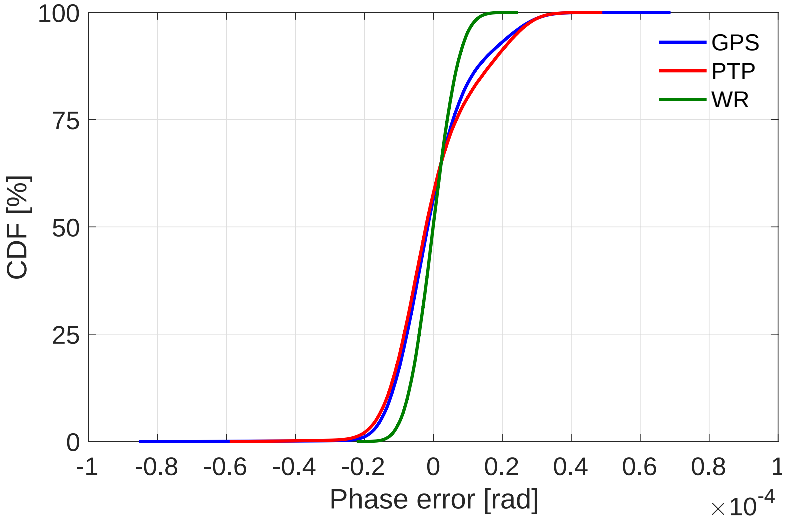

(a) Phase error CDF at 47.5 Hz.

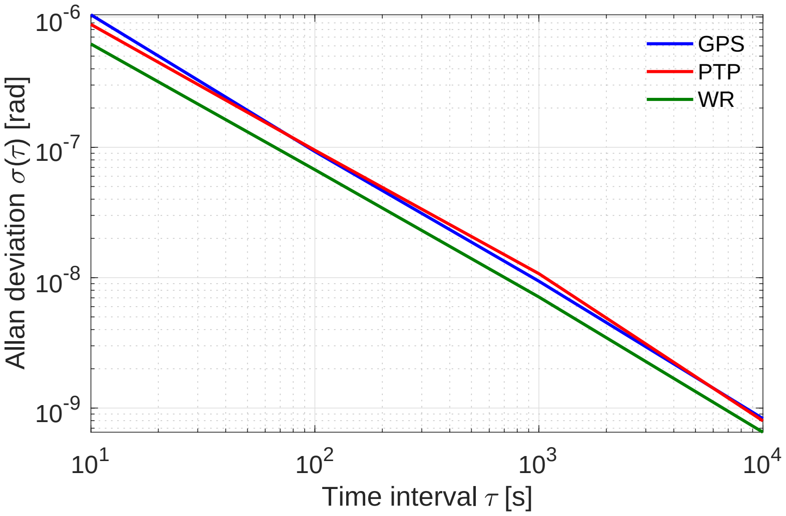

(b) Phase error Allan deviation at 47.5 Hz.

Figure 6.8 – P-class: phase error cumulative distribution functions (top) and phase error Allan deviation as a function of the time interval τ (bottom) as provided by GPS (blue), PTP (red) and WR (green) PMUs over a 24-hour test. The test waveform consists of a single fundamental tone whose amplitude, frequency and phase are set equal to 300 V, 47.5 Hz, and 0 rad, respectively.

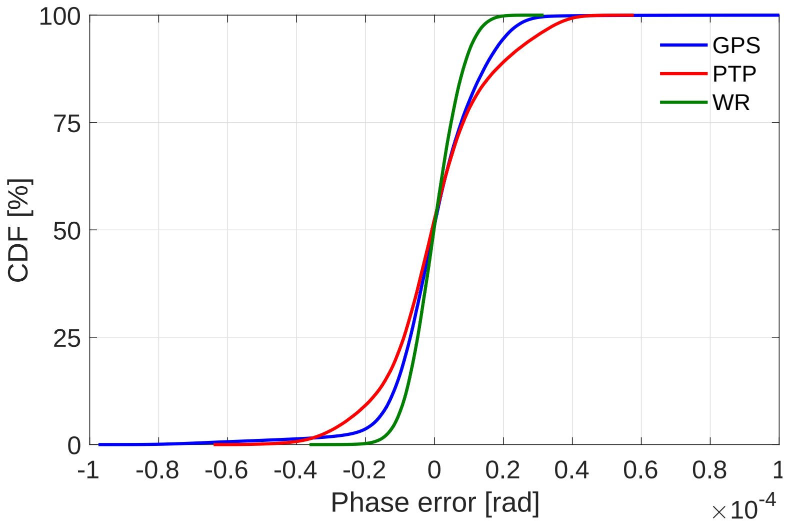

(a) Phase error CDF at 52.5 Hz.

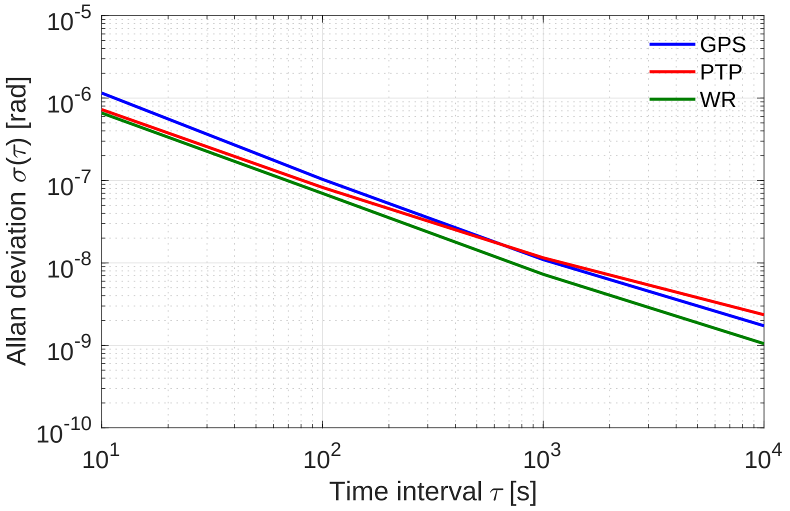

(b) Phase error Allan deviation at 52.5 Hz.

Figure 6.9 – P-class: phase error cumulative distribution functions (top) and phase error Allan deviation as a function of the time interval τ (bottom) as provided by GPS (blue), PTP (red) and WR (green) PMUs over a 24-hour test. The test waveform consists of a single fundamental tone whose amplitude, frequency and phase are set equal to 300 V, 52.5 Hz, and 0 rad, respectively.

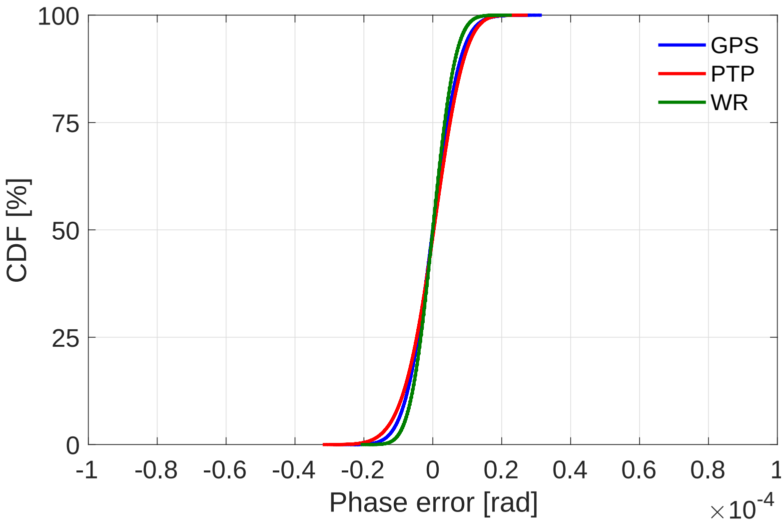

(a) Phase error CDF at 50 Hz.

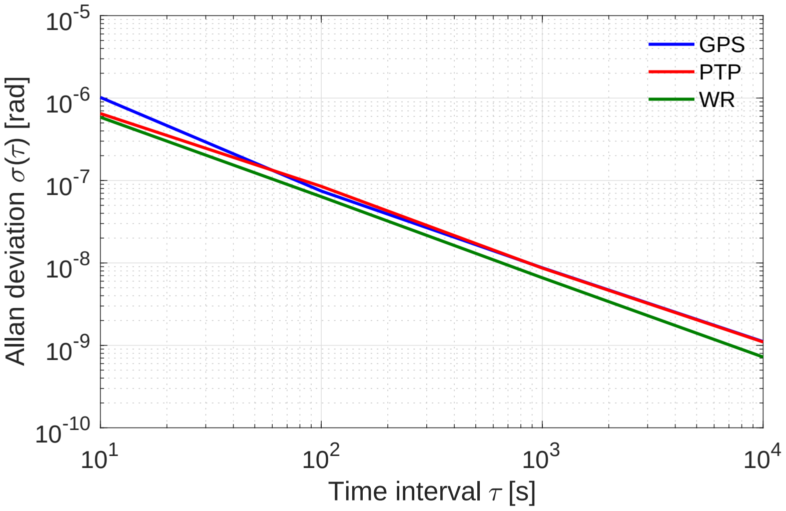

(b) Phase error Allan deviation at 50 Hz.

Figure 6.10 – M-class: phase error cumulative distribution functions (top) and phase error Allan deviation as a function of the time interval τ (bottom) as provided by GPS (blue), PTP (red) and WR (green) PMUs over a 24-hour test. The test waveform consists of a single fundamental tone whose amplitude, frequency and phase are set equal to 300 V, 50 Hz, and 0 rad, respectively.

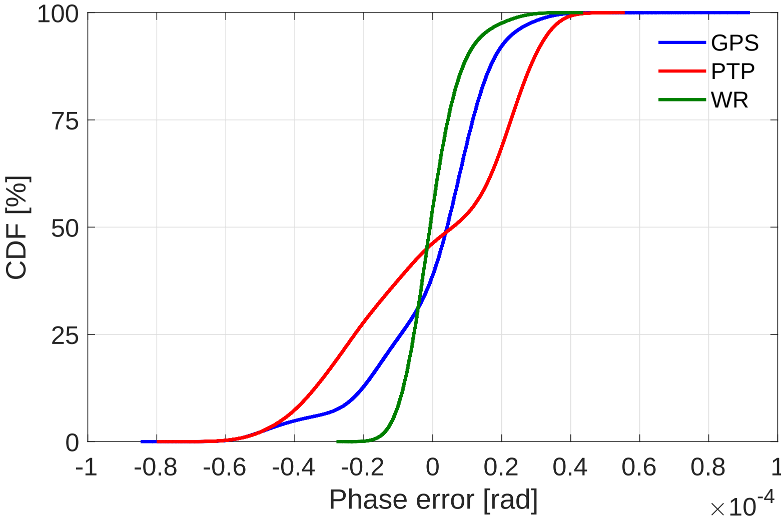

(a) Phase error CDF at 50 Hz.

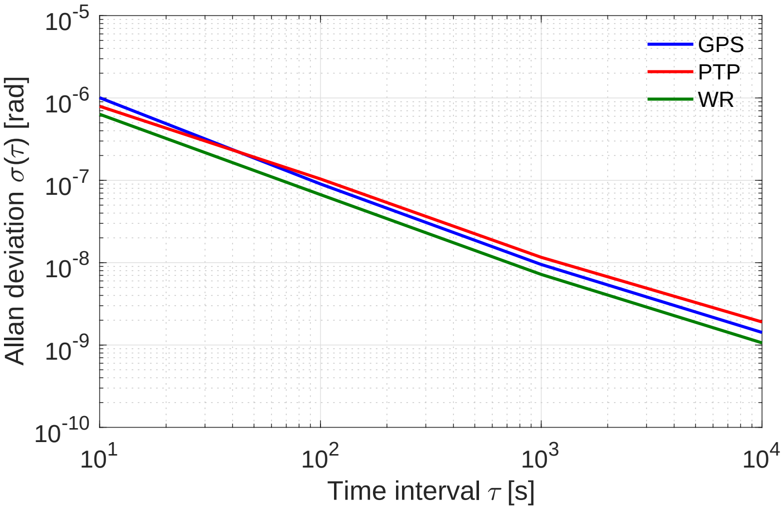

(b) Phase error Allan deviation at 50 Hz.

Figure 6.11 – Worst-case scenario: phase error cumulative distribution functions (top) and phase error Allan deviation as a function of the time interval τ (bottom) as provided by GPS (blue), PTP (red) and WR (green) PMUs over a 24-hour test. The test waveform consists of a single fundamental tone whose amplitude, frequency and phase are set equal to 300 V, 50 Hz, and 0 rad, respectively.

Table 6.3 – Phase Error [μrad]- Statistical Distribution Features

	Normal				
	P-class			M-class	P-class
	47.5 Hz	50 Hz	52.5 Hz	50 Hz	50 Hz
min	-85.5	-90.8	-97.5	-28.9	-84.7
GPSmax	68.8	85.9	109.2	31.9	92.0
std	11.3	7.4	13.3	6.4	18.1
min	-59.1	-40.4	-64.1	-31.6	-80.1
PTPmax	49.0	32.6	57.8	27.5	55.7
std	12.3	8.2	15.7	7.2	25.9
min	-22.2	-25.0	-36.3	-21.1	-27.9
WR max	24.6	26.7	31.6	22.9	43.6
std	5.9	5.8	7.1	5.1	8.1

synchronization techniques, in the sense that the lower the accuracy of the timing module, the more disperse the phase error distribution. The error introduced by the algorithm is dominating and masking the potential improvement of the phase estimate given by this the WR technology. Nevertheless, an improvement of 10 μrad is achieved for the WR-PMU with respect to the GPS counterpart.

Similar considerations are valid also for the Allan deviations presented in Fig. 6.11b: independently from the considered time interval τ, the WR confirms to be characterized by a lower phase variability (equal to 1 nrad at 10^4 s), whereas PTP and GPS provide nearly coincident performance.

Finally, Table 6.3 reports the main features of the phase error statistical distributions obtained in the different operating conditions and PMU configurations. For each time dissemination technique and fundamental frequency value, the minimum and maximum phase errors are computed, as well as its standard deviation. In all the considered configurations, the WR outperforms PTP and GPS, with a worst-case standard deviation of 8.1 μrad. In this regard, it is worth noticing how the WR synchronization produces a phase variability that is comparable with the synchrophasor accuracy limit (i.e., 5 μrad for P-class and 4 μrad for M-class). In other words, the WR-PMU is capable of minimizing the time dissemination uncertainty contribution and thus optimizing the performance of the actual synchrophasor estimation algorithm. It is also interesting to observe that GPS is typically characterized by a lower standard deviation, but a larger min-max range than PTP. This phenomenon is due to the fact that even if GPS estimates are characterized by a reduced variability, they might present sudden variations or outliers that affect the definition of maximum and minimum error.

6.1.5 Discussion

The Section presented the use of the WR time synchronization protocol for synchrophasor networks. The WR is characterized by a time uncertainty of 1 ns, that is superior to those of state-of-the-art time dissemination technologies used for PMU applications, i.e., 50 ns for GPS and 1 μs for PTP. The IEEE Std. C37.118 requires a maximum synchronization uncertainty of 1 μs for PMUs operating in transmission networks, but this value is lowered to 10 ns for distribution PMUs. Therefore, the WR is a suitable time dissemination technique for PMUs operating at any power system level.

The Section presented the integration of the WR protocol in a specifically developed WR-PMU, and assessed its performance with respect to a GPS-PMU and a PTP-PMU. The three PMUs were characterized by the same synchrophasor estimation algorithm and by the same hardware platform, with the exception of the time synchronization technique. The results demonstrated the advantage of using the WR instead of GPS, as it is characterized by a more deterministic phase error, experimentally quantified in 8 μrad.

6.2 Time Deterministic Phasor Data Concentration

The Phasor Data Concentrator (PDC) is a key element of any synchrophasor network, as it is located between the various PMUs and the applications consuming the synchrophasor data [178]. If not properly designed, the PDC might represent a “single point of failure” for the associated wide-area monitoring and control applications and eventually increase their overall latency way above the maximum allowed limits.

According to the IEEE Guide C37.244-2013 [178], the most relevant functionalities of a PDC are *data aggregation* and *data pushing*, which are meant to mitigate the latency variations introduced by the various components of the synchrophasor network. Data aggregation enables to aggregate data coming from multiple PMUs into a time-aligned dataset and is typically implemented by means of a dedicated buffer. Time-alignment is not mandatory but is a de-facto standard PDC function that leverage the PMU measurement time-stamps. Data pushing enables to forward the time-aligned dataset to the subsequent applications and is typically performed by setting the so-called *PDC wait time*, i.e., the amount of time the PDC actively waits for data frames with a given time-stamp. Once the dataset is completely filled, or a maximum wait time has elapsed, the PDC pushes the dataset to the supplied applications. In [178] two logic are defined for setting the PDC wait time: an *absolute* time logic, where the data pushing is performed once a specific UTC time is reached, and a *relative* time logic, in which the PDC waits for a specified relative time triggered by an event, that could be the arrival of the first data with a specific time-stamp.

Within this context, this Section presents the architecture of a PDC that implements both the data aggregation and data pushing functions as presented in [178]. Then, it compares the timing performance of the aforementioned logic in terms of reliability, determinism and reduction of the overall latency, by validating them in two real PMU deployments that adopt different telecom infrastructures. The first one is based on optical fiber links that transmit synchrophasor data measured by 15 PMUs installed in the sub-transmission network of the city of Lausanne, Switzerland. The second one adopts a 4G LTE wireless infrastructure to support the data streaming of 10 PMUs installed in a distribution network supplying the city of Huissen, the Netherlands.

The Section includes results of publications [16, 17] and is structured as follows. Section 6.2.2 analyzes and decomposes the synchrophasor network latencies in their various contributions to highlight the influence of the PDC latency. Section 6.2.3 illustrates the proposed PDC architecture. Section 6.2.4 presents the test bed of the two field trials and the performance assessment.

6.2.1 State of the Art and Related Works

The functional and performance requirements of a generic PDC are defined in [178]. Nevertheless, this guide does not contain any implementation detail. In this respect, [179] and [180] present two possible PDC designs and highlight the relevant inconsistencies that could arise from an inaccurate PDC implementation and eventually affect the overall system operation. In [181] and [182] test methodologies for validating core PDC features, together with the functional and communication needs of a generic PDC are proposed. Reference [183] provides the general design for a flexible PDC integrating a relative time data pushing logic, including a database for synchrophasor data and a graphical user interface.

Several recent works pay particular attention to the PDC wait time. In [184] an optimal stopping approach to the PDC relative wait time is presented in order to maximize the throughput of synchrophasor data delivery. In [185] and [186] a similar approach is proposed for a PDC used for wide-area damping control. Reference [187] focuses on the impact of some PDC settings, and particularly the relative wait time, on the timeliness and incompleteness of the outgoing data stream.

6.2.2 Synchrophasor Network Latency Analysis

When designing a PMU-based monitoring system, one important design parameters is the *PDC reporting latency*, i.e., the time difference between the instant a set of synchrophasor data characterized by the same time-stamp is pushed by the PDC to the subsequent applications and the time-stamp itself [188]. Depending on the supplied applications, this parameter can vary between few hundreds of milliseconds (e.g., hard real-time applications like synchrophasor-based fault management systems [74]), to few tens of seconds (e.g., soft real-time applications like voltage control [189]) [157].

The PDC reporting latency can be decomposed in its individual contributions in order to have a better understanding of the various latency sources (see Fig. 6.12):

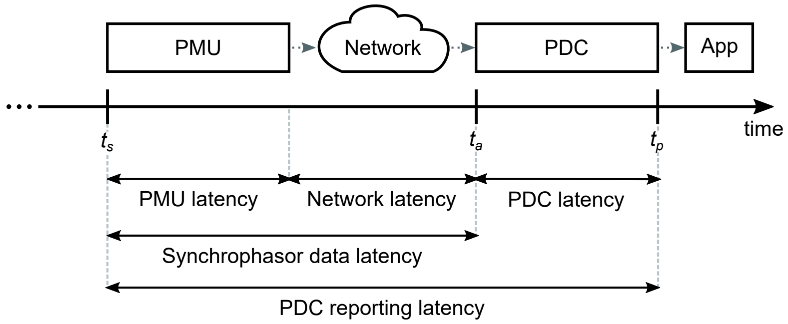

Figure 6.12 – The PDC reporting latency decomposed in its individual contributions, being t_s the synchrophasor time-stamp, t_a the data frame arrival time and t_p the dataset push time.

- The *PMU measurement reporting latency* is defined in the IEEE Std. C37.118 [19] as the time delay between the instant a specific event occurs in the power system and the instant the same event is reported by the PMU. This latency is mainly influenced by the adopted window length to estimate the synchrophasor and by the time spent in estimating the synchrophasors. It can be reduced by shortening the window length and, independently of the selected synchrophasor estimation technique, by adopting more performing hardware platforms. However, such a contribution turns out to be quite deterministic compared to others.

- The *communication network latency* is the time difference between the instant a PMU has transmitted a data frame on its physical channel and the instant the same data frame hits the PDC network interface. Together with the PMU measurement reporting latency, it defines the so-called *synchrophasor data latency*. Synchrophasor data can be carried over any wired or wireless communication layer that has sufficient bandwidth and reduced data transmission latency to support PMU data streams characterized by a specific reporting rate and message size. Depending on the adopted information and communication technology, this contribution might introduce relatively high delays and non-deterministic latency variations.

- The *PDC latency* is defined as the time difference between the instant a time-aligned dataset is pushed to the supplied applications and the instant the first message with a given time-stamp hits the PDC. The PDC latency is composed of two contributions: (i) the PDC wait time that starts when the first message with a specific time-stamp enters the PDC and ends when the last one arrives or the associated timeout expires; (ii) the PDC processing time, i.e., the amount of time needed by the PDC to complete the production of an aggregated dataset. Typically the former by far outweighs the latter. It is worth pointing out that a well designed PDC does not introduce any latency: it simply acts as a buffer that mitigates the real-time variation of the synchrophasor data latency, by waiting the necessary amount of time to gather most of the incoming data frames characterized by the same time-stamp. Reference [178] does not define a specific limit value to the PDC latency, it just emphasizes the fact that it should be as low as possible.

6.2.3 The Proposed PDC Architecture

A high-level design of the proposed PDC architecture is shown in Fig. 6.13. It implements most of the functions described in [178]. However, for the sake of brevity, the focus is only on those affecting the PDC reporting latency and the data incompleteness.

For each connected PMU, the PDC opens a socket (UDP or TCP) on a specific local port and continuously listens to incoming PMU data frames. When a new datagram is received, data validation is performed and invalid frames are discarded. The frame follows a different path based on its type. Once the configuration frame for a given PMU is received, the parsing of data frames coming from that specific PMU can start (as it is known, configuration frames enable the PDC to interpret the data frames). Finally, the PDC time-aligns the data and pushes the aggregated dataset to the supplied applications.

To accomplish the data aggregation and data pushing functions, a circular fixed-size data buffer is adopted (see Fig. 6.14). The buffer is implemented as a 2D array, having N columns, one for each PMU, and M rows, one for each stored time-stamp. During the initialization phase, a specific column of this buffer is assigned to each PMU data stream, based on the stream IDCODE, a number that identifies a specific PMU data stream [21]. The number of rows M is hereafter called buffer depth and represents the amount of time-stamps that are stored in the buffer. The buffer history length T_h can be derived from the buffer depth and the PMU reporting rate as $T_h = M/F_r = M \cdot T_r$, being $F_r = 1/T_r$ the PMU reporting rate and T_r the PMU reporting interval. Each row represents a time-aligned dataset gathering data frames with a specific time-stamp t_s from all PMUs. A pointer p points to the next line to be pushed to real-time applications. The line order is such that time-stamps are monotonically increasing within the circular buffer. When the buffer is filled new data overwrites the old one. This avoids to rotate the buffer's elements when data are released.

Stand-alone Logic for Data Aggregation

In the developed PDC, data aggregation is performed with time-alignment. A new data frame is filled in position (m, n) of the buffer, being m the buffer line corresponding to its time-stamp t_s and n the column corresponding to its PMU ID.

Before inserting the data frame in a specific buffer position (m, n), the buffer lines are updated depending on the received time-stamp t_s unless $t_s < t_{min}$, in which case the data frame is discarded. If $t_{min} \leq t_s \leq t_{max}$ the buffer time-stamps are not updated. If $t_s > t_{max}$, the oldest lines are first fed to soft real-time applications and then replaced with the newest ones. In this case, starting from the line characterized by the minimum time-stamp t_{min}, a set of $((t_s - t_{max})/T_r) \in \mathbb{N}$ empty lines, characterized by newer time-stamps up to t_s, overwrites the older ones. If a data-frame characterized by a time stamp greater than the actual UTC time is received (i.e., a time-stamp coming from the future), the data frame is discarded. This plausibility check is possible only by synchronizing the PDC to an absolute time reference.

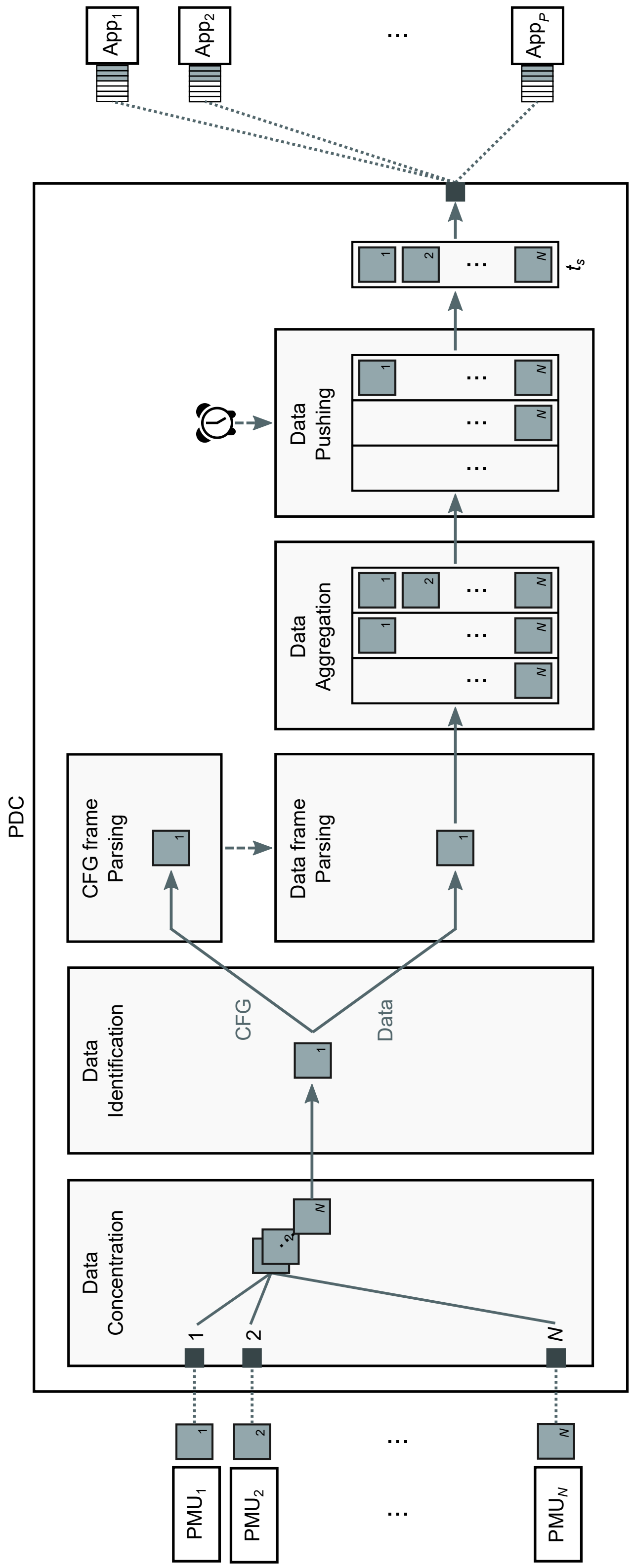

Figure 6.13 – Architecture of the proposed PDC collecting data frames from N PMUs and pushing time-aligned datasets to P applications.

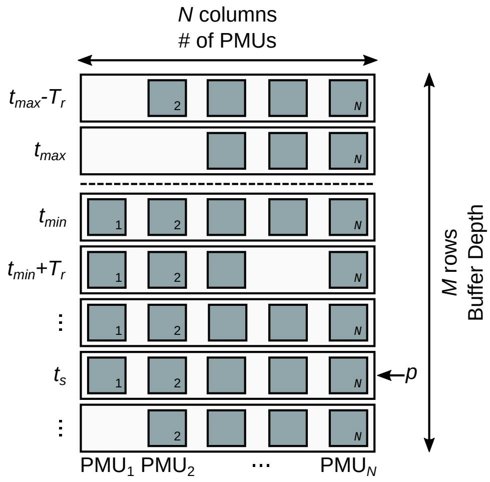

Figure 6.14 – Layout of the circular buffer used to aggregate and time-align the incoming data flows generated by N PMUs. It can store up to M time-aligned datasets characterized by time-stamps in the range $t_{min} < t_s < t_{max}$. A pointer p points the next line to be pushed.

Such a data aggregation logic, that overwrites older lines whenever a newer time-stamp is received at the PDC, gathers data frames independently of the adopted data pushing logic without causing any memory leak.

Absolute and Relative Time Data Pushing Logic

In order to present a possible implementation of the absolute and relative time data pushing logic, let us consider the aggregation process of data frames characterized by time-stamp t_s coming from a set of N PMUs (see Fig. 6.15). Let us also assume that the arrival times of the first and last data frames hitting the PDC are $t_{a,i}$ and $t_{a,j}$ respectively, i.e., the arrival times of the data frames generated by the i-th and j-th PMUs.

In case an absolute time data pushing logic is adopted, the PDC must be synchronized to an absolute time reference. The wait time refers to the data frames time-stamp t_s and elapses at:

$$t_p = t_s + T_{abs} \tag{6.4}$$

being t_p the PDC push time and T_{abs} the absolute PDC wait time.

Besides, in case a relative time data pushing logic is adopted, the wait time counter is triggered by the reception of the first data frame characterized by a time-stamp t_s and elapses at time:

$$t_p = t_{a,i} + T_{rel} \tag{6.5}$$

being T_{rel} the relative wait time. From equation (6.5), it is evident that adopting a relative time data pushing logic might not always guarantee to fulfill the latency requirements of the supplied application, which might be affected by the real-time variations of the network latency (i.e., the jitter of the inter-arrival times).

At time t_p the aggregated dataset is pushed to the supplied applications and the pointer p is incremented (modulo the buffer depth M). The introduction of the pointer p guarantees that, even if data frames arrive in the PDC out of order, the time-aligned datasets are always pushed based on the time-stamp order. For both absolute or relative time data pushing logic, when the wait time has elapsed, the time-aligned dataset is pushed even if some data have not yet reached the PDC and the missing data is indicated by rising a proper flag. In such a case, the subsequent applications are assumed to cope with incomplete datasets by using replacement techniques or historical information (e.g. [190, 191]). Consequently, a delayed packet that reaches the PDC when its corresponding dataset has already been pushed, is lost and it is no longer available for further applications.

Even though this Section does not deal with the optimal selection of the PDC wait time, it is evident that this parameter plays a crucial role in the overall PDC design. It must be selected as a trade-off between the desired dataset completeness and the latency requirements of the power system application being served by the PDC. In case of non real-time applications, to reduce dataset incompleteness due to late data arrival, longer PDC wait times can be set, with the consequent increase of the overall latency of the system. Such an approach cannot be adopted for real-time applications and the PDC wait time must be set accordingly.

In the case of absolute time logic, T_{abs} has to be set according to the measured synchrophasor data latency in order to push time-aligned datasets that are mostly complete. In this case the minimum allowed buffer depth is:

$$M = \left\lceil \frac{T_{abs} - T_{min}}{T_r} \right\rceil + 1 \tag{6.6}$$

where $\lceil \cdot \rceil$ represents the ceiling function and T_{min} the minimum possible PMU measurement reporting latency.

Besides, in case of relative time, T_{rel} has to be set according to the measured time needed to receive all data frames of a specific dataset. Similarly to equation (6.6), the resulting minimum buffer length is computed as:

$$M = \left\lceil \frac{T_{rel}}{T_r} \right\rceil + 1 \tag{6.7}$$

Several instances of the presented data pushing logic can run in parallel on the same buffer. Each one has its own PDC wait time setting and its own pointer p. In such a case, the actual buffer depth M is defined by the maximum PDC wait time. Therefore, the data aggregation process in a buffer line that has already been pushed to a hard real-time application continues until the limit allowed by the buffer depth. Consequently, datasets that are more likely to be complete are fed to soft real-time applications (for instance, a local database).

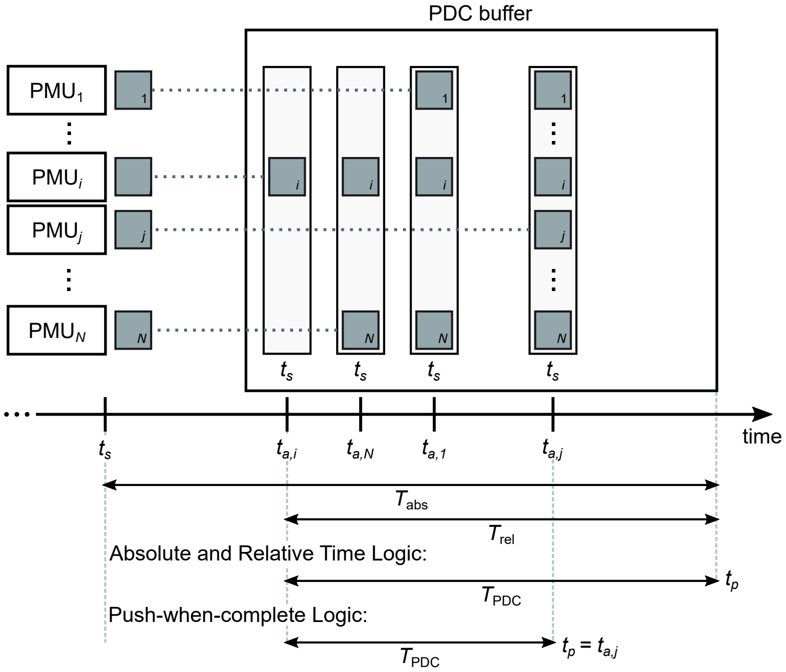

Figure 6.15 – Comparison between the various data pushing logic in the case of a PDC gathering data frames from N PMUs characterized by time-stamp t_s. The arrival times of the first and the last data frame characterized by time-stamp t_s are indicated by $t_{a,i}$ and $t_{a,j}$.

Push-when-complete Logic

If the synchrophasor network is properly designed and the PDC wait time correctly set, most of the datasets are completed before the timeout elapses. According to the logic presented so far, these datasets would keep on waiting in vain for the wait time to elapse before being pushed. In this respect, a consistent approach would push the dataset once it is complete regardless of the wait time. The majority of the datasets will be then pushed according to this logic, unless data frames are lost or delayed. In such a case the absolute or relative time logic would take over and push uncompleted datasets once the PDC wait time has elapsed.

Such a logic has the main advantage of minimizing the PDC reporting latency, that is reduced to the synchrophasor data latency of the latest received data frame, and enables to increase the time budget allocated for the other functionalities.

On the contrary, the main drawback of such an approach is that the data pushing time t_p varies based on the data frames arrival time. Hence, the supplied applications should be designed in order to properly cope with non-deterministic datasets arrival. In this respect the easiest solution is to embed dedicated FIFO (First-In-First-Out) data structures in each one of the supplied applications, in order to take care of the non-deterministic synchrophasor data latency (see Fig. 6.13).

6.2.4 Performance Assessment

The proposed PDC architecture and the presented data pushing logic have been implemented using LabVIEW and experimentally validated in two different field trials. The first is a PMU installation in the 125 kV sub-transmission network of Lausanne, Switzerland, that adopts a telecommunication infrastructure based on optic fiber links. The second refers to the PMU-based monitoring system of a 10 kV distribution feeder located in Huissen, the Netherlands, that exploits a public 4G LTE wireless network. In both field trials, synchrophasor data are streamed using the UDP protocol, as it represents the recommended protocol to deal with the high reporting rates of PMUs, by sacrificing the data reliability to the traffic speed [192].

In order to characterize the latency contributions highlighted in Fig. 6.12, in both field trials the PDC was equipped with a GPS receiver providing absolute time information with a resolution of 1 ms, due to the limited precision of the LabVIEW *get time* function. The data flow was tracked along the whole process by measuring the data frame time-stamps t_s, their arrival times t_a and the PDC push time t_p. The synchrophasor data latency of each data frame and the PDC reporting latency of each time-aligned dataset were computed for the various data pushing logic presented in Section 6.2.3. In particular, four different data pushing logic were examined over an observation window of 24 hours:

1. Absolute time logic (hereafter referred as Logic 1);
2. Absolute time integrating push-when-complete logic (hereafter referred as Logic 2);
3. Relative time logic (hereafter referred as Logic 3);
4. Relative time integrating push-when-complete logic (hereafter referred as Logic 4).

For each field trial, the experimental results are presented by means of three histograms representing the probability density function (PDF) of the following quantities:

a) The aggregated synchrophasor data latency from all PMUs;

b) The comparison between the PDC reporting latency in Logic 1 and 2;

c) The comparison between the PDC reporting latency in Logic 3 and 4.

Also, for each data pushing logic, the data-set incompleteness is presented by means of a table showing the percentage of incomplete data-sets pushed by the PDC during the 24 hours observation window.

In order to properly set the PDC wait time, a preliminary test was performed to measure the characteristic synchrophasor data latencies of both field trials together with their jitter over a time window of 24 hours. This quantity has then been set to guarantee the collection of the majority of the data frames with a particular time-stamp, independently of the adopted data pushing logic.

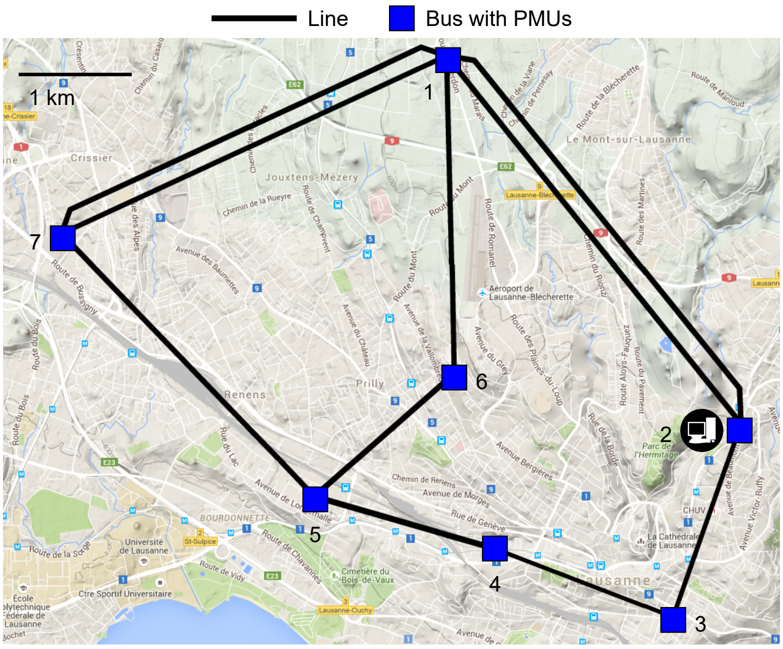

Figure 6.16 – Network topology of the SiL 125 kV sub-transmission grid showing the PMUs and PDC locations.

Experimental validation in the SiL field trial

Services Industriels de Lausanne (SiL), the Distribution Network Operator (DNO) of the city of Lausanne, has deployed a PMU-based advanced and upgradable monitoring system on its 125 kV sub-transmission network that eventually will constitute the backbone of their future SCADA system. The electrical network is composed of 7 electrical substations connected through 15 cabled and overhead lines (see Fig. 6.16) and has been equipped with 15 PMUs that monitor the current flows and nodal voltages (the number of PMUs installed in each substation is proportional to the number of power lines being monitored).

The PMUs are based on the National Instruments Grid Automation System, a programmable CompactRIO platform with PMU capability that meets the IEEE Std. C37.118 measurement requirements for both classes P and M [193]. The PMUs are configured to meet the P-class performance requirements, implementing the synchrophasor estimation algorithm presented in Chapter 3 Section 3.2.3. The PMUs adopt an observation window of 60 ms, stream the data frames with a reporting rate of 50 fps, and are characterized by a mean PMU measurement reporting latency of 44 ms.

Each PMU is equipped with 8 voltage and 8 current channels, therefore can be connected to maximum 2 three-phase (plus neutral) power lines. Depending on the number of lines that are effectively monitored, the total UDP frame size can vary between 134 bytes when streaming a single set of phasors (together with frequency, ROCOF and power values) and 198 bytes when streaming 2 sets of phasors.

The PDC is running on a workstation placed in the control room of SiL (see Fig. 6.16) equipped with an Intel Xeon Processor at 2.4 GHz, 8 GB of RAM and running Windows Server 2008. The PDC supplies a real-time linear state estimator of the sub-transmission grid of Lausanne, a user interface that displays in real-time both the measured and the estimated values and a local database.

The telecommunication physical channel is the legacy optical fiber of SiL. Each substation is equipped with a switch connecting the optical fiber and the PMUs through an Ethernet cable. The communication is established through a dedicated Virtual LAN (VLAN). Such a solution, among the available communication technologies, represents the favorite one when deploying a synchrophasor network, as it guarantees a fast and reliable data delivery in almost any operating condition.

The experimental results are presented in Fig. 6.17. Both the absolute and relative PDC wait time were set by analyzing the aggregated synchrophasor data latencies from all PMUs measured along an interval of 24 hours, as shown in Fig. 6.17a. The histogram represents the aggregated data, because an analysis by PMU data stream showed no significant differences among the various PMUs. As it can be noticed, they are characterized by a mean value of 44 ms and standard deviation of 2 ms. Nevertheless, as more than 99.99% of the packets is received with a latency smaller than 60 ms, the absolute PDC wait time T_{abs} was set to this value. Besides, the average amount of time needed to receive all data frames with specific time-stamp is 3 ms, whereas more than 99.99% of datasets takes less than 20 ms to complete. Hence, the relative PDC wait time T_{rel} was set to 20 ms.

The comparison between Logic 1 and 2 (Fig. 6.17b) shows the improvement introduced by adopting the push-when-complete logic, that enables to reduce the PDC reporting latency by 14 ms. Nevertheless, the latter increases the jitter of the PDC reporting latency that is less deterministic compared to Logic 1 as it is always influenced by the arrival time of the last-received data frame with a specific time-stamp. The push-when-complete logic also reduces the PDC reporting latencies when adopting a relative time data pushing logic, with an average improvement of 15 ms (see Fig. 6.17c comparing Logic 3 and 4). In such a case the PDC reporting latency jitter is slightly improved by adopting Logic 4 but it is still non-deterministic as in case of Logic 1.

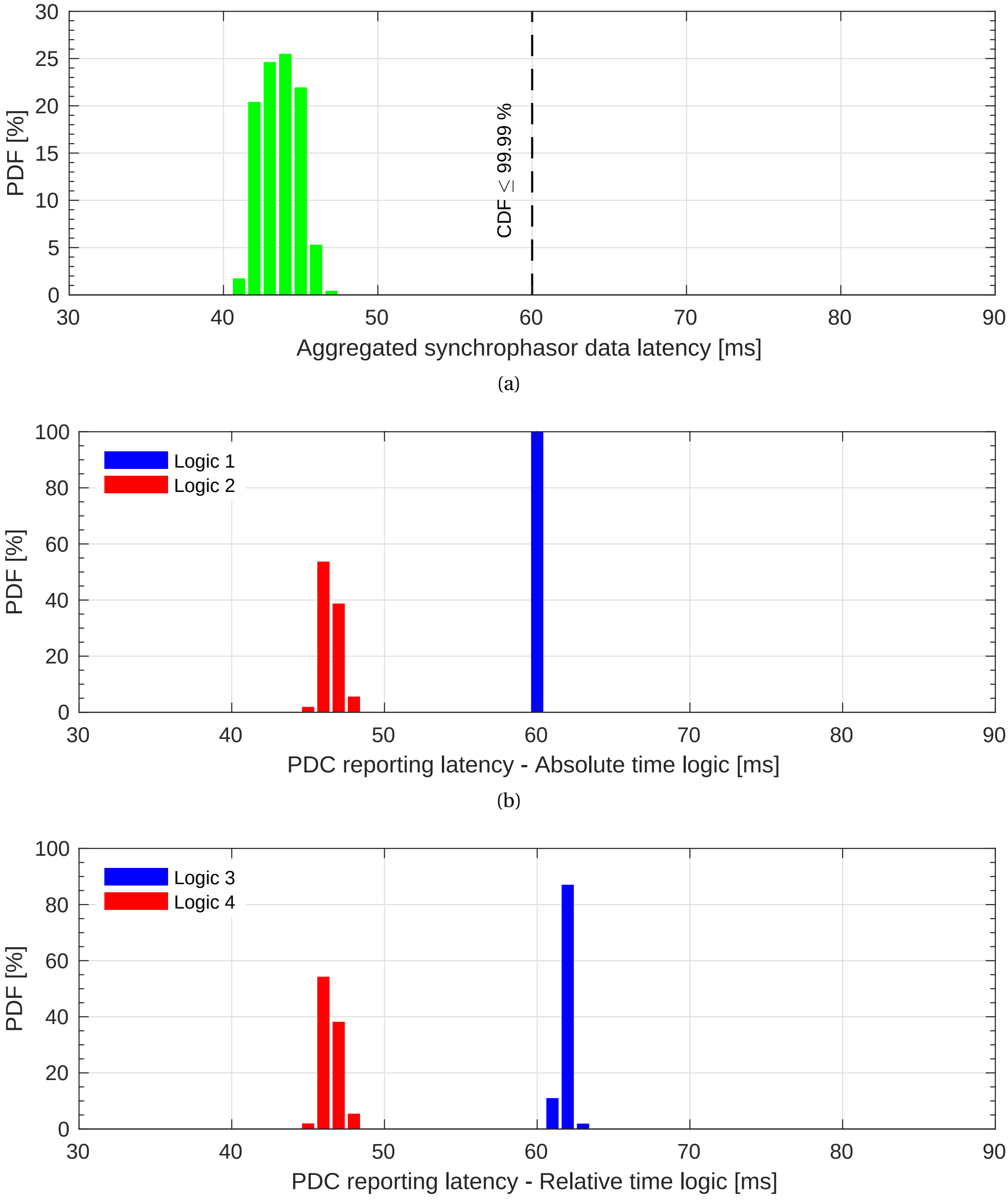

(a)

(b)

(c)

Figure 6.17 – Experimental results in the SiL field trial showing the PDF of: (a) the combined synchrophasor data latencies; (b) the PDC reporting latency when adopting an absolute time logic (Logic 1) and when integrating it with a push-when-complete logic (Logic 2); c) the PDC reporting latency when adopting a relative time logic (Logic 3) and when integrating it with a push-when-complete logic (Logic 4).

Table 6.4 – Dataset incompleteness when adopting different data pushing logic in the SiL field-trial.

	% of incomplete datasets			
Missing data frames	**Logic 1**	**Logic 2**	**Logic 3**	**Logic 4**
1	$2.3{\cdot}10^{-5}$	$2.3{\cdot}10^{-5}$	0	0
2	0	0	0	0
3	$6.8{\cdot}10^{-5}$	$6.8{\cdot}10^{-5}$	$4.5{\cdot}10^{-5}$	$4.5{\cdot}10^{-5}$
>3	$1.5{\cdot}10^{-3}$	$1.5{\cdot}10^{-3}$	$5{\cdot}10^{-4}$	$5{\cdot}10^{-4}$
Total	$1.6{\cdot}10^{-3}$	$1.6{\cdot}10^{-3}$	$5.4{\cdot}10^{-4}$	$5.4{\cdot}10^{-4}$

Based on the adopted PDC wait time setting (T_{abs} = 60 ms, T_{rel} = 20 ms), the incompleteness of the time-aligned data-sets is presented in Table 6.4. As expected, when transmitting data frames through a dedicated wired telecom infrastructure, the data-set incompleteness is negligible and in the order of few parts per million regardless of the adopted data pushing logic. Nevertheless, occasionally the PMU data frames are simultaneously delayed by a considerable amount of time and do not reach the PDC before the expiration of the absolute PDC wait time. This causes the PDC to push empty data-sets in case of Logic 1 and 2, determining a total data-set incompleteness that is one order of magnitude higher compared to Logic 3 and 4.

Experimental validation in the Alliander field trial

Alliander, one of the DNOs of the Netherlands, has deployed, in the framework of the FP7 project C-DAX (Cyber-secure DAta and Control Cloud for Power Grids) [194] a PMU-based monitoring system on a medium voltage (10 kV) distribution feeder. The feeder is composed of 1 primary substation and 17 secondary substations supplying the surroundings of the city of Huissen, connected as shown in Fig. 6.18 by means of underground cables. 10 PMUs, based on the NI CompactRIO platforms have been installed in 10 buses according to Figure 6.18, and are synchronously streaming synchrophasor data with a reporting rate of 50 fps. One PMU is installed in Bus 1 (primary substation) and measures the phase to ground voltages and the three-phase currents flowing in the feeder. The rest of the PMUs are installed in the secondary substations to measure their phase to ground voltages and their absorbed currents. In both cases the PMUs stream two sets of phasors, together with frequency and ROCOF, for a total UDP frame size of 116 bytes. The PMUs are configured to meet the P performance class by adopting the same synchrophasor estimation algorithm running in the SiL field trial. Nevertheless, the meteorological characterization highlighted a PMU measurement reporting latency of 38 ms that is slightly lower than the SiL case due to the lower number of PMU input channels (3 voltages and 3 currents instead of 8 voltages and 8 currents).

PMU data are streamed through a public 4G LTE network, provided by the local service provider Vodafone, to a PDC running in the Alliander data center in Haarlem (see Fig. 6.18). The PDC supplies a real-time linear state estimator, a monitoring user interface and a local database [17]. It is integrated in a Linux RedHat server equipped with an Intel Xeon CPU at 2.00 GHz and 64 GB of RAM that supplies a real-time state estimation process used to monitor the nodal voltage and line power flow variations of the feeder.

In order to support the PMU data stream, each PMU has been connected to dedicated 4G routers from Garderos [195] through the CompactRIO Ethernet switched interface. The Wide Area Network (WAN) interface of the routers connects to the Vodafone network through a dedicated IP address range without any specific service level implemented, so that the PMU traffic is not prioritized. The advantages of such a wireless solution are its high availability, its cost-effectiveness and its easy deployment. Nevertheless, the main drawback is that the latency depends on the real-time availability of the wireless physical mean and on the instantaneous network load, which leads, as it will be demonstrated later, to short-term variations of the network latency and eventual data incompleteness or packet reordering.

Figure 6.19 shows the experimental results. Similarly to what stated previously, both the absolute and relative PDC wait times have been set according to the measured synchrophasor data latencies shown in Fig. 6.19a. As it can be noticed, by adopting a 4G telecom infrastructure, the measured synchrophasor data latency shows a bimodal distribution characterized by a mean value of 70 ms that, as expected, is higher than the SiL case. The same distribution can be observed by analyzing each PMU data stream separately. Such a behavior could be attributed to the varying conditions of the wireless medium (e.g., interference, noise, congestion, etc.) across the duration of the measurement. However, as the public 4G network operator did not provide any additional detail on the network topology and data traffic, a deeper investigation was not possible. Moreover, the measured distribution highlights a behavior that is typical of 4G LTE networks, that is the presence of several outliers scattered through time and through PMU data stream, characterized by a synchrophasor data latency up to 1 second. Figure 6.20 presents a boxplot of the end-to-end latency measured over 24-hours, across all PMU data streams. As can be noticed, the vast majority of values is concentrated in the 20-50 ms range with a median value that is lower than 37 ms and more than 90% of data received within 45 ms. The figure further shows several outliers in the range of several hundreds of milliseconds. For this reason, the absolute PDC wait time has been set to 100 ms, as a trade-off between the lowest achievable PDC reporting latency and an acceptable dataset completeness. In particular, before this time, more than 99.84% of data frames are received at the PDC, which is acceptable for the supplied applications, whereas augmenting the threshold up to 1 second would not bring a significant improvement. Besides, the average amount of time needed to receive all data frames with specific time-stamp is 22 ms, and more than 98.91% of datasets are completed within 40 ms. Hence, the relative PDC wait time T_{rel} was set to 40 ms.

The improvements introduced by adopting the push-when-complete logic are visible for both absolute and relative time logic. In particular, Figures 6.19b and 6.19c show an average reduction of the PDC reporting latency of 18 and 19 ms respectively. This comes at the price of a higher jitter of the PDC reporting latency that, in such a case is highly affected by the real-time variation of the 4G network latency. Looking at the same figures it is also evident

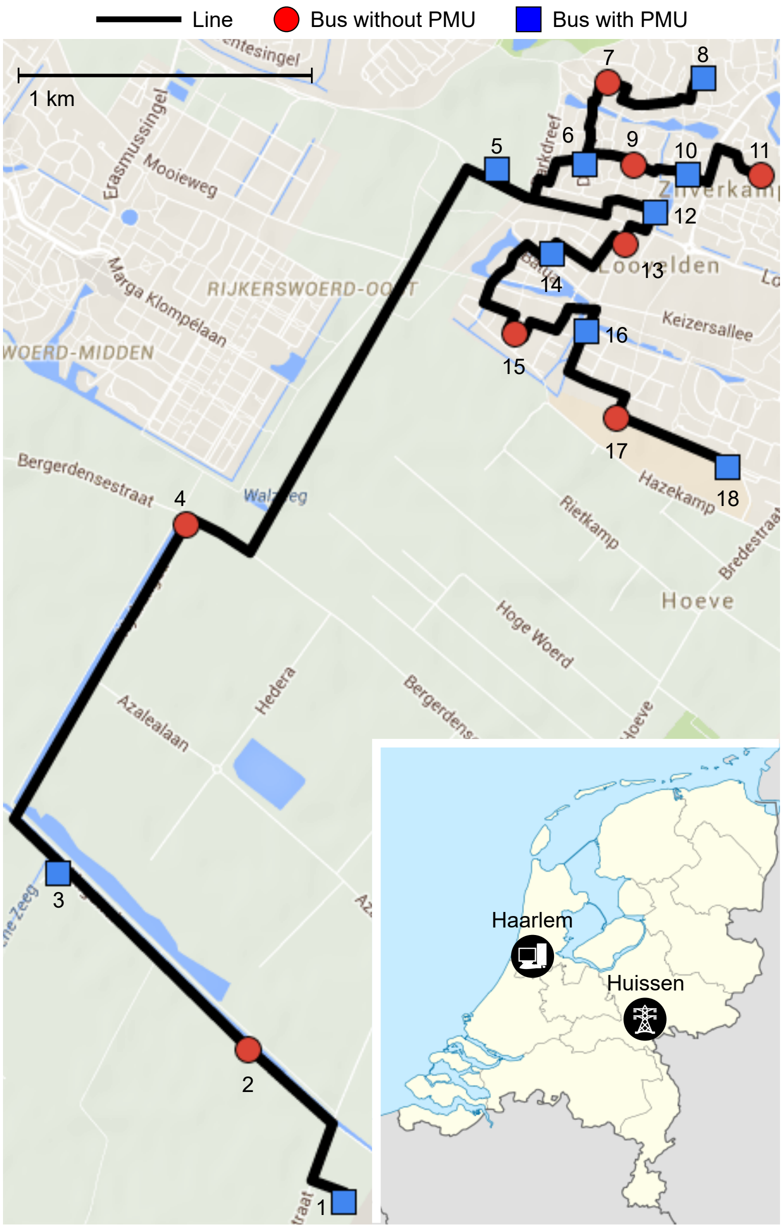

Figure 6.18 – Network topology of the Alliander 10 kV feeder showing the PMUs and PDC locations.

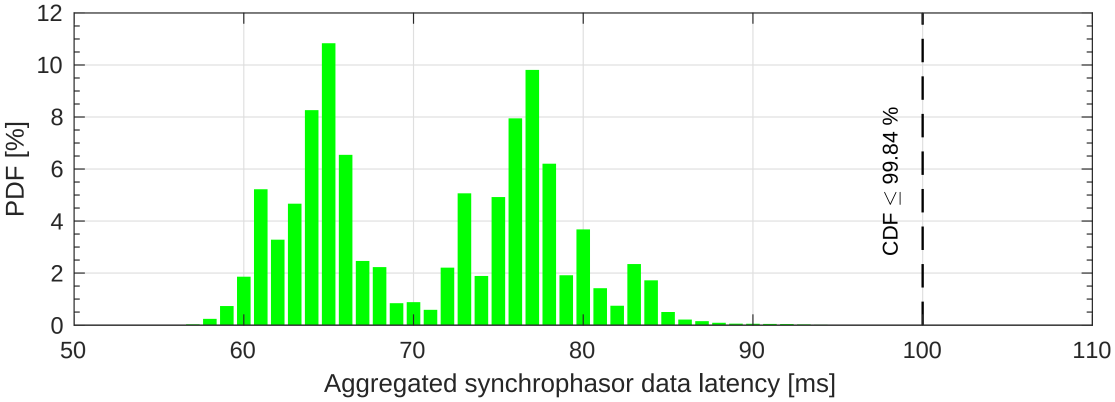

(a)

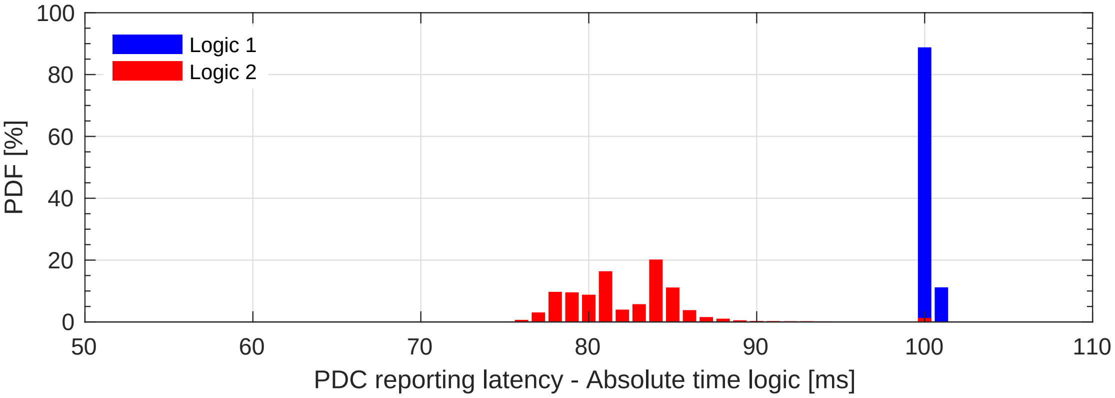

(b)

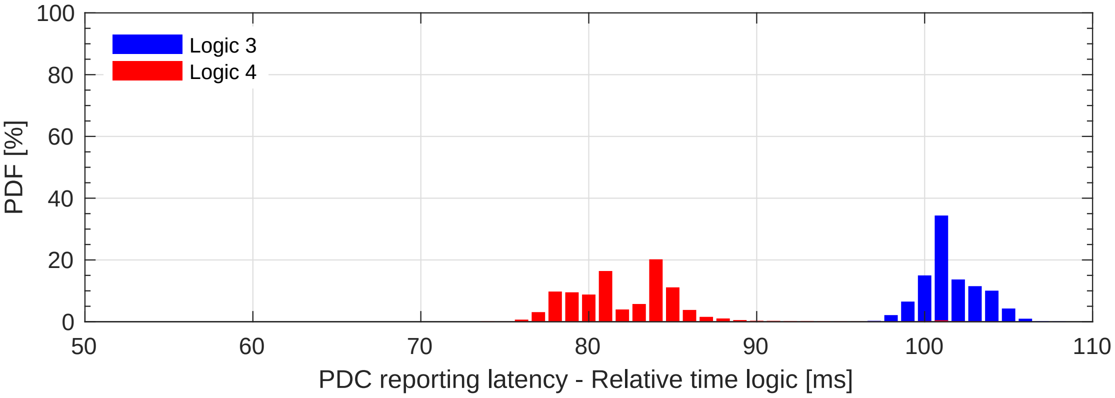

(c)

Figure 6.19 – Experimental results in Alliander field trial: a) PDF of the aggregated synchrophasor data latencies from the 10 PMUs; b) PDF of the PDC reporting latency when adopting an absolute time logic alone (Logic 1) and when integrating the push-when-complete logic (Logic 2); c) PDF of the PDC reporting latency when adopting a relative time logic alone (Logic 3) and when integrating the push-when-complete logic (Logic 4).

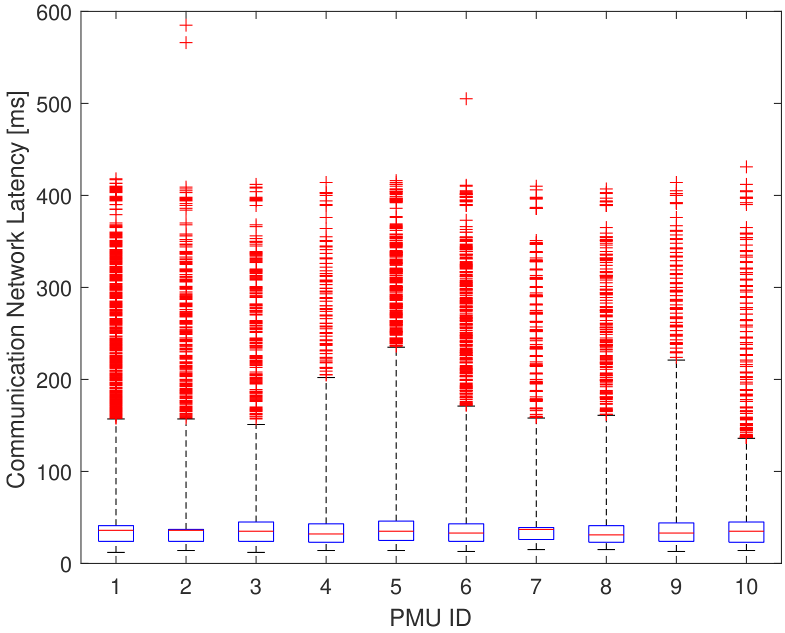

Figure 6.20 – Boxplot representation of the communication network latency per PMU data stream during 24-hours. The bottom and top edges of the boxes have been modified to indicate the 10th and 90th percentiles respectively, whereas the maximum whisker length is specified as 10 times the interquartile range.

Table 6.5 – Dataset incompleteness when adopting different data pushing logic in the Alliander field-trial.

	% of incomplete datasets			
Missing data frames	**Logic 1**	**Logic 2**	**Logic 3**	**Logic 4**
1	1.295	1.295	1.193	1.192
2	0.027	0.027	0.018	0.018
3	0.009	0.009	0.005	0.005
>3	0.042	0.042	0.013	0.013
Total	1.372	1.372	1.229	1.229

how the only logic that guarantees a certain determinism in the PDC reporting latency is Logic 1 as it is the only one that is not influenced by the data frame arrival times.

Finally, the dataset incompleteness is presented in Table 6.5. Compared to the SiL case, the 4G network performance, and particularly its latency variations, considerably affect the dataset completeness that is strongly influenced by the choice of the absolute and relative PDC wait time. In particular, based on the adopted PDC wait time settings, (T_{abs} = 100 ms, T_{rel} = 40 ms), the reported cumulative data incompleteness is around 1.4% in the case of Logic 1 and 2 and around 1.2% in the case of Logic 3 and 4.

6.2.5 Discussion

This Section presented the architecture of a PDC that integrates both the absolute and relative time data pushing logic together with a third one that enables to minimize the PDC latency without decreasing the data completeness. The performance of the developed PDC was experimentally assessed within the context of two real PMU installations that adopt different communication infrastructures. The first one is based on optical fiber links, the second one on a wireless 4G LTE public network.

The assessment of the PDC performance quantified the influence of the adopted telecom infrastructure and PDC data pushing logic on the achievable PDC reporting latency. In particular the experimental validation demonstrated that the push-when-complete logic is characterized by the lowest PDC latency, that is only influenced by the synchrophasor data latency: in the case of optical fiber links the PDC latency is on average 3 ms, whereas in the case of a 4G network, this value increases to 12 ms. Nevertheless, the latency reduction introduced by this logic involves a reduced determinism of the outgoing PDC data flow. As a consequence, in order to correctly operate, this logic has to be properly coupled with dedicated FIFO structures to mitigate the variations in the PDC reporting latency.

On the contrary, the only logic that, independently of the network characteristics, is capable of guaranteeing a constant PDC reporting latency and the consequent mitigation of the synchrophasor data latency variations is the absolute one. In such a case, the PDC reports time-aligned datasets at a constant reporting rate (corresponding to the PMU one) with a PDC reporting latency that is fixed and coincides with the absolute PDC wait time. In such a case, the average PDC latency is 16 ms in the case of optical fiber links and 30 ms in the case of 4G network.

Finally, the Section discussed the importance of properly selecting the PDC wait time that influence both the PDC reporting latency and the dataset completeness. The latter, particularly in the case of non-deterministic networks, might be degraded up to values that do not enable to exploit any longer the availability of synchrophasor data. Regardless of the adopted data pushing logic, in the case of optical fiber links the cumulative dataset incompleteness is in the order of few parts per million, whereas in the case of 4G network is in the order of 1%.

7 Beyond Synchrophasors: Modeling of Power System Signals Using the Hilbert Transform

Power systems are rapidly evolving towards low-inertia grids due to the high share of power electronics-interfaced renewable generation replacing traditional synchronous machines. This transition drastically changes the system dynamics, leading to unprecedented electromechanical transients characterized by rapid frequency changes and, potentially, unstable system behavior. The consequence is that the phasor concept, that is based on a static signal model, may not thoroughly describe the resulting system dynamics. In this evolving scenario, a scientific formulation for the modeling and the analysis of reduced-inertia grids is still missing. Taking inspiration from the theory on analytic signals, the Chapter proposes an innovative approach to formulate power systems governing laws based on the Hilbert transform. Elementary circuit laws are solved with the Hilbert transform and a way to reconstruct the instantaneous power is shown. The performance of the proposed method is assessed in a simulated environment during representative operating conditions, i.e., amplitude modulations, frequency ramps and step changes, in synthetic and real-world data-sets and during a contingency analysis.

The chapter includes results of publication [18].

7.1 Introduction and State of the Art

Power grids are undergoing major changes that call for rethinking the way we manage electricity [26, 27, 28, 29, 30]. The main involved aspect is that power generation is getting decentralized rather than produced in large synchronous power plants. This accounts for large shares of distributed non-synchronous energy providers (typically renewable resources and Battery Energy Storage Systems (BESS)) feeding energy into the grid. The consequence is that electrical systems are largely reducing their aggregated inertia of their generation asset, challenging traditional situational awareness and control schemes [31, 32, 33, 34]. In particular, transient operating conditions are expected to take place more frequently and to be characterized by rapid frequency dynamics.

The three real-world examples already presented in Chapter 2 demonstrate and quantify this evolution [39, 40, 44]. More specifically, Fig. 2.2 shows the frequency decay that took place in South Australia on September 2016 before the system went in blackout, with an estimated ROCOF of roughly -6.25 Hz/s [39]. The figure further shows the effect of the European inter-area oscillation on December 2016, that triggered undamped oscillations at 0.15 Hz [40]. The interconnected European system even with significantly reduced inertia still shows an acceptable frequency behavior. However, in case of split operation after a significant disturbance, a low-inertia scenario would result in unstable frequency behavior [196]. Finally, the figure moves from transmission to distribution systems, that is where the major share of converter-interfaced distributed generation is being installed. The harmonically distorted waveforms produced by the inverter of a BESS installed at EPFL are characterized by a THD of 15% [6, 7].

As discussed in Chapter 2, these operating conditions cannot be described using traditional power system analysis tools because the concept of a single-tone phasor cannot entirely represent signals characterized by broad DFT spectra. However, the capability of accurately describing the power system behavior is strongly related to the paradigm employed to formulate its governing physical laws. The traditional approach towards power system analysis, on the one hand, has driven the development of network modeling techniques based on the concept of phasor. In this sense, the phasor extraction can be seen as a signal compression, driven by the necessity of providing a concise and exhaustive description of the information contained in the time-domain signals. On the other hand, the phasor concept has supported also the implementation of system-awareness applications (e.g., PMUs and state estimators).

In this regard, power system operators are nowadays experiencing difficulties in interpreting phasor data estimated during large transients and are concerned about potentially wrong control actions relaying on those estimates. The emerging trend is to build situational awareness systems that leverage on the raw time-domain data [197]. For instance, many PMU vendors are considering the idea of transferring the so-called point-on-wave data along with the PMU data stream [198, 199, 200]. Those data could be collected at the data concentration point and then further analyzed by highly powerful computation tools. However, this solution, besides being extremely bandwidth-demanding for the underlying telecommunication infrastructure, is simply postponing the problem of successfully compressing the information related to the considered power system event.

Within this context, the Chapter investigates mathematical transformations to go beyond the concept of phasor and envisions a treatise in which the signal dynamics are preserved unaltered and thus can be suitably estimated, potentially leading to novel techniques to operate and control power networks. The Chapter proposes a novel approach inspired by the theory on analytic signals. The method relies on the Hilbert Transform (HT), that enables the tracking of signal dynamics thanks to the possibility to identify the whole frequency-domain spectrum and not only the fundamental frequency component.

In the current literature, the HT has been applied to the analysis of power signals, because of the capability to extract an instantaneous envelope of the signal under analysis [201, 202, 92]. This peculiar property is typically employed, in combination with singular value decomposition [93] or wavelet transform [94], for a nearly real-time monitoring of power quality indices. This property may further lead to the definition of the so-called dynamic phasors [203]. Also, analytic signals have been used to formulate circuit theory fundamental laws supporting frequency adaptive simulation of power system transients [204, 205, 206, 207].

The Chapter discusses the advantages of an HT-based representation of circuit theory governing laws and of typical power system transients. First, it presents elementary circuit theory concepts and shows a way to reconstruct the instantaneous power using the HT. Then, by defining equivalent expressions of signals representing typical power system dynamics, it derives their representation using both Fourier Transform (FT) and HT. Specifically, amplitude modulations, frequency ramps and amplitude steps are considered as representative transient operating conditions. The comparison of the obtained spectra enables us to highlight the limitation of FT-based analysis in non-stationary conditions and, conversely, the HT capability of accurately tracking the evolution of instantaneous power flows. Finally, the validation of these purely theoretical findings is performed by analyzing the results of dedicated time-domain simulations by means of the DFT and HT. In particular, a simple 2-bus system is used to reproduce the three above defined transients as well as real-world datasets. The IEEE 39-bus system is used to include a contingency analysis on a large scale power grid.

The Chapter is structured as follows. Section 7.2 provides the theoretical foundations of the proposed HT-based approach. Section 7.3 describes the validation method. Section 7.4 assesses the proposed approach performance in representative operative conditions. Section 7.5 discusses possible implications of the proposed HT-based analysis.

7.2 Representation of Power System Transients using the Hilbert Transform and Analytic Signals

This section aims at providing the theoretical basis of the proposed investigation. First, in Section 7.2.1 electrical circuit governing laws are presented using the HT. Then, in Section 7.2.2 typical power system transients using the FT and HT are formulated, showing the potential of relying on an HT-based approach. Finally, in Section 7.2.3 a way to reconstruct the true instantaneous power using analytic signals is presented, therefore proving the applicability of the HT for studying power system dynamics. It is worth pointing out that the theoretical foundations regarding the Hilbert transform are presented in Chapter 4 Section 4.2.

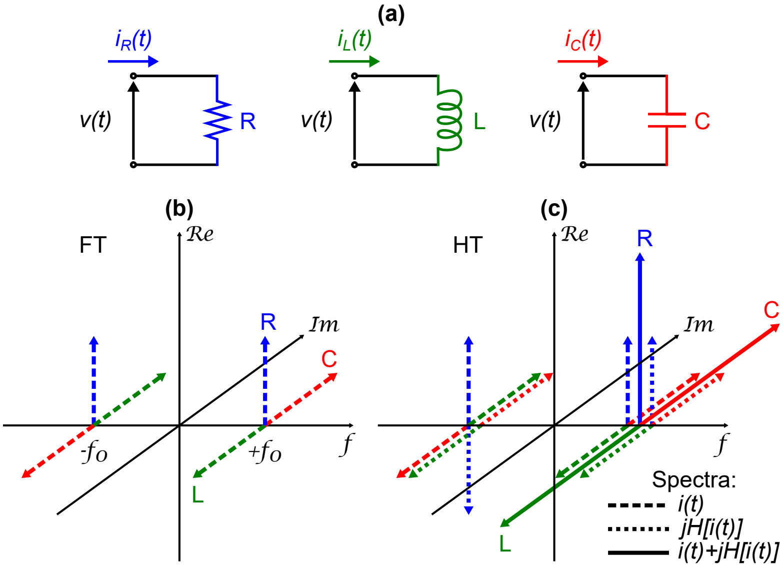

Figure 7.1 – Elementary circuit theory: resistive, inductive and capacitive bipole (a). Frequency domain representation of current flowing though R (blue), L (red), C (green) using the FT (b) and the HT (c). The dashed phasors represent the spectrum of the current $i(t)$, the dotted phasors their Hilbert transform $j \cdot \mathscr{H}[i(t)]$ and the solid phasors represents the corresponding analytic signals $\hat{i}(t) = i(t) + j \cdot \mathscr{H}[i(t)]$.

7.2.1 Elementary Circuit Theory

Some observation can be made regarding elementary circuit theory that can inspire the definition of the fundamental Kirchhoff's laws using the HT. Let us consider a generic passive bipole supplied by voltage $v(t)$ on its terminals (see Fig. 7.1(a)):

$$v(t) = V \cos(\omega_0 t) \tag{7.1}$$

Let us consider the current i_R flowing through a generic resistor R:

$$i_R(t) = v(t)/R = I_R \cos(\omega_0 t) \tag{7.2}$$

being $I_R = R/V$. By applying the FT, we obtain:

$$\mathscr{F}[i_R(t)] = I_R/2 \cdot [\delta(\omega - \omega_0) + \delta(\omega + \omega_0)] \tag{7.3}$$

If we apply the HT instead, we get:

$$\mathscr{H}[i_R(t)] = \tilde{i}_R(t) = I_R \sin(\omega_0 t) \tag{7.4}$$

whose spectral representation can be derived from the FT:

$$\mathscr{F}[\tilde{i}_R(t)] = I_R/2 \cdot [\delta(\omega - \omega_0) - \delta(\omega + \omega_0)] \tag{7.5}$$

Finally, the analytic signal associated with the current i_R is computed as:

$$\hat{i}_R(t) = i_R(t) + j \cdot \tilde{i}_R(t) = I_R \cdot [\cos(\omega_0 t) + j \sin(\omega_0 t)] = I_R e^{j\omega_0 t} \tag{7.6}$$

whose frequency domain representation consists only of positive frequency components:

$$\mathscr{F}[\hat{i}_R(t)] = \mathscr{F}[i_R(t)] + \mathscr{F}[\tilde{i}_R(t)] = I_R \cdot \delta(\omega - \omega_0) \tag{7.7}$$

Let us now consider the current i_L flowing through a generic inductance L:

$$i_L(t) = \int \frac{di_L(t)}{dt} = \int \frac{v(t)}{L} = I_L \sin(\omega_0 t) \tag{7.8}$$

being $I_L = V/L\omega_0$, whose FT is:

$$\mathscr{F}[i_L(t)] = -j \cdot I_L/2 \cdot [\delta(\omega - \omega_0) - \delta(\omega + \omega_0)] \tag{7.9}$$

The resulting HT and analytic signal, together with the associated spectral representations are:

$$\mathscr{H}[i_L(t)] = \tilde{i}_L(t) = -I_L \cos(\omega_0 t), \qquad \mathscr{F}[\tilde{i}_L(t)] = -j \cdot I_L/2 \cdot [\delta(\omega - \omega_0) + \delta(\omega + \omega_0)] \tag{7.10}$$

$$\hat{i}_L(t) = I_L \cdot [\sin(\omega_0 t) - j \cos(\omega_0 t)] = -j \cdot I_L e^{j\omega_0 t}, \qquad \mathscr{F}[\hat{i}_L(t)] = -j \cdot I_L \cdot \delta(\omega - \omega_0) \tag{7.11}$$

Also in the case of a generic inductance the spectral representation of the analytic signal results in only positive frequency components.

Let us finally consider the current i_C flowing through the generic capacitor C:

$$i_C(t) = C \frac{di_C(t)}{dt} = -I_C \sin(\omega_0 t) \tag{7.12}$$

being $I_C = VC\omega_0$, whose FT is:

$$\mathscr{F}[i_C(t)] = j \cdot I_C/2 \cdot [\delta(\omega - \omega_0) - \delta(\omega + \omega_0)] \tag{7.13}$$

Similarly to the previous cases, the resulting HT and analytic signal, and the associated spectral representations are:

$$\mathscr{H}[i_C(t)] = \tilde{i}_C(t) = +I_C \cos(\omega_0 t), \qquad \mathscr{F}[\tilde{i}_C(t)] = j \cdot I_C/2 \cdot [\delta(\omega - \omega_0) + \delta(\omega + \omega_0)] \tag{7.14}$$

$$\hat{i}_C(t) = I_c \cdot [-\sin(\omega_0 t) + j \cos(\omega_0 t)] = j \cdot I_c e^{j\omega_0 t}, \qquad \mathscr{F}[\hat{i}_C(t)] = j \cdot I_C \cdot \delta(\omega - \omega_0) \tag{7.15}$$

Once again, the spectral representation of the analytic signal associated with the current flowing through a generic capacitor does not consist of negative frequency components.

Figures 7.1(b) and (c) show the spectral composition of the currents flowing through fundamental circuit elements using the FT and HT, respectively. The figures present a three-dimensional space, where each frequency f (X-axis) defines a complex YZ-plane, characterized by the real axis Re and the perpendicular imaginary axis Im. In particular, the dashed arrows in Fig. 7.1(b) represent the current phasors $i(t)$ obtained using the FT applied to the current through a resistor as in (7.3) (blue), an inductance as in (7.9) (green), and a capacitor as in (7.13) (red). As it is well-known, they are all characterized by two Dirac functions, one in the positive and one in the negative frequency domain.

Figure 7.1(c) instead refers to the HT formulation. In particular, the dashed arrows correspond to the same current phasors as in Fig. 7.1(b), whereas the dotted arrows represent the spectral representation of the HT, as in (7.5) for the resistance (blue), as in (7.10) for the inductance (green), and as in (7.14) for the capacitor (red). Finally, the solid arrows refer to the spectral representation of the corresponding analytic signals $\hat{i}_R(t)$, $\hat{i}_L(t)$, $\hat{i}_C(t)$, as in (7.7), (7.11) and (7.15), respectively. They are obtained by summing the dashed and the dotted phasors, therefore, the contributions relative from the negative frequency range are eliminated. For the positive frequency domain, instead, each phasor in Fig. 7.1(b) maintains the same polarity whereas its amplitude is doubled.

7.2.2 Application to Realistic Scenarios

The HT enables the analysis of realistic signals typical of power system transients, where traditional DFT-based techniques fail to give an appropriate phasor representation. For instance, let us start with the case of a generic power system signal whose amplitude is modulated by a cosine whose frequency is much slower than the fundamental one. To fix ideas, this signal may represent a nodal voltage. This phenomenon typically appears during inter-area oscillations between large system regions. Formally, an amplitude modulation can be modeled as [11]:

$$x(t) = A_0(1 + k_a \cos(2\pi f_a t)) \cdot \cos(2\pi f_0 t + \varphi_0) \tag{7.16}$$

being f_0, A_0 and φ_0 the fundamental tone frequency, amplitude and initial phase, respectively, f_a the modulation frequency ($f_a \ll f_0$) and k_a the modulation factor.

In this case, the signal FT can be expressed as:

$$\begin{aligned}\mathscr{F}[x(t)] =& A_0/2 \cdot \left[\delta(f - f_0)e^{j\varphi_0} + \delta(f + f_0)e^{-j\varphi_0} + \right. \\ & + k_a/2 \cdot \left[\delta(f - (f_0 + f_a))e^{j\varphi_0} + \delta(f + (f_0 + f_a))e^{-j\varphi_0} + \right. \\ & \left.\left. + \delta(f - (f_0 - f_a))e^{j\varphi_0} + \delta(f + (f_0 - f_a))e^{-j\varphi_0}\right]\right]\end{aligned} \tag{7.17}$$

The spectrum is characterized by three pairs of bins in the positive and negative frequency domain: one at frequency f_0 and two centered around it at $f_0 \pm f_a$. In such a scenario, an FT-based signal analyzer (tailored to investigate signals around the rated power system frequency) could fail to provide a correct spectrum interpretation because of the interference generated by the modulating tones. Conversely, the HT-based approach enables us to derive a single component analytic signal:

$$\hat{x}(t) = A_0(1 + k_a \cos(2\pi f_a t)) \cdot e^{j(2\pi f_0 t + \varphi_0)} \tag{7.18}$$

i.e., a phasor rotating at the fundamental frequency f_0, while its amplitude is pulsating at the modulation frequency f_a.

The second case under investigation consists in a power system whose frequency is decaying with a descending ramp trend, as typical of the stages anticipating a severe system collapse. A frequency ramp can be modeled as [11]:

$$x(t) = A_0 \cdot \cos(2\pi f_0 t + \varphi_0 + R\pi t^2) \tag{7.19}$$

being R the ramp rate. The signal FT can be formulated as:

$$\mathscr{F}[x(t)] = \frac{A}{2\sqrt{2}} e^{j\left[\frac{\pi(f-f_0)^2}{R} - \frac{\pi}{4} + \varphi_0\right]} + \frac{A}{2\sqrt{2}} e^{-j\left[\frac{\pi(f+f_0)^2}{R} - \frac{\pi}{4} + \varphi_0\right]} \tag{7.20}$$

where the notation ω indicates the phasor angular velocity or pulsation. In this context, it should be noticed how difficult it is to distinguish the fundamental tone from the spurious contributions introduced by the time varying frequency.

By contrast, the HT provides the following analytic signal:

$$\hat{x}(t) = A_0 \cdot e^{j(2\pi f_0 t + \varphi_0 + R\pi t^2)} \tag{7.21}$$

that can be regarded as a dynamic phasor, characterized by constant amplitude and rotating with a ramping frequency.

The final case under investigation refers to a situation where FT-based methods provide largely discrepant results, i.e., a signal whose amplitude experiences a step, modeled as [11]:

$$x(t) = A_0(1 + k_s h(t)) \cdot \cos(2\pi f_0 t + \varphi_0) \tag{7.22}$$

being k_s the step factor and $h(t)$ the Heaviside function, that is null for $t < 0$ and 1 for $t \geq 0$. The signal FT is:

$$\mathscr{F}[x(t)] = A/2\,(1 + k_s/2) \cdot [\delta(f - f_0)e^{j\varphi_0} + \delta(f + f_0)e^{-j\varphi_0}] + \frac{k_s A}{j4\pi(f - f_0)} e^{j\varphi_0} + \frac{k_s A}{j4\pi(f + f_0)} e^{-j\varphi_0} \tag{7.23}$$

This formulation still maintains the information regarding the fundamental tone, but contains

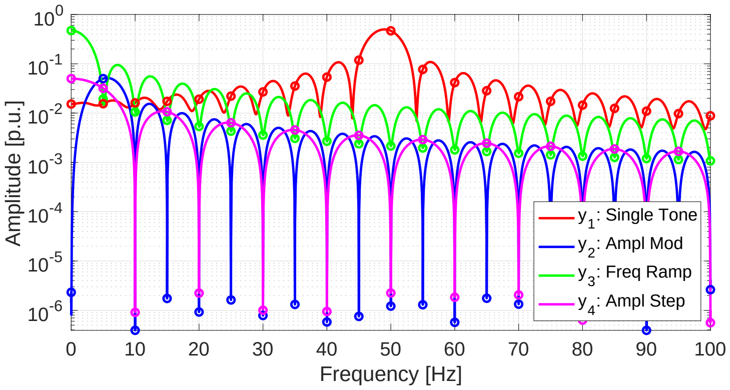

Figure 7.2 – DFT modules of a single tone cosine signal y_1 (red), of an amplitude modulation term y_2 (blue), of a frequency ramp term y_3 (green) and of an amplitude step y_4 (pink). The DFT is computed using an observation interval of 200 ms and a sampling frequency of 10 kHz.

also two hyperbolic terms whose contributions are spread over the whole frequency spectrum. In such a scenario, an FT-based approach fails in providing an appropriate reconstruction of the signal under investigation due to the scattering of the spectrum bins that largely bias the information related to the fundamental tone.

The HT, instead, provides an analytic signal formulation where the amplitude step information is entirely preserved:

$$\hat{x}(t) = A_0(1 + k_s h(t)) \cdot e^{j(2\pi f_0 t + \varphi_0)} \tag{7.24}$$

Equations (7.18), (7.21) and (7.24) are derived assuming the following property of the Hilbert transform: the HT of the product of two signals with non-overlapping spectra is equal to the product of the low-frequency term by the HT of the high-frequency term [96]. In this regard, Fig. 7.2 shows the DFT modules of four signals, computed using an observation interval of 200 ms and a sampling frequency of 10 kHz. In particular, the red plot represents the spectrum of a single tone signal y_1 pulsating at 49 Hz, with amplitude A_0 = 1 p.u. and phase φ_0 = 0 rad:

$$y_1(t) = A_0 \cos(2\pi f_0 t + \varphi_0) \tag{7.25}$$

The blue plot represents the modulating term in (7.16), characterized by a typical modulation amplitude for power systems k_a = 0.1 p.u., and modulation frequency f_a = 5 Hz:

$$y_2(t) = k_a \cos(2\pi f_a t) \tag{7.26}$$

The green plot refers to the frequency ramp in (7.19), with a ramping factor R = -6.25 Hz/s:

$$y_3(t) = \cos(R\pi t^2) \tag{7.27}$$

Finally, the pink plot represents the amplitude step in (7.22), applied in the central point of

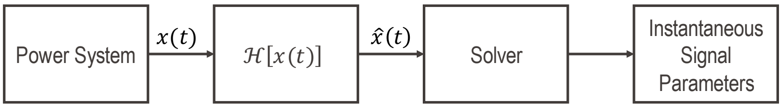

Figure 7.3 – Power system solver based on analytic signals.

the window, considering a typical step amplitude for power systems $k_s = 0.1$ p.u.:

$$y_4(t) = k_s \cdot h(t) \tag{7.28}$$

The Figure shows that, for parameters selection typical of power systems and in the frequency range [45, 55] Hz, the DFT bins corresponding to the fundamental tone y_1 are at least two orders of magnitude bigger than the DFT bins of the interfering tones y_2, y_3 and y_4. Therefore, even though it is not formally verified that the two signals are characterized by non-overlapping spectra, it is practically satisfied by typical power systems signals when the frequency resolution is in the order of few Hz (observation intervals of hundreds of ms).

7.2.3 Reconstruction of the Electrical Power using the Hilbert Transform

The theoretical foundations contained in the previous Sections 7.2.1 and 7.2.2, show that, in principle, it is possible to build a solver that uses analytic signals to retrieve the instantaneous parameters associated to real power system signals, also in non stationary operating conditions. The block scheme of such solver is shown in Fig. 7.3. In particular, the solver should integrate the Kirchhoff's circuit laws associated to the portion of the electrical grid under analysis (as presented in Section 7.2.1) as well as the expression of typical power system operating conditions (as presented in Section 7.2.2). Nevertheless, the formulation of the solver is out of the scope of this Thesis. In the absence of an appropriate solver, the following treatise is proposed to retrieve the instantaneous power associated to power system signals.

Let us consider two signals representing a generic voltage $v(t)$ and current $i(t)$ of a power system. The instantaneous power is computed as the product among the two waveforms:

$$p(t) = v(t) \cdot i(t) \tag{7.29}$$

By applying (4.4), the analytic signals associated to the voltage, current and instantaneous power can be expressed as:

$$\hat{v}(t) = v(t) + j \cdot \mathscr{H}[v(t)] = v(t) + j \cdot \tilde{v}(t) \tag{7.30}$$

$$\hat{i}(t) = i(t) + j \cdot \mathscr{H}[i(t)] = i(t) + j \cdot \tilde{i}(t) \tag{7.31}$$

$$\hat{p}(t) = p(t) + j \cdot \mathscr{H}[p(t)] = p(t) + j \cdot \tilde{p}(t) \tag{7.32}$$

Furthermore, the product between the analytic signals of voltage and current is:

$$\hat{p}'(t) = \hat{v}(t)\cdot\hat{i}(t) = [v(t)+j\cdot\tilde{v}(t)]\cdot[i(t)+j\cdot\tilde{i}(t)] = v(t)i(t)-\tilde{v}(t)\tilde{i}(t)+j\cdot[\tilde{v}(t)i(t)+v(t)\tilde{i}(t)] \quad (7.33)$$

In a similar way, the product between the analytic signals of voltage and current complex conjugate (*conj*) is:

$$\hat{p}''(t) = \hat{v}(t)\cdot conj(\hat{i}(t)) = [v(t)+j\cdot\tilde{v}(t)]\cdot[i(t)-j\cdot\tilde{i}(t)] = v(t)i(t)+\tilde{v}(t)\tilde{i}(t)+j\cdot[\tilde{v}(t)i(t)-v(t)\tilde{i}(t)] \quad (7.34)$$

It is interesting to compute the sum of (7.33) and (7.34):

$$\hat{p}'''(t) = \hat{p}'(t) + \hat{p}''(t) = 2v(t)\cdot i(t) + 2j\cdot\tilde{v}(t)\cdot i(t) \quad (7.35)$$

whose real part is proportional to the instantaneous power:

$$real(\hat{p}'''(t)) = 2p(t) \quad (7.36)$$

Voltage and current signals can be modeled as sinusoids pulsating at the same frequency f:

$$v(t) = V\cos(2\pi f t + \varphi_v), \qquad i(t) = I\cos(2\pi f t + \varphi_i) \quad (7.37)$$

The instantaneous power is given by the waveforms' product:

$$p(t) = v(t)\cdot i(t) = \frac{1}{2}VI[\cos(\varphi_v - \varphi_i) + \cos(4\pi f t + \varphi_v + \varphi_i)] \quad (7.38)$$

As expected, the resulting instantaneous power pulsates at a frequency that is double the power system frequency. The voltage and current HTs are obtained by shifting the spectra by $\pm\pi/2$, resulting in the following analytic signals:

$$\hat{v}(t) = v(t) + j\cdot\tilde{v}(t) = V\cos(2\pi f t + \varphi_v) + j\cdot V\sin(2\pi f t + \varphi_v) \quad (7.39)$$

$$\hat{i}(t) = i(t) + j\cdot\tilde{i}(t) = I\cos(2\pi f t + \varphi_i) + j\cdot I\sin(2\pi f t + \varphi_i) \quad (7.40)$$

By computing the HT of the instantaneous power, the following is obtained:

$$\tilde{p}(t) = \frac{1}{2}VI\sin(4\pi f t + \varphi_v + \varphi_i) \quad (7.41)$$

However, by comparing this result with (7.38), it can be noted that the information regarding the constant offset is lost. That is to say that the HT of the instantaneous power computed by simply using its definition is useless with respect to (7.38). Similarly, computing the analytic signal of $p(t)$ is:

$$\hat{p}(t) = p(t) + j\cdot\tilde{p}(t) = \frac{1}{2}VI[\cos(\varphi_v - \varphi_i) + \cos(4\pi f t + \varphi_v + \varphi_i) + j\cdot\sin(4\pi f t + \varphi_v + \varphi_i)] \quad (7.42)$$

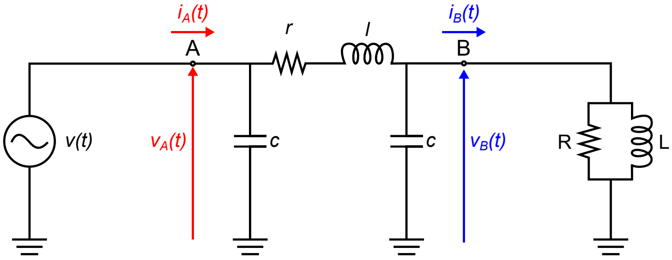

Figure 7.4 – Block diagram of the adopted EMTP-RV simulation model. The generator is characterized by nominal voltage of 380 kV, and is connected to a 100 MW load through a 100 km ACSR overhead line.

that, compared to (7.38), maintains the constant offset information, but introduces an imaginary complex term.

As in (7.33) and (7.34), $\hat{p}'$ and $\hat{p}''$ can be computed as:

$$\hat{p}'(t) = VI \cdot [\cos(4\pi f t + \varphi_v + \varphi_i) + j \cdot \sin(4\pi f t + \varphi_v + \varphi_i)] \tag{7.43}$$

$$\hat{p}''(t) = VI \cdot [\cos(\varphi_v - \varphi_i) + j \cdot \sin(\varphi_v - \varphi_i)] \tag{7.44}$$

Finally, as in (7.35), the sum of the obtained quantities is:

$$\hat{p}'''(t) = VI \cdot [\cos(\varphi_v - \varphi_i) + \cos(4\pi f t + \varphi_v + \varphi_i)] + j \cdot VI \cdot [\sin(\varphi_v - \varphi_i) + \sin(4\pi f t + \varphi_v + \varphi_i)] \tag{7.45}$$

whose real part corresponds to twice the instantaneous power in (7.38), exactly as in (7.36), demonstrating that $\hat{p}'''$ can be used to derive the instantaneous power of an electrical grid.

7.3 Validation Models and Algorithm

This Section provides the modeling and algorithmic details for the numerical validation of the proposed HT-based analysis. To this end, two models and two different simulation environments are used to generate datasets characterized by significant power system dynamics. First, a simple 2-bus model is simulated using the EMTP-RV simulation environment, in order to replicate the waveforms described in Section 7.2. Second, the IEEE 39-bus model implemented within the OPAL-RT environment is adopted in order to emulate the operating conditions of large-scale networks [68, 69]. An algorithm that enables the performance comparison of DFT- and HT-based approaches is provided. Finally, the possibility of extending the analysis to an approach based on functional basis is discussed.

7.3.1 Simple 2-bus Model

Without loss of generality, in order to use a repeatable example, let us refer to the simple model in Fig. 7.4, that consists of a time-varying 3-phase voltage generator powering a generic load

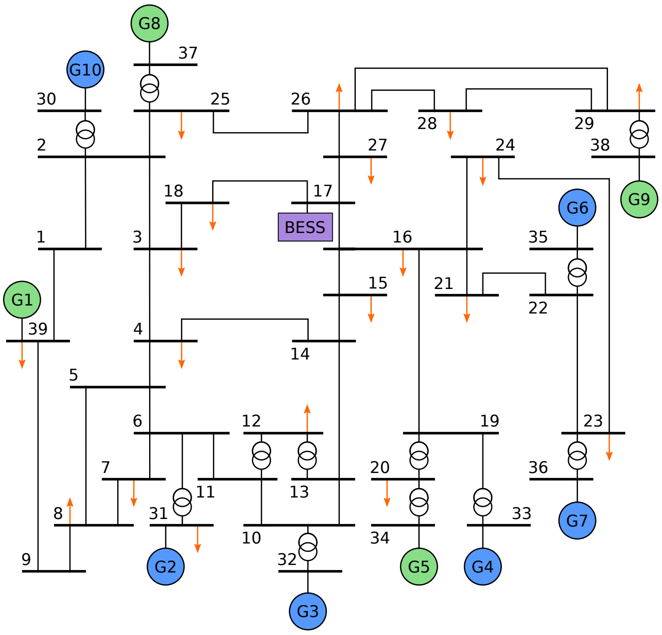

Figure 7.5 – Block diagram of the modified 39-bus power grid Opal-RT simulation model. The system is characterized by nominal voltage of 345 kV. The model consists in 10 generators (circles) and 19 loads (orange arrows). The total installed capacity is 10 GW, that is partitioned in three possible configurations: (I) 10 synchronous generators, (II) 6 synchronous generators (blue circles) and 4 wind farms (green circles), and (III) like (II) plus a BESS (purple rectangle).

through a transmission line, characterized by steady-state rated voltage of 380 kV at 50 Hz. The model is used to perform off-line simulations within the EMTP-RV simulation environment [208, 209].

The voltage source has been modeled by means of a look-up-table providing point-on-wave data representing a generic dynamic voltage supplying the line. A 100 km aluminum conductors steel reinforced (ACSR) overhead line is considered, characterized by commonly adopted parameters: diameter 31.5 mm, $r = 0.02\ 10^{-3}\ \Omega/\text{m}$, $x = 0.268\ 10^{-3}\ \Omega/\text{m}$, $c = 13.7\ 10^{-10}\ \text{F/m}$. The transmission line is modeled using a lumped constants π equivalent, and the load by means of an R-L parallel equivalent, where R and L have been tuned in order to get a total load of 100 MW and 0.9 power factor in case of a purely sinusoidal voltage at 50 Hz.

7.3.2 The IEEE 39-bus Model

In order to test the proposed technique over large-scale power systems, the Opal-RT eMEGAsim PowerGrid Real Time Simulator (RTS) [67] is used to implement a detailed dynamic model of the IEEE 39-bus power system, also known as 10-machine New-England power system [68, 69], represented in Fig. 7.5. This model represents a widely-employed benchmark for performance evaluation and comparison of several monitoring and control applications. In more detail, the simulated power system has a nominal voltage of 345 kV, and consists in 39 buses, 10 generators and 19 loads. In order to take into account the effects of distributed renewable generation, the benchmark is modified leading to three possible configurations of the IEEE 39-bus power system [210, 5]:

I. The original 10-synchronous machine system, with total installed capacity of 10 GW;

II. An inertia-reduced system that includes wind farms instead of generators G1, G5, G8, and G9, for a total wind installed capacity of 4 GW. The wind plants are modeled as aggregated type-3 turbines;

III. An inertia-reduced system that includes the same wind farms of configuration II and a 200 MW Battery Energy Storage System (BESS) in bus 17. The battery is connected to the grid through a dedicated voltage source converter (VSC).

Moreover, in order to emulate realistic load and generation patterns, wind and load profiles coming from real measurements are used. The network is modeled in Simulink and the simulations are run using the Opal-RT eMEGAsim RTS. Thorough details about this model are provided in [210, 5], and it is available online [211].

7.3.3 The Validation Algorithm

In the simulated scenario, the time-domain 3-phase waveforms of voltage and current are known in each node, therefore can be post-processed via DFT and HT, as described in Algorithm 8.

First, the true instantaneous power $p(t)$ is computed as the product between voltage and current waveforms (line 1 in Alg. 8). The investigation focuses on instantaneous power, to avoid the non-unique interpretation of active and reactive power (and the underlying hypothesis of steady-state phasor) in case of a broad signal spectrum [212]. The 3-phase power is obtained by summing the contribution of each phase $\{a, b, c\}$. In order to emulate realistic operating conditions, measurement uncertainty is simulated by means of a purely additive and uncorrelated white Gaussian noise component with SNR = 80 dB (line 4 and 16).

When the DFT is adopted, the signals are analyzed using a method inspired by the IEC Std. 61000-4-7 [213]: by means of sliding windows of 200 ms, the observation interval is shifted sample-by-sample (given the sampling frequency of 10 kHz, this corresponds to steps of 100 μs) (line 5). For each window, the FT is approximated by means of the DFT computed via a Fast FT (FFT) algorithm (line 6). The adopted window length (corresponding to 10 cycles at the nominal power system frequency) determines a 5 Hz granularity in the frequency domain. In order to reduce spectral leakage effects, the signal is windowed with the Hanning weighing function $w(t)$. In order to reduce the effects of spectrum granularity, for each observation window the frequency $\tilde{f}(t)$, amplitude $\tilde{A}(t)$ and phase $\tilde{\varphi}(t)$ are estimated by means of the Interpolated DFT (IpDFT) (line 7) (whose details are provided in Chapter 3 Section 3.2).

Algorithm 8

```
1. True Power: True 3-phase power computation
$p(t) = \sum_{abc} v(t) \cdot i(t)$
2. FT computation:
if $\mathscr{F}[\cdot]$
    for $x(t) = \{v(t), i(t)\}_{abc}$
        $x(t) = x(t) + \mathscr{N}(t)$                                  ▷ Noise adding
        for $t = 0 \rightarrow end, \Delta t = 200ms$                   ▷ Signal partition into consecutive intervals
            $X(k) = \mathscr{F}[x(t) \cdot w(t)] \approx DFT\,[x(t) \cdot w(t)]$     ▷ Hanning windowing and DFT
            $\left\{\tilde{f}(t), \tilde{A}(t), \tilde{\varphi}(t)\right\} = IpDFT\,[X(k)]$   ▷ Find tone parameters via IpDFT
            $\tilde{x}_{\mathscr{F}}(t) = \tilde{A}(t) cos(2\pi \tilde{f}(t) \Delta t/2 + \tilde{\varphi}(t))$   ▷ Time domain signal reconstruction
        end for
        $\tilde{p}_{\mathscr{F}}(t) = \sum_{abc} \tilde{v}_{\mathscr{F}}(t) \cdot \tilde{i}_{\mathscr{F}}(t)$   ▷ FT 3-phase power estimation
        $\Delta p_{\mathscr{F}}(t) = \tilde{p}_{\mathscr{F}}(t) - p(t)$        ▷ FT power error computation
    end for
end if
3. HT computation:
if $\mathscr{H}[\cdot]$
    for $x(t) = \{v(t), i(t)\}_{abc}$
        $x(t) = x(t) + \mathscr{N}(t)$                                  ▷ Noise adding
        $\hat{x}_{\mathscr{H}}(t) = x(t) + j \cdot \mathscr{H}[x(t)] \approx filter[x(t)]$   ▷ Analytic signal via Hilbert filter
    end for
    $\hat{p}'(t) = \sum_{abc} \hat{v}(t) \cdot \hat{i}(t)$                  ▷ Power estimation as in (7.33)
    $\hat{p}''(t) = \sum_{abc} \hat{v}(t) * \hat{i}(t)$                     ▷ Power estimation as in (7.34)
    $\hat{p}'''(t) = \hat{p}'(t) + \hat{p}''(t)$                            ▷ Power estimation as in (7.35)
    $\tilde{p}_{\mathscr{H}}(t) = real(\hat{p}'''(t))/2$                    ▷ HT 3-phase power estimation
    $\Delta p_{\mathscr{H}}(t) = \tilde{p}_{\mathscr{H}}(t) - p(t)$          ▷ HT power error computation
end if
```

1.3

For the sake of conciseness, this analysis is not repeated for different window lengths or windowing functions. It is worth observing that as for any DFT-based approach, the longer the observation window, the smaller the spectrum granularity and thus the higher the frequency domain accuracy. By contrast, a shorter window length results in a faster response time in passing from one steady state to the other. In this study the focus is on the accuracy of the estimates, rather than on their responsiveness, therefore, a fairly long observation interval is adopted. These estimates are used to approximate the time domain trend of the sinusoidal component in the considered observation interval. The estimated signal $\tilde{x}_{\mathscr{F}}(t)$ is constructed by extracting the central point of each of the consecutive sliding windows (line 8). The 3-phase power is obtained by summing the contribution from each phase (line 10) resulting in power errors (line 11).

As regards the HT, first the analytic signal of the noisy waveforms is computed (line 17). The HT is however based on a singular integral operator (see (4.1)) and thus non solvable in closed form. The analytic signal may therefore be approximated by means of a filter emulating the HT response. The filter adopts a 10 kHz sampling frequency, the filter order is set to 31 and the transition width to 50π radians per sample. As shown in Fig. 7.6, the magnitude response of the adopted filter is nearly equal to zero (the ideal value) for the positive frequency domain, whereas it is lower than -120 dB in the negative frequency range, achieving a high rejection of the long-range interference coming from the negative frequency components.

Finally, the quantities defined in equations (7.33)-(7.35) (line 19-21) are computed. As in (7.36), the estimated power $\tilde{p}_{\mathscr{H}}(t)$ is computed as the real part of $\hat{p}'''(t)$ (line 22) and the corresponding power errors are consequently computed (line 23).

7.4 Validation Over Real-World Scenarios

This Section describes the results that enable the validation of the HT-based analysis proposed in Section 7.3.3. Three different datasets are analyzed. The first one is obtained using EMTP-RV and is inspired by the signals formulated in Section 7.2, representing approximations of actual power system operating conditions. The second dataset is still obtained using EMTP-RV and refers to real-world events. In particular, the waveforms taking place in Australia on September 2016 and in Europe during an inter-area oscillation on December 2016 are replicated (see Fig. 2.2). The third set of data is obtained simulating a large contingency within the 39-bus model using Opal-RT. For each operating condition, the results are presented by means of two plots showing the instantaneous active power computed using the FT and the HT as in Algorithm 8. The upper plot represents the power in phase a and the true reference power, the bottom plot represents the 3-phase power error. The results are presented for one bus only, but similar considerations hold for the other buses of the considered network.

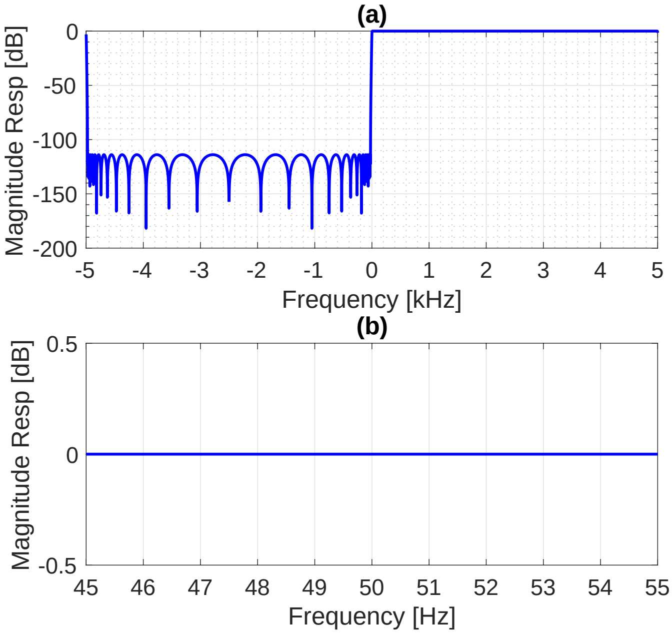

Figure 7.6 – Magnitude response of the filter approximating the ideal HT over the whole frequency bandwidth (a) and over the power system operating conditions (b). Filter order 31, transition width 50π.

7.4.1 Theoretical Operating Conditions

By using Matlab environment, a plausible situational awareness context is simulated, with a sampling frequency of 10 kHz. Voltage waveforms are synthesized with a nominal voltage of 380 kV, for a total duration of 4 seconds for each test. These waveforms are used to model the output of the voltage source presented in Fig. 7.4. Then, as discussed in Section 7.3, voltage and current signals provided by EMTP-RV simulations are analyzed as in Algorithm 8. In more details, the following scenarios are simulated:

a) Amplitude modulation, being $f_a = 5$ Hz the modulation frequency and $k_a = 0.1$ the modulation depth in (7.16);

b) Negative frequency ramp with $50 \leq f_0 \leq 46$, being $R = -6$ Hz/s the ramp rate in (7.19);

c) Amplitude step, being $k_s = 0.1$ the step factor in (7.22).

Regarding the amplitude modulation case, Fig. 7.7 shows that the DFT does not enable us to correctly interpret a signal whose fundamental component is modulated. Indeed, the obtained signal spectrum is largely biased by the interference produced by the modulating term, leading to imprecise parameters estimation. Both voltage and current are inaccurately measured, leading to a maximum power error in the order of 50 MW. By contrast, it is evident that the HT preserves the information needed to entirely reconstruct the analyzed signal: the maximum attained power errors are in the order of 10 W.

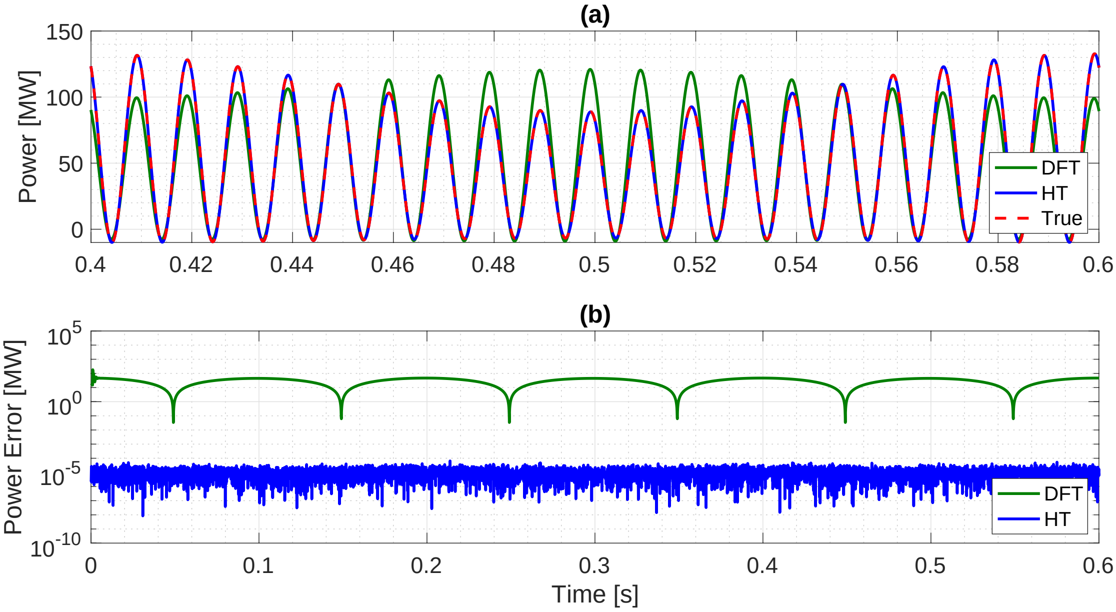

Figure 7.7 – Signal characterized by an amplitude modulation with modulating frequency of 5 Hz: Instantaneous single-phase active power (a) and three-phase power error (b) computed using the DFT (green) and the HT (blue). The red line represents the true power.

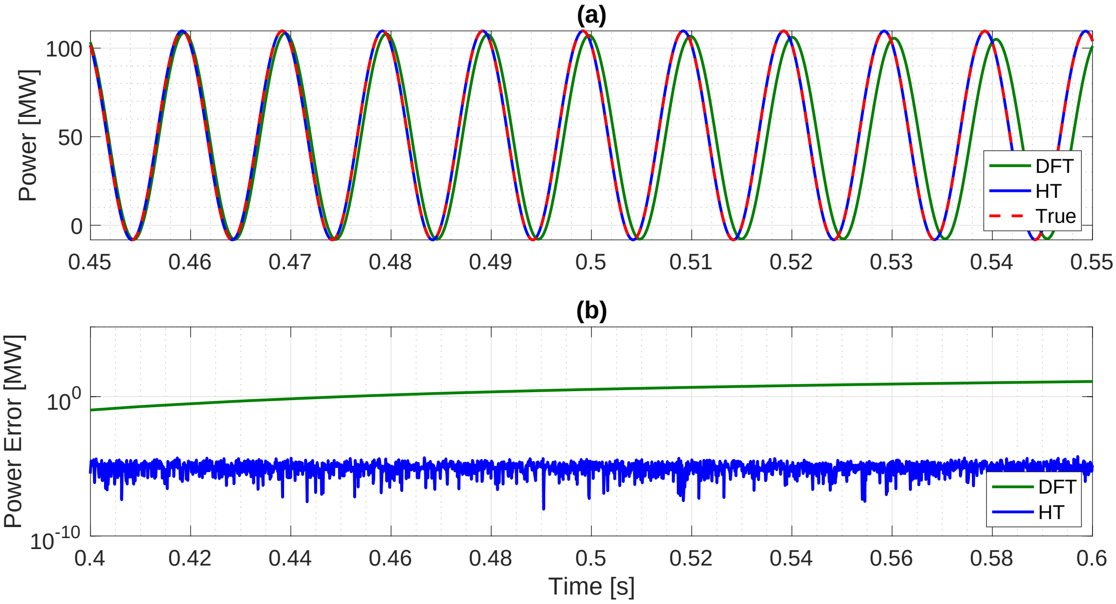

Figure 7.8 – Signal characterized by a negative frequency ramp of -6 Hz/s: Instantaneous single-phase active power (a) and three-phase power error (b) computed using the DFT (green) and the HT (blue). The red line represents the true power.

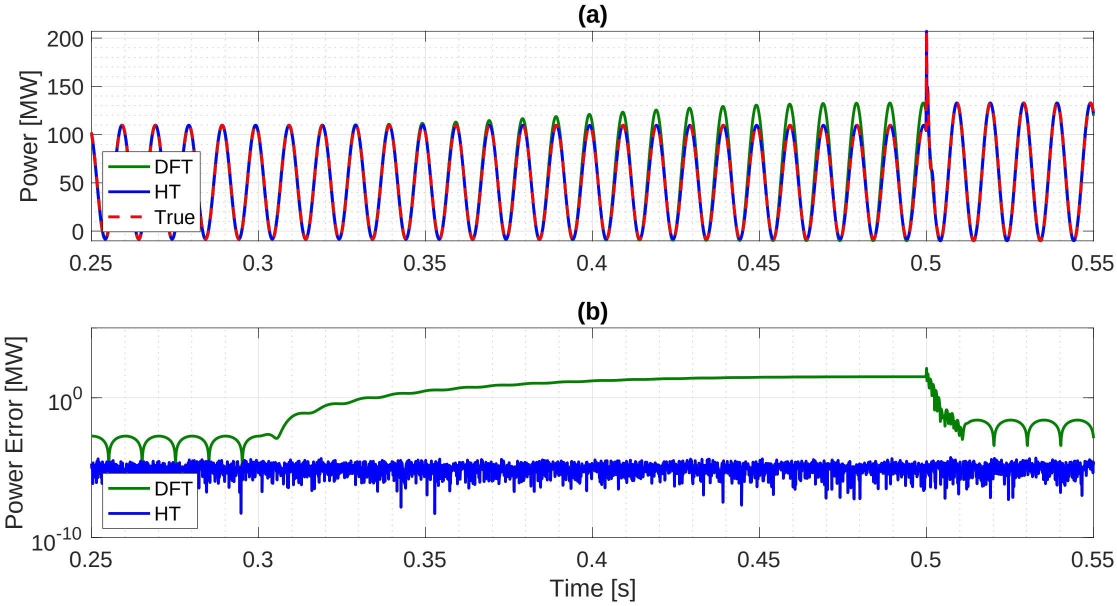

Figure 7.9 – Signal characterized by a 10% amplitude step: Instantaneous single-phase active power (a) and three-phase power error (b) computed using the DFT (green) and the HT (blue). The red line represents the true power.

Regarding the frequency ramp case, Fig. 7.8 shows that as the frequency deviates from its nominal value, the DFT provides erroneous results due to spectral leakage. The maximum obtained power error is in the order of 10 MW. Conversely, the HT is able to follow instantaneously the signal dynamics experienced during a frequency ramp, providing an almost-perfect signal reconstruction. Also in this operating condition, the HT provides errors lower than 10 W.

Regarding the amplitude step case, the DFT spectrum does not contain the information needed to infer the signal parameters during such sudden waveform deformations. Fig. 7.9, shows that over the whole period during which the step is contained in the sliding window (i.e., 200 ms), the FT provides wrong results reaching 30 MW error when the step appears in the center of the window and therefore the spectrum reconstruction is the most wanting. On the contrary, the HT enables us to follow the signal throughout the whole time interval, matching almost sample-by-sample the signal parameters. Again, the maximum attained power error is in the order of 10 W.

7.4.2 Real-world Operating Conditions

The second set of waveforms, refers to real-world events. Particularly, the waveforms taking place in Australia during the blackout on September 2016 and in Europe during the inter-area oscillations on December 2016 are replicated [39, 40]. Based on PMU estimates of fundamental frequency, amplitude and initial phase, the time-domain waveform as sampled at 10 kHz are recovered, through the approach in [11]. Specifically, at each reporting time based on the PMU estimates of frequency, amplitude and phase, the fundamental component trend is recovered in the time domain. These datasets are used to replicate the voltage source in Fig. 7.4.

Regarding the Australian blackout, as illustrated in Fig 2.2, the signal is characterized by two criticalities: first the amplitude step occurring at 1.6 s, then the sudden frequency drop at 2.7 s. As discussed so far, the two events are difficult to analyze adopting DFT-based tools because the signal spectrum is so spread that it is ambitious to infer the waveform parameters. Conversely, the HT has proven to be potentially suitable for analyzing both situations. As a matter of fact, the results in Fig. 7.10 confirm the inappropriateness of the DFT to represent both the amplitude step and the frequency drop, exhibiting errors in the order of 100 MW. Besides, the HT is characterized by a maximum error lower than 10 W.

Regarding the European inter-area oscillation, Fig. 7.11 confirms the improvement of adopting the HT in stead of the DFT, as the instantaneous power estimates are always characterized by a smaller error: maximum error lower than 10 W for the HT and 5 MW for the DFT. The HT proves to be a suitable tool also for analyzing real-world waveforms.

7.4.3 Large-scale Power System

In order to evaluate the appropriateness of the proposed technique to model large-scale power grids, dedicated simulations of emergency scenarios are carried out using the 39-bus model in Opal-RT environment. In particular, the outage of generator G6 is simulated, with a total tripped power of 800 MW, leading a load imbalance that determines a strong system dynamic. The generator is tripped at second 180 and the transient lasts for roughly 100 seconds. The same contingency has been replicated in the three configurations of the IEEE-39 bus, in order to highlight the effects of reducing the inertia of the generation asset.

Fig. 7.12, 7.13 and 7.14 show the power profiles recorded in bus 39, but similar results hold for all the buses of the network. As it is shown in the figures, during the whole transient the DFT does not provide a truthful representation of the power system behavior, leading to errors in the order of 300 MW. Conversely, the HT provides an accurate transient tracking providing errors always lower than 60 kW.

7.4.4 Functional Analysis

An alternative solution for approximating the signal HT is provided by functional analysis [214]. The acquired signal $x(t)$ is projected over a pre-defined vector basis of analytic signals whose kernel is defined as:

$$(1 + g_A(t)) \cdot e^{j(2\pi g_f(t)t + g_\varphi(t))} \tag{7.46}$$

where the functions g_A, g_f and g_φ account for the time-variations of amplitude, frequency and phase of the fundamental component, and might follow different trends like ramps, sinusoids or step changes. Differently from the filtering approach, the projection over a basis

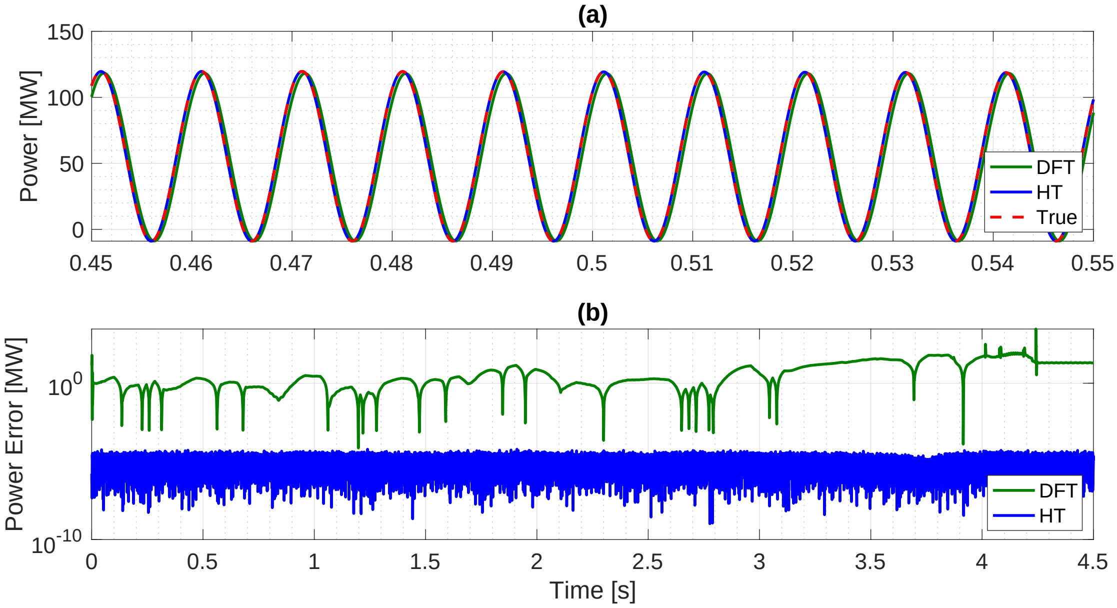

Figure 7.10 – Signal replicating the waveforms that took place in Australia during the blackout on September 28, 2016: Instantaneous single-phase active power (a) and three-phase power error (b) computed using the DFT (green) and the HT (blue). The red line represents the true power.

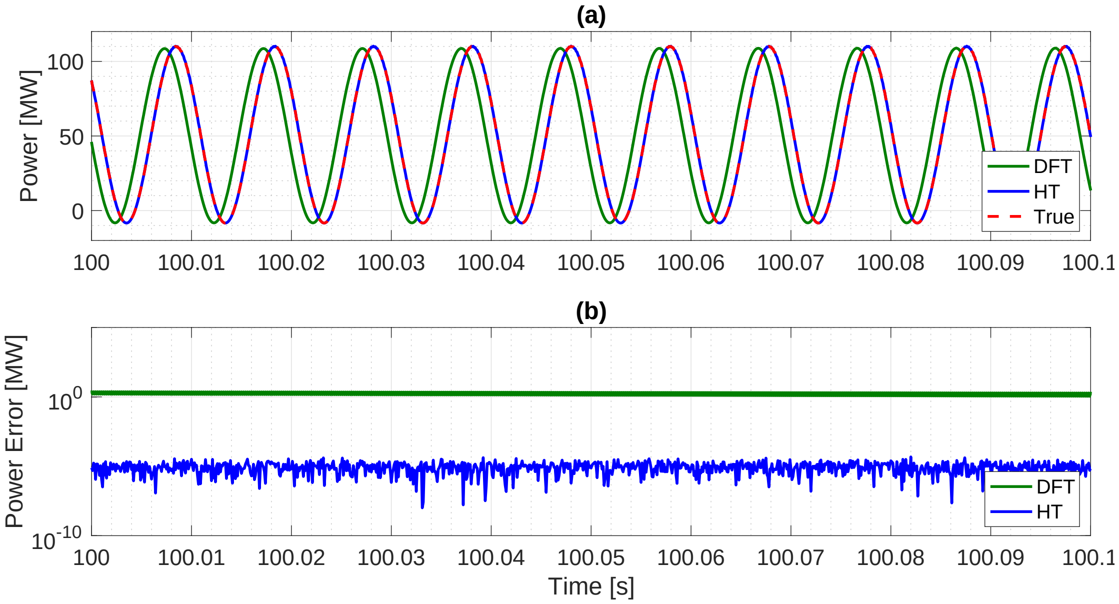

Figure 7.11 – Signal replicating the waveforms that took place in Switzerland during the inter-area oscillation on December 1, 2016: Instantaneous single-phase active power (a) and three-phase power error (b) computed using the DFT (green) and the HT (blue). The red line represents the true power.

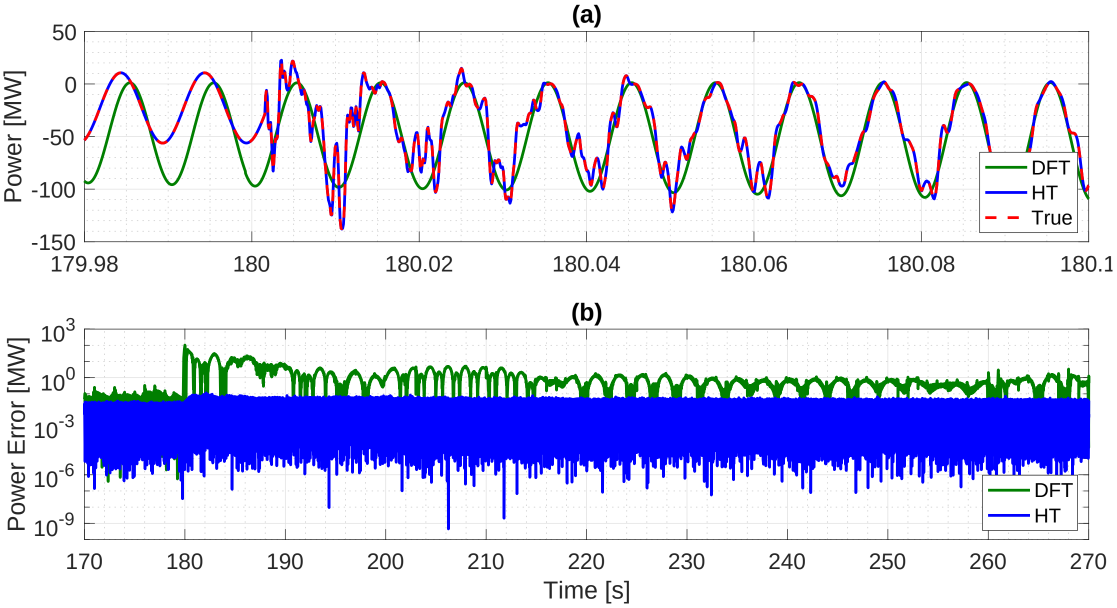

Figure 7.12 – IEEE 39-bus Configuration I: Signals at bus 39 in case of tripping generator G6 at second 180. Instantaneous single-phase active power (a) and three-phase power error (b) computed using the DFT (green) and the HT (blue). The red line represents the true power.

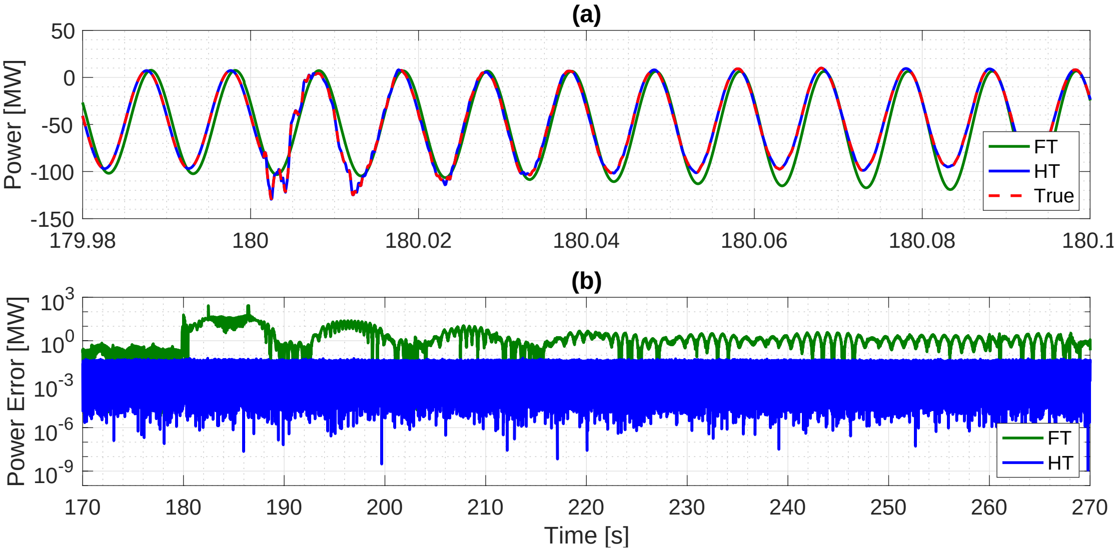

Figure 7.13 – IEEE 39-bus Configuration II: Signals at bus 39 in case of tripping generator G6 at second 180. Instantaneous single-phase active power (a) and three-phase power error (b) computed using the DFT (green) and the HT (blue). The red line represents the true power.

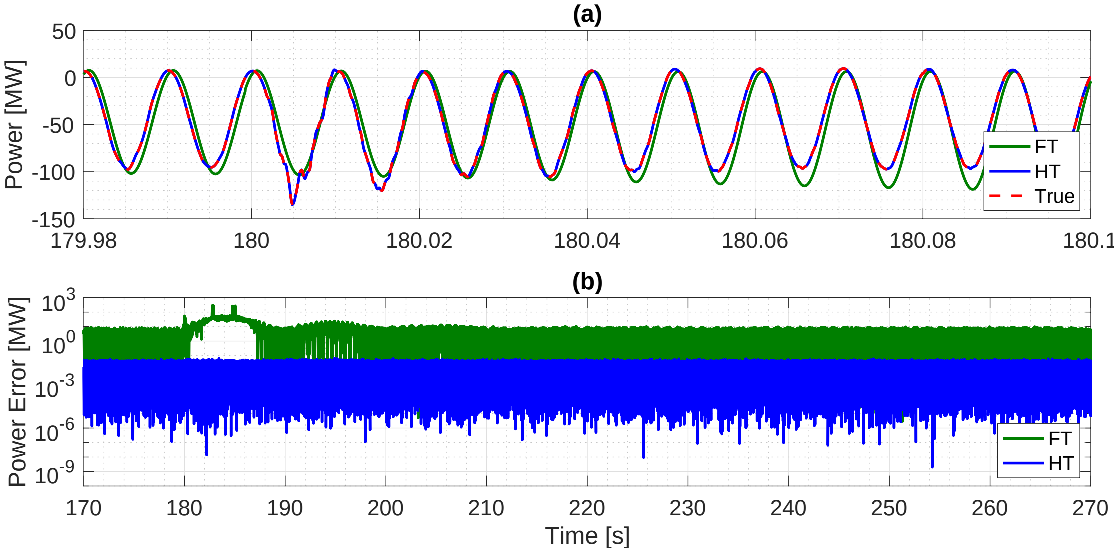

Figure 7.14 – IEEE 39-bus Configuration III: Signals at bus 39 in case of tripping generator G6 at second 180. Instantaneous single-phase active power (a) and three-phase power error (b) computed using the DFT (green) and the HT (blue). The red line represents the true power.

would allow to identify a mathematical model of the parameters' evolution that, de facto, would enable the compression of the time domain information into few coefficients of (7.46). However, its performance depends on the number of possible realizations of (7.46) included in the basis: the larger the more accurate, but also the more computationally demanding and numerically ill-conditioned due to the high correlation between the various vectors.

It is worth mentioning that the possible implementations of the dictionary of vectors that span the possible space of solutions are uncountable. However, as in power systems we can define a limited set of possible disturbances, the functional analysis could be reduced to a finite number of vectors according to (7.46). In this view, also the traditional DFT corresponds to a projection over a functional basis that consists of Dirichlet kernels centered around the bin central frequencies. The advantage of the Fourier formulation is that each vector is maximally uncorrelated from the others and thus it is easier to discriminate which one is the best approximation. In a dynamic approach, instead, all the vectors associated to a given frequency are strongly correlated. As a consequence, the problem becomes non-convex and there is the risk to end in a sub-optimal solution instead of the global-optimum. Conversely, the advantage of including dynamic phasors in the dictionary lies in the possibility to account for phenomena characterized by a wider frequency bandwidth. In the case of traditional DFT, the signal is projected over complex exponentials: if the signal does not contain any component at the given frequency, the corresponding coefficient will be zero or at least negligible. In other words the projection operator has filtered out that contribution. An HT-based approach, instead, would enable the set of vectors to cover a wider spectral bandwidth, larger than a simple Dirichlet kernel and thus could also approximate wide-band events.

A possible solution via functional basis is provided in this Section, in order to demonstrate the prospective application of such an approach. In particular, a dictionary of vectors that span the possible space of solutions is constructed. The acquired signal is then projected over this dictionary. Finally, the vector that minimizes the residuals is selected as solution. It is sufficient to multiply the selected vector for the corresponding projection coefficient to obtain the best approximated trend.

First, the frequency of the fundamental tone is limited to a finite bandwidth between 48 and 52 Hz with a step of 0.01 Hz. Then, inspired by the IEEE Std. C37.118 [19], for each frequency of interest, the following vectors are included in the basis:

- A sinusoid in steady-state ($g_A = 0$, $dg_f/dt = 0$ and $g_\varphi = 0$ in (7.46)):
- A sinusoid characterized by an amplitude modulation $g_A(t) = 1 + k_a \cdot \cos(2\pi f_a t)$, being $k_a = 10\%$ and $f_a = [1, 5]$ Hz with steps of 0.01 Hz, while dg_f/dt and g_φ are null;
- A sinusoid with frequency ramp $g_\varphi(t) = R \cdot \pi t^2$, being $R = [-6, 6]$ Hz/s with steps of 0.01 Hz/s, while g_A and dg_f/dt are null.

Figure 7.15 presents the results in case of analyzing the same waveforms of case (b) of Section 7.4.1. In particular, the case of a signal characterized by a negative frequency ramp with $50 \leq f_0 \leq 46$, being $R = -6$ Hz/s the ramp rate in (7.19) is analyzed, considering the results provided by EMTP-RV simulations. It is worth noticing that the functional basis implementation provides results that are comparable with the ones obtained using the filter implementation in Algorithm 8.

7.5 Discussion

The Chapter proposed an HT-based approach for studying broadband power system dynamics as an alternative to the traditional phasor-based representation. First, the FT and HT of three large power system dynamics have been compared, and the limitations of FT-based analysis in non-stationary conditions have been discussed, as well as the HT capability of tracking the evolution of the signals. Then, a numerical analysis has been carried out, based on two strategies for the estimation of instantaneous power, relying on DFT and HT representation. The accuracy to correctly compute the transmitted instantaneous power of the proposed transforms has been assessed in both synthetic and real-world datasets. To this end, dedicated time-domain simulations have been carried out.

Both theoretical and numerical results confirm that the HT is a suitable tool to be used in power system modeling and operation. Indeed, the HT provides superior results when computing the instantaneous power in all the considered operating conditions, leading to power errors up to 100 times smaller than in the case of using an DFT-based representation.

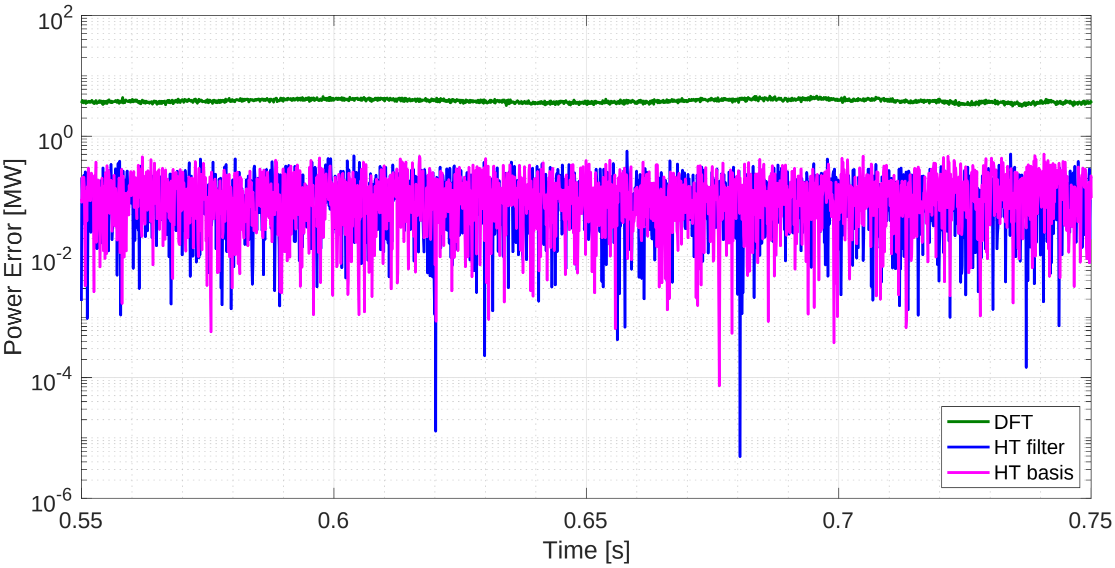

Figure 7.15 – Signal characterized by a negative frequency ramp of -6 Hz/s: Instantaneous three-phase power error computed using the DFT (green), the HT as in Algorithm 8 (blue) and the HT using functional analysis.

The treatise presented in this Chapter opens new scenarios for modern power systems modeling, as it demonstrated the possibility to leverage on HT-based power system analysis, provided that an appropriate functional basis is formulated. On the one hand, HT-based situational awareness systems that rely on a broad spectrum could be deployed. For instance, we could think of PMUs capable of computing the analytic signal rather than the fundamental component synchrophasor. On the other hand, based on circuit theory fundamental laws in the HT domain, we could think of HT-based tools for power systems dynamics analysis.

8 Conclusion

The Thesis proposed, developed, and experimentally validated new technologies for real-time situational awareness to be used in reduced-inertia power systems. For electrical grids operating in quasi-stationary conditions, the distributed sensing of *synchrophasors* via time-synchronized PMUs was investigated, including all the involved technological aspects. When the steady-state assumption is violated, the synchrophasor model does no longer preserve a truthful representation of the grid actual state. Therefore, a new approach based on the Hilbert transform was proposed.

The first contribution of the Thesis was investigating enhanced signal processing tools that comply with the stringent requirements of modern synchrophasor estimators, in terms of accuracy and responsiveness. Two original methods were proposed. They are based on the interpolated DFT (i-IpDFT) and the Hilbert transform (HT-IpDFT), and are resilient to harmonic and inter-harmonic interfering tones, even if adopting extremely short observation intervals. The i-IpDFT was specifically designed to deal with inter-harmonic tones that fall within the PMU pass-band and, therefore, degrade the performance of most synchrophasor estimators. In particular, the interfering components are detected, estimated, and suitably compensated from the original spectrum through a dedicated iterative routine. A window length of 3-cycles at the nominal power system frequency is adopted (60 ms at 50 Hz) in order to successfully handle the high share of spectral leakage, but still distinguish between adjacent tones. As an evolution, the HT-IpDFT was designed to prefilter the acquired signal via the Hilbert transform, and thus confine the spectral analysis to the positive frequency range. Then, the i-IpDFT is used to filter out spurious contributions and estimate the synchrophasors. In this reduced-leakage scenario, the observation interval is further scaled down up to 2-cycles, corresponding to 40 ms at 50 Hz.

The performance assessment of the proposed algorithms demonstrated that they fulfill all the requirements defined in the IEEE Std. C37.118, for both P- and M-class at the same time. They are characterized by the responsiveness demanded by protection applications and the accuracy of measurement applications, without the need of switching between the two classes. Therefore, the reliability of subsequent mission-critical actions is preserved despite high signal distortion. The implementation of the developed estimators into embedded PMUs demonstrated their prospective deployability into real-scale grids.

Regarding accuracy, the i-IpDFT and the HT-IpDFT exhibited a maximum TVE in the order of $0.0x\%$ and $0.x\%$ in static and dynamic operating conditions, respectively. As a consequence, the type-testing of PMUs embedding those algorithms requires a validation system whose accuracy is at least one order of magnitude better. Achieving such a stringent level of accuracy was the second goal of the Thesis that was accomplished by means of an advanced PMU calibrator. The validation platform consists of a forward path, to generate the reference waveforms, and a return path, to re-acquire the waveforms and estimate their reference parameters through a non-linear least-squares fitting algorithm. The two actions are suitably synchronized to a highly stable timing source. The metrological characterization of the PMU calibrator was carried out within the whole range of tests defined in the IEEE Std. C37.118, as well as in user-defined scenarios. The TVE associated with the reference synchrophasors proved to be in the order of $0.00x\%$ in static and $0.0x\%$ in dynamic conditions.

Then, the Thesis studied other technological aspects expected to improve the overall reliability of synchrophasor networks. The initial challenge was ensuring the seamless synchronization of wide-area devices and guaranteeing high-precision time-stamping of PMU-data. In particular, a cutting-edge time dissemination protocol named White Rabbit was integrated into an FPGA-based PMU. The White Rabbit is a sub-nanosecond accurate timing system, intended to connect thousands of nodes through already existing Ethernet networks. The protocol can be used to substitute or complement the GPS, without resulting in expensive installation costs as the time information exchange can potentially rely on the legacy telecom infrastructure used to stream PMU-data. The experimental validation confirmed that the protocol minimizes the time uncertainty contribution, thus optimizing the PMU performance in terms of phase estimation, in comparison with state-of-the-art time dissemination methods (i.e., GPS and PTP).

The next goal was to improve the overall time-determinism of PMU-data delivery and to reduce the packet loss. Specifically, the design of a low-latency phasor data concentrator enabled mitigating the latency variations introduced by the underlying communication infrastructure. The experimental validation proved that the proposed architecture reduces the end-to-end latency, regardless of the adopted physical layer. Results showed that the function also preserves data-completeness. The performance assessment was carried out in two real-scale grids that adopted optical fiber links and 4G LTE to support PMU-related traffic. This last trial further validated the feasibility of exploiting the 4G LTE technology for PMU-based applications.

The last contribution of the Thesis was proposing a new approach for power systems modeling under non-stationary operating conditions that goes beyond the concept of phasor. Indeed, the main limitation of the synchrophasor technology lies in the ill-posed mathematical model used to formulate the rules governing steep electromechanical transients that are expected to take place in modern and future grids experiencing large shares of power-electronics interfaced generators. The proposed method was inspired by the theory on analytic signals and is based on the Hilbert transform. Such transformation enables the tracking of system dynamics that are preserved unaltered over the entire frequency spectrum. The conservation of energy in the Hilbert transform domain demonstrated its potential applicability to transient analysis. The performance of the proposed approach was assessed in a simulated environment and compared to a traditional phasor-based methodology. Results proved the Hilbert transform capability of accurately tracking the evolution of instantaneous power flows. This last contribution of the Thesis opens the floor to new scenarios for power system modeling.

Future Works

The proposed technologies can be integrated into situational awareness tools, to monitor and control modern grids more effectively and reliably. However, more research is still required in this direction. The following points are suggested for further investigation:

- The proposed synchrophasor estimators would benefit from a more effective strategy to detect small amplitude interfering tones and transient events. Also, the assessment of the algorithms' performance under off-standard operating conditions is advised.
- The presented PMU calibrator should rely on a non-multiplexed card for the generation and re-acquisition of the generated waveforms. This would reduce the delay between the two actions. Also, the White Rabbit protocol could be used to synchronize the boards, to further reduce timing errors.
- The integration of multiple time dissemination techniques within the same device would improve the overall PMU robustness in terms of redundancy. A procedure to switch among the most reliable synchronization source is needed.
- The use of wireless communication networks to support synchrophasor-data traffic would drastically reduce the PMU installation cost and time, in sites where the cabled infrastructure is not present. Examination of novel wireless technologies is advised, with a particular focus on cyber-security and data-availability issues.
- Study and define a comprehensive vector basis kernel to perform functional analysis with the Hilbert transform. The latter would enable the identification of a mathematical model for each parameter, and, therefore, the compression the time domain information into few coefficients. This would be beneficial for developing Hilbert-based sensing technologies.

Bibliography

[1] A. Derviškadić, Y. Zuo, G. Frigo, and M. Paolone, "Under frequency load shedding based on PMU estimates of frequency and ROCOF," in *2018 IEEE PES Innovative Smart Grid Technologies Conference Europe (ISGT-Europe)*, pp. 1–6, Oct. 2018.

[2] G. Frigo, A. Derviškadić, C. Narduzzi, and M. Paolone, "Synchrophasor-based ROCOF measurements: Feasibility in real-world scenarios," in *2018 IEEE 9th International Workshop on Applied Measurements for Power Systems (AMPS)*, pp. 1–6, Sept. 2018.

[3] G. Frigo, A. Derviškadić, Y. Zuo, and M. Paolone, "PMU-based ROCOF measurements: Uncertainty limits and metrological significance in power system applications," *IEEE Transactions on Instrumentation and Measurement*, pp. 1–1, 2019.

[4] G. Frigo, A. Derviškadić, Y. Zuo, and M. Paolone, "Taylor-Fourier model on a real-time simulator: Design, implementation and characterization," in *2019 IEEE Milano PowerTech*, pp. 1–6, June 2019.

[5] Y. Zuo, G. Frigo, A. Derviškadić, and M. Paolone, "Impact of synchrophasor estimation algorithms in ROCOF-based under-frequency load-shedding," *IEEE Transactions on Power Systems*, 2019.

[6] G. Frigo, A. Derviškadić, A. Bach, and M. Paolone, "Statistical model of measurement noise in real-world PMU-based acquisitions," in *First IEEE International Conference on Smart Grid Synchronized Measurements and Analytics (SGSMA)*, 2019.

[7] G. Frigo, A. Derviškadić, P. A. Pegoraro, C. Muscas, and M. Paolone, "Harmonic phasor measurements in real-world PMU-based acquisitions," in *2019 IEEE International Instrumentation and Measurement Technology Conference (I2MTC)*, 2019.

[8] A. Derviškadić, P. Romano, and M. Paolone, "Iterative-interpolated DFT for synchrophasor estimation: A single algorithm for P- and M-class compliant PMUs," *IEEE Transactions on Instrumentation and Measurement*, vol. 67, pp. 547–558, Mar. 2018.

[9] A. Derviškadić, P. Romano, and M. Paolone, "Iterative-interpolated DFT for synchrophasor estimation in M-class compliant PMUs," in *2017 IEEE Manchester PowerTech*, pp. 1–6, June 2017.

[10] G. Frigo, A. Derviškadić, and M. Paolone, “Reduced leakage synchrophasor estimation: Hilbert transform plus interpolated DFT,” *IEEE Transactions on Instrumentation and Measurement*, pp. 1–16, 2018.

[11] G. Frigo, D. Colangelo, A. Derviškadić, M. Pignati, C. Narduzzi, and M. Paolone, “Definition of accurate reference synchrophasors for static and dynamic characterization of PMUs,” *IEEE Transactions on Instrumentation and Measurement*, vol. 66, pp. 2233–2246, Sept. 2017.

[12] G. Frigo, A. Derviškadić, D. Colangelo, J.-P. Braun, and M. Paolone, “Characterization of uncertainty contributions in a high-accuracy PMU validation system,” *Measurement*, 2019.

[13] R. Razzaghi, A. Derviškadić, and M. Paolone, “A white rabbit synchronized PMU,” in *2017 IEEE PES Innovative Smart Grid Technologies Conference Europe (ISGT-Europe)*, pp. 1–6, Sept. 2017.

[14] A. Derviškadić, R. Razzaghi, Q. Walger, and M. Paolone, “The white rabbit time synchronization protocol for synchrophasor networks,” *IEEE Transactions on Smart Grid, Special Section on Theory and Application of PMUs in Power Distribution Systems*, 2019.

[15] A. Derviškadić, G. Frigo, and M. Paolone, “Impact of time dissemination technologies on synchrophasor estimation accuracy,” in *First IEEE International Conference on Smart Grid Synchronized Measurements and Analytics (SGSMA)*, 2019.

[16] A. Derviškadić, P. Romano, M. Pignati, and M. Paolone, “Architecture and experimental validation of a low-latency phasor data concentrator,” *IEEE Transactions on Smart Grid*, vol. 9, pp. 2885–2893, July 2018.

[17] A. Derviškadić, P. Romano, C. Get, W. Koong Chai, C. Develder, L. Zanni, M. Pignati, and M. Paolone, “Design and experimental validation of an LTE-based synchrophasor network in a medium voltage distribution grid,” in *2018 Power Systems Computation Conference (PSCC)*, pp. 1–7, June 2018.

[18] A. Derviškadić, G. Frigo, and M. Paolone, “Beyond phasors: Continuous-spectrum modeling of power systems using the Hilbert transform,” *Submitted to IEEE Transactions on Power Systems, arXiv preprint arXiv:1906.11154*, 2019.

[19] “IEEE Standard for Synchrophasor Measurements for Power Systems,” *IEEE Std C37.118.1-2011 (Revision of IEEE Std C37.118-2005)*, pp. 1–61, Dec. 2011.

[20] “IEEE Standard for Synchrophasor Measurements for Power Systems – Amendment 1: Modification of Selected Performance Requirements,” *IEEE Std C37.118.1a-2014 (Amendment to IEEE Std C37.118.1-2011)*, pp. 1–25, Apr. 2014.

[21] “IEEE Standard for Synchrophasor Data Transfer for Power Systems,” *IEEE Std C37.118.2-2011 (Revision of IEEE Std C37.118-2005)*, pp. 1–53, Dec. 2011.

[22] A. Phadke and J. Thorp, *Synchronized Phasor Measurements and Their Applications*. Springer, Cham, 2017.

[23] “IEEE/IEC International Standard - Measuring relays and protection equipment - Part 118-1: Synchrophasor for power systems - Measurements,” *IEC/IEEE 60255-118-1:2018*, pp. 1–78, Dec. 2018.

[24] A. G. Phadke and B. Kasztenny, “Synchronized phasor and frequency measurement under transient conditions,” *IEEE Transactions on Power Delivery*, vol. 24, pp. 89–95, Jan 2009.

[25] G. Barchi, D. Macii, and D. Petri, “Synchrophasor estimators accuracy: A comparative analysis,” *IEEE Transactions on Instrumentation and Measurement*, vol. 62, pp. 963–973, May 2013.

[26] F. Milano, F. Dörfler, G. Hug, D. J. Hill, and G. Verbič, “Foundations and challenges of low-inertia systems (invited paper),” in *2018 Power Systems Computation Conference (PSCC)*, pp. 1–25, June 2018.

[27] W. Winter, K. Elkington, G. Bareux, and J. Kostevc, “Pushing the limits: Europe’s new grid: Innovative tools to combat transmission bottlenecks and reduced inertia,” *IEEE Power and Energy Magazine*, Jan 2015.

[28] P. Tielens and D. V. Hertem, “The relevance of inertia in power systems,” *Renewable and Sustainable Energy Rev*, vol. 55, pp. 999 – 1009, 2016.

[29] B. Kroposki, B. Johnson, Y. Zhang, V. Gevorgian, P. Denholm, B. Hodge, and B. Hannegan, “Achieving a 100% renewable grid: Operating electric power systems with extremely high levels of variable renewable energy,” *IEEE Power and Energy Magazine*, vol. 15, pp. 61–73, March 2017.

[30] D. Groß and F. Dörfler, “On the steady-state behavior of low-inertia power systems,” *IFAC-PapersOnLine*, vol. 50, no. 1, pp. 10735 – 10741, 2017. 20th IFAC World Congress.

[31] F. R. S. Sevilla, P. Korba, K. Uhlen, E. Hillberg, G. Lindahl, and W. Sattinger, “Evaluation of the ENTSO-E initial dynamic model of continental Europe subject to parameter variations,” in *2017 IEEE Power Energy Society Innovative Smart Grid Technologies Conference (ISGT)*, pp. 1–2, April 2017.

[32] H. Pulgar-Painemal, Y. Wang, and H. Silva-Saravia, “On inertia distribution, inter-area oscillations and location of electronically-interfaced resources,” *IEEE Transactions on Power Systems*, vol. 33, pp. 995–1003, Jan 2018.

[33] N. Nguyen and J. Mitra, “Reliability of power system with high wind penetration under frequency stability constraint,” *IEEE Transactions on Power Systems*, vol. 33, pp. 985–994, Jan 2018.

[34] F. K. Tuffner, K. P. Schneider, J. Hansen, and M. A. Elizondo, "Modeling load dynamics to support resiliency-based operations in low-inertia microgrids," *IEEE Transactions on Smart Grid*, vol. 10, pp. 2726–2737, May 2019.

[35] G. Chang, C. Hatziadoniu, W. Xu, P. Ribeiro, R. Burch, W. M. Grady, M. Halpin, Y. Liu, S. Ranade, D. Ruthman, N. Watson, T. Ortmeyer, J. Wikston, A. Medina, A. Testa, R. Gardinier, V. Dinavahi, F. Acram, and P. Lehn, "Modeling devices with nonlinear voltage-current characteristics for harmonic studies," *IEEE Transactions on Power Delivery*, vol. 19, pp. 1802–1811, Oct. 2004.

[36] S. A. Papathanassiou and F. Santjer, "Power-quality measurements in an autonomous island grid with high wind penetration," *IEEE Transactions on Power Delivery*, vol. 21, pp. 218–224, Jan. 2006.

[37] S. Elphick, P. Ciufo, G. Drury, V. Smith, S. Perera, and V. Gosbell, "Large scale proactive power-quality monitoring: An example from Australia," *IEEE Transactions on Power Delivery*, vol. 32, pp. 881–889, April 2017.

[38] L. Cristaldi, A. Ferrero, and S. Salicone, "A distributed system for electric power quality measurement," *IEEE Transactions on Instrumentation and Measurement*, vol. 51, pp. 776–781, Aug 2002.

[39] AEMO, "Black System South Australia 28 September 2016," tech. rep., Australian Energy Market Operator, 2017.

[40] ENTSO-E, "Analysis of CE inter-area oscillations of 1^{st} December 2016," tech. rep., European Network of Transmission System Operators for Electricity, 2017.

[41] NASPI, "Synchrophasor monitoring for distribution systems: Technical foundations and applications," tech. rep., NASPI Distribution Task Team, 2018.

[42] A. von Meier, E. Stewart, A. McEachern, M. Andersen, and L. Mehrmanesh, "Precision micro-synchrophasors for distribution systems: A summary of applications," *IEEE Transactions on Smart Grid*, vol. 8, pp. 2926–2936, Nov 2017.

[43] F. Sossan, E. Namor, R. Cherkaoui, and M. Paolone, "Achieving the dispatchability of distribution feeders through prosumers data driven forecasting and model predictive control of electrochemical storage," *IEEE Transactions on Sustainable Energy*, vol. 7, pp. 1762–1777, Oct. 2016.

[44] DESL-EPFL, "Point-on-wave Data of EPFL-campus Distribution Network." [Online]. Available: https://github.com/DESL-EPFL/. Accessed: 2019-07-01.

[45] M. Paolone and P. Romano, *Advances in Power System Modelling, Control and Stability Analysis*, ch. 3: DFT-based synchrophasor estimation processes for Phasor Measurement Units applications: algorithms definition and performance analysis. F. Milano, Ed. Edison, NJ, USA: IET, 2015.

[46] Joint Committee for Guides in Metrology (JCGM), "International vocabulary of basic and general terms in metrology (VIM)," *JCGM 200:2012*, 2012.

[47] Joint Committee for Guides in Metrology (JCGM), "Guide to the expression of uncertainty in measurement (GUM)," *JCGM 100:2008*, 2008.

[48] D. Macii, D. Fontanelli, G. Barchi, and D. Petri, "Impact of acquisition wideband noise on synchrophasor measurements: A design perspective," *IEEE Transactions on Instrumentation and Measurement*, vol. 65, pp. 2244–2253, Oct. 2016.

[49] A. J. Roscoe, G. M. Burt, and G. Rietveld, "Improving frequency and ROCOF accuracy during faults, for P class phasor measurement units," in *2013 IEEE International Workshop on Applied Measurements for Power Systems (AMPS)*, pp. 97–102, Sept 2013.

[50] W. Dickerson, "Effect of PMU analog input section performance on frequency and ROCOF estimation error," in *2015 IEEE International Workshop on Applied Measurements for Power Systems (AMPS)*, pp. 31–36, Sept 2015.

[51] A. Riepnieks and H. Kirkham, "Rate of change of frequency measurement," in *2016 57th International Scientific Conference on Power and Electrical Engineering of Riga Technical University (RTUCON)*, pp. 1–5, Oct 2016.

[52] A. J. Roscoe, A. Dyśko, B. Marshall, M. Lee, H. Kirkham, and G. Rietveld, "The case for redefinition of frequency and ROCOF to account for AC power system phase steps," in *2017 IEEE International Workshop on Applied Measurements for Power Systems (AMPS)*, pp. 1–6, Sept. 2017.

[53] T. Amraee, M. G. Darebaghi, A. Soroudi, and A. Keane, "Probabilistic under frequency load shedding considering RoCoF relays of distributed generators," *IEEE Transactions on Power Systems*, vol. 33, pp. 3587–3598, July 2018.

[54] P. Gupta, R. S. Bhatia, and D. K. Jain, "Active ROCOF relay for islanding detection," *IEEE Transactions on Power Delivery*, vol. 32, pp. 420–429, Feb 2017.

[55] W. Freitas, Wilsun Xu, C. M. Affonso, and Zhenyu Huang, "Comparative analysis between ROCOF and vector surge relays for distributed generation applications," *IEEE Transactions on Power Delivery*, vol. 20, pp. 1315–1324, April 2005.

[56] P. Romano and M. Paolone, "Enhanced interpolated-DFT for synchrophasor estimation in FPGAs: Theory, implementation, and validation of a PMU prototype," *IEEE Transactions on Instrumentation and Measurement*, vol. 63, pp. 2824–2836, Dec. 2014.

[57] M. Bertocco, G. Frigo, C. Narduzzi, C. Muscas, and P. A. Pegoraro, "Compressive sensing of a Taylor-Fourier multifrequency model for synchrophasor estimation," *IEEE Transactions on Instrumentation and Measurement*, vol. 64, pp. 3274–3283, Dec. 2015.

[58] G. Trudel, J. P. Gingras, and J. R. Pierre, "Designing a reliable power system: Hydroquebec's integrated approach," *Proceedings of the IEEE*, vol. 93, pp. 907–917, May 2005.

[59] A. Borghetti, C. A. Nucci, M. Paolone, G. Ciappi, and A. Solari, "Synchronized phasors monitoring during the islanding maneuver of an active distribution network," in *2010 Innovative Smart Grid Technologies (ISGT)*, pp. 1–8, Jan 2010.

[60] C. Narduzzi, M. Bertocco, G. Frigo, and G. Giorgi, "Fast-TFM—multifrequency phasor measurement for distribution networks," *IEEE Transactions on Instrumentation and Measurement*, vol. 67, pp. 1825–1835, Aug. 2018.

[61] P. Cote, S. Cote, and M. Lacroix, "Programmable load shedding-systems: Hydro-Quebec's experience," in *2001 Power Engineering Society Summer Meeting. Conference Proceedings (Cat. No.01CH37262)*, vol. 2, pp. 818–823 vol.2, July 2001.

[62] I. Kamwa, S. R. Samantaray, and G. Joos, "Wide frequency range adaptive phasor and frequency PMU algorithms," *IEEE Transactions on Smart Grid*, vol. 5, pp. 569–579, March 2014.

[63] I. Kamwa, S. R. Samantaray, and G. Joos, "Compliance analysis of PMU algorithms and devices for wide-area stabilizing control of large power systems," *IEEE Transactions on Power Systems*, vol. 28, pp. 1766–1778, May 2013.

[64] P. Castello, C. Muscas, P. A. Pegoraro, and S. Sulis, "Analysis of PMU response under voltage fluctuations in distribution grids," in *2016 IEEE International Workshop on Applied Measurements for Power Systems (AMPS)*, pp. 1–5, Sep. 2016.

[65] "IEEE guide for the application of protective relays used for abnormal frequency load shedding and restoration," *IEEE Std C37.117-2007*, pp. 1–55, Aug 2007.

[66] ENTSO-E, "Technical background and recommendations for defence plans in the continental Europe synchronous area," tech. rep., European Network of Transmission System Operators for Electricity, 2010.

[67] "Opal-RT eMEGAsim PowerGrid real-time digital hardware in the loop simulator." [Online]. Available: https://www.opal-rt.com/. Accessed: 2019-07-01.

[68] T. Athay, R. Podmore, and S. Virmani, "A practical method for the direct analysis of transient stability," *IEEE Transactions on Power Apparatus and Systems*, vol. PAS-98, pp. 573–584, March 1979.

[69] R. Byerly, D. Sherman, and R. Bennon, "Phase II: frequency domain analysis of low-frequency oscillations in large electric power systems. Volume 1. Basic concepts, mathematical models, and computing methods.," tech. rep., Westinghouse Electric Corp., Pittsburgh, PA (USA). Advanced Systems, 1982.

[70] P. Romano, M. Pignati, and M. Paolone, "Integration of an IEEE Std. C37.118 compliant PMU into a real-time simulator," in *2015 IEEE Eindhoven PowerTech*, pp. 1–6, June 2015.

[71] "Interharmonics in power systems," tech. rep., IEEE Interharmonic Task Force, Cigré 36.05/CIRED 2 CC02 Voltage Quality Working Group, 1997.

[72] A. J. Roscoe, "Exploring the relative performance of frequency-tracking and fixed-filter phasor measurement unit algorithms under C37.118 test procedures, the effects of interharmonics, and initial attempts at merging P-class response with M-class filtering," *IEEE Transactions on Instrumentation and Measurement*, vol. 62, pp. 2140–2153, Aug. 2013.

[73] P. Castello, J. Liu, C. Muscas, P. A. Pegoraro, F. Ponci, and A. Monti, "A fast and accurate PMU algorithm for P+M class measurement of synchrophasor and frequency," *IEEE Transactions on Instrumentation and Measurement*, vol. 63, pp. 2837–2845, Dec. 2014.

[74] M. Pignati, L. Zanni, P. Romano, R. Cherkaoui, and M. Paolone, "Fault detection and faulted line identification in active distribution networks using synchrophasors-based real-time state estimation," *IEEE Transactions on Power Delivery*, vol. 32, pp. 381–392, Feb. 2017.

[75] D. Belega and D. Petri, "Sine-wave parameter estimation by interpolated DFT method based on new cosine windows with high interference rejection capability," *Digital Signal Processing*, vol. 33, pp. 60 – 70, 2014.

[76] D. Agrez, "Weighted multipoint interpolated DFT to improve amplitude estimation of multifrequency signal," *IEEE Transactions on Instrumentation and Measurement*, vol. 51, pp. 287–292, Apr. 2002.

[77] D. Belega, D. Petri, and D. Dallet, "Frequency estimation of a sinusoidal signal via a three-point interpolated DFT method with high image component interference rejection capability," *Digital Signal Processing*, vol. 24, pp. 162–169, 2014.

[78] D. Belega and D. Petri, "Accuracy analysis of the multicycle synchrophasor estimator provided by the interpolated DFT algorithm," *IEEE Transactions on Instrumentation and Measurement*, vol. 62, pp. 942–953, May 2013.

[79] T. Radil, P. M. Ramos, and A. Cruz Serra, "New spectrum leakage correction algorithm for frequency estimation of power system signals," *IEEE Transactions on Instrumentation and Measurement*, vol. 58, pp. 1670–1679, May 2009.

[80] A. Ferrero, S. Salicone, and S. Toscani, "A fast, simplified frequency-domain interpolation method for the evaluation of the frequency and amplitude of spectral components," *IEEE Transactions on Instrumentation and Measurement*, vol. 60, pp. 1579–1587, May 2011.

[81] D. Belega, D. Petri, and D. Dallet, "Impact of harmonics on the interpolated DFT frequency estimator," *Mechanical Systems and Signal Processing*, vol. 66–67, pp. 349 – 360, 2016.

[82] V. K. Jain, W. L. Collins, and D. C. Davis, "High-accuracy analog measurements via interpolated FFT," *IEEE Transactions on Instrumentation and Measurement*, vol. 28, pp. 113–122, June 1979.

[83] T. Grandke, "Interpolation algorithms for discrete fourier transforms of weighted signals," *IEEE Transactions on Instrumentation and Measurement*, vol. 32, pp. 350–355, June 1983.

[84] F. J. Harris, "On the use of windows for harmonic analysis with the discrete fourier transform," *Proceedings of the IEEE*, vol. 66, pp. 51–83, Jan. 1978.

[85] K. Duda and S. Barczentewicz, "Interpolated DFT for $\sin^{\alpha}(x)$ windows," *IEEE Transactions on Instrumentation and Measurement*, vol. 63, pp. 754–760, Apr. 2014.

[86] "IEEE Guide for Synchronization, Calibration, Testing, and Installation of Phasor Measurement Units (PMUs) for Power System Protection and Control," *IEEE Std C37.242-2013*, pp. 1–107, Mar. 2013.

[87] "National Instruments CompactRIO Controller." [Online]. Available: http://www.ni.com/en-us/shop/select/compactrio-controller. Accessed: 2019-07-01.

[88] "National Instruments CompactRIO 9039 Controller." [Online]. Available: http://www.ni.com/en-us/support/model.crio-9039.html. Accessed: 2019-07-01.

[89] "National Instruments NI 9225 C Series Voltage Input Module." [Online]. Available: http://www.ni.com/en-us/support/model.ni-9225.html. Accessed: 2019-07-01.

[90] "National Instruments NI 9227 C Series Current Input Module." [Online]. Available: http://www.ni.com/en-us/support/model.ni-9227.html. Accessed: 2019-07-01.

[91] J. W. Stahlhut, T. J. Browne, G. T. Heydt, and V. Vittal, "Latency viewed as a stochastic process and its impact on wide area power system control signals," *IEEE Transactions on Power Systems*, vol. 23, pp. 84–91, Feb. 2008.

[92] C. Qian and M. Kezunovic, "A power waveform classification method for adaptive synchrophasor estimation," *IEEE Transactions on Instrumentation and Measurement*, vol. 67, pp. 1646–1658, July 2018.

[93] M. Sahani and P. K. Dash, "Automatic power quality events recognition based on Hilbert Huang transform and weighted bidirectional extreme learning machine," *IEEE Transactions on Industrial Informatics*, vol. 14, pp. 3849–3858, Sep. 2018.

[94] I. Urbina-Salas, J. R. Razo-Hernandez, D. Granados-Lieberman, M. Valtierra-Rodriguez, and J. E. Torres-Fernandez, "Instantaneous power quality indices based on single-sideband modulation and wavelet packet-Hilbert transform," *IEEE Transactions on Instrumentation and Measurement*, vol. 66, pp. 1021–1031, May 2017.

[95] S. Affijulla and P. Tripathy, "Development of phasor estimation algorithm for P-class PMU suitable in protection applications," *IEEE Transactions on Smart Grid*, vol. 9, pp. 1250–1260, March 2018.

[96] S. L. Hahn, *Hilbert transforms in signal processing*. Artech House, 1996.

[97] P. Henricci, *Applied and Computational Complex Analysis, Volume 1: Power Series Integration Conformal Mapping Location of Zero.* John Wiley & Sons, 1988.

[98] M. Alavi-Sereshki and J. Prabhakar, "A tabulation of Hilbert transforms for electrical engineers," *IEEE Transactions on Communications*, vol. 20, pp. 1194–1198, Dec. 1972.

[99] R. N. Bracewell, *The Fourier Transform and Its Applications*, vol. 31999. McGraw-Hill New York, 1963.

[100] V. Cizek, "Discrete Hilbert transform," *IEEE Transactions on Audio and Electroacoustics*, vol. 18, pp. 340–343, Dec. 1970.

[101] I. Kollar, R. Pintelon, and J. Schoukens, "Optimal FIR and IIR Hilbert transformer design via LS and minimax fitting," *IEEE Transactions on Instrumentation and Measurement*, vol. 39, pp. 847–852, Dec. 1990.

[102] M. Sabri and W. Steenaart, "Discrete Hilbert transform filtering," *IEEE Transactions on Acoustics, Speech, and Signal Processing*, vol. 25, pp. 452–454, Oct. 1977.

[103] L. Peretto, P. Rinaldi, R. Sasdelli, and R. Tinarelli, "A system for the measurement of the starting instant of impulsive transients [power systems]," in *Proceedings of the 21st IEEE Instrumentation and Measurement Technology Conference (IEEE Cat. No.04CH37510)*, vol. 2, pp. 1394–1398 Vol.2, May 2004.

[104] L. Peretto, P. Rinaldi, R. Sasdelli, R. Tinarelli, and A. Fioravanti, "Implementation and characterization of a system for the evaluation of the starting instant of lightning-induced transients," *IEEE Transactions on Instrumentation and Measurement*, vol. 56, pp. 1955–1960, Oct 2007.

[105] A. Riepnieks, H. Kirkham, A. J. Faris, and M. Engels, "Phase jumps in PMU signal generators," in *2017 IEEE Power Energy Society General Meeting*, pp. 1–5, July 2017.

[106] "IEEE Synchrophasor Measurement Test Suite Specification–Version 3," *IEEE Synchrophasor Measurement Test Suite Specification–Version 3*, pp. 1–38, July 2019.

[107] J. P. Braun and S. Siegenthaler, "The metrological characterization of PMUs," in *Workshop on Synchrophasor Estimation Processes for Phasor Measurement Units*, EPFL, 2014.

[108] G. Stenbakken and T. Nelson, "Static calibration and dynamic characterization of PMUs at NIST," in *2007 IEEE Power Engineering Society General Meeting*, pp. 1–4, June 2007.

[109] Y. Tang, G. N. Stenbakken, and A. Goldstein, "Calibration of phasor measurement unit at NIST," *IEEE Transactions on Instrumentation and Measurement*, vol. 62, pp. 1417–1422, June 2013.

[110] J. Braun and C. Mester, "Reference grade calibrator for the testing of the dynamic behavior of phasor measurement units," in *2012 Conference on Precision electromagnetic Measurements (CPEM 2012)*, pp. 410–411, July 2012.

[111] U. Pogliano, J. Braun, B. Volj, and R. Lapuh, “Software platform for PMU algorithms testing,” in *2012 Conference on Precision electromagnetic Measurements (CPEM 2012)*, pp. 412–413, July 2012.

[112] D. Colangelo, D. Hoogenboom, E. Dierikx, G. Rietveld, and G. Frigo, “Metrological characterization of a PMU calibrator in the 25 hz to 3 khz range,” in *2017 IEEE Manchester PowerTech*, pp. 1–6, June 2017.

[113] B. Trinchera, D. Serazio, and U. Pogliano, “Asynchronous phase comparator for characterization of devices and PMU calibrator,” in *2016 Conference on Precision Electromagnetic Measurements (CPEM 2016)*, pp. 1–2, July 2016.

[114] G. Rietveld, J. Braun, R. Martin, P. Wright, W. Heins, N. Ell, P. Clarkson, and N. Zisky, “Measurement infrastructure to support the reliable operation of smart electrical grids,” *IEEE Transactions on Instrumentation and Measurement*, vol. 64, pp. 1355–1363, June 2015.

[115] M. Acanski, G. Rietveld, and D. Hoogenboom, “Accurate phase calibration of PMUs and PMU calibrators,” in *2016 Conference on Precision Electromagnetic Measurements (CPEM 2016)*, pp. 1–2, July 2016.

[116] R. Garcia-Valle, G. Yang, K. E. Martin, A. H. Nielsen, and J. Østergaard, “DTU PMU laboratory development — testing and validation,” in *2010 IEEE PES Innovative Smart Grid Technologies Conference Europe (ISGT Europe)*, pp. 1–6, Oct 2010.

[117] J. Fernandez, “The virginia tech calibration system,” Master’s thesis, Virginia Polytechnic Institute and State University, 2011.

[118] C. Qian and M. Kezunovic, “Synchrophasor reference algorithm for PMU calibration system,” in *2016 IEEE/PES Transmission and Distribution Conference and Exposition (T D)*, pp. 1–5, May 2016.

[119] “Fluke Corporation, 6135A/PMUCAL Phasor Measurement Unit Calibration System.” [Online]. Available: http://us.flukecal.com/products/electrical-calibration/electrical-calibrators/, 2013. Accessed: 2019-07-01.

[120] Q. Guo, F. Chen, and R. Piacentini, “Virtual-instrumentation-based PMU calibrator for IEEE c37.118.1-2011 compliance testing,” in *CIGRE Grid of the Future Symposium*, 2014.

[121] “National Instruments PXI Systems.” [Online]. Available: https://www.ni.com/en-us/shop/pxi.html. Accessed: 2019-07-01.

[122] “National Instruments PXI-1042Q PXI Chassis.” [Online]. Available: http://www.ni.com/en-us/support/model.pxi-1042q.html. Accessed: 2019-07-01.

[123] “National Instruments PXI-8110 PXI Controller.” [Online]. Available: http://www.ni.com/en-us/support/model.pxi-8110.html. Accessed: 2019-07-01.

[124] "National Instruments PXI-6682 PXI Synchronization Module." [Online]. Available: http://www.ni.com/pdf/manuals/372292a.pdf. Accessed: 2019-07-01.

[125] "National Instruments PXI-6289 PXI Multifunction IO Module." [Online]. Available: http://www.ni.com/en-us/support/model.pxi-6289.html. Accessed: 2019-07-01.

[126] "Stanford Research Systems, Rubidium Frequency Standard - FS725, Ver 1.3." [Online]. Available: www.thinksrs.com/products/FS725.htm, 2015. Accessed: 2019-07-01.

[127] "Meinberg Funkuhren GmbH & Co. KG, GPS Clock for Computers (PCI/PCI-X Bus) - GPS169PCI." [Online]. Available: www.meinbergglobal.com/english/archive/gps169pci.htm, 2011. Accessed: 2019-07-01.

[128] "OMICRON electronics GmbH, Voltage and current amplifier - CMS 356." [Online]. Available: https://www.omicronenergy.com/en/products/cms-356/. Accessed: 2019-07-01.

[129] G. A. F. Seber and C. J. Wild, *Estimation Methods*, pp. 21–89. John Wiley & Sons, Inc., 2005.

[130] P. Carbone, J. Schoukens, and A. Moschitta, "Dynamic signal measurements based on quantized data," *IEEE Transactions on Instrumentation and Measurement*, vol. 66, pp. 223–233, Feb 2017.

[131] CEI, "EN 50160 Voltage Characteristics in Public Distribution Systems," *EN 50160:2010/A1:2015*, pp. 1–14, Sep 2015.

[132] G. Crotti, D. Gallo, D. Giordano, C. Landi, and M. Luiso, "Industrial comparator for smart grid sensor calibration," *IEEE Sensors Journal*, vol. 17, pp. 7784–7793, Dec 2017.

[133] E. Mohns, A. Mortara, H. Cayci, E. Houtzager, S. Fricke, M. Agustoni, and B. Ayhan, "Calibration of commercial test sets for non-conventional instrument transformers," in *2017 IEEE International Workshop on Applied Measurements for Power Systems (AMPS)*, pp. 1–6, Sep. 2017.

[134] "Keysight Technologies, 3458A Multimeter." [Online]. Available: https://literature.cdn.keysight.com/litweb/pdf/03458-90014.pdf, 2014. Accessed: 2019-07-01.

[135] "Stanford Research Systems, Universal Time Interval Counter - SR620." [Online]. Available: www.thinksrs.com/products/SR620.htm, 2006. Accessed: 2019-07-01.

[136] R. Lapuh, B. Voljč, and M. Lindič, "Evaluation of agilent 3458a time jitter performance," *IEEE Transactions on Instrumentation and Measurement*, vol. 64, pp. 1331–1335, June 2015.

[137] NASPI, "Time synchronization in the electric power system," tech. rep., NASPI Time Synchronization Task Force, 2018.

[138] "Application of phasor measurement units for monitoring power system dynamic performance," tech. rep., Cigré Working Group C4.34, 2017.

[139] X. Jiang, J. Zhang, B. J. Harding, J. J. Makela, and A. D. Domínguez-García, "Spoofing GPS receiver clock offset of phasor measurement units," *IEEE Transactions on Power Systems*, vol. 28, pp. 3253–3262, Aug. 2013.

[140] "IEEE Standard for a Precision Clock Synchronization Protocol for Networked Measurement and Control Systems," *IEEE Std 1588-2008 (Revision of IEEE Std 1588-2002)*, pp. 1–300, July 2008.

[141] J. Serrano, P. Alvarez, M. Cattin, E. G. Cota, P. M. J. H. Lewis, T. Włostowski, *et al.*, "The white rabbit project," in *Proceedings of ICALEPCS TUC004, Kobe, Japan*, 2009.

[142] M. Lipiński, T. Włostowski, J. Serrano, and P. Alvarez, "White rabbit: a PTP application for robust sub-nanosecond synchronization," in *2011 IEEE International Symposium on Precision Clock Synchronization for Measurement, Control and Communication (ISPCS)*, pp. 25–30, Sept. 2011.

[143] M. Lipiński, E. van der Bij, J. Serrano, T. Włostowski, G. Daniluk, A. Wujek, M. Rizzi, and D. Lampridis, "White rabbit applications and enhancements," in *2018 IEEE International Symposium on Precision Clock Synchronization for Measurement, Control, and Communication (ISPCS)*, pp. 1–7, Sept. 2018.

[144] F. Ramos, J. L. Gutiérrez-Rivas, J. López-Jiménez, B. Caracuel, and J. Díaz, "Accurate timing networks for dependable smart grid applications," *IEEE Transactions on Industrial Informatics*, vol. 14, pp. 2076–2084, May 2018.

[145] D. M. Anand, K. G. Brady, C. Nguyen, E. Song, K. Lee, Y. Li-Baboud, A. Goldstein, and G. FitzPatrick, "Measurement tools for substation equipment: Testing the interoperability of protocols for time transfer and communication," in *2018 IEEE International Symposium on Precision Clock Synchronization for Measurement, Control, and Communication (ISPCS)*, pp. 1–6, Sept. 2018.

[146] D. W. Allan, "Statistics of atomic frequency standards," *Proceedings of the IEEE*, vol. 54, pp. 221–230, Feb. 1966.

[147] E. Costa, "Simulation of the effects of different urban environments on GPS performance using digital elevation models and building databases," *IEEE Transactions on Intelligent Transportation Systems*, vol. 12, pp. 819–829, Sept. 2011.

[148] D. P. Shepard, T. E. Humphreys, and A. A. Fansler, "Evaluation of the vulnerability of phasor measurement units to GPS spoofing attacks," *International Journal of Critical Infrastructure Protection*, vol. 5, no. 3, pp. 146 – 153, 2012.

[149] C. Konstantinou, M. Sazos, A. S. Musleh, A. Keliris, A. Al-Durra, and M. Maniatakos, "GPS spoofing effect on phase angle monitoring and control in a real-time digital simulator-based hardware-in-the-loop environment," *IET Cyber-Physical Systems: Theory Applications*, vol. 2, no. 4, pp. 180–187, 2017.

[150] P. Risbud, N. Gatsis, and A. Taha, "Vulnerability analysis of smart grids to GPS spoofing," *IEEE Transactions on Smart Grid*, pp. 1–1, 2018.

[151] S. Barreto, M. Pignati, G. Dán, J.-Y. Le Boudec, and M. Paolone, "Undetectable timing-attack on linear state-estimation by using rank-1 approximation," *IEEE Transactions on Smart Grid*, vol. 9, pp. 3530–3542, July 2018.

[152] "IEEE Standard for Ethernet," *IEEE Std 802.3-2015 (Revision of IEEE Std 802.3-2012)*, pp. 1–4017, Mar. 2016.

[153] D. Mills, J. Martin, J. Burbank, and W. Kasch, "Network time protocol version 4: Protocol and algorithms specification," tech. rep., 2010.

[154] S. Barreto, A. Suresh, and J.-Y. Le Boudec, "Cyber-attack on packet-based time synchronization protocols: The undetectable delay box," in *2016 IEEE International Instrumentation and Measurement Technology Conference Proceedings*, pp. 1–6, May 2016.

[155] "IEEE Standard Profile for Use of IEEE 1588 Precision Time Protocol in Power System Applications," *IEEE Std C37.238-2017 (Revision of IEEE Std C37.238-2011)*, pp. 1–42, June 2017.

[156] "IEC/IEEE International Standard - Communication networks and systems for power utility automation - Part 9-3: Precision time protocol profile for power utility automation," *IEC/IEEE 61850-9-3 Edition 1.0 2016-05*, pp. 1–18, May 2016.

[157] "IEC International Standard - Communication networks and systems in substations - Part 5: Communication requirements for functions and device models.," *61850-5 IEC:2003(E)*, July 2003.

[158] "IEC International Standard - Instrument transformers – Part 9: Digital interface for instrument transformers," *IEC 61869-9 Edition 1.0 2016-04*, pp. 1–18, Apr. 2016.

[159] H. F. Albinali and A. P. S. Meliopoulos, "Resilient protection system through centralized substation protection," *IEEE Transactions on Power Delivery*, vol. 33, pp. 1418–1427, June 2018.

[160] P. Castello, P. Ferrari, A. Flammini, C. Muscas, and S. Rinaldi, "A new IED with PMU functionalities for electrical substations," *IEEE Transactions on Instrumentation and Measurement*, vol. 62, pp. 3209–3217, Dec 2013.

[161] M. Lixia, A. Benigni, A. Flammini, C. Muscas, F. Ponci, and A. Monti, "A software-only PTP synchronization for power system state estimation with PMUs," *IEEE Transactions on Instrumentation and Measurement*, vol. 61, pp. 1476–1485, May 2012.

[162] CERN, "The White Rabbit Project." [Online]. Available: http://white-rabbit.web.cern.ch/, 2017. Accessed: 2019-07-01.

[163] J. L. Gutiérrez-Rivas, J. López-Jiménez, E. Ros, and J. Díaz, "White rabbit HSR: A seamless subnanosecond redundant timing system with low-latency data capabilities for the smart grid," *IEEE Transactions on Industrial Informatics*, vol. 14, pp. 3486–3494, Aug. 2018.

[164] E. F. Dierikx, A. E. Wallin, T. Fordell, J. Myyry, P. Koponen, M. Merimaa, T. J. Pinkert, J. C. J. Koelemeij, H. Z. Peek, and R. Smets, "White rabbit precision time protocol on long-distance fiber links," *IEEE Transactions on Ultrasonics, Ferroelectrics, and Frequency Control*, vol. 63, pp. 945–952, July 2016.

[165] G. Fantino, G. Cerretto, and C. D. Costa, "White rabbit time transfer on medium and long fibre hauls at INRIM," in *Proceedings of the 46th Annual Precise Time and Time Interval Systems and Applications Meeting, Boston, Massachusetts*, pp. 45–51, Dec. 2014.

[166] H. Li, G. Gong, W. Pan, Q. Du, and J. Li, "Temperature effect on white rabbit timing link," *IEEE Transactions on Nuclear Science*, vol. 62, pp. 1021–1026, June 2015.

[167] M. Rizzi, M. Lipiński, P. Ferrari, S. Rinaldi, and A. Flammini, "White rabbit clock synchronization: Ultimate limits on close-in phase noise and short-term stability due to FPGA implementation," *IEEE Transactions on Ultrasonics, Ferroelectrics, and Frequency Control*, vol. 65, pp. 1726–1737, Sept. 2018.

[168] "Timing Characteristics of Synchronous Ethernet Equipment Slave Clock (EEC)," *ITU-T Rec. G.8262*, Aug. 2007.

[169] O. Ronen and M. Lipiński, "Enhanced synchronization accuracy in IEEE 1588," in *2015 IEEE International Symposium on Precision Clock Synchronization for Measurement, Control, and Communication (ISPCS)*, pp. 76–81, Oct. 2015.

[170] G. Daniluk and T. Włostowski, "White rabbit: Sub-nanosecond synchronization for embedded systems," in *Proceedings of the 43rd Annual Precise Time and Time Interval Systems and Applications Meeting*, Nov. 2011.

[171] "National Instruments CompactRIO 9068 Controller." [Online]. Available: http://www.ni.com/en-us/support/model.crio-9068.html. Accessed: 2019-07-01.

[172] "National Instruments NI 9467 C Series Synchronization Module." [Online]. Available: http://www.ni.com/en-us/support/model.ni-9467.html. Accessed: 2019-07-01.

[173] "Trimble Bullet III GPS Antenna." [Online]. Available: https://www.trimble.com/timing/bullet-gps-antenna.aspx. Accessed: 2019-07-01.

[174] "Tekron NTS100." [Online]. Available: https://tekron.com/news/release/tekron-nts100-network-time-server-new-product. Accessed: 2019-07-01.

[175] "CompactRIO white rabbit (CRIO-WR)." [Online]. Available: https://www.ohwr.org/projects/crio-wr/wiki. Accessed: 2019-07-01.

[176] "Seven Solutions White Rabbit Switch." [Online]. Available: http://sevensols.com/index.php/products/white-rabbit-switch/. Accessed: 2019-07-01.

[177] "Meinberg GPS180PEX: Low Profile GPS Clock." [Online]. Available: https://www.meinbergglobal.com/english/products/pci-express-gps-clock.htm. Accessed: 2019-07-01.

[178] "IEEE Guide for Phasor Data Concentrator Requirements for Power System Protection, Control, and Monitoring," *IEEE Std C37.244-2013*, pp. 1–65, May 2013.

[179] M. Adamiak, M. Kanabar, J. Rodriquez, and M. Zadeh, "Design and implementation of a synchrophasor data concentrator," in *IEEE PES Conference on Innovative Smart Grid Technologies - Middle East (ISGT Middle East), 2011*, pp. 1–5, Dec 2011.

[180] M. Kanabar, M. Adamiak, and J. Rodrigues, "Optimizing wide area measurement system architectures with advancements in phasor data concentrators (PDCs)," in *IEEE Power and Energy Society General Meeting (PES), 2013*, pp. 1–5, July 2013.

[181] Y. Guan, M. Kezunovic, A. Sprintson, and M. Yan, "Verifying interoperability and application performance of PDCs in synchrophasor system solution," in *North American Power Symposium (NAPS), 2012*, pp. 1–6, Sept 2012.

[182] H. Retty, J. Delport, and V. Centeno, "Development of tests and procedures for evaluating phasor data concentrators," in *2013 IEEE Grenoble PowerTech*, pp. 1–5, June 2013.

[183] A. Armenia and J. H. Chow, "A flexible phasor data concentrator design leveraging existing software technologies," *IEEE Transactions on Smart Grid*, vol. 1, pp. 73–81, June 2010.

[184] M. He and J. Zhang, "Deadline-aware concentration of synchrophasor data: An optimal stopping approach," in *IEEE International Conference on Smart Grid Communications (SmartGridComm), 2014*, pp. 296–301, Nov 2014.

[185] K. Zhu, M. Chenine, L. Nordström, S. Holmström, and G. Ericsson, "Design requirements of wide-area damping systems - using empirical data from a utility IP network," *IEEE Transactions on Smart Grid*, vol. 5, pp. 829–838, March 2014.

[186] K. Zhu, S. Rahimi, L. Nordström, and B. Zhang, "Design phasor data concentrator as adaptive delay buffer for wide-area damping control," *Electric Power Systems Research*, vol. 127, pp. 22 – 31, 2015.

[187] M. Chenine and L. Nordström, "Investigation of communication delays and data incompleteness in multi-PMU wide area monitoring and control systems," in *International Conference on Electric Power and Energy Conversion Systems, 2009. EPECS '09.*, pp. 1–6, Nov 2009.

[188] A. Phadke and J. Thorp, "Communication needs for wide area measurement applications," in *5th International Conference on Critical Infrastructure (CRIS), 2010*, pp. 1–7, Sept. 2010.

[189] T. Van Cutsem and C. Vournas, *Voltage stability of electric power systems*, vol. 441. Springer Science & Business Media, 1998.

[190] M. Pignati, L. Zanni, S. Sarri, R. Cherkaoui, J.-Y. Le Boudec, and M. Paolone, "A pre-estimation filtering process of bad data for linear power systems state estimators using PMUs," in *Power Systems Computation Conference (PSCC), 2014*, pp. 1–8, Aug 2014.

[191] K. D. Jones, A. Pal, and J. S. Thorp, "Methodology for performing synchrophasor data conditioning and validation," *IEEE Transactions on Power Systems*, vol. 30, pp. 1121–1130, May 2015.

[192] M. Hoefling, F. Heimgaertner, D. Fuchs, M. Menth, P. Romano, T. Tesfay, M. Paolone, J. Adolph, and V. Gronas, "Integration of IEEE C37.118 and publish/subscribe communication," in *IEEE International Conference on Communications (ICC), 2015*, pp. 764–769, June 2015.

[193] "National Instruments NI Grid Automation System." [Online]. Available: https://www.ni.com/en-us/innovations/white-papers/15/what-is-the-ni-grid-automation-system-.html. Accessed: 2019-07-01.

[194] "Cyber-secure data and control cloud for power grids." [Online]. Available: http://cdax.ilabt.imec.be. Accessed: 2019-08-01.

[195] "R-1300 series industrial-grade routers." [Online]. Available: https://www.garderos.com/products.

[196] ENTSO-E, "Frequency stability evaluation criteria for the synchronous zone of continental europe, requirements and impacting factors," tech. rep., European Network of Transmission System Operators for Electricity, RG-CE System Protection and Dynamics Sub Group, 2016.

[197] NASPI, "Data mining techniques and tools for synchrophasor data," tech. rep., NASPI Engineering Analysis Task Team, 2018.

[198] S. Murphy and B. Bengfort and M. Andersen and K. Jones, "PingThings Point-on-Wave." [Online]. Available: https://www.naspi.org/sites/default/files/2019-04/02_dominion_jones_escaping_pow_20190416.pdf, 2019. Accessed: 2019-08-01.

[199] G. Zweigle, "Streaming Time-Series Platform for Power System Operations Reliability and Resilience." [Online]. Available: https://www.naspi.org/sites/default/files/2019-04/03_sel_zweigle_streaming_time_series_20190416.pdf, 2019. Accessed: 2019-08-01.

[200] J. Follum and P. Etingov and F. Tuffner and H. Wang and U. Agrawal and D. Kosterev and S. Yang and T. Faris, "Analyzing Point-on- Wave Measurements with the Archive Walker Tool." [Online]. Available: https://www.naspi.org/sites/default/files/2019-04/04_pnnl_follum_analyzing_pow_measure_20190416.pdf, 2019. Accessed: 2019-08-01.

[201] B. Boashash, "Estimating and interpreting the instantaneous frequency of a signal. I. fundamentals," *Proceedings of the IEEE*, vol. 80, pp. 520–538, April 1992.

[202] Z. Nowomiejski, "Generalized theory of electric power," *Archiv für Elektrotechnik*, vol. 63, pp. 177–182, May 1981.

[203] P. C. See, V. C. Tai, M. Molinas, K. Uhlen, and O. B. Fosso, "Enhanced active power filter control for nonlinear non-stationary reactive power compensation," *arXiv preprint arXiv:1206.4232*, 2012.

[204] K. Strunz, R. Shintaku, and F. Gao, "Frequency-adaptive network modeling for integrative simulation of natural and envelope waveforms in power systems and circuits," *IEEE Transactions on Circuits and Systems I: Regular Papers*, vol. 53, pp. 2788–2803, Dec 2006.

[205] P. Zhang, J. R. Marti, and H. W. Dommel, "Synchronous machine modeling based on shifted frequency analysis," *IEEE Transactions on Power Systems*, vol. 22, pp. 1139–1147, Aug 2007.

[206] F. Gao and K. Strunz, "Multi-scale simulation of multi-machine power systems," *International Journal of Electrical Power and Energy Systems*, vol. 31, no. 9, pp. 538 – 545, 2009. Power Systems Computation Conference (PSCC) 2008.

[207] H. Ye and K. Strunz, "Multi-scale and frequency-dependent modeling of electric power transmission lines," *IEEE Transactions on Power Delivery*, vol. 33, pp. 32–41, Feb 2018.

[208] J. Mahseredjian, S. Dennetière, L. Dubé, B. Khodabakhchian, and L. Gérin-Lajoie, "On a new approach for the simulation of transients in power systems," *Electric Power Systems Research*, vol. 77, no. 11, pp. 1514 – 1520, 2007. Selected Topics in Power System Transients - Part II.

[209] J. Mahseredjian, "Simulation des transitoires électromagnétiques dans les réseaux électriques," *Édition Les Techniques de l'Ingénieur*, 2008.

[210] Y. Zuo, F. Sossan, M. Bozorg, and M. Paolone, "Dispatch and primary frequency control with electrochemical storage: a system-wise verification," in *2018 IEEE PES Innovative Smart Grid Technologies Conference Europe (ISGT-Europe)*, Oct. 2018.

[211] DESL-EPFL, "Extension of the IEEE 39-bus Test Network for the Study of Fundamental Dynamics of Modern Power System." [Online]. Available: https://github.com/DESL-EPFL/, 2018. Accessed: 2019-08-01.

[212] A. Ferrero and G. Superti-Furga, “A new approach to the definition of power components in three-phase systems under nonsinusoidal conditions,” *IEEE Transactions on Instrumentation and Measurement*, vol. 40, pp. 568–577, June 1991.

[213] “IEC Std 61000-4-7:2002(E),” *Part 4-7: Testing and Measurement Techniques - General Guide on Harmonics and Interharmonics Measurements and Instrumentation, for Power Supply Systems and Equipment Connected Thereto*, 2002.

[214] M. Vetterli, J. Kovačević, and V. K. Goyal, *Foundations of Signal Processing.* Cambridge University Press, Cambridge, 2014.

ASJA DERVIŠKADIĆ

+41 (0)78 733 90 44 ⋄ asja.derviskadic@gmail.com
Chemin Eugène-Grasset 10 ⋄ 1006 Lausanne, Switzerland
Nationality: Bosnia and Herzegovina ⋄ Date of birth: 19.03.1990 ⋄ Gender: Female

RESEARCH INTERESTS

- Smart grids
- Phasor Measurement Units (PMU) and synchrophasor networks
- Enhanced synchrophasor estimation algorithms for PMUs
- Time synchronization techniques for synchrophasor networks

EDUCATION

EPFL – École Polytechnique Fédérale de Lausanne September 2015 - Present
PhD in Electrical Engineering, Distributed Electrical System Laboratory *Lausanne, Switzerland*

- Thesis title: "Synchronized Sensing for Wide-Area Situational Awareness of Electrical Grids in Non-Stationary Operating Conditions" (supervisor: Prof. Mario Paolone).

Università degli Studi di Roma "La Sapienza" September 2012 - March 2015
M.Sc. in Electric Engineering *Rome, Italy*

- Thesis title: "Development of a PMU-based Real Time State Estimator of subtransmission networks: theory and experimental validation based on the Lausanne 125 kV grid" (supervisor: Prof. Fabio Massimo Gatta).
- Final mark: 110/110 with honors.

Università degli Studi di Roma "La Sapienza" September 2009 - December 2012
B.Sc. in Electric Engineering *Rome, Italy*

- Thesis title: "Design and Implementation of a Measurement System for Continuous Monitoring of the Operating Parameters of a Photovoltaic System Relevant for Fire Prevention" (supervisor: Prof. Luca Podestà)
- Final mark: 110/110.

SELECTED PUBLICATIONS

1. A. Derviškadić, P. Romano, M. Pignati, M. Paolone, "Architecture and Experimental Validation of a Low-Latency Phasor Data Concentrator," in IEEE Transactions on Smart Grid, vol. 9, no. 4, pp. 2885-2893, July 2018.
2. A. Derviškadić, P. Romano, M. Paolone, "Iterative-Interpolated DFT for Synchrophasor Estimation: A Single Algorithm for P- and M-class Compliant PMUs," in IEEE Transactions on Instrumentation and Measurements, vol. 67, no. 3, pp. 547-558, March 2018.
3. A. Derviškadić, R. Razzaghi, Q. Walger, M. Paolone, "The White Rabbit Time Synchronization Protocol for Synchrophasor Networks," in IEEE Transactions on Smart Grid, 2019.

SCIENTIFIC PUBLICATIONS

Journal papers

1. A. Derviškadić, R. Razzaghi, Q. Walger, M. Paolone, "The White Rabbit Time Synchronization Protocol for Synchrophasor Networks," in IEEE Transactions on Smart Grid, 2019.
2. Y. Zuo, G. Frigo, A. Derviškadić, M. Paolone, "Impact of Synchrophasor Estimation Algorithms in ROCOF-based Under-Frequency Load-Shedding," in IEEE Transactions on Power Systems, 2019.
3. G. Frigo, A. Derviškadić, Y. Zuo, M. Paolone, "PMU-Based ROCOF Measurements: Uncertainty Limits and Metrological Significance in Power System Applications," in IEEE Transaction on Instrumentation and Measurements, 2019.
4. G. Frigo, A. Derviškadić, D. Colangelo, J.-P. Braun, M. Paolone, "Characterization of Uncertainty Contributions in a High-Accuracy PMU Validation System," in Measurement, vol. 146, pp. 72–86, Nov. 2019.
5. G. Frigo, A. Derviškadić, M. Paolone, "Reduced Leakage Synchrophasor Estimation: Hilbert Transform Plus Interpolated DFT," in IEEE Transaction on Instrumentation and Measurements, 2018.
6. A. Derviškadić, P. Romano, M. Pignati, M. Paolone, "Architecture and Experimental Validation of a Low-Latency Phasor Data Concentrator," in IEEE Transactions on Smart Grid, vol. 9, no. 4, pp. 2885-2893, July 2018.
7. A. Derviškadić, P. Romano, M. Paolone, "Iterative-Interpolated DFT for Synchrophasor Estimation: A Single Algorithm for P- and M-class Compliant PMUs," in IEEE Transactions on Instrumentation and Measurements, vol. 67, no. 3, pp. 547-558, March 2018.
8. G. Frigo, D. Colangelo, A. Derviškadić, M. Pignati, C. Narduzzi, M. Paolone, "Definition of accurate reference synchrophasors for static and dynamic characterization of PMUs," in IEEE Transaction on Instrumentation and Measurements, vol. 66, no. 9, pp. 2233-2246, Sept. 2017.

Journal papers under revision

9. A. Derviškadić, G. Frigo, M. Paolone, "Beyond Phasors: Modeling of Power Systems Signals using the Hilbert Transform," submitted to IEEE Transactions on Power Systems, 2019.

Conference papers

10. G. Frigo, A. Derviškadić, M. Paolone, "Impact of Fundamental Frequency Definition in IpDFT-based PMU Estimates in Fault Conditions," 2019 IEEE International Workshop on Applied Measurements for Power Systems (AMPS), Aachen, 2019, pp. 1-6.
11. P. Castello, C. Muscas, P. A. Pegoraro, A. Derviškadić, G. Frigo, M. Paolone, "Real-Scenario Testing of an Active Phasor Data Concentrator," 2019 IEEE International Workshop on Applied Measurements for Power Systems (AMPS), Aachen, 2019, pp. 1-6.
12. A. Derviškadić, G. Frigo, M. Paolone, "Impact of Time Dissemination Technologies on Synchrophasor Estimation Accuracy," 2019 International Conference on Smart Grid Synchronized Measurements and Analytics (SGSMA), College Station, 2019, pp. 1-8.
13. G. Frigo, A. Derviškadić, A. Bach, M. Paolone, "Statistical Model of Measurement Noise in Real-World PMU-based Acquisitions," 2019 International Conference on Smart Grid Synchronized Measurements and Analytics (SGSMA), College Station, 2019, pp. 1-8.
14. G. Frigo, A. Derviškadić, Y. Zuo, M. Paolone, "Taylor-Fourier Model on a Real-Time Simulator: Design, Implementation and Characterization," 2019 IEEE Milano PowerTech, Milano, 2019, pp. 1-6.

15. G. Frigo, A. Derviškadić, P. A. Pegoraro, C. Muscas, M. Paolone, "Harmonic Phasor Measurements in Real-World PMU-Based Acquisitions," 2019 IEEE International Instrumentation and Measurement Technology Conference (I2MTC), Auckland, 2019, pp. 1-6.

16. A. Derviškadić, Y. Zuo, G. Frigo, M. Paolone, "Under Frequency Load Shedding Based on PMU Estimates of Frequency and ROCOF," 2018 IEEE PES Innovative Smart Grid Technologies Conference Europe (ISGT-Europe), Sarajevo, 2018, pp. 1-6.

17. G. Frigo, A. Derviškadić, C. Narduzzi, M. Paolone, "Synchrophasor- Based ROCOF Measurements: Feasibility in Real-World Scenarios," 2018 IEEE International Workshop on Applied Measurements for Power Systems (AMPS), Bologna, 2018, pp. 1-6.

18. A. Derviškadić, et Al, "Design and Experimental Validation of an LTE-Based Synchrophasor Network in a Medium Voltage Distribution Grid," 2018 Power Systems Computation Conference (PSCC), Dublin, 2018, pp. 1-7.

19. R. Razzaghi, A. Derviškadić, M. Paolone, "A White Rabbit Synchronized PMU," 2017 IEEE PES Innovative Smart Grid Technologies Conference Europe (ISGT-Europe), Torino, 2017, pp. 1-6.

20. A. Derviškadić, P. Romano, M. Paolone, "Iterative-Interpolated DFT for Synchrophasor Estimation in M-class Compliant PMUs," 2017 IEEE Manchester PowerTech, Manchester, 2017, pp. 1-6.

Conference papers under revision

21. A. Derviškadić, M. Paolone, "Design and Experimental Validation of an FPGA-based PMU Simultaneously Compliant with P and M Performance Classes," submitted to 2020 Power Systems Computation Conference (PSCC), Porto, 2020, pp. 1-7.

22. L. Zanni, A. Derviškadić, M. Pignati, C. Xu, P. Romano, R. Cherkaoui, A. Abur, M. Paolone, "PMU-based Linear State Estimation of Lausanne Subtransmission Network: Experimental Validation," submitted to 2020 Power Systems Computation Conference (PSCC), Porto, 2020, pp. 1-7.

23. Q. Walger, Y. Zuo, A. Derviškadić, G. Frigo, M. Paolone, "OPF-based Under Frequency Load Shedding Tracking the Dynamic Frequency Trajectory," submitted to 2020 Power Systems Computation Conference (PSCC), Porto, 2020, pp. 1-7.

PRESENTATIONS AT CONFERENCES AND SEMINARS

Oral Presentations

1. A. Derviškadić, G. Frigo, M. Paolone, "Synchronized Sensing for Wide-Area Situational Awareness of Electrical Grids in Non-Stationary Operating Conditions," Presented at the Joint Workshop DTU-EPFL, EPFL, Lausanne, Switzerland, September 2nd, 2019.

2. A. Derviškadić, G. Frigo, M. Paolone, "Impact of Time Dissemination Technologies on Synchrophasor Estimation Accuracy," Paper presented at the 2019 International Conference on Smart Grid Synchronized Measurements and Analytics (SGSMA), Texas A&M University, College Station, TX, USA, May 20-23, 2019.

3. A. Derviškadić, G. Frigo, M. Paolone, "Point-on-wave Data of EPFL-campus Distribution Network," Presented at the NASPI Work Group meeting, San Diego, CA, USA, April 16-17, 2019.

4. M. Paolone, A. Derviškadić, "Advancements in Smart Grids Technologies," Presented at the CERN-EPFL meeting, Geneva, Switzerland, March 28th, 2019.

5. A. Derviškadić, G. Frigo, M. Paolone, "Real-time Situational Awareness in Modern Power Grids via Phasor Measurement Units," Presented at the DESL-PV lab Common Workshop, CSEM, Neuchâtel, Switzerland, January 22nd, 2019.

6. A. Derviškadić, et Al, “Design and Experimental Validation of an LTE-Based Synchrophasor Network in a Medium Voltage Distribution Grid,” Paper presented at the 2018 Power Systems Computation Conference (PSCC), University College Dublin, Dublin, Ireland, June 11-15, 2018.
7. A. Derviškadić, P. Romano, R. Razzaghi, M. Pignati, M. Paolone, “High-Performance PMUs for the Monitoring of Active Distribution Networks: new Synchrophasor Extraction Techniques and Time Dissemination,” Presented at the QEERI – EPFL Workshop, Hamad Bin Khalifa University (HBKU) Research and Development Complex, Doha, Qatar, May 2-3, 2018.
8. A. Derviškadić, Y. Zuo, G. Frigo, M. Paolone, “Under-Frequency Load Shedding based on PMU Frequency and ROCOF Measurement,” Presented at the NASPI Work Group meeting, Albuquerque, NM, USA, April 24-26, 2018.
9. A. Derviškadić, P. Romano, M. Paolone, “Iterative-Interpolated DFT for Synchrophasor Estimation in M-class compliant PMUs,” Paper presented at the 2017 IEEE Manchester PowerTech, University of Manchester, Manchester, UK, June 18-22, 2017.
10. A. Derviškadić, P. Romano, M. Pignati, M. Paolone, “Architecture and Experimental Validation of a Low-Latency Phasor Data Concentrator,” IEEE Transactions on Smart Grid paper presented at the 2017 IEEE Manchester PowerTech, University of Manchester, Manchester, UK, June 18-22, 2017.
11. R. Razzaghi, A. Derviškadić, M. Paolone, “A White Rabbit Synchronized PMU,” Paper presented at the 2017 IEEE PES Innovative Smart Grid Technologies Conference Europe (ISGT-Europe), Politecnico di Torino, Torino, Italy, September 26-29, 2017.
12. A. Derviškadić, M. Paolone, “A Highly Accurate Calibration System for PMUs Operating in Distribution Networks,” Presented at the combined final dissemination workshop of SmartGrid-II, FutureGrid and GridSens projects, Metrology for future smart grid technologies, Haarlem, The Netherlands, April 18-20, 2017.
13. A. Derviškadić, R. Razzaghi, M. Paolone, “A White Rabbit Synchronized PMU,” Presented at the NASPI Work Group meeting, National Institute of Standards and Technology (NIST), Gaithersburg, MD, USA, March 22-23, 2017.
14. A. Derviškadić, M. Paolone, “Synchrophasor Network and Low-Latency Phasor Data Concentrator,” Presented at the workshop PMU-based Real-Time State Estimation of the 125 kV Subtransmission Network of Lausanne, Lausanne, Switzerland, December 5th, 2016.
15. D. Colangelo, G. Frigo, A. Derviškadić, “Measurement Tools for Smart Grid Stability and Quality,” Presented at the ENG52 Smart Grids II M30 meeting, Istituto Nazionale di Ricerca Metrologica (INRIM), Torino, Italia, 18-19 October 2016,

Poster Presentations

16. A. Derviškadić, G. Frigo, M. Paolone, “Point-on-wave Data of EPFL-campus Distribution Network,” Presented at the NASPI Work Group meeting, San Diego, CA, USA, April 16-17, 2019.
17. A. Derviškadić, Y. Zuo, G. Frigo, M. Paolone, “Under Frequency Load Shedding based on PMU Estimates of Frequency and ROCOF,” Paper presented at the 2018 IEEE PES Innovative Smart Grid Technologies Conference Europe (ISGT-Europe), Sarajevo, Bosnia and Herzegovina, October 21-25, 2018.
18. A. Derviškadić, P. Romano, M. Paolone, “Iterative-Interpolated DFT for Synchrophasor Estimation: A single Algorithm for P- and M-Class Compliant PMUs,” IEEE Transactions on Instrumentation and Measurements paper presented at the IEEE International Instrumentation and Measurement Technology Conference (I2MTC), Houston, TX, USA, May 14-17, 2018.

19. A. Derviškadić, Y. Zuo, G. Frigo, M. Paolone, "Under-Frequency Load Shedding based on PMU Frequency and ROCOF Measurement," Presented at the NASPI Work Group meeting, Albuquerque, NM, USA, April 24-26, 2018.
20. A. Derviškadić, R. Razzaghi, M. Paolone, "A White Rabbit Synchronized PMU," Presented at the 2017 SCCER-FURIES Annual Conference, EPFL, Lausanne, Switzerland, November 2nd, 2017.
21. A. Derviškadić, P. Romano, M. Paolone, "Iterative-Interpolated DFT for Synchrophasor Estimation in M-class compliant PMUs," Presented at the 2016 SCCER-FURIES Annual Conference, EPFL, Lausanne, Switzerland, December 2nd, 2016.
22. A. Derviškadić, P. Romano, M. Pignati, M. Paolone, "Architecture and Experimental Validation of a Low-Latency Phasor Data Concentrator," Presented at the 2016 SCCER-FURIES Annual Conference, EPFL, Lausanne, Switzerland, December 2nd, 2016.
23. P. Romano, A. Derviškadić, L. Zanni, M. Pignati, J.-Y. Le Boudec, M. Paolone, "Real-Time State Estimation of the EPFL-campus Medium Voltage Grid by using PMUs," Presented at the 2015 SCCER-FURIES Annual Conference, EPFL, Lausanne, Switzerland, November 25th, 2015.
24. A. Derviškadić, P. Romano, L. Zanni, M. Pignati, R. Cherkaoui, M. Paolone, "Real Time Monitoring of the Lausanne 125 kV Subtransmission Network using PMUs," Presented at the 2015 SCCER-FURIES Annual Conference, EPFL, Lausanne, Switzerland, November 25th, 2015.

AWARDS

Best Poster Award at the 2015 SCCER-FURIES Annual Conference: P. Romano, A. Derviškadić, L. Zanni, M. Pignati, J.-Y. Le Boudec, M. Paolone, "Real-Time State Estimation of the EPFL-campus Medium Voltage Grid by using PMUs," Lausanne, Nov. 2015.

PATENTS

A. Derviškadić, P. Romano, M. Paolone, "Method for estimating synchrophasors during static and dynamic conditions," patent filed, International Patent Application n°PCT/IB2017/053414, June 2017.

INVOLVEMENT IN RESEARCH PROJECTS

ENG52 SmartGrid II September 2015 - May 2017

- Measurement tools for smart grid stability and quality
- Development of new calibration methods and technologies for Phasor Measurement Unit (PMU) expected to operate in distribution networks.

SiL RT-PMU September 2014 - January 2017

- Real-time state estimation of the 125 kV sub-transmission network of Lausanne operated by Services industriels de Lausanne (SiL) by means of Phasor Measurement Units (PMUs).

QEERI Smart Grid April 2016 - April 2019

- Development of new synchrophasor estimation methods and technologies for Phasor Measurement Units (PMUS) expected to operate in distribution networks.
- Integration of innovative time dissemination technologies in synchrophasor networks.

LANGUAGE SKILLS

Italian and Bosnian	Mother tongue.
English	Full professional proficiency.
French	Conversant.
German and Chinese	Learner.

UNIVERSITY SERVICE

Member of the EPFL-EDEE Student Commitee November 2016 - August 2019

- Proposing improvements to the Electrical Engineering Doctoral Program (EDEE) with the Doctoral Programme Director (Prof. Pascal Frossard and Prof. Anja Skrivervik)
- Organization of networking and scientific events, seeking to create a strong community among EDEE doctoral students

TEACHING EXPERIENCE

- Teaching Assistant for the “Smart Grids Technologies” course, M.Sc. in Electrical Engineering, EPFL, 2016-present.
- Teaching Assistant for the “Distribution de l’énergie électrique” course (Power distribution networks), B.Sc. in Electrical Engineering, EPFL, 2017-present.
- Teaching Assistant for the “Laboratory in energy conversion” course, B.Sc. in Electrical Engineering, EPFL, 2018-present.

SUPERVISED STUDENT PROJECTS

- Q. Walger, “OPF-based Under Frequency Load Shedding using Phasor Measurement Units,” Master Semester project, Summer 2018-2019.
- D. Incesu, “Synchronized High Accuracy Voltage Generation and Acquisition for Phasor Measurement Unit Calibration,” Bachelor Semester project, Summer 2018-2019.
- L. Couelle, “Uncertainty and Stability in Time Dissemination Technologies for Synchrophasor Extraction” Bachelor Semester project, Summer 2018-2019.
- K. De Gol, “Analysis of Power Signal Disturbances in Real-World Distribution Networks,” Master Semester project, Fall 2018-2019.
- A. Bach, “Integration of a csTFM-based Phasor Measurement Unit into a Real-Time Simulator,” Master Semester project, Spring 2017-2018.
- B. Marques, “Characterization of Time and Phase Reference Uncertainty of a Phasor Measurement Unit Calibrator,” Bachelor Semester project, Spring 2017-2018.
- Q. Walger, “Using the White Rabbit Time Synchronization Protocol in FPGA-based Phasor Measurement Unit,” Bachelor Semester project, Spring 2016-2017.
- R. Daher, “Determine the Electrical Model of Lausanne 125 kV grid,” Bachelor Semester project, Fall 2015-2016.

PEER REVIEWS

- Elsevier Sustainable Energy, Grids and Networks Journal, since 2017
- IEEE Transactions on Instrumentation and Measurement, Smart Grid, Power Systems, Industrial Electronics, since 2017
- IEEE Power Engineering Letters, since 2017
- IET Generation, Transmission & Distribution, since 2018
- IEEE PowerTech Conference, 2017 and 2019
- Power Systems Computation Conference (PSCC), 2018
- Smart Grid Synchronized Measurements and Analytics Conference (SGSMA), 2019
- IEEE PES Innovative Smart Grid Technologies Conference (ISGT), 2017 and 2018

Ce document a été imprimé au Centre d'impression EPFL,
imprimerie climatiquement neutre, certifiée myClimate.